Multifunctional Graphene Oxide Nanomedicine for Breast Cancer Therapy

THESIS

Submitted in partial fulfillment

of the requirements for the degree of

DOCTOR OF PHILOSOPHY

By

ASIF MOHD ITOO

ID. No. 2019PHXF0452H

Under the Supervision of

Prof. Swati Biswas

BIRLA INSTITUTE OF TECHNOLOGY AND SCIENCE, PILANI

2024

BIRLA INSTITUTE OF TECHNOLOGY AND SCIENCE, PILANI

CERTIFICATE

This is to certify that the thesis titled "**Multifunctional Graphene Oxide Nanomedicine for Breast Cancer Therapy**," submitted by **ASIF MOHD ITOO**, ID No. **2019PHXF0452H**, for an award of a Ph.D. from the Institute, embodies original work done by him under my supervision.

Signature of the Supervisor:

Name in capital letters: SWATI BISWAS

Designation **:** Professor

Date **:** 24th May 2024

DECLARATION

I declare that this thesis has been composed solely by myself and that it has not been submitted, in whole or in part, in any previous application for a degree. The content of the thesis is original and is the outcome of my research work. Any relevant material taken from the open literature has been referred to and cited, as per established ethical norms and practices.

Asif Mohd Itoo

Acknowledgement

The satisfaction that accompanies the successful completion of any task is incomplete without the mention of the names of those people who made it possible in time with their blessings, guidance, support, instrumental help, and/or revitalizing tasks.

First and foremost, I would like to thank the almighty Allah for providing me with the patience and strength to undertake this research.

I would like to express my heartfelt gratitude to all those who have contributed to the successful completion of this thesis. I extend my deepest gratitude to my thesis supervisor, Prof. Swati Biswas, for her unwavering support, invaluable insights, and constant encouragement throughout this research journey. As I reflect on the completion of this significant milestone, I am extremely aware that her mentorship has been the cornerstone of my success. From the inception of this research endeavour to its culmination, her expertise, wisdom, and encouragement have been instrumental in shaping both the trajectory of my work and my growth as a researcher. Her dedication to excellence and commitment to fostering a nurturing research environment has created an atmosphere where intellectual curiosity thrives, and I have been fortunate to be a beneficiary of this. Her keen insights and constructive feedback have not only refined the scholarly aspects of my thesis but have also challenged me to think critically and approach challenges with resilience. Her mentorship extended beyond the academic realm, as she generously shared her experiences, offered valuable life lessons, and provided unwavering support during moments of doubt. I am profoundly grateful for the countless h that she devoted to discussions, the patience with which she addressed my queries, and the genuine interest that she took in my progress. Respected ma’am, your mentorship has been a guiding light, illuminating the path to success and instilling in me a sense of confidence and purpose. I am truly grateful for the privilege of having you as my supervisor.

I am deeply grateful to my mentor, Prof. Balaram Ghosh, whose unparalleled guidance and unwavering support have been the cornerstone of my academic journey. Your profound expertise, patience, and enthusiasm for the subject matter have continuously inspired and motivated me to pursue excellence. Throughout the research process, you have consistently provided valuable insights, pushing me to explore new avenues of thought and encouraging me to embrace challenges as opportunities for growth. Your mentorship extended beyond the realms of academia, as you generously shared your wisdom, offering invaluable career advice and cultivating essential skills that will undoubtedly shape my future endeavours. I am truly fortunate to have had such an exceptional mentor who not only believed in my potential but also invested wholeheartedly in my professional development. You have always created a friendly, conducive environment in the laboratory and made my time memorable at BITS-Pilani. My thesis would not have reached its fruition without your mentorship, and for that, I extend my deepest appreciation and gratitude.

I am wholeheartedly thankful to Prof. Balaram Ghosh, Department of Pharmacy, BITS-Pilani, Hyderabad campus, who acted as a Doctoral Advisory Committee (DAC) member for his detailed, constructive comments and support throughout this work.

I wish to express my warm and sincere thanks to Prof. Onkar Kulkarni, Department of Pharmacy, BITS-Pilani, Hyderabad campus, who acted as a Doctoral Advisory Committee (DAC) member for his suggestions and invaluable time to review my dissertation report.

I wish to express my gratitude to Prof. Ahmed Kamal, Prof. D. Sriram, Prof. P. Yogeeswari, Prof. Punna Rao Ravi, Prof. Onkar Prakash Kulkarni, Prof. Arti Dhar, Dr. Akash Chaurasiya, Dr. Nirmal Jain, Dr. Srinivas Prasad K, Dr. Abhijeet Rajendra Joshi, and Dr. Yuvraj Singh for giving me unrestricted access to use instruments and facilities in laboratories.

I also express my profound gratitude to Prof. Sajeli Begum, Professor and Head of the Department of Pharmacy, for her support and for extending the facilities to work at the institute.

It is my duty to express my sincere thanks to the Chancellor, BITS-Pilani for providing the necessary infrastructural support to carry out my research work. I am sincerely thankful to Prof. Soumyo Mukherji, Director; Prof. V. Ramgopal Rao, Vice-Chancellor; Col Soumyabrata Chakraborty (Retd), Registrar; Prof. Venkata Vamsi Krishna Venuganti, Dean, Academic - Graduate Studies and Research; Prof. Alivelu Manga Parimi, Associate Dean, Academic - Graduate Studies and Research; and Prof. P. Yogeeswari, Dean, General Administration for facilitating my research work at the institute.

I would like to thank the central analytical laboratory of BITS-Pilani, Hyderabad Campus, for providing me with a scientific platform to excel in my career.

I am fortunate to have met nice colleagues and lab mates on the BITS Pilani campus, where I got an opportunity to work with them on various occasions. I am grateful to Mr. Milan Paul, Mrs. Sri Ganga, Mr. Nageswara Rao, Mr. Praful, Ms. Varshini, Mr. Naitik, Ms. Shishira, Mr. Tarun, Ms. Himaja, Mr. Sanjeev, Ms. Darakshan begum, and Ms. Nikitha. Thanks, all of you, for your remembrance and for being a source of happiness.

I express my sincere thanks to seniors Dr. Himanshu Bhatt, Dr. Soniya Kumbham, Ch Sai Sanjay, and Dr. Yamini Bobde, Dr. Sravani, Dr. Ganesh, who were very supportive, their attention and timely concern for my Ph.D. gave me a lot of enthusiasm.

I am thankful to Mrs. Sarita, Mrs. Rekha, Mrs. Sunita, Mr. Rajesh, Mr. Upalaiah, Mr. Mallesh, Mr. Kumar, Mr. Narsimha, and Mr. Tirumalaiah for their kind cooperation during the lab in the entire tenure of my Ph.D.

I am indebted to the BITS-Pilani Hyderabad campus and Lady Tata Memorial Trust for providing me with a scholarship and necessary financial support to pursue my Ph.D. work without any hindrance.

I would like to thank everybody who was important in the successful completion of this research work that I may have inadvertently failed to mention.

Above all, what I am today is because of the love, care, support, and blessings of my father Gh Nabi Itoo, and my mother, Late Shafiqa Akther, who always supported me and gave me the freedom to choose my own goals and then helped me to achieve those goals.

I don’t have words to express my feelings towards my sisters, Rohie Jan, Beauty Jan, and Nelofar Nabi, to whom I am heavily in debt for the love and affection showered on me, which has contributed in a big way in achieving this goal.

Asif Mohd Itoo

ABSTRACT

Breast cancer (BC) is the most prevalent form of cancer in women globally, accounting for 266,120 new cases and 40,920 fatalities per year (V. Thakur & Kutty, 2019). The prevalence of BC poses a notable public health issue, anticipating that approximately 12.5% of women in the United States will experience the onset of invasive BC over the course of their lives (Alkabban & Ferguson, 2019). In 2023, the United States had 55,720 newly diagnosed instances of *in situ* BC and 297,790 newly diagnosed cases of invasive BC, as per recent estimates (Alkabban & Ferguson, 2019; Giaquinto et al., 2022; Siegel et al., 2023). Presently, BC is commonly treated through a variety of methods, including surgical intervention, hormonal therapy, radiation therapy, chemotherapy, immunotherapy, and targeted therapies (Giaquinto et al., 2022; Siegel et al., 2023). The process of targeted drug delivery entails the utilization of specialized carriers, including antibodies, vitamins, and peptides, to convey drugs to tumor sites with precision while simultaneously reducing the exposure of healthy tissues to the drugs (Zhong et al., 2014). Among the highly targeted, selective, and successful anticancer therapies, photothermal therapy (PTT) is another therapeutic modality that uses photothermal conversion agents to convert light energy into heat, resulting in the localized killing of cancer cells. Because of its specificity in both place and time, as well as its synergistic benefits and low invasiveness, this method has attracted attention as an innovative treatment option (Rajani et al., 2020; Zou et al., 2016). Nanoparticle-based drug delivery systems (NDDSs) have shown significant promise for cancer treatment by enabling specific targeting of tumors, enhancing drug stability, increasing circulation half-life, improving bioavailability, improving intracellular trafficking, reducing toxicity while boosting the efficacy of chemotherapeutic agents, and the capacity to get around biological restrictions.

First, A bioinspired chitosan/vitamin E conjugate (Ch/VES, 1:4) was synthesized, optimized based on chitosan's molecular weight (15, 300 KDa), and was assembled to entrap oxaliplatin

(OXPt). ^{1}H NMR, infrared spectroscopy, chromatography, X-ray photoelectron spectroscopy, X-ray diffraction, drug release, hemolysis, and stability studies were performed to characterize OXPt@Ch/VES micelles. The therapeutic efficacy of the micelles was tested *in vitro* in ER+/PR+/HER2- and triple-negative sensitive/resistant breast cancer cells, MCF-7 and MDA-MB-231 via cellular uptake, cytotoxicity, nuclear staining, DNA fragmentation, mitochondrial membrane potential, ROS generation, apoptosis, and cell cycle assays and *in vivo* using 4T1(Luc)-tumor-bearing mice. OXPt@Ch/VES Ms exhibited decreased IC50 towards MCF-7, MDA-MB-231 (sensitive/ resistant) than OXPt. OXPt@Ch/VES Ms caused extensive DNA damage, mitochondrial depolarization, apoptosis, and cell-growth arrest (G2/M). OXPt@Ch/VES Ms treatment retarded tumor growth significantly, prolonged survival, and decreased nephrotoxicity than OXPt. The OXPt@Ch/VES Ms could serve as a potential nanomedicine to overcome conventional OXPt-mediated drug resistance/ nephrotoxicity in breast cancer.

Secondly, combining photothermal and chemotherapy is an emerging strategy for tumor irradiation in a minimally invasive manner, utilizing photothermal transduction agents and anticancer drugs. The present work developed a 2D carbon nanomaterial graphene oxide (GO)-based nanoplatform that converted to 3D colloidal spherical structures upon functionalization with an amphiphilic polymer mPEG-PLA (1: 0.5/1/2) and entrapped doxorubicin (Dox) physically. The Dox@GO(mPP) (1/0.5) NPs displayed the least particle size (161 nm), the highest stability with no aggregation, the highest Dox loading (6.3 %) and encapsulation efficiency (70 %). The therapeutic efficacy was determined *in vitro* and *in vivo* using murine (4T1) and human triple-negative breast cancer cells (MDA-MB-231), and 4T1-Luc-tumor bearing mouse models. The results demonstrated that the Dox@GO(mPP) (1/0.5) NPs treatment with laser (+L) (808 nm) was highly efficient in inducing apoptosis, cell cycle arrest (G2/M) phase, significant cytotoxicity, mitochondrial membrane depolarization, ROS

generation, and photothermal effect leading to a higher proportion of cell death than free Dox, and Dox@GO(mPP) (1/0.5) NPs (-L). The anticancer studies in mice harboring the 4T1-Luc tumor showed that a combination of Dox@GO(mPP) (1/0.5) NPs (+L) effectively reduced tumor development and decreased lung metastasis. The developed nanoplatform could be a promising combination chemo-photothermal treatment option for triple-negative breast cancer. Thirdly, Graphene oxide (GO) and GO-based nanocomposites provide excellent promise in drug delivery and photothermal therapy due to their exceptional near-infrared optical absorption and high specific surface area. In this study, we have effectively conjugated an oxaliplatin (IV) prodrug, PEGylated graphene oxide, and PEGylated biotin (PB) in a single platform for breast cancer treatment. This platform demonstrates promising prospects for targeted drug delivery and the synergistic application of photothermal-chemotherapy when exposed to NIR-laser irradiation. The resulting nanocomposite (GO(OX)PB (1/1/0.2) NPs) displayed an exceptionally large surface area, minimal particle size (195.7 nm), specific targeting capabilities, a high drug load capacity (43.56 %) and entrapment efficiency (89.48 %) and exhibit excellent photothermal conversion efficiency and photostability when exposed to NIR-laser irradiation (808 nm). The therapeutic effectiveness was assessed both *in vitro* and *in vivo* conditions employing human breast cancer cells (MCF-7), mouse mammary gland adenocarcinoma cells (4T1), and 4T1-Luc tumor-bearing mouse models. The findings demonstrated that GO(OX)PB (1/1/0.2) NPs (+L) were highly effective in causing significant cytotoxicity, G2/M phase cell cycle arrest, ROS generation, mitochondrial membrane depolarization, apoptosis, and photothermal effect. This resulted in a greater percentage of cell death compared to free OX, GO(OX)PEG (1/1/0.2) NPs (±L), and GO(OX)PB (1/1/0.2) NPs (−L). The *in vivo* therapeutic studies on 4T1-Luc tumor-bearing mice revealed that a combination of GO(OX)PB (1/1/0.2) NPs (+L) caused complete destruction of the tumor, no tumor recurrence, prolonged survival, reduced lung metastasis, and mitigated nephrotoxicity.

The examination of serum and blood components demonstrated minimal systemic toxicity of GO(OX)PB (1/1/0.2) NPs. The developed nanoplatform, in this context, may serve as a potential nanomedicine to address conventional nephrotoxicity in breast cancer and prevent metastasis by combining chemo-photothermal therapy.

CONTENTS

Certificate……...i

Acknowledgement……ii-vi

Abstract……...vi-x

Table of contents…….……....xi-xx

List of Tables ……...xx-xxii

List of Figures……...…….xxiii-xxviii

List of Abbreviations ……..……...xxix-xxx

Chapter 1 ..... ***1***

1. Introduction..... ***2***

1.1 Pathogenesis of breast cancer ***9***

1.2 Risk Factors of Breast Cancer..... ***10***

1.2.1 Aging..... 11

1.2.2 Family history 11

1.2.3 Reproductive factors 12

1.2.4 Estrogen..... 12

1.2.5 Lifestyle..... 13

1.2.6 Genes related to breast cancer. 14

1.3 Current common treatment strategies of breast cancer ***16***

1.3.1 Systemic treatment of BC 16

1.3.1.1 Chemotherapy 16

1.3.1.2 Endocrine Therapy 17

1.3.1.3 HER2 targeted therapy 17

1.3.1.4 Immunotherapy 18

1.3.2 Local treatment and local therapy of BC 18

1.3.2.1 Surgery 18

1.3.2.2 Radiotherapy 19

1.4 Obstacles of current treatment strategies of BC ***19***

1.5 Nanomedicine-based approaches for breast cancer ***22***

1.5.1 Organic NDDS 23

1.5.1.1 Liposomes 24

1.5.1.2 Micelles 25

1.5.1.3 Polymeric Nanoparticles 26

1.5.1.4 Solid lipid nanoparticles (SLNs) 28

1.5.1.5 Dendrimers 28

1.5.2 Inorganic NDDS 29

1.5.2.1 Gold Nanoparticles 30

1.5.2.2 Mesoporous silica NPs (MSN) 31

1.5.2.3 Magnetic iron oxide NPs 32

1.5.2.4 Nanotubes 32

1.5.2.5 Quantum dots (QDs) 33

1.5.2.6 Graphene 34

1.6 Graphene oxide as a drug delivery cargo ***36***

1.6.1 Loading ability 36

1.6.2 Mechanism of loading 37

1.6.2.1 Covalent interaction 37

1.6.2.2 Noncovalent interaction 40

1.6.3 Stability information 42

1.6.4 Mechanism of targeting 43

1.6.4.1 Passive Targeting 43

1.6.4.2 Active Targeting 46

1.6.4.3 Tumor microenvironment targeting 48

1.6.4.4 Receptor-mediated internalization 49

1.6.4.5 Organelle specific Targeting 51

1.6.5 Multifunctional graphene oxide applications 53

1.6.5.1 Cancer-targeted graphene oxide 53

1.6.5.1 Bioimaging/theranostic applications 53

1.6.5.2 Chemo-photothermal therapy 54

1.6.5.3 Chemo-photodynamic therapy 55

1.6.5.4 Drug/gene delivery applications 56

1.7 Doxorubicin as anticancer agent ***57***

1.7.1 Physicochemical properties of doxorubicin 57

1.8 Oxaliplatin as anticancer agen*t* ***58***

1.8.1 Physicochemical properties of Oxaliplatin 61

Chapter 2 Oxaliplatin delivery via chitosan/vitamin E conjugate based nanoassembly for improved efficacy and MDR-reversal in breast cancer ***64***

2.1 Introduction ***65***

2.2 Materials and methods ***68***

2.2.1 Materials 68

2.2.2 Methods ***69***

2.2.2.1 Synthesis and characterization of Chitosan-Vitamin E succinate (Ch/$(VES)_4$) conjugates 69

2.2.3 Preparation and characterization of OXPt@Ch/VES micelles ***72***

2.2.3.1 Preparation of OXPt@Ch/VES micelles 72

2.2.3.2 Physico-chemical characterization of OXPt@Ch/VES micelles: size, surface charge, morphology, drug loading (DL), and entrapment efficiency (EE) 72

2.2.3.3 Kinetic stability Analysis 73

2.2.3.4 Differential scanning calorimetry (DSC) 73

2.2.3.5 X-ray diffraction (XRD) 74

2.2.3.6 X-ray photon electron spectroscopy (XPS) Analysis 74

2.2.4 In-vitro release study ***74***

2.2.5 Hemolysis test ***75***

2.2.6 Cell culture ***75***

2.2.6.1 Cellular uptake 75

2.2.6.2 *In vitro* cytotoxicity study 76

2.2.6.3 Annexin V assay 76

2.2.6.4 Cell cycle analysis 77

2.2.6.5 DNA fragmentation assay 77

2.2.6.6 Nuclear Staining assay 78

2.2.6.7 ROS detection assay 78

2.2.6.8 Mitochondrial membrane potential study 78

2.2.6.9 Generation of OXPt-resistant cells 79

2.2.6.10 Platinum content in the cell 79

2.2.6.11 Anti P-glycoprotein efficacy studies 79

2.2.7 In vivo study ***80***

2.2.7.1 Pharmacokinetic study 80

2.2.7.2 Determination of Therapeutic efficacy *in vivo* 80

2.2.7.3 *In vivo* Fluorescence imaging analysis 81

2.2.8 Immunohistochemistry ***81***

2.2.8.1 TUNEL Assay in Tumor Cryosections 81

2.2.8.2 ROS Production in Tumor Tissues 82

2.2.8.3 Immuno-histochemical analysis of Ki67 82

2.2.8.4 H & E staining 82

2.2.9 Statistics 83

2.3. Results & Discussion ***83***

2.3.1. Physicochemical Characterization of the Ch/$(VES)_4$ conjugate and OXPt@Ch/VES Ms 83

2.3.2. In vitro assays ***95***

2.3.2.1 Cellular uptake 95

2.3.2.2 *In vitro* cytotoxicity 96

2.3.2.3 Apoptosis assay 99

2.3.2.4 Cell cycle analysis 100

2.3.2.5 DNA fragmentation study and nuclear staining 102

2.3.2.6 Mitochondria membrane potential (MMP) and ROS detection assay 102

2.3.2.7 Anti P-glycoprotein efficacy study and platinum content in the cell 103

2.3.3 Pharmacokinetic study ***103***

2.3.4 In vivo study ***105***

2.3.4.1 Tumor Inhibition Study 105

2.3.5 Immunohistochemistry ***107***

2.3.5.1 TUNEL Assay on Tumor Cryosections. 107

2.3.5.2 ROS Production in Tumor Tissues 108

2.3.5.3 Immuno-histochemical analysis of Ki67 108

2.4. Conclusion 109

2.5 Acknowledgment ***110***

Chapter 3 Polymeric graphene oxide nanoparticles loaded with doxorubicin for combined photothermal and chemotherapy in triple negative breast cancer ***111***

3.1 Introduction ***112***

3.2. Materials and methods ***115***

3.2.1 Materials 115

3.2.2 Methods ***116***

3.2.2.1 Synthesis of Graphene oxide 116

3.2.2.2 Synthesis of mPEG-PLA di-block copolymer 116

3.2.2.3 Synthesis and characterization of GO(mPP) Conjugate 117

3.2.3 Preparation and characterization of Dox@GO(mPP) NPs ***118***

3.2.3.1 Preparation of Dox@GO(mPP) NPs 118

3.2.3.2 Physico-chemical characterization of Dox@GO(mPP) NPs 118

3.2.3.3 Kinetic stability analysis 119

3.2.3.4 Differential scanning calorimetry (DSC) and thermogravimetric analysis (TGA) 119

3.2.3.5 XRD analysis.....120

3.2.3.6 X-ray photoelectron spectroscopy (XPS) analysis.....120

3.2.3.7 Photothermal heating effect. 120

3.2.3.8 *In vitro* drug release study.....120

3.2.3.9 Hemolysis study 121

3.2.3.10 Cyclic voltammetry.....122

***3.2.4 Cell culture studies*.....122**

3.2.4.1 *In vitro* cell cytotoxicity assay 122

3.2.4.2 Cellular uptake studies 123

3.2.4.3 Annexin V assay.....123

3.2.4.5 Cell cycle analysis.....124

3.2.4.6 Reactive oxygen species (ROS) assay 125

3.2.4.7 Mitochondrial membrane potential (MMP) Study.....125

3.2.4.8 Nuclear staining assay.....126

3.2.5 *In vivo* studies.....126

3.2.5.1 Pharmacokinetic (pK) study.....126

3.2.5.2 Determination of *in vivo* therapeutic efficacy, *in vivo* fluorescence imaging, and biodistribution analysis 127

***3.2.6 Immunohistochemistry* 128**

3.2.6.1 TUNEL assay 128

3.2.6.2 Immuno-histochemical analysis for hematoxylin & eosin (H&E) staining and Ki-67 129

3.2.6.3 ROS production in tumor tissues 130

3.2.7 Statistics 130

***3.3.0 Results and Discussion* 130**

3.3.1 Physiochemical characterization of Dox@GO(mPP) NPs 130
3.3.1.1 XRD analysis.....132
3.3.1.2 FTIR analysis 133
3.3.1.3 XPS analysis.....134
3.3.1.4 UV analysis 135
3.3.1.5 Cyclic voltammetry.....136
3.3.1.6 Entrapment efficiency (% EE) and drug loading (% DL).....137
3.3.1.7 Particle size and zeta potential 139
3.3.1.8 DSC and TGA analysis 141
3.3.1.9 *In vitro* drug release.....142
3.3.1.10 Hemolysis study 143
3.3.2 Photothermal heating effect ***143***
3.3.3 In vitro assays.....***148***
3.3.3.1 Cellular uptake study, intracellular ROS generation, and MTT assay.....148
3.3.3.2 Nuclear staining assay.....152
3.3.3.3 Annexin V-FITC/propidium iodide apoptosis assay.....153
3.3.3.4 Cell cycle analysis and mitochondria membrane potential (MMP) study 153
3.3.4 Pharmacokinetic Study.....***156***
3.3.5 In vivo biodistribution.....***157***
3.3.6 In vivo antitumor activity of Dox@GO(mPP) (1/0.5) NPs ***159***
3.3.6.1 In vivo fluorescence imaging.....***162***
3.3.6.2 Immuno-histochemical analysis.....***163***
3.3.6.3 Metastasis study.....***165***
3.4. Conclusion.....***167***
3.5 Acknowledgments.....***168***
Chapter 4 Biotinylated graphene oxide-conjugated platinum (IV) prodrug nanoparticles for targeted and chemophothermal combination therapy in breast cancer ***169***

4.1 Introduction ***170***

4.2. Materials and methods ***173***

4.2.1 Materials 173

4.2.2 Methods ***174***

4.2.2.1 Synthesis of Graphene oxide (GO) 174

4.2.2.2 Synthesis of Oxaliplatin prodrug, OX(IV) 174

4.2.2.3 Synthesis of GO(OX)(IV) Conjugate 175

4.2.2.4 Synthesis of Pegylated Biotin (PB) copolymer 175

4.2.2.5 Synthesis of GO(OX)PEG conjugate 176

4.2.2.6 Synthesis of GO(OX)PB conjugate 176

4.2.3 Preparation and characterization of GO(OX)PB NPs ***177***

4,2.3.1 Preparation of GO(OX)PB NPs 177

4.2.3.2 Physico-chemical characterization of GO(OX)PB NPs 177

4.2.3.3 Thermal Analysis 178

4.2.3.4 X-ray Diffractometry (XRD) analysis 179

4.2.4.5 X-ray photoelectron spectroscopy 179

4.2.4.6 Raman Spectroscopy 179

4.2.4.7 *In vitro* drug release study 180

4.2.4.8 Hemolysis study 180

4.2.5 Photothermal effect ***181***

4.2.6 In vitro cell culture studies ***182***

4.2.6.1 Combined chemo and photothermal therapy effects *in vitro* 182

4.2.6.2 Cellular uptake study 183

4.2.6.3 Raman spectra analysis of GO inside cells 185

4.2.6.4 *In vitro* cell Platinum content 185

4.2.6.5 Live/Dead cell assay 185

4.2.6.6 Mitochondrial membrane potential (MMP) study and Reactive oxygen species (ROS) assay 186

4.2.6.7 Annexin V assay 187

4.2.6.8 Cell cycle analysis 188

4.2.7 In vivo studies ***188***

4.2.7.1. Pharmacokinetic (pk) study 188

4.2.7.2. Nephrotoxicity study 189

4.2.7.3 *In vivo* therapeutic efficacy, *in vivo* fluorescence imaging, and biodistribution analysis 190

4.2.8 Immunohistochemistry ***191***

4.2.8.1 TUNEL assay 191

4.2.8.2 ROS production and immune-histochemical analysis of Ki-67 in tumor tissue 192

4.2.8.3 Hematoxylin and Eosin (H&E) staining 192

4.2.9 Statistics 193

4.3 Results and Discussion ***193***

4.3.1 Preparation and Characterization of GO(OX)PB (1/1/0.2) NPs 193

4.3.2 Photothermal effect of GO(OX)PB (1/1/0.2) NPs ***216***

4.3.3 In vitro assays ***218***

4.3.3.1 Cellular internalization studies 218

4.3.3.2 Cytotoxicity study and live/dead cell assay 225

4.3.3.3 Intracellular ROS generation assay, Mitochondria Membrane Potential (MMP) study, and Annexin V assay 229

4.3.3.4 Cell cycle analysis 230

4.3.4 Pharmacokinetic (pK) and Nephrotoxicity Study ***233***

4.3.5 In vivo Distribution ***235***

4.3.6 In vivo antitumor activity ***238***

4.4 Conclusion ***248***

4.5 Acknowledgements ***249***

Chapter 5 Comparison of Polymeric micelles/graphene oxide nanoparticles.....*250*

5.1 Introduction.....*251*

5.2 Comparison of physicochemical characteristics.....*252*

5.3 Conclusion.....*255*

Chapter 6.....*256*

Conclusion.....*256*

Chapter 7.....*266*

Future Scope of work.....*266*

Chapter 8.....*263*

References.....*263*

Appendix.....*331*

Publications.....*332*

Manuscripts under communication.....*333*

Patent.....*333*

Conference Presentations/Proceedings.....*333*

Biography.....*335*

List of Tables

Table 1.1 Approved nanomedicines for breast cancer treatment…….6-7

Table 1.2 Genes linked to the development of breast cancer…….….13-14

Table 2.1 Relative molecular weight of each conjugate and estimation of the number of VES and attached to each chitosan molecule by SEC analysis……85

Table 2.2 Determination of percent Drug loading, Encapsulation efficiency, Particle size and Zeta potential (Ch=15KDa)……88

Table 2.3 C1s, O1s and N1s binding energies evaluated from a deconvolution procedure of corrected XPS spectra for chitosan, chitosan vitamin E succinate and Oxaliplatin micelle formulation…….90

Table 2.4 Kinetic release mathematical models of OXPt@Ch/VES Ms formulation at various pH's…….…….93

Table 2.5 The table represents the pharmacokinetic parameters of the free oxaliplatin and OXPt@Ch/VES micelle formulation. Note: Each point represents the mean ± SD of three rats…….…….104

Table 3.1 GPC analysis of mPEG-PLA…….….134

Table 3.2 Physiochemical characterization of Dox@GO(mPP) NPs…….……139

Table 3.3 Release kinetic study of Dox@GO(mPP) (1/0.5) NPs in different pHs with or without laser……...…….146-147

Table 3.4 IC-50 value of Free Dox, GO(mPP) –L, GO(mPP) (+L), Dox@GO(mPP) (1/0.5) NPs (–L), and Dox@GO(mPP) (1/0.5) NPs (+L) in 4T1 and MDA-MB-231 cells……...…...….151

Table 3.5 Mean plasma concentration-time profiles of Dox after IV administration of a single 5 mg/kg dose of free Dox, Dox@GO, and Dox@GO(mPP) (1/0.5) NPs to rats……...……159

Table 4.1 XPS compositional analysis, and fitted parameters of the C 1s, O 1s, and Pt4f spectra of the graphene oxide, GO(OX) (1/1), GO(OX)PEG (1/1/0.2) NPs, and GO(OX)PB (1/1/0.2) NPs…….....……206-207

Table 4.2 Physiochemical characterization of GO(OX) NPs……...……208-209

Table 4.3 Release kinetics of GO(OX)PEG (1/1/0.2) NPs in various pHs……..…214

Table 4.4 Release kinetics of GO(OX)PB (1/1/0.2) NPs in various pHs……...…215

Table 4.5 Photothermal conversion efficiency parameters…….218

Table 4.6 IC-50 value of Free OX, GO(OX)PEG (1/1/0.2) NPs (-L), GO(OX)PB (1/1/0.2) NPs (-L), GO(OX)PEG (1/1/0.2) NPs (+L), and GO(OX)PB (1/1/0.2) NPs (+L) in MCF-7 and 4T1 cells……..….229

Table 4.7 The pharmacokinetic (pK) parameters of free OX, GO(OX)PEG (1/1/0.2) NPs, and GO(OX)PB (1/1/0.2) NPs in female Wistar rats…….236

Table 5.1 Physicochemical characterization of micelles and polymeric NPS……256

Table 5.2 *In vitro* cytotoxicity study……..….257

List of Figures

Figure 1.1 The statistics regarding breast cancer and nanomedicines.. 4

Figure 1.2 Showcases the utilization of nanoparticles in cancer therapy. These tiny particles offer targeted drug delivery, multifunctionality, and controlled release, minimizing side effects and enhancing treatment efficacy. Through surface modifications and responsiveness to stimuli, nanoparticles hold promise for improving cancer treatment outcomes……8

Figure 1.3 A diagrammatic representation illustrating the risk factors and preventative measures for BC.....11

Figure 1.4 Various types of nanoparticles used to deliver drugs in cancer treatment. 23

Figure 1.5 Applications of multifunctional graphene oxide. 36

Figure 1.6. Schematic illustration of active targeting vs passive targeting of nanoparticles..44

Figure 1.7 Chemical structure of doxorubicin 58

Figure 1.8 Chemical structure of Oxaliplatin (Diaminocyclohexane Oxalatoplatinum).....61

Figure 2.1 Synthetic scheme of Ch/(VES)4 conjugates (A); ^{1}H NMR spectrum of Ch/(VES)4 conjugate (B); FTIR spectra of Ch (15 KDa), VES and Ch/(VES)4 conjugate (C); Illustration of supramolecular micellar nanoaggregates formed by Ch/(VES)4 copolymer (D). 71

Figure 2.2 Synthetic scheme of chitosan rhodamine B vitamin E succinate conjugate.....71

Figure 2.3 GPC analysis of chitosan (15KDa) and chitosan vitamin E succinate conjugate in 1 % acetic acid used as mobile phase. 85

Figure 2.4 CMC of Chitosan-Vitamin E succinate conjugate of chitosan Molecular weight 15KDa and 300KDa.....86

Figure 2.5 Physicochemical characterization of OXPt@Ch/VES Ms formulation.. 89

Figure 2.6 Survey spectra analysis and Deconvoluted XPS spectra analysis of O1s, N1s, and C1s and Pt (IV) of chitosan, Chitosan vitamin E succinate conjugate and OXPt@Ch/VES Ms formulation.....90

Figure 2.7 Kinetic release mathematical models of OXPt@Ch/VES Ms formulation at various pH's.....93

Figure 2.8 Cellular uptake study.....96

Figure 2.9 Nuclear staining (left) and DNA fragmentation (right) treated with free OXPt and OXPt@Ch/VES Ms formulation at OXPt concentration of 50µM (A); Study on the generation of ROS in MCF-7 and MDA-MBA-231 cells for 24 h (B, C); Anticancer activity of free OXPt, OXPt@Ch/VES micelle and Ch/$(VES)_4$ copolymer by MTT assay.....98

Figure 2.10. Quantitative assessment of Apoptosis in MCF-7 and MDA-MB-231 cells (A); Change in mitochondria membrane Potential (B); Pt uptake (ng of Pt per 10^6 cells) (C); Flow cytometry data of MDA MB-231-S and MDA MB 231-R cell lines treated with anti-P-gp antibody (D).....100

Figure 2.11 Cell cycle analysis of MCF-7 cells, MDA-MBA-231-S and MDA-MBA-231-R after 24h of treatment with free OXPT and OXPt@Ch/VES Ms Formulation (A, C, E); the bar graph represents the percent cells in G1, S, and G2 phase (B, D, F).....101

Figure 2.12 Assessment of Therapeutic efficacy of free OXPt and OXPt@Ch/VES micelle formulation in 4T1-LUC tumor-bearing BALB/C mice.....106

Figure 2.13 Analysis of in-vivo biodistribution by IVIS imaging of 4T1 LUC Tumor bearing mice after the I.V administration of free OXPt and OXPt@Ch/VES Ms formulation at OXPt concentration of 5mg/kg, images captured at predetermined post injection time periods.....107

Figure 2.14 Immunohistochemistry analysis 109

Figure 3.1 Schematic illustration for the preparation of Dox@GO(mPP) NPs.....131

Figure 3.2 XRD patterns of Graphite and Graphene oxide (GO) (A); XPS survey spectra of graphite and GO (B); C1s survey spectra of graphite (C); O1s survey spectra of GO (D); C1s survey spectra of GO (E); XPS survey spectra of GO(mPP) (F); C1s survey spectra of GO

(mPP) (G); O1s survey spectra of GO(mPP) (H); UV-vis spectra of GO, GO(mPP) and Dox@GO(mPP) (1/0.5) NPs in water and methanol (I); Cyclic voltammetry analysis (J)...137

Figure 3.3 XRD analysis of free Dox, Dox@GO, and Dox@GO(mPP) NPs in various ratios (A). FTIR spectra analysis of graphite, graphene oxide, GO(mPP), and mPEG-PLA using the KBR pellet technique (B); 1H-NMR spectrum of mPEG-PLA (C); FTIR spectra analysis of GO(mPP) conjugates in various ratios using the KBR pellet technique (D). FTIR spectra analysis of Dox@GO(mPP) NPs in different ratios using the KBR pellet technique (E).....138

Figure 3.4 Fluorescence Spectra analysis of free Dox and Dox@GO(mPP) (1/0.5) NPs (A). Particle size analysis of Dox@GO(mPP) (1/0.5) NPs for 21 days (B). Fluorescence spectra analysis of Dox@GO(mPP) (1/0.5) NPs for 21 days (C).....139

Figure 3.5 Kinetic stability Study (A). TGA thermogram of Dox@GO(mPP) NPs in various ratios (B). DSC thermogram of GO and GO-mPEG-PLA in various ratios (C). DSC thermogram of Dox@GO(mPP) NPs in various ratios (D).....141

Figure 3.6 Physiochemical characterization of Dox@GO(mPP) NPs.....144

Figure 3.7 Release kinetic study of Dox@GO(mPP) (1/0.5) NPs in different pHs.....145

Figure 3.8 Cellular internalization study of free Dox and Dox@GO(mPP) (1/0.5) NPs (± L) (0.25 W/cm^2) in MDA-MB-231 (A) and 4T1 (B) cells.....149

Figure 3.9 Anticancer activity of free Dox, Go(mPP) (± L), and Dox@GO(mPP) (1/0.5) NPs (± L) (0.25 W/cm2) by MTT assay.....150

Figure 3.10 Cytotoxicity study of Free Dox, GO(mPP) (–L), GO(mPP) (+L), Dox@GO(mPP) (1/0.5) NPs (–L), and Dox@GO(mPP) (1/0.5) NPs (+L) in 4T1 and MDA-MB-231 cells..152

Figure 3.11 Annexin V assay (A) and cell cycle analysis (B).....154

Figure 3.12 Qualitative and quantitative assessment of MMP in MDA-MB-231 and 4T1 cells treated with free Dox and Dox@GO(mPP) (1/0.5) NPs (± L) (0.25 W/cm2) by fluorescence microscopy (A), and flow cytometry (B). Intracellular ROS generation in MDA-MB-231 and

4T1 cells treated with free Dox and Dox@GO(mPP) (1/0.5) NPs (± L) by fluorescence microscopy (C, D).....156

Figure 3.13 Examination of *in vivo* biodistribution of a free DOX, Dox@GO, and Dox@GO(mPP) NPs in 4T1-LUC tumor-bearing mice using a technique called IVIS imaging at Dox dose of 5 mg/kg.....158

Figure 3.14 Evaluating the effectiveness of free Dox and Dox@GO(mPP) (1/0.5) NPs (± L) (0.25, 0.5 W/cm2) (808 nm) in treating 4T1-LUC tumor bearing BALB/C mice. 160

Figure 3.15 Immunohistochemistry Analysis 164

Figure 3.16 Reduction of metastasis of 4T1-Luc cells in lungs by Dox@GO(mPP) (1/0.5) NPs (± L) treatment (power density 0.25, 0.5 W/cm^2).....166

Figure 4.1 ^{1}H NMR spectrum of Dihydroxy oxaliplatin (IV).....196

Figure 4.2 ^{1}H NMR spectrum of carboxylated oxaliplatin (IV). 196

Figure 4.3 1H NMR spectrum of pegylated biotin (PB).....197

Figure 4.4 Mass spectrum of Dihydroxy Oxaliplatin(IV) (A).....197

Figure 4.5 Mass spectrum of Carboxylated oxaliplatin(IV) (B).....198

Figure 4.6 MALDI-Toff analysis of Pegylated biotin 198

Figure 4.7 FTIR analysis of graphite, GO, and GO conjugates.....199

Figure 4.8 XRD analysis of GO(OX)PEG NPs (A); XPS survey spectra of graphite and graphene oxide (B); C1s and O1s spectra of graphene oxide (C).....204

Figure 4.9 Physiochemical characterization of GO(OX) conjugates.....205

Figure 4.10 DTG and TGA analysis of GO, free OX, GO(OX)PEG (1/1/0.2) NPs, and GO(OX)PB (1/1/0.2) NPs.....207

Figure 4.11 SEM analysis of GO(OX)PEG (1/1/0.2) NPs (A); Stability analysis of GO(OX)PB (1/1/0.2) NPs at room temperature and 4 ºC (B).....209

Figure 4.12 Physiochemical characterizations of GO(OX)PB (1/1/0.2) NPs.....210

Figure 4.13 Release kinetics of GO(OX)PEG (1/1/0.2) NPs and GO(OX)PB (1/1/0.2) NPs in various pHs. 213

Figure 4.14 The graph of negative ln θ vs. time to calculate the slope to determine the photothermal conversion efficiency.....217

Figure 4.15 FTIR analysis of Rhodamine B and RhB loaded GO(OX)PB (1/1/0.2) NPS (A); UV analysis of GO, RhB and RhB loaded GO(OX)PEG (1/1/0.2) NPS (B); Fluorescence spectra analysis of Rhodamine B and RhB loaded GO(OX)PB (1/1/0.2) NPs (C). 219

Figure 4.16 *In vitro* photothermal effect on cellular uptake through a cellular internalization study of GO(OX)PEG (1/1/0.2) NPs and GO(OX)PB (1/1/0.2) NPs (±L) at 0.5 W/cm2 in MCF-7 cells. 221

Figure 4.17 Confocal microscopy imaging depicting the z-stack analysis of cellular internalization in MCF-7 cells. 223

Figure 4.18 Cellular Internalization mechanism of GO(OX)PB (1/1/0.2) NPs (A); Time course entry of GO(OX)PB(1/1/0.2) NPs by Raman Spectroscopy for 8 h (B); Qualitative and quantitative analysis of Mitochondrial membrane depolarization in MCF-7 treated cells by confocal microscopy (C), and flow cytometry (D); and evaluation of Pt content in cells by AAS (E). The significance of the difference was assessed by ANOVA, **P < 0.01, *P < 0.05. ..224

Figure 4.19 *In vitro* cytotoxicity activity of free OX, GO(OX)PEG (1/1/0.2) NPs, and GO(OX)PB (1/1/0.2) NPs (± L) (0.5 W/cm2) by MTT assay 227

Figure 4.20 *In vitro* cytotoxicity activity of free OX, GO(OX)PEG (1/1/0.2) NPs, and GO(OX)PB (1/1/0.2) NPs (± L) (0.5 W/cm^2) by MTT assay.....228

Figure 4.21 *In vitro* photothermal effect on live/dead cell assay and intracellular ROS generation.....232

Figure 4.22 Annexin V Assay (A) and cell cycle analysis (C) 233

Figure 4.23 *In vivo* biodistribution analysis of GO(OX)PEG (1/1/0.2)-RhB NPs and GO(OX)PB (1/1/0.2)-RhB NPs in 4T1 tumor-bearing mice utilizing IVIS imaging.....237

Figure 4.24 Evaluation of the *in vivo* anti-tumoral effect of free OX, GO(OX)PEG (1/1/0.2) NPs and GO(OX)PB (1/1/0.2) NPs (±L) (1 W/cm2) in 4T1-Luc tumor-bearing mice.....240

Figure 4.25 *In vivo* images of 4T1-LUC tumor-bearing mice following intravenous injection of free OX, GO(OX)PEG (1/1/0.2) NPs and GO(OX)PB (1/1/0.2) NP formulation at an OX dosage of 5 mg/kg employing IVIS imaging System. 242

Figure 4.26 Immunohistochemistry *in vivo*. 244

Figure 4.27 Suppression of lung metastasis......247

LIST OF ABBREVIATIONS AND SYMBOLS

ACN	Acetonitrile
AO	Acridine orange
BC	Breast Cancer
Ch	Chitosan
DAPI	4′,6-Diamidino-2-phenylindole dihydrochloride
DL	Drug loading
DLS	Dynamic light scattering
DMEM	Dulbecco's Modified Eagle Medium
DMSO	Dimethyl sulfoxide
DSC	Differential scanning calorimetry
EE	Encapsulation efficiency
EDC	N-(3Dimethylaminopropyl)-N′-ethyl carbodiimide hydrochloride
FITC	Fluorescein isothiocyanate
FTIR	Fourier transform infrared spectroscopy.
GPC	Gel Permeation Chromatography
GO	Graphene Oxide
H & E	Haematoxylin and eosin
HPLC	High performance liquid chromatography
^{1}H NMR	Proton Nuclear Magnetic Resonance
IC50	Half maximal inhibitory concentration
IVIS	*In vivo* imaging system
mPEG	Methoxy polyethylene glycol
MTT	3-(4,5-dimethylthiazol-2-yl)-2,5-di-phenyltetrazolium bromide
MWCO	Molecular weight cut-off

mg	Milligram
Min	Minute
mL	Millilitre
mm	Millimetre
mmol	Millimole
NHS	N-hydroxysuccinimide
nm	Nanometre
PBS	Phosphate Buffer Saline
PB	Pegylated Biotin
PLA	Polylactic acid
PDI	Polydispersity Index
PI	Propidium iodide
RT	Room temperature
SD	Standard deviation
SEM	Scanning electron microscope
TEA	Triethylamine
THF	Tetrahydrofuran
TNBC	Triple Negative Breast Cancer
XRD	X-ray Diffraction
XPS	X-ray Photoelectron spectroscopy
μg	Microgram
μL	Microlitre
μM	Micromolar

Chapter 1

Introduction

1. Introduction

Breast cancer, an extremely prevalent and frequently diagnosed form of cancer affecting millions of women worldwide, poses a significant threat to their lives, with an estimated annual impact of ~2-2.5 million individuals. Female breast cancer stands out as the most identified cancer on a global scale (Sung et al., 2021). According to data from the World Health Organization (http://gco.iarc.fr/), breast cancer comprises over 24% of the estimated new cancer cases in females worldwide. This cancer holds the highest occurrence rate in females across 154 countries, with China and the United States being the foremost contributors, accounting for 17.6% and 11.2% of global breast cancer cases, respectively (**Fig. 1.1**). In India, BC is the most prevalent kind of cancer among women. The WHO figured that over 170,000 Indian women are afflicted by BC, an increase of 14% above the country's overall cancer incidence rate (Jain et al., 2020a). Recent statistics indicate that newly estimated cases of female breast cancer make up 30% of all new cancer diagnoses in women in the United States (Sung et al., 2021). In China, the incidence of breast cancer has been rapidly increasing over the past three decades (Fang et al., 2020), constituting 19.2% of newly diagnosed women's cancer cases in the country (R. Feng et al., 2019). As of now, metastatic breast cancers remain considered incurable (Giuliano et al., 2017), contributing to a high mortality rate associated with breast cancer. Additionally, breast cancers exhibit a high degree of heterogeneity. Based on distinct features, BC is divided into many molecular subtypes, such as progesterone receptor (PR)/estrogen (ER) positive, luminal (A, and B), human epidermal growth factor receptor 2 (HER2) type (Saraiva et al., 2017). The subtypes of BC that are positive for the progesterone receptors (PR), and estrogen (ER) two of the recognized subtypes, account for around 70 % of all reported instances . Triple-negative BC (TNBC) is a subtype of BC that only occurs in around 20 % of cases and lacks the expression of HER-2, ER, and PR (G. Xiong et al., 2018). TNBC has an aggressive phenotype and a greater risk of metastasis, comparable to basal-like BC (which occurs in roughly 75% of TNBC cases). Multiple tumor suppressor genes may have

undergone genetic changes and genomic instability, which would explain the higher risk of metastasis (Chalakur-Ramireddy & Pakala, 2018). Around the world, the proportion of TNBC cases ranged from 7 to 28%, with India having the highest occurrence (K. K. Thakur et al., 2018).

TNBC, although having diverse clinical, morphological, and biochemical features, does share several common pathological and clinical indicators (van Maaren et al., 2019). In persons with advanced cancer (metastatic stage), chemotherapy is often not targeted and effective, which may potentially result in patient mortality (Massagué & Obenauf, 2016). Approximately 80-90% of deaths resulting from breast cancer are attributed to metastases. Despite significant advancements in surgical treatments, hormone therapy, radiation treatment, and chemotherapy that have reduced mortality and improved survival rates, around 20-30% of patients originally identified at an early stage still progress to develop metastatic disease (Chaffer & Weinberg, 2011; Sauer, 2017). The increasing incidence of breast cancer is associated with environmental degradation and lifestyle decisions that disrupt oestrogen balance. The risk of breast cancer is elevated for women in the age range of 40 to 55, particularly if there is a familial predisposition to the disease (Elgebaly et al., 2018; Smith et al., 2019). Multiple studies have shown a positive correlation between an elevated body mass index (BMI) and an increased risk of cancer development in post-menopausal women (Berrino et al., 2001). Moreover, excessive fat consumption might alter the levels of circulating oestrogens, potentially leading to hormonally dependent breast cancer (Lahmann et al., 2003). A woman's risk of developing a tumour is increased if she has a family history of breast cancer or has been exposed to ionising radiation. Prolonged exposure to ionising radiation, particularly in the early stages, may significantly increase the likelihood of developing breast cancer (Lauby-Secretan et al., 2015). Breast cancer may arise because of several contributing factors, such as environmental, behavioural, hormonal, genetic, and dietary factors.

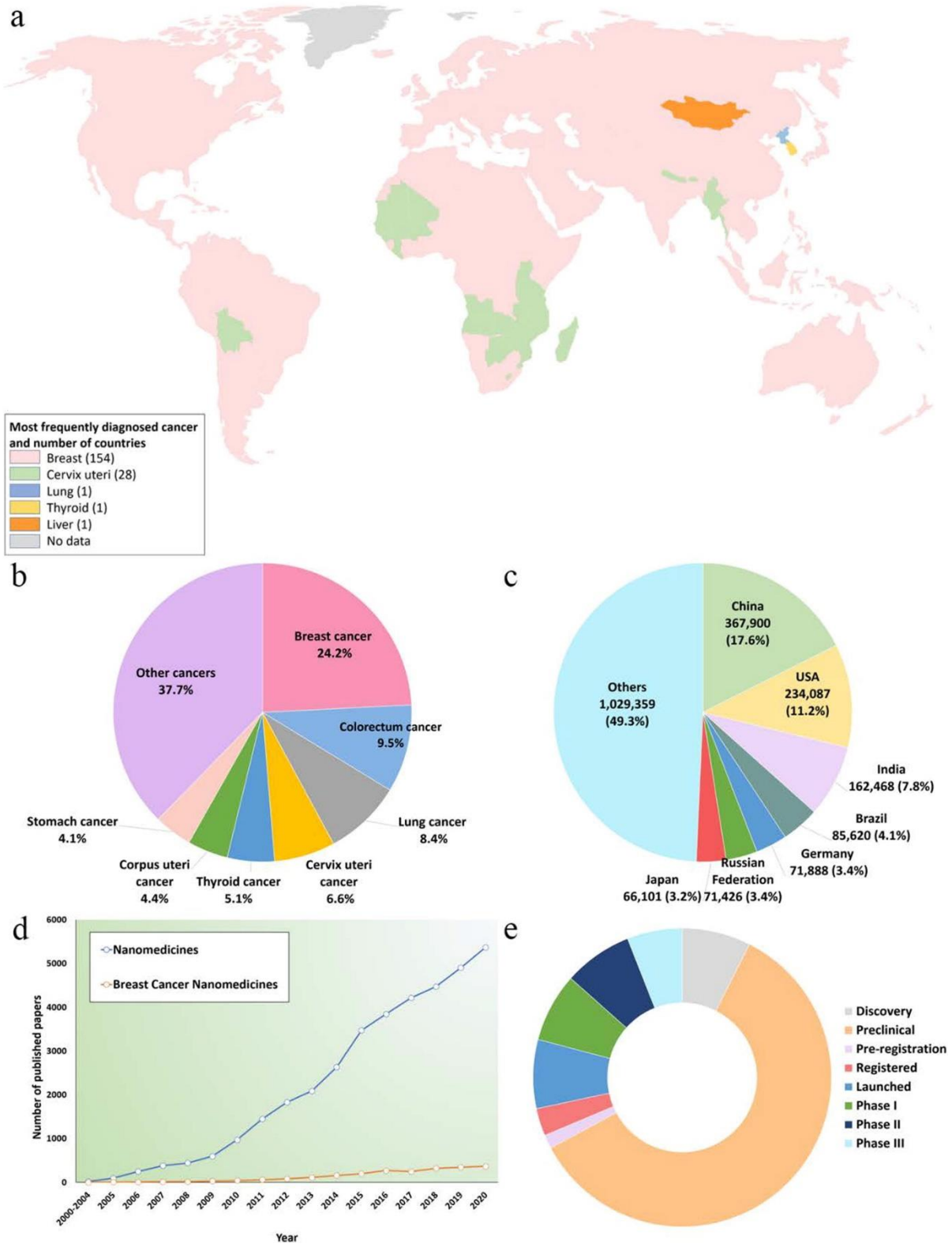

Figure 1.1 The statistics regarding breast cancer and nanomedicines. The most often diagnosed cancer in women globally (a). Global distribution of new instances of women's cancer by percentage (b). The following countries have the greatest incidence of new instances of breast

cancer in women, according to statistics from the World Health Organisation (c). The number of yearly articles on nanomedicine and breast cancer nanomedicine, collected from PubMed (d). Status of novel breast cancer nanomedicines based on data from Clarivate Analytics (e). Adapted with permission from ref. (Y. Jiang et al., 2022).

There is a correlation between the use of oral contraceptives and post-menopausal hormone therapy and an increase in the occurrence of condition (Vogel, 2008). Tumour heterogeneity, exemplified by BC stem cells (BCSCs) and tumour microenvironments, is a significant factor contributing to the failure of chemotherapy and the development of drug resistance in breast cancer (BC) and triple-negative breast cancer (TNBC). Managing triple-negative breast cancer (TNBC) and breast cancer (BC) might be challenging as a result. The advancement of nanotechnology, however, provides a different viewpoint on medicinal approaches. Nanotechnology stands out because to its capacity to alter surfaces, encapsulate a greater number of pharmaceuticals, and possess nano-scale dimensions and extended circulation half-lives. Additionally, it offers both active and passive targeting alternatives. These qualities signify a fundamental shift in the approach to treating BC and TNBC.

Anti-cancer medications are somewhat linked to suboptimal pharmacological characteristics. The primary drawback of traditional chemotherapy medicines is the presence of adverse effects. The bulk of chemotherapy medicines have hydrophobic properties, making them unsuitable for intravenous administration. To improve the solubility of chemotherapeutic medicines with low water solubility, such as paclitaxel (PTX), solubilizers like Cremophor EL are used. However, it is important to note that the usage of these solubilizers may lead to unwanted consequences, including hypersensitivity responses (Gelderblom et al., 2001). Additional detrimental characteristics, such as low stability, inadequate pharmacokinetics (PK), unfavourable biodistribution and tissue permeability, absence of tumour selectivity, and insufficient tumour concentration, further undermine the efficacy of anti-cancer medications

(Allen & Cullis, 2004). Nanomedicine, an interdisciplinary approach, has been extensively studied over the last several decades with great expectations to overcome challenges in cancer pharmacotherapy (**Fig. 1.1**).The use of nanocarriers for the delivery of anti-cancer therapies, also known as nanomedicines, has the potential to boost the therapeutic effectiveness of the treatments, safeguard them from degradation, minimise toxicity to the body, and improve their pharmacokinetic profile and distribution (**Fig. 1.2**). Furthermore, with the integration of specific molecules for targeting and careful engineering of the materials used in nanocarriers, targeted nanomedicine may accurately direct anti-cancer medications to the intended location of action, thereby achieving precision medicine.

Significant preclinical investigations using non-targeted and targeted nanocarriers for the administration of anti-cancer medications have shown promising outcomes in the context of breast cancer therapy. It is pleasing to see that several innovative nanomedicines have received clinical approval for the treatment of breast cancer (**Table 1.1**). Additional nanomedicines are now being advanced into clinical trials for breast cancer treatment, as seen in Figure 1e. With the introduction of advanced technologies in biology, material science, pharmacology, imaging, and computer science, nanomedicine is a very active study topic. Significant advancements are consistently being made in this field.

Table 1.1. Approved nanomedicines for breast cancer treatment.

Nanocarrier	**Marketed name**	**Application and Status**	**Ref.**
Liposome (Doxorubicin(DOX) hydrochloride)	Doxil®/Caelyx®	Metastatic breast cancer (Approved by U.S. FDA)	(Barenholz, 2012)
Liposome (Doxorubicin(DOX) hydrochloride	Lipo-Dox®	Metastatic breast cancer (Approved in Taiwan)	(Allen & Cullis, 2013)

Liposome (Dox citrate)	Myocet®	Breast cancer (Approved in Canada and Europe)	(C. C. Liu et al., 2017)
Antibody-drug conjugate (SN-38)	Sacituzumab govitecan	Metastatic Triple negative breast cancer (Approved by U.S. FDA)	(Wahby et al., 2021)
Antibody-drug conjugate (Maytansinoid)	Kadcyla®/Ado-trastuzumab emtansine/T-DM1	HER2-positive metastatic breast cancer (Approved by U.S. FDA)	(Lambert & Chari, 2014)
Protein nanoparticle (PTX)	Abraxane®/Nab-paclitaxel	Metastatic breast cancer (Approved by U.S. FDA and European medical agency)	(Sofias et al., 2017)
Polymeric micelle (PTX)	Genexol®PM/ Cynviloq™	Metastatic or recurrent breast cancer (Approved in South Korea)	(J. Shi et al., 2017)

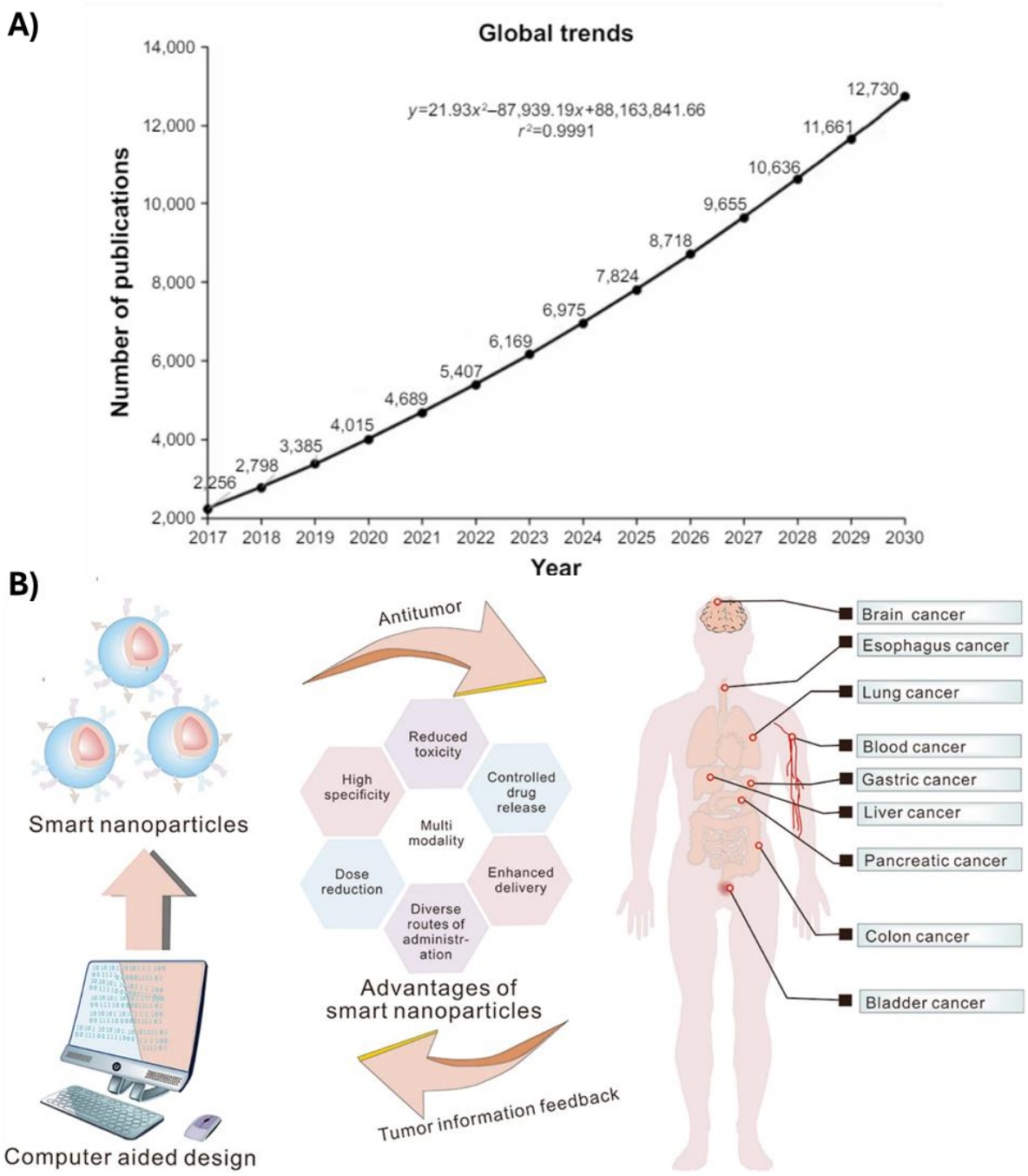

Figure 1.2 Cumulative volume of articles related to nanotechnology and triple negative breast cancer: global trends for 2030 (A). Utilization of nanoparticles in cancer therapy. These tiny particles offer targeted drug delivery, multifunctionality, and controlled release, minimizing side effects and enhancing treatment efficacy. Through surface modifications and responsiveness to stimuli, nanoparticles hold promise for improving cancer treatment outcomes.

1.1 Pathogenesis of breast cancer

Breast tumours usually arise from the excessive growth of the ductal tissue, which may then develop into either cancerous tumours that spread to other parts of the body or non-cancerous tumours, depending on ongoing exposure to various cancer-causing factors. The tumour microenvironment, including stromal factors and macrophages, has substantial influence on the progression and growth of breast cancer. Rats exposed to carcinogens specifically in the stromal tissue, and not in the extracellular matrix or the epithelium, may develop abnormal growths in the mammary gland (Maffini et al., 2004; Sonnenschein & Soto, 2016). Macrophages may generate an inflammatory milieu that has mutagenic characteristics, promoting the growth of new blood vessels (angiogenesis) and assisting cancer cells in avoiding detection by the immune system (Dumars et al., 2016; B.-Z. Qian & Pollard, 2010). The identification of discernible DNA methylation patterns between tumor-associated and normal microenvironments implies that epigenetic modifications taking place within the cancer microenvironment may contribute to the proliferation of cancer (Basse & Arock, 2015; Polyak, 2007). Cancer stem cells (CSCs) have recently been identified as a separate subgroup of cells inside cancer, and they have been linked in tumour genesis, evasion, and recurrence. These cells have the ability to develop into either progenitor cells or stem cells that come from normal tissue. Moreover, they possess the ability to regenerate themselves and show resilience to traditional treatment methods like radiation and chemotherapy (Baumann et al., 2008; M. Zhang et al., 2017). The identification of BC stem cells (bCSCs) was first reported by (Al-Hajj et al., 2003), which have the ability to initiate new tumors in immunocompromised mice even with a small number of just 100 bCSCs. It is anticipated that the origin of these cells is luminal epithelial progenitors, rather than basal stem cells (Molyneux et al., 2010). Several signaling pathways, such as p53, Notch, Wnt, Hedgehog, and HIF and PI3K, are involved in the invasion, proliferation, and self-renewal of bCSCs (Y. S. Sun et al., 2017). However, additional

investigation is necessary to gain a comprehensive understanding of bCSCs and to develop innovative strategies for their direct elimination.

There are two theoretical frameworks that explain the beginning and progression of BC: the cancer stem cell theory and the stochastic theory (Polyak, 2007; Sgroi, 2010). As to the cancer stem cell hypothesis, all sorts of tumours may be attributed to a certain group of cells called progenitor cells or cancer stem cells. The emergence of distinct tumour characteristics is ascribed to the acquisition of epigenetic and genetic alterations in these cells. This idea suggests that targeting cancer stem cells might be a successful and effective method for treating many types of cancerous growths. Conversely, the stochastic hypothesis posits that each tumour subtype originates from a distinct kind of cell, which might be a progenitor cell, stem cell, or differentiated cell. Each individual breast cell has the potential to gradually accumulate random mutations. Once a critical number of mutations has been reached, the breast cell may undergo a transformation into a tumour cell. Although there is factual evidence supporting both possibilities, none of the current theories provide a complete explanation for the origin of human BC.

1.2 Risk Factors of Breast Cancer

The multiple risk factors that are implicated in the BC is depicted in a schematic diagram given below (**Fig. 1.3)**

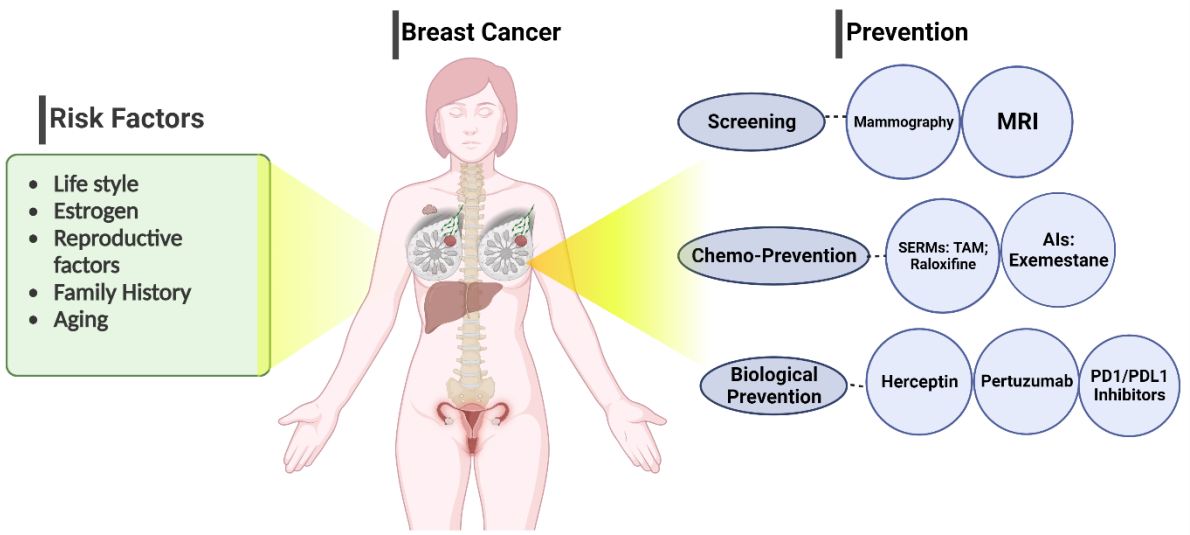

Figure 1.3 A diagrammatic representation illustrating the risk factors and preventative measures for BC.

1.2.1 Aging

Apart from gender, aging represents a significant contributing factor in the susceptibility to BC, as the occurrence of this disease is strongly associated with advancing age. In the year 2016, almost all BC-related deaths in the United States, amounting to 99.3%, observed in females who were above the age of 40, with 71.2% occurring in women aged 60 or above (Siegel et al., 2018). Hence, it is imperative to schedule mammography screenings in advance for women aged 40 or older.

1.2.2 Family history

According to (Brewer et al., 2017), family factors account for around 25% of BC cases. Women with a familial predisposition to BC, particularly those who have a mother or sister who has the illness, are more likely to have it. The findings of a cohort study conducted in the United Kingdom, which involved a sample size of more than 113,000 women, revealed that those who had a first-degree relative diagnosed with BC had a 1.75-fold higher likelihood of developing the same disease, relative to those who did not have any affected relatives. Women's with two or more first-degree relatives who have been diagnosed with BC are subject to an elevated risk

of the ailment by a factor of 2.5 or greater (Brewer et al., 2017). Mutations in BC-related genes, such BRCA1 and BRCA2, help to explain the hereditary predisposition to the disease.

1.2.3 Reproductive factors

Reproductive variables, including early onset of menstruation, delayed onset of menopause, delayed age of first pregnancy, and low parity, are known to enhance the risk of BC. The incidence of breast cancer exhibits a 3% elevation in risk for each year of delayed onset of menopause, while the risk decreases by 5% or 10% for each year of delayed onset of menstruation or each additional birth, respectively. A hazard ratio of 1.54 was observed in a recent cohort study conducted in Norway. The findings suggest a higher susceptibility for individuals who gave birth to their first child at an advanced age (≥35 years) in comparison to those who gave birth at a younger age (<20 years). The reproductive factors, parity, and age at first birth, exhibit a robust correlation with the estrogen receptor (ER) status, with varied odds ratios (OR) observed for ER+ and ER- BC. Parity displayed OR of 0.7 and 0.9 for ≥3 births and nulliparae, respectively. The study found that age at first birth had OR of 1.6 and 1.2 for individuals aged 30 years or older and under 25 years, respectively, for both ER- and ER+ BC (Rosato et al., 2014).

1.2.4 Estrogen

BC risk is associated with both endogenous and exogenous estrogens. Premenopausal women ovaries generate the majority of endogenous estrogen, which may be lowered with ovariectomy to lessen the risk of BC (Hormones & Group, 2013). Exogenous estrogen sources include hormone replacement therapy (HRT), and oral contraceptives. Despite improvements in oral contraceptive formulations to reduce harmful effects, nonetheless, women of Iranian and African American descent continue to face a higher risk of developing BC (Soroush et al., 2016). A decrease in risk was observed among women who discontinued the use of oral contraceptives for a period exceeding ten years. Studies have indicated that HRT, which

involves administering exogenous estrogen or other hormones to women who are postmenopausal or menopausal, may increase the risk of developing BC. HRT users had a 1.66 relative risk of BC compared to non-users, according to the Million Women Study carried out in the UK (Collaborators, 2003). A study was conducted on a cohort of 22,929 Asian women to examine the potential influence of HRT on the risk of developing BC. According to the study, the hazard ratios for breast cancer were 1.48 and 1.95 after 4 and 8 years of HRT use, respectively (J.-Y. Liu et al., 2016). However, the risk of BC significantly decreased after stopping HRT for two years. The hazard ratio for developing a new breast tumor among BC survivors who use HRT is 3.6, indicating a high risk of recurrence (Fahlén et al., 2013). The incidence rate of BC in the United States has decreased by approximately 7% following the disclosure of the adverse effects of HRT in the Women's Health Initiative randomized controlled trial in 2003, which resulted in a decline in HRT usage (Ravdin et al., 2007).

1.2.5 Lifestyle

The Contemporary lifestyles, marked by an overindulgence in alcohol consumption and a high consumption of dietary fat, may have the propensity to elevate the risk of developing BC. Alcohol consumption has been found to elevate estrogen-related hormones in the bloodstream, thereby inducing the activation of estrogen receptor pathways. Based on a meta-analysis of 53 epidemiological studies, it has been determined that the ingestion of 35-44 g of alcohol per day can increase the vulnerability to BC by 32%. Additionally, the risk ratio of breast cancer escalates by 7.1% with each additional intake of 10 g of alcohol per day (Hamajima et al., 2002; Jung et al., 2016). The current Western diet is characterized by a high abundance of fats, particularly saturated fats. Consuming excessive amounts of fat has been linked to increased mortality (RR=1.3) and unfavourable outcomes in patients with BC (Makarem et al., 2013). The potential correlation between smoking and the risk of developing breast cancer remains a topic of discussion. However, it has been observed that mutagens found in cigarette smoke

have been identified in the breast fluid of non-lactating women. Furthermore, the probability of developing BC is greater in women who both smoke and consume alcohol (RR=1.54) (Knight et al., 2017). Contemporary evidence suggests that smoking, particularly during adolescence and early adulthood, entails a higher risk of BC incidence (Catsburg et al., 2015; Kispert & McHowat, 2017).

The significant progress has been achieved in clinical and theoretical investigations related to BC, as evidenced by **Fig. 1.3**. Current prevention strategies, such as screening, chemoprevention, and biological prevention, have demonstrated higher precision and efficacy compared to historical approaches. Despite the reduction in BC mortality rates, it remains the primary cause of cancer-related deaths among women aged 20-59 years.

1.2.6 Genes related to breast cancer.

Many genes that are connected to BC have been discovered. As demonstrated in **Table 2**, oncogenes and anti-oncogenes both exhibit mutations and abnormal amplification, which are essential for the processes of tumor initiation and development.

Table 1.2 Genes linked to the development of breast cancer.

Function	**Location**	**Gene**	**Breast cancer abnormality**	**Ref.**
oncogene	11q13	CCND1 (Cyclin D1)	50% of breast tumors exhibit overexpression.	(Inoue & Fry, 2015)
	3q26.3	PIK3CA	Mutations are present in 37% of HR+/HER2- metastatic BC and 40% of early BC cases.	(Lefebvre et al., 2016)
	17q12	HER2	Around 20% of primary BCs show detection of HER2 overexpression.	(Y. S. Sun et al., 2017)

Anti-oncogenes	17q21 and 13q12	BRCA1/2	BRCA1/2 mutations cause around 20-25% of inherited BCs and 5-10% of all BCs.	(Y. S. Sun et al., 2017)
Tumor suppressor gene	18q21.33	Maspin	Maspin expression is present in 20-80% of invasive BCs.	(Berardi et al., 2013)
	3p14.2	FHIT	FHIT hyper-methylation rate is 8.4 times higher in BC than in normal breast tissues.	(Su et al., 2015)
	16q22.1	CDH1 (E-cadherin	85% of lobular breast carcinomas exhibit CDH1 inactivation.	(Desmedt et al., 2016)
	11q22-q23	ATM	ATM mutation generally increases the risk by 2-3 times, and in women under 50 years, the risk is raised by 5-9 times.	(M. Choi et al., 2016)
	10q23.3	PTEN	Up to 33% of BCs experience loss of PTEN protein expression.	(Loibl et al., 2016)
	13q14.2	RB1	20-35% of BCs exhibit Rb1 inactivation.	(Cheng et al., 2010)
	17q21.3	NME1	SNP of NME1 gene is linked to a greater risk of BC-specific mortality (HR=1.4) and early-stage cancer patients (HR=1.7).	(Roberts et al., 2017)
	17p13.1	P53	30% of BCs have mutations.	(Hientz et al., 2017)

1.3 Current common treatment strategies of breast cancer

When deciding on a good treatment strategy for breast cancer, it is crucial to consider criteria such as the subtypes, stage, and grade of the cancer, as well as the age, physical condition, and medical condition of the patients. The primary objective of treating non-metastatic breast cancer is to eradicate the tumour and prevent the spread of cancer cells to other parts of the body, as well as to minimise the chances of the cancer returning (Waks & Winer, 2019). The objective of treating metastatic breast cancer is to alleviate symptoms and extend the lifespan of patients. Typically, the standard therapeutic approach for breast cancer involves both systemic and local therapy.

1.3.1 Systemic treatment of BC

1.3.1.1 Chemotherapy

Chemotherapy is the primary and widely used systemic treatment approach for breast cancer. The primary mechanism by which most conventional cytotoxic chemotherapeutic drugs combat cancer is through the inhibition of the rapid proliferation and growth of cancer cells (Omidi et al., 2022). This typically leads to the death of cancer cells by selectively targeting them at various stages of the cell cycle (Chabner & Roberts Jr, 2005). The chemotherapy drugs commonly used to treat breast cancer include anthracyclines (doxorubicin, epirubicin), taxanes (PTX, docetaxel), platinum agents (cisplatin, carboplatin, oxaliplatin), and cyclophosphamide. These drugs have been studied and discussed in various research papers (Garutti et al., 2019; Penel et al., 2012; Saloustros et al., 2008; Yamaguchi et al., 2015). Chemotherapeutic drugs may provide anti-tumor effects whether administered orally, intravenously, or intrathecally (Zagouri et al., 2013). Furthermore, it has been shown that the use of a mixture of many drugs in therapy may typically enhance the effectiveness of anti-tumor treatment, beyond what can be accomplished by using a single chemotherapeutic agent (Junnuthula et al., 2022). In

addition, chemotherapy encompasses adjuvant chemotherapy and neoadjuvant chemotherapy. Adjuvant chemotherapy refers to the administration of chemotherapy after surgery for breast cancer patients who have lymphatic metastases or a high risk of recurrence (Peto et al., 2012). Neoadjuvant chemotherapy, administered to patients prior to surgery, assesses the tumor's response to chemotherapy, reduces the tumour stage, and enhances the possibility of breast conservation surgery. This treatment is particularly valuable for patients with locally advanced and inoperable breast cancer (Davey et al., 2021; X. Sun et al., 2022; H. Wang & Mao, 2020).

1.3.1.2 Endocrine Therapy

Endocrine therapy is the primary therapeutic modality for breast cancer patients who have hormone receptor positive tumours (ER positive and/or PR positive). This medication may be used as either a neoadjuvant or adjuvant therapy for patients diagnosed with Luminal A or Luminal B subtypes of breast cancer (Lerebours et al., 2021; Zelnak & O'Regan, 2015). The objective of endocrine treatment is to inhibit the activity of oestrogen or reduce the concentration of oestrogen, which may promote the proliferation of breast cancer cells. The drugs used in endocrine therapy primarily consist of selective oestrogen receptor modulators (SERMs) such as tamoxifen and toremifene, selective oestrogen receptor degraders (SERDs) like fulvestrant, and aromatase inhibitors (AIs) including letrozole, anastrazole, and exemestane (Lumachi et al., 2011; Reinbolt et al., 2015).

1.3.1.3 HER2 targeted therapy

The HER2 enriched subtype is characterised by the overexpression of HER2, resulting in accelerated tumour growth, more aggressive progression, and worse survival outcomes when compared to the Luminal A and B subtypes (Boix-Montesinos et al., 2021). Consequently, HER2 targeted treatment is crucial for patients who have been diagnosed with the HER2-enriched subtypes. Currently, the primary medications used for HER2 targeted treatment are of monoclonal antibodies (trastuzumab and pertuzumab), tyrosine kinase inhibitors (neratinib,

lapatinib, etc.), and an antibody-drug combination called trastuzumabemtansine (T-DM1) (Bredin et al., 2020).

1.3.1.4 Immunotherapy

Immunotherapy is a systemic therapeutic approach for breast cancer that activates the patients' innate immune system to prevent, control, and kill cancer cells (Ahmad et al., 2022; Fraguas-Sánchez et al., 2022). Immunotherapy works by enhancing the immune system's ability to selectively recognise and eliminate cancerous cells (Fraguas-Sánchez et al., 2022). Furthermore, immunotherapeutic drugs can not only address the original tumour but also hinder the occurrence of distant metastases and decrease the likelihood of recurrence (Gavas et al., 2021). Patients with triple-negative breast cancer (TNBC) are more likely to have positive outcomes with immunotherapy compared to those with other forms of breast cancer. This is attributed to the presence of mutations, tumor-infiltrating lymphocytes (TILs), and elevated levels of programmed death ligand 1 (PD-L1) expression (Kwapisz, 2021). Atezolizumab, a PD-L1 inhibitor, received approval for use in combination with nab-paclitaxel for treating patients with locally advanced or metastatic TNBC whose tumours show PD-L1 expression (Kwapisz, 2021).

1.3.2 Local treatment and local therapy of BC

1.3.2.1 Surgery

Mastectomy and lumpectomy, often known as breast-conserving surgery, are the primary surgical procedures used to treat various stages of breast cancer (Sharma et al., 2010). Research has shown that mastectomy and lumpectomy, when combined with radiation, have comparable results in terms of both recurrence rates and overall survival (Fisher et al., 2002). Furthermore, the abnormal condition of axillary lymph nodes in breast cancer patients is a crucial prognostic factor. When comparing sentinel lymph node biopsy (SLNB) to axillary lymph node dissection (ALND), it is shown that ALND often results in more severe postoperative sequelae, including paraesthesia and lymphedema (C. Z. Li et al., 2015). Thus, SLNB, a conclusive technique for

ruling out axillary metastases, has replaced ALND as the primary approach for assessing the axilla in most patients with early BC .

1.3.2.2 Radiotherapy

Radiation therapy is a medical procedure that employs powerful radiation to eliminate cancer cells. This treatment has been used for over a hundred years to treat many types of cancer. The discovery of the impact of radiation on tumour cells was first made via the treatment of a lady with locally advanced breast cancer. Since then, radiation has been a fundamental component in the treatment of breast cancer (Jason & Formenti, 2018). Radiation therapy primarily consists of two types of treatments: external beam radiation (EBRT) and internal radioisotope therapy (RIT) (W. Liu et al., 2021). Radiation treatment may be administered to the breast after breast-conserving surgery, the chest wall after mastectomy, and the regional lymph nodes (Boyages, 2017) in order to eradicate malignant cells and minimise the likelihood of cancer recurrence.

1.4 Obstacles of current treatment strategies of BC

The advancements in cancer treatment technology have significantly improved the usual therapeutic approaches for breast cancer. These advancements have resulted to a drop in the death rate and increased the chances of recovery for most cancer patients (J. J. Lee et al., 2017). However, there are still some challenges that arise while treating BC with current therapy approaches. The use of chemotherapy as the main treatment for BC is well recognised, however, traditional chemotherapy methods still have many notable limitations. Firstly, the distribution of chemotherapeutic drugs lacks selectivity for tumours. Chemotherapeutic agents inhibit the rapid proliferation and growth of cancer cells, as well as the growth of normal cells in the body, due to their non-specific targeting of tumours. This leads to unavoidable adverse effects, including hair loss, nausea, vomiting, diarrhoea, mouth ulcers, fatigue, increased vulnerability to infections, suppression of bone marrow function resulting in decreased white

blood cell count, anaemia, and increased susceptibility to bruising or bleeding (Łukasiewicz et al., 2021; Omidi et al., 2022). Furthermore, there were other adverse effects unique to certain drugs, such anthracyclines-induced cardiotoxicity and cisplatin-induced ototoxicity and nephrotoxicity (Dilruba & Kalayda, 2016; Saleh et al., 2021). Furthermore, drug resistance poses an additional challenge for traditional chemotherapeutic agents, diminishing the effectiveness of medication therapy in cancer cells. The phenomenon of drug resistance may be categorised into two types: inherent resistance and acquired resistance, based on the timing of its onset (X. Wang et al., 2019).

The underlying mechanisms of chemoresistance are highly intricate and encompass various factors such as heightened drug efflux, tumour heterogeneity, enhanced DNA damage repair, epigenetic modifications, inhibition of cell death (apoptosis suppression), modification of drug targets, inactivation of anticancer drugs, alterations in drug metabolism, and changes in the tumour microenvironment (Mansoori et al., 2017; X. Wang et al., 2019). Drug efflux transporters, namely efflux pumps, are primarily associated with the development of multidrug resistance in tumours. Efflux transporters are a part of the ATP-binding cassette (ABC) transporter superfamily. The human genome has 48 ABC genes, which are categorised into seven subfamilies (ABCA-ABCG) (Gote et al., 2021). The principal ATP-binding cassette (ABC) transporters linked with multidrug resistance in breast cancer (BC) are P-glycoprotein (P-gp/MDR1/ABCB1), multidrug resistance-associated protein 1 (MRP1/ABCC1), and breast cancer resistance protein (BCRP/ABCG2), as described by (Rizwanullah et al., 2021). Furthermore, the limited ability of chemotherapeutic medicines to dissolve in solution and their elevated levels of toxicity further impact the efficacy of chemotherapy. Most chemotherapeutic medications, whether derived from plants or synthesised, are hydrophobic and need solvents to create the dose. However, this solvent use increases the toxicity of the drug preparations and restricts the dosage that may be administered . Ultimately, the limited duration of activity and

inadequate resistance to chemical degradation also undermine the effectiveness of chemotherapeutic medications, impeding their capacity to be delivered and absorbed at the tumour site and impeding the desired dosage-response relationship (Malik et al., 2022).

In addition, most chemotherapy medicines are unable to penetrate the blood-brain barrier (BBB), hence restricting their effectiveness in treating brain metastases of breast cancer (Mills et al., 2020). Regrettably, 30% of early-stage breast cancer cases have a recurrence, with the majority of these cases being metastases (Burguin et al., 2021). The predominant side effects of endocrine treatment include hot flashes and nocturnal sweats, vaginal dryness, heightened susceptibility to thromboembolic events, and bone-related complications such as osteoporosis (Condorelli & Vaz-Luis, 2018). Additionally, the issue of drug resistance to hormone treatments is a significant difficulty in the treatment of breast cancer (AlFakeeh & Brezden-Masley, 2018). While trastuzumab and pertuzumab have demonstrated favourable outcomes in the management of HER2-enriched BC, it is important to acknowledge that both intrinsic and acquired resistance frequently occur during treatment. Therefore, it is crucial to gain a comprehensive understanding of the underlying mechanisms of drug resistance to inform the advancement of novel HER2 targeted medications (Rimawi et al., 2015).

Likewise, medication resistance is a significant challenge in the field of immunotherapy. In addition, a significant drawback of immunotherapy, especially when used in combination with other treatments, is the emergence of immune-related side effects that result in numerous unpleasant responses in the skin and gastrointestinal system, such as rash, itching, diarrhoea, and inflammation of the colon (García-Aranda & Redondo, 2019). In addition to the possibility of recurrence, surgery as a temporary measure also results in long-term negative consequences such as alterations in anatomy, persistent discomfort, phantom breast pain, lymphedema, and other related issues (Lovelace et al., 2019). The administration of radiotherapy can lead to various side effects, including radiation dermatitis, radiation pneumonia, myelosuppression,

cardiac and pulmonary injury, radiation-induced malignancy, fatigue, swelling, lymphedema, and other complications. These side effects can significantly impact a person's ability to carry out their daily activities (Lovelace et al., 2019; X. Sun et al., 2022).

Regarding the previously described hindrances of traditional therapies, the difficulties in treating breast cancer include surmounting resistance to several drugs and preventing its recurrence, as well as mitigating or evading the adverse effects caused by therapy. Hence, it is essential to devise innovative therapeutic approaches to efficiently treat BC, hence tackling the unfulfilled medical need encountered by BC patients.

1.5 Nanomedicine-based approaches for breast cancer

Nanotechnology offers diverse methodologies for the visualization, monitoring, diagnosis, and delivery of chemotherapeutic agents to the tumor site. The utilization of nanoparticles has demonstrated enhanced drug delivery effectiveness and decreased toxicity, and they can also surmount biological barriers, thereby enhancing their anticancer activity. Nanomedicine represents a confluence of diverse fields, including information technology, molecular biology, engineering, medicine, pharmaceutics, and material science. The amalgamation of nanoscience and medicine provides a powerful tool to probe the intricacies of biological systems and gain insights into their underlying mechanisms. Nanocarriers have the ability to traverse the cellular membrane and other obstructions, thereby enhancing drug permeation and transportation. To ensure their clinical viability, it is crucial to address key factors such as biocompatibility, circulation duration, and stability, which can be effectively achieved through the use of nanomedicine. Nanoparticles used in nanomedicine, such as drug-encapsulated micelles, liposomes, and NPs, exhibit distinctive properties that enable them to breach the biological membrane and transport the enclosed drug into cells (**Fig. 1.4**). The parameters that dictate elimination mechanisms, biodistribution, and ,cellular absorption, include particle size, morphology, and surface characteristics. The predominant nanoparticles employed in BC

therapy include gold nanoparticles, polymeric nanoparticles, micelles, solid lipid nanoparticles and liposomes, among a range of other nanoparticle types.

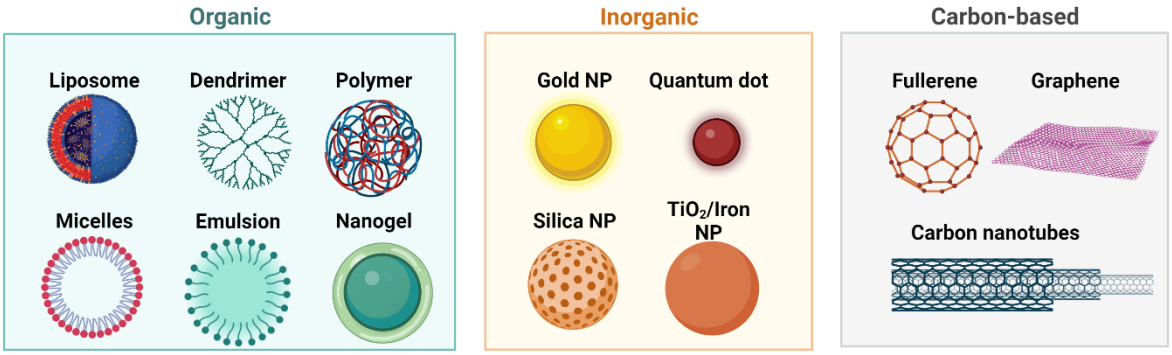

Figure 1.4 Various types of nanoparticles used to deliver drugs in cancer treatment.

1.5.1 Organic NDDS

The most common NDDSs are organic nanoplatforms, which have the benefits of being simple to modify, less poisonous, and more biocompatible. They consist of liposomes (Zalba & Garrido, 2013), lipid particles (Z.-T. Cao et al., 2016), dendrimers (Kapp et al., 2010), micelles (Xiao et al., 2012), and polymers (Duncan & Vicent, 2010). Polymers are typically self-assembled using amphiphilic block molecules consisting of hydrophilic and hydrophobic blocks, resulting in a core-shell configuration. Dendrimers are a class of macromolecules characterized by regular branching patterns and synthesized through the employment of natural or synthetic building blocks, such as nucleotides, amino acids, and sugars. Dendritic drug conjugates are formed by the conjugation of drugs to dendrimers for the purpose of drug loading. Due to their exceptional biodegradability and biocompatibility, liposomes, which are comprised of one or two lipid layers, are currently the most extensively investigated non-invasive drug delivery systems in clinical trials (Dai et al., 2017; Zalba & Garrido, 2013). NDDSs, liposomes possess the capacity to encapsulate both hydrophilic drugs and hydrophobic drugs with a high rate of loading, minimal water content, and favorable chemical resistance. Liposomes have therefore advanced to clinical studies. Nonetheless, their efficacy necessitates additional investigation. The clinical trial assessing the efficacy of ISP-77, a liposomal cisplatin

nanoparticle, was prematurely terminated as a result of its lack of effectiveness (E. S. Kim et al., 2001; Seetharamu et al., 2010).

1.5.1.1 Liposomes

In 1964, Bangham and Horne introduced liposomes as spherical vesicles composed of an aqueous core surrounded by a phospholipid outer layer, with a size range of approximately 50 to 200 nm. The utilization of liposomes in the precise administration of therapeutic agents, encompassing both hydrophobic and hydrophilic drugs, is attributed to their phospholipid bilayers comprising of biodegradable, biocompatible, and non-immunogenic constituents (Singh et al., 2017). Their minute dimensions facilitate their infiltration through vascular pores, leading to tumor localization. Additionally, it has been recorded that P-glycoprotein (P-gp) inhibition was achieved by employing anionic membrane lipids, wherein liposomes were utilized for the transportation of rhodamine 123 as a substrate for P-gp. As a result, the retention of rhodamine 123 within MCF-7/P-gp cells was found to increase, providing evidence for the functional transfer of its substrate by P-gp (Kang et al., 2009). In 1965, the FDA granted its initial approval to Doxil®, a liposomal formulation of doxorubicin, for the treatment of AIDS-related Kaposi's sarcoma, ovarian cancer, and multiple myeloma (U.S. FDA, 1995). In 2016, the drug received further approval for the treatment of breast cancer (Tran et al., 2020). In a study, (Xing et al., 2013) have reported the development of liposomes for targeted BC therapy. The liposomes were functionalized using AS1411, a DNA aptamer with a high affinity for nucleolin, and Doxorubicin was incorporated as a payload. The functionalization of liposomes with AS1411 aptamer resulted in increased cellular uptake and cytotoxicity in MCF-7 BC cells, as compared to liposomes that were not targeted. Furthermore, the utilization of liposomes specifically designed for doxorubicin delivery demonstrated enhanced infiltration into tumor tissue, leading to superior antineoplastic efficacy against xenograft MCF-7 breast cancer cells in immuno-deficient nude mice. The study exhibits that liposomes functionalized with AS1411

aptamer have the potential to detect nucleolin overexpression on the surface of MCF-7 cells, thereby enabling targeted drug delivery with high selectivity (Xing et al., 2013). In another study, Haiqiang Cao *et al*. reported the envelopment of a liposomal drug carrier with an isolated macrophage membrane to enhance targeted transport to metastatic regions. The enhancement of macrophage membrane resulted in an increase in the uptake of emtansine liposome by metastatic 4T1 breast cancer cells, while also exhibiting inhibitory effects on cellular viability. *In vivo*, the liposome was facilitated in its ability to target metastatic cells and exert a significant inhibitory effect on lung metastasis of BC through its association with the macrophage membrane. The findings suggested a biomimetic approach that utilizes the biological characteristics of macrophages to improve the therapeutic efficacy of nanoparticles *in vivo* for the treatment of cancer metastasis (H. Cao et al., 2016). In addition, a variety of liposomes that are selectively modified with arginine8–glycine–aspartic acid (R8GD) have been developed for the purpose of encapsulating daunorubicin and emodin individually. The synergistic effect of the two specific liposomes demonstrated pronounced cytotoxicity against MDA-MB-435S cells, leading to a significant inhibition of vasculogenic mimicry (VM) formation and subsequent tumour cell metastasis. According to the research findings, the utilization of targeted liposomes led to the selective accumulation of chemotherapeutic agents at the tumor site, thereby inducing a noticeable antitumor response (Fu et al., 2020).

1.5.1.2 Micelles

Micelles are self-assembled structures composed of amphiphilic molecules which possess hydrophilic heads and hydrophobic tails. These structures exhibit a particle size distribution within the range of 10 to 100 nanometers. Micelles offer various benefits such as extended circulation periods in the bloodstream, minimal toxicity, and increased accumulation in tumors. In addition, they are frequently employed for delivering anticancer drugs with limited water solubility. Pluronic block copolymers, comprising of poly(ethylene oxide) and poly(propylene

oxide) in a triblock configuration, are extensively employed for the formulation of drug delivery micelles. Micelles have been utilized for delivering numerous anticancer drugs specifically to BC cells. In a study, (Z. Gong et al., 2020) devised a bimodal therapeutic strategy that employed stable micelles altered with fibronectin-specific CREKA peptides. This approach effectively packed two hydrophobic chemotherapeutic agents, vinorelbine (V) and doxorubicin (D), in an aqueous solution. The designation of C-DVM was assigned to this newly developed construct in the novel. According to their findings, the utilization of small C-DVM micelles proved to be an effective strategy for co-delivery of drugs into 4T1 cells while also inducing disruption of microtubule structures. Additionally, C-DVM displayed a potent capacity to eliminate and hinder the invasion of 4T1 cells. Furthermore, a pharmacokinetic study conducted *in vivo* demonstrated that C-DVM extended the half-life of drug circulation and resulted in higher drug accumulation in lung metastatic foci after 24 h. Moreover, the anticancer studies in mice harboring tumor showed that the C-DVM effectively reduced tumor development and decreased lung metastasis. The developed nanoplatform could be a promising treatment option for metastatic breast cancer.(Z. Gong et al., 2020).

1.5.1.3 Polymeric Nanoparticles

Polymeric nanoparticles (NPs) are tiny particles with a size >1000 nm with the ability to load drug within or on to the surface-adsorbed onto the polymeric core. These nanoparticles can accommodate anticancer drugs through various methods, such as dissolution, entrapment, encapsulation, or adsorption within the polymer matrix. The selection of polymers for the fabrication of nanoparticles can encompass natural polymers, such as gelatin, alginate, cellulose, and chitosan, as well as synthetic polymers like poly(lactic-co-glycolic acid) (PLGA), polylactide (PLA), and poly-ε-caprolactone (PCL). Moreover, they are frequently employed for delivering anticancer drugs in BC therapy. In a study, Katiyar *et al*., developed polymeric NPs for BC therapy using combination of Piperine and rapamycin (PIP and RPM).

PLGA was chosen as the polymer due to its moderate ability to reverse MDR, which may confer supplementary advantages. The nanoparticles that were prepared demonstrated consistent drug release *In vitro* for several weeks. The initial release pattern followed a zero-order kinetics with non-Fickian transport, after which it shifted to Higuchi kinetics with Fickian diffusion. The findings indicate that the introduction of a chemosensitizer has led to an enhanced uptake of the RPM, which is a P-gp substrate. The pharmacokinetic analysis demonstrated a more favorable absorption profile of RPM when delivered through polymeric nanoparticles in comparison to its suspension form. Furthermore, the bioavailability of RPM was significantly improved by 4.8 times when administered in combination with the chemosensitizer. Based on an *In vitro* study using cell lines, it has been observed that the efficacy of nanoparticles is superior to that of free drug solutions. The findings suggest that the utilization of a blend of PIP and RPM nanoparticles could be a potentially promising strategy in the management of BC (Katiyar et al., 2016). Biodegradable PCEC nanoparticles were developed and evaluated by Xiong *et al.* for their potential to carry both curcumin and paclitaxel at once. The study investigated the efficacy of the drug delivery system (PTX-CUR-NPs) in inhibiting BC growth through *In vitro* and *in vivo* experiments. The study findings revealed a gradual and sustained release pattern of paclitaxel and curcumin from the drug delivery system, with no initial burst effect. Moreover, the PTX-CUR-NPs exhibited a dose-dependent cytotoxic effect against MCF-7 cells, with a higher rate of apoptosis than the free drugs (PTX + CUR). The results of the cellular uptake study demonstrated that the PCEC polymeric nanoparticles loaded with the drugs were more efficiently taken up by tumor cells *in vitro*. *In vivo* studies demonstrated noteworthy impediment of neoplasm proliferation, prolonged viability and decreased adverse reactions compared to the free PTX + CUR drugs. Additionally, treatment with PTX-CUR-NPs brought about reduced Ki67 expression, and

heightened TUNEL positivity indicative of increased apoptosis in tumor cells, signifying the therapeutic potential of the drug delivery system (K. Xiong et al., 2020).

1.5.1.4 Solid lipid nanoparticles (SLNs)

Solid lipid nanoparticles (SLNs) are a type of nanoparticle that are composed of solid lipids. The utilization of SLNs, which were first introduced in 1991, presents a superior and alternative carrier system compared to conventional colloidal carriers like liposomes, polymeric nano and microparticles, and emulsions. SLNs were first introduced as a promising drug delivery system for oral administration (Mehnert & Mäder, 2012). Since then, SLNs have garnered significant interest in the field of cancer treatment due to their favorable characteristics, such as a physical stability, high drug capacity, biocompatibility, and desirable drug release profile. SLNs are a promising area of research in the field of nanotechnology, offering numerous potential applications in clinical medicine, drug delivery, and scientific research across various disciplines. Geeta et al., reported the development of transferrin targeted SLNs for BC therapy. In the present study, transferrin-conjugated solid lipid nanoparticles (SLNs) were created with the intention of improving the localization of tamoxifen citrate in breast cancer. The proposed formulations demonstrated higher cytotoxic effect MCF-7 BC cells than free drug in a concentration and time dependent manner. For cellular internalization, both Confocal microscopy and Flow cytometry analysis has been performed and demonstrated higher uptake of SLN in MCF-7 cells than free drug. The Results suggested that the developed nanoformulation can be a promising targeted nanomedicine for BC therapy.

1.5.1.5 Dendrimers

Due to their predictable structure and constrained size distribution, dendrimers provide a viable alternative for the targeted administration of Pt drugs. This distinguishes them from other polymeric technologies, which could struggle to achieve equivalent regularity (C. C. Lee et al., 2005). A type of polymer known as dendrimer is distinguished by its highly branching structure

and many end groups. This particular design enables the effective encapsulation or conjugation of many medicinal molecules, either on the dendrimer's surface or within its core (C. C. Lee et al., 2005). The number of branching cycles carried out during the synthesis process, which gives information on the number of branches and terminal groups present in the dendrimer architecture, is used to determine the dendrimer generation. As the generation number increases, a dendrimer's breadth increases linearly while the number of functional groups on its perimeter increases exponentially (Scott et al., 2005). The relationship between a dendrimer's generation number and the number of functional groups on its perimeter may have a big impact on a dendrimer's ability to load drugs and how quickly those drugs are released. The development of dendrimer-based drug delivery systems may need to take into account this exponential expansion of functional groups. More control over loading and release kinetics may be achieved by adding degradable connections between the drug and dendrimer (Gillies & Frechet, 2005). Dendrimers may be made from a wide range of substances, such as DNA, polysaccharides, poly(aryl ethers), polypeptides, polyamines, and polyamidoamines. According to (Boas & Heegaard, 2004), this leads to a broad range of dendrimer structures.

1.5.2 Inorganic NDDS

The advanced functionality, distinctive surface properties, high drug-carrying capacity, and superior stability of inorganic NDDS make them indispensable in the field of cancer therapy (Lin et al., 2016). The class of inorganic NDDS primarily comprises upconversion NPs (UCNPs) (Ai et al., 2016), silica nanocarriers (including mesoporous silica nanoparticles or MSNs) (W. Zhang et al., 2016), and carbon-based nanocarriers (such as graphenes and nanotubes) (Wong et al., 2013; M. Zheng et al., 2014), Fe_2O_3 nanocarriers (P. Ma et al., 2017), and Au NPs (Nam et al., 2018). Inorganic NDDS offer several advantages. Firstly, they are typically created through soft templating to form a nanoporous structure, which enables the delivery of drug combinations. This type of structure boasts a significant surface area, which

provides ample binding sites for small-molecule drugs and genes. Additionally, certain inorganic NDDS, like gold NPs, possess remarkable optical properties that allow them to convert light into heat, making them ideal for use in photothermal therapy (PPT) (Nam et al., 2018; Zhao et al., 2017). Certain inorganic NDDS have the potential to function as CT imaging agents or MRI, which holds great promise for their use in theranostics (Detappe et al., 2019; Lin et al., 2014; Z. Zhou et al., 2012). The primary hindrance to the clinical implementation of inorganic NDDSs has been identified as acute and chronic toxicity, resulting in a low rate of approval. For its therapeutic use, thorough research on the long-term toxicity of inorganic NDDSs is thus greatly sought (Mohammadpour et al., 2019).

1.5.2.1 Gold Nanoparticles

Gold nanoparticles, characterized by a gold core and a size of less than 150 nm, possess inert and non-toxic properties, as reported by Manju and Sreenivasan (2010). In view of their biocompatibility, gold nanoparticles have gained attention as promising carriers for anticancer agents, as highlighted by Singh et al. (2017). Arvizo et al. (2010) have reported various benefits of gold nanoparticles, including radio-sensitization and photothermal therapy. Furthermore, García Calavia et al. conducted a study demonstrating the use of a lactose derivative for stabilizing and dispersing phthalocyanine-functionalized gold nanoparticles in aqueous solutions. In a 2018 work, Garca Calavia et al. produced and modified gold nanoparticles with a mixed monolayer composed of a zinc phthalocyanine and a lactose derivative. The phthalocyanine-gold nanoparticles were coated with lactose, which led to the production of water-dispersible nanoparticles that could produce singlet oxygen and cause cell death when exposed to radiation. The *in vitro* targeting efficacy of lactose-functionalized gold nanoparticles carrying lactose phthalocyanine towards the galectin-1 receptor located on the surface of SK-BR-3 and MDA-MB-231 BC cells was investigated. The results indicate that lactose has significant potential as a selective targeting agent for galactose-binding receptors

that are upregulated in breast cancer cells. Previous studies have reported the ability of gold nanoparticles to bind with antibodies that are specific to tumor cell surface antigens that are overexpressed (Lim et al., 2011). Multiple scientific investigations have demonstrated that gold nanoparticles (AuNPs) have the potential to increase the availability of drugs at specific sites, improve the effectiveness of cancer treatments such as chemotherapy, radiotherapy, photothermal therapy (PTT), and photodynamic therapy (PDT), and influence gene expression. *in vitro* and *in vivo* studies have verified the ability of AuNPs to impede the growth, progression, and spread of triple-negative BC (TNBC) cells. These mechanistic properties of AuNPs represent an attractive avenue for developing drugs with improved therapeutic effectiveness against TNBC. Consequently, utilizing AuNPs for TNBC therapeutics may represent a promising approach (Akter et al., 2023).

1.5.2.2 Mesoporous silica NPs (MSN)

Mesoporous silica is an emerging inorganic biomaterial that has garnered attention for its potential use in various biomedical applications. In 1992, scientists from Mobil Corporation were the first to inform the design of MSN with a nanostructured pore size (Y. Zhou et al., 2018). The nanoporous structure renders it an exceptional fit for usage as a sustained or controlled drug delivery system. Hongyan He *et al*., reported the synthesis of MSN-oxaliplatin conjugates in the antineoplastic drug delivery (He et al., 2014). The surface of MSN featuring 1,2-bidentate carboxyl groups underwent a reaction with 1,2-diamine cyclohexanol Pt(II) di nitrate (DACH-Pt-$(NO_3)_2$), an active antineoplastic agent clinically similar to oxaliplatin, leads to the formation of MSN-Pt. ICP-MS measurements indicated that the conjugate contained 9.7% Pt content. Confocal laser scanning microscopy (CLSM) revealed that HepG-2 cells quickly internalized MSN-Pt, which subsequently accumulated in lysosomes and endosomes. The *in vitro* cytotoxicity study conducted on MSN-Pt exhibited enhanced cytotoxic effect against HepG-2 cells compared to free drug. The increased intracellular uptake of Pt and higher

binding to DNA (Pt-DNA adducts) exhibited by MSN-Pt as compared to free oxaliplatin contributed to its superior efficacy. These findings suggested that the MSN conjugates loaded with Pt have significant potential in cancer therapy due to their enhanced therapeutic efficacy and reduced adverse effects.

1.5.2.3 Magnetic iron oxide NPs

The application of iron oxide NPs in magnetic resonance imaging (MRI) was effectively demonstrated. Despite its potential applications, producing superparamagnetic iron oxide NPs remains a challenging task for scientists. A recent breakthrough in nanotechnology has enabled researchers to fabricate iron oxide NPs with precise sizes and shapes, as desired (Z. Gao et al., 2018; Ibarra et al., 2018). Superparamagnetic ferric oxide NPs were designed utilizing a thermal decomposition technique and loaded with both artemisinin and cisplatin to increase the drug payload and provide a synergistic effect. Additionally, flow cytometry examination showed a considerable rise in the generation of reactive oxygen species (ROS) and the apoptotic rate in A549/R cells treated with these NPs. The mechanism underlying the local hyperthermia effect of magnetic NPs is generated through hysteresis loss. The localized heat generated by these NPs increased their permeability and led to improved drug release. Cell-penetrating peptide-functionalized magnetic NPs loaded with cisplatin were synthesized for the purpose of treating nasopharyngeal cancer. Fluorescent labeling was employed to assess the biocompatibility and cell-penetrating efficacy of the nanoparticles (Z. Gao et al., 2018).

1.5.2.4 Nanotubes

Nanotubes are tubular structures exhibiting nanoscale dimensions, primarily defined by their diameter, wherein the cylindrical shape is a prominent characteristic; instances of nanotubes comprise Multi-Walled Carbon Nanotubes (MWCNTs) and Single-Walled Carbon Nanotubes (SWCNTs) alongside cyclic peptide nanotubes and nanotubes synthesized via templates (Martin & Kohli, 2003; Matsumura et al., 2007). Nanotubes present intriguing benefits

compared to spherical nanoparticles when it comes to drug delivery purposes. The presence of open terminations and a considerable internal capacity (in proportion to the tube's total capacity) enables the facile incorporation of pharmaceutical compounds at significant loading levels. Furthermore, the outer and inner surfaces of nanotubes offer the possibility of selective chemical or biochemical modifications, which can be leveraged to conjugate targeting ligands or graft PEG (polyethylene glycol) to enhance the biocompatibility of the nanotubes (Matsumura et al., 2007). Despite long-term accumulation *in vivo*, SWCNTs demonstrate low toxicity levels (S. T. Yang et al., 2008). In a study, Badea *et al.*, assessed the efficacy of SWCNTs in facilitating the transportation of cisplatin (CDDP) in order to enhance its cytotoxic effect on MDA-MB-231 breast cancer cells (Badea et al., 2021).

1.5.2.5 Quantum dots (QDs)

Quantum dots (QDs) are semiconductor materials that have a nanometre-scale size ranging from 2 to 10 nm (Nitheesh et al., 2021). They consist of a crystalline metalloid core and a surrounding shell (Tharkar et al., 2015). Quantum dots (QDs) possess distinct optical characteristics, a wide range of excitation wavelengths, and a highly concentrated and symmetrical emission profile. These traits make them suitable for applications such as bioimaging, biolabeling, and biosensing (Fatima et al., 2021). Dong and his colleagues developed a very adaptable and extremely compact Ag2Te quantum dots (QDs) for the purpose of achieving high-performance computed tomography (CT) imaging-guided photonic tumour heating. In addition, due to their remarkable photo-thermal conversion efficiency of 50.5%, these Ag2Te quantum dots (QDs) demonstrated little toxicity and exceptional biocompatibility. Furthermore, they exhibited a significant tumour suppression rate of 94.3% on 4T1 cells in xenograft animal models, as reported by (L. Dong et al., 2020).

1.5.2.6 Graphene

Graphene is a fundamental component of various graphitic materials, which may be wrapped into 1D structures (carbon nanotubes (CNTs)), packed into spherical structures (0D fullerenes), or piled into 3D-layered systems (graphite) (Geim, 2009; Imani et al., 2018). Graphene is similar to fullerenes and CNTs, with different wall thicknesses, diameters, lengths, and surface compositions. Graphene may be considered a planar aromatic macromolecule that comprises a layer of the 6-atom ring with an π-conjugated structure. This planar shape can immobilize a wide range of compounds, including metals, medicines, biomolecules, and fluorescent probes, including cells (L. Feng, Wu, et al., 2013; Gonçalves et al., 2013; Kakran & Li, 2012; H. Shen et al., 2012; Teodorescu et al., 2017; Y. Wang et al., 2011; K. Yang et al., 2013). It is no surprise that graphene has sparked a lot of attention due to its many potential uses in nanomedicine and biomedicine. For example, when appropriately modified, graphene may serve as a beautiful platform for delivering anticancer/gene delivery drugs and other therapeutics (L. Feng & Liu, 2011; Justin et al., 2016; Pan et al., 2012; R. Qian et al., 2019; B. Zhu et al., 2017). Graphene has many advantages over carbon nanotubes, including a cheap cost, ease of manufacture and customization, a greater surface area with two exterior surfaces, and the lack of hazardous metal particles. As a result, graphene has challenged CNTs supremacy in various applications, including drug delivery, attributable to its reduced toxicity and improved biocompatibility (Mendes et al., 2013). The loading ratio (weight ratio of loaded drug to carriers) of graphene nanomaterials (GNMs) may approach 200 percent in the case of drug delivery, which is much greater than nanoparticles and other drug delivery methods (Davis et al., 2008; Y. Zhang et al., 2010). Dai's group in 2008 was the first to show that PEG-functionalized graphene oxide (NGO) may be employed as a new drug nano-carrier to load anticancer drugs through non-covalent physisorption and had in-vitro cellular absorption capability (Z. Liu et al., 2008b; X. Sun et al., 2008). In recent years, many research groups have looked at graphene, graphene oxide (GO), and other graphene derivatives for drug delivery

applications (Jasim et al., 2021). Due to its unique geometrical and structure characteristics, graphene may be used as the preferable material for therapeutic applications. Despite these outstanding chemical and physical features (Castro Neto et al., 2009; Geim, 2009; C. Lee et al., 2008), graphene is challenging to employ in biomedical applications due to its high hydrophobic nature; therefore, its derivatives, like graphene oxide (GO), are frequently utilized as preferable materials. GO possesses many oxygen-based moieties compared to graphene, namely epoxy and hydroxyl groups on the sheet's basal plane and carbonyl, carboxyl, hydroxyl, lactone, and phenol structures towards the sheet edge (D. Chen et al., 2012; Di Santo et al., 2019). These functional groups further improve GO's suitability for biomedical applications. For example, the propensity of the epoxy and hydroxyl groups to form hydrogen bonds considerably enhances the performance of GO in a polar solvent, and the presence of carboxyl and hydroxyl groups on the sheet edge makes GO more amenable to modification and functionalization (D. Chen et al., 2012). More significantly, GO is the most famous nanostructured material capable of converting light energy into heat and causing hyperthermia, ultimately resulting in the thermal elimination of cancer cells (Chang et al., 2016; W. Jiang et al., 2018; Shao et al., 2017). Earlier studies have shown that nanosized graphene oxide (NGO) has better photothermal efficiency than large-scale randomized GO (P. Gong et al., 2018; Yan et al., 2019). GO also has a huge specific surface area, which allows several drugs to be loaded onto the GO surface through electrostatic attraction, π−π stacking interactions, van der waals forces, and hydrogen bonding (Goenka et al., 2014; J. Liu et al., 2013; K. Yang et al., 2013). The outstanding load capacity and photothermal effect of GO make it a multifunctional therapeutic nanoplatform for photothermal-photodynamic or photothermal-chemotherapy combination therapies (**Fig. 1.5**).

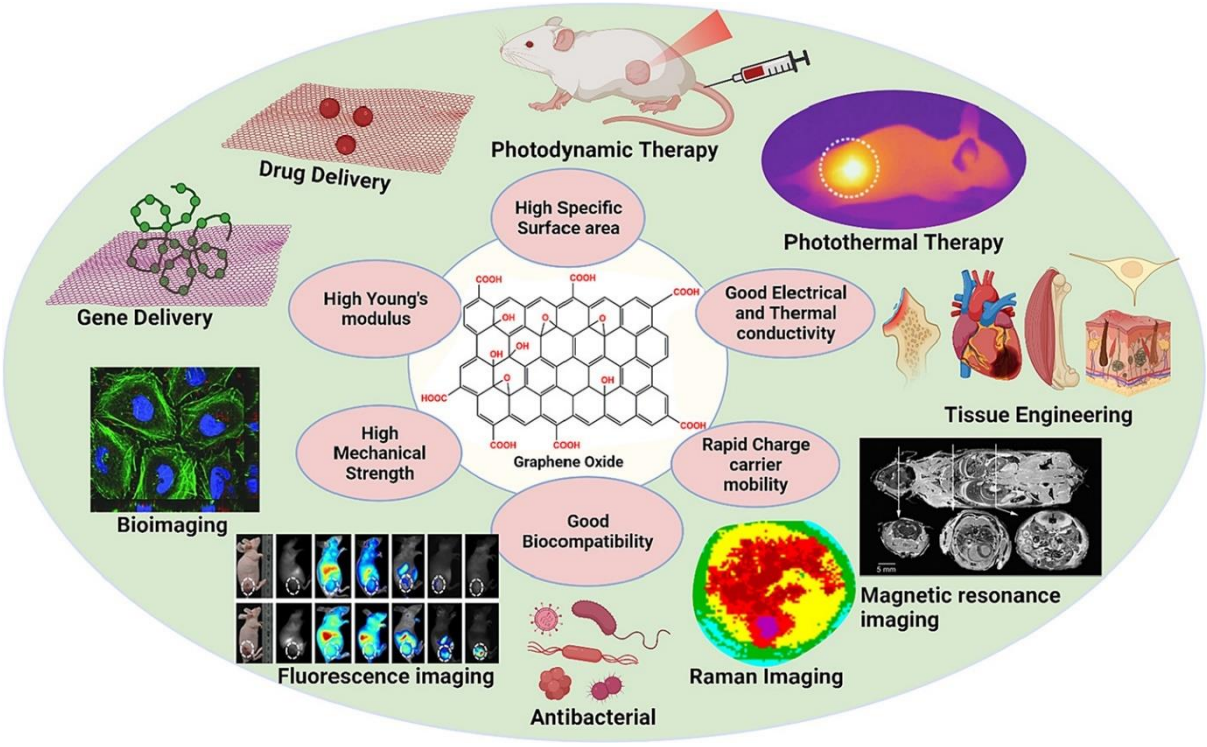

Figure 1.5 Applications of multifunctional graphene oxide.

1.6 Graphene oxide as a drug delivery cargo

1.6.1 Loading ability

A single sheet of carbon with partially filled sp^2 -orbits below and above the plane is graphene. The large surface area, excellent heat conductivity, optical transparency, and high mechanical and elastic strength help to make it worthwhile. It is often used as a semiconductor in electronic devices. New quasi-particles are produced due to the interaction between electrons and graphene. The two most significant components in this class are graphene nano-ribbons and quantum dots, both made of graphene. Ballistic transport is shown by these particles, with electrons traveling up to a micrometer without being scattered (Crevillen et al., 2019). The electrical conductivity of graphene is excellent. It has a lesser solubility in water than other compounds. As a result, many changes have been performed to produce chemically altered graphene, graphene oxide, and layered graphene oxide. It has been discovered that graphene oxide and its derivatives are excellent for generating biocompatible nanocomposites. That's why they are widely utilized in sol-gel chemistry.

In general, a wide range of applications for graphene and its derivatives have been found in the delivery of drugs and the area of advanced medicine. Normal surface functionalization of graphene nanomaterials with polymer helps in their compatibility with the biological system by reducing their toxicity (Bai & Husseini, 2019). Graphene nanomaterials respond to various stimuli, including changes in the magnetic field, electric field, radiation, temperature, pH, and other variables. Based on internal and external signals, they were able to regulate the release of the drug (K. Yang et al., 2016). These stimuli also aid in improving therapeutic bioavailability, the passage of medicines over biological barriers, and the reduction of adverse effects. Because of the abundance of functional groups on the wall surface of graphene nanomaterials, graphene oxides (GOs) have piqued the curiosity of researchers. Graphene was successfully used to entrap DOX and camptothecin using π-π-stacking and hydrophobic interaction. The presence of hydroxyl and carboxyl groups on the surface of GOs facilitates interaction with the hydroxyl and amino groups on the surface of DOX (Pattnaik et al., 2020). Drug release was higher at acidic pH when compared to physiological pH of 7.4 and 6.5. To test the drug-loading ability of graphene nanoparticles, methotrexate (an anticancer drug) was immobilized on the graphene surface. The electrochemical approach was used to show carrier capacity and cellular capacity in 4T1 cancer cell lines (Karimi Shervedani et al., 2018). 5-fluorouracil-loaded GO, a pH-Stimuli sensitive drug delivery system, was designed**,** which released the drug in a controlled fashion at an acidic pH of 5.8 (tumor environment); however, in a normal physiological pH of 7.4, the drug release was drastically reduced (Aliabadi et al., 2018).

1.6.2 Mechanism of loading

1.6.2.1 Covalent interaction

The occurrence of defects and reactive oxygen groups in the graphene framework functions as a site of reactivity, facilitating the surface functionalization of graphene and graphene oxide

(GO) through covalent chemical bonding. Several techniques exist for archiving covalent changes, including electrophilic addition, nucleophilic substitution, addition, and condensation. The epoxy groups of GO are the key reactive sites for nucleophilic substitution reactions. They enable the coupling of amino functionality ($– NH_2$) groups having lone pair of electrons with epoxy groups. This is a straightforward reaction that takes place at ambient temperature in an aqueous phase, making it an excellent technique for large-scale graphene modification with a variety of molecules such as aromatic amines, aliphatic amines, amino acids, silanes, polymers, amine-terminated biomolecules, ionic liquids, enzymes, and nanoparticles (Dikin et al., 2007; Dreyer et al., 2010; Loh et al., 2010). Bourlinos et al. established the covalent coupling of several primary amines from two to eighteen carbon atoms and amino acids to graphene (Bourlinos et al., 2003). Wang et al. designed hydrophilic GO sheets with covalently attached allyl-amines using the solvothermal technique (G. Wang et al., 2009). Polyethylene glycol (PEG) is a biocompatible hydrophilic polymer that has been utilized to functionalize many nanomaterials to enhance biocompatibility, reduce unspecific adsorption to biological molecules and cells, and enhance *in vivo* pharmacokinetics for better tumor targeting. Dai and colleagues have successfully coupled PEG to GO for drug delivery applications. The exfoliation-prepared pegylated graphene oxide (PEG-GO) composites showed high stability in physiological solutions (Z. Liu et al., 2008b). Robinson et al. have verified similar findings (Robinson et al., 2011). Other polymers like polyethyleneimine (PEI) (B. Chen et al., 2011)**,** poly(vinyl alcohol) (PVA) (Sahoo et al., 2011)**,** poly(N-isopropyl acrylamide) (PNIPAM) (Pan et al., 2011)**,** chitosan (Bao et al., 2011; Depan et al., 2011; Rana et al., 2011)**,** amphiphilic copolymers (H. Hu et al., 2012; Kakran et al., 2011)**,** and polysebacic anhydride (PSA) (J. Gao et al., 2011)**,** have been attached onto GO sheets by covalent techniques to improve their biocompatibility. These PEI-modified GOs were used to render functionalized graphene oxide more water-soluble. Then folic acid (FA) was added to target

CBRH-7919 cancer cells specifically, suggesting that these polymer changes may be used to target cancer cells. Although there are fewer functional groups on graphene sheets, covalent techniques may be used to modify them. Other polymers that have been effectively used to modify graphene covalently include PAA (Gollavelli & Ling, 2012), PLL (poly-L-lysine) (Shan et al., 2009), and PEG, PEI (G. Wei et al., 2012). Shan et al. (Shan et al., 2009) have synthesized a PLL covalently functionalized graphene that is water-soluble and biocompatible. Graphene sheets served as connectors in assembling poly-L-active lysine amino groups, generating a biocompatible environment for further functionalization, such as connecting bioactive compounds. Several groups used diazonium salt chemistry to perform an electrophilic substitution reaction with graphene, which involves the displacement of a hydrogen atom by an electrophile (Bekyarova et al., 2009; G. Wei et al., 2012). It was discovered that para-nitro aniline diazonium ions might be grafted onto the graphene surface to produce organo-soluble graphene. Stankovich et al. described surface modification by condensation reaction utilizing a range of isocyanate compounds, demonstrating facile dispersion of isocyanate-modified graphene (Stankovich, Piner, Nguyen, et al., 2006). Organic di-isocyanates have also been effective in altering and cross-linking GO (D. D. Zhang et al., 2009). Small molecules may be grafted onto the GO surface employing thionyl chloride ($SOCl_2$), which forms a covalent (amide bond) with amino functional groups (L. Zhang et al., 2010)(X. Yang et al., 2011). Zhang et al. (L. Zhang et al., 2010) used sulfonic acid groups (-SO_3H) to functionalize GO sheets, followed by covalent grafting of folic acid (FA) molecules. The FA-conjugated GO (FA– GO) was effectively distributed and stable for many months in a physiological solution and in the D-Hanks buffer. It's vital to remember that some of these covalent changes of GO might be reduced to R-GO, altering the original material's interfacial characteristics.

1.6.2.2 Noncovalent interaction

In the modification of graphene and GO, non-covalent modifications such as electrostatic interaction, coordination bonds, Van der Waals forces, π-π stacking interaction, and hydrogen bonding have been widely exploited. Non-covalent functionalization can be accomplished through surfactant or small molecule adsorption, polymer wrapping, and interconnections with biomolecules or porphyrins such as peptides and DNA. This is a well-researched method for surface functionalization of carbon sp^2 materials that have been widely used for carbon nanotubes (CNTs). Stankovich et al. used poly(sodium 4-styrene sulphonate) to achieve the first non-covalent functionalization of graphitic nanoplatelets (PSS) (Stankovich, Piner, Chen, et al., 2006). Polymers and organic compounds with π-π stacking interaction and pyrene functional groups with graphene are the most effective way to functionalize. Liu et al. (J. Liu et al., 2010) synthesized various pyrene-ending polymers that were used to modify R-GO via π-π stacking interaction. In one study, Feng et al. (L. Feng et al., 2011) employed non-covalent electrostatic interactions to modify GO through PEI polymer, resulting in GO–PEI complexes with excellent physiological stability, reduced cytotoxicity to cells, and high positive charges. The amphipathic polymers are most often utilized to coat GO to enhance its drug loading capacity, anti-biofouling capability, and solubility. A nano-supramolecular assembly was constructed by Yang et al. (Y. Yang et al., 2012) employing folic acid (FA)-functionalized -cyclodextrin and GO that were non-covalently coupled by an adamantane-grafted porphyrin via a stacking interaction between them. A new folate-decorated and graphene-based therapeutic system for DOX was designed by linking DOX to GO via π-π stacking interaction and to embody GO with folic acid-linked chitosan to enhance the stability of the nanocarrier system in an aqueous medium (Depan et al., 2011). Decorations using nanoparticles (NPs) such as Au, Ni, Pt, TiO_2, Pd, Cu, Ag, Fe_3O_4 Co_3O_4, MnO_2, and ZnO benefit from the massive p-conjugated structure, extensive structural flaws on R-GO, and functional groups on GO. Graphene and graphene derivatives have been successfully used in various drug delivery

systems (W. Chen et al., 2011; X. Huang et al., 2012; J. Shen et al., 2010; X. T. Zheng & Li, 2012)**.** Because of their intriguing magnetic and optical characteristics and their capacity to integrate drug delivery with biosensing and external stimuli delivery capabilities, these graphene/nanoparticle composites have gotten a lot of attention.

Yang et al. (X. Yang et al., 2009) devised a technique for chemically depositing Fe_3O_4 nanoparticles onto GO that is simple, effective, and scalable. This hybrid displayed super-paramagnetic characteristics and high loading capacity for the anticancer medicine DOX. It was also discovered that it congregates in acidic environments and may be re-dispersed reversibly in basic environments. To functionalize GO, it may be possible to exploit both nanoparticles and polymers in certain instances. A multifunctional super-paramagnetic graphene Fe_3O_4 hybrid nanocomposite (GO–IONP) was produced by Ma et al., which was then conjugated with a biodegradable, nontoxic PEG polymer to achieve excellent physiological stability (X. Ma et al., 2012). This pegylated nanocomposite (GO–IONP–PEG) complex, which permits magnetized targeted drug delivery and has an excellent optical absorbance from visible to near-infrared light, may be employed for targeted photothermal elimination of cancer cells controlled by a magnetic field. However, biocompatibility and drug delivery applications for graphene functionalized with such tiny nanostructures may need more stringent testing in biological investigations.

Additionally, there are potential drawbacks to using non-covalent techniques. Non-covalent adsorption of polymers onto GO surfaces is less durable than covalent adsorption and is susceptible to external environmental variations on interaction with biological systems *in vitro* or *in vivo,* making prospective drug delivery systems less stable. Non-covalently functionalized GO may load a lower quantity of aromatic drugs because the conjugated regions of the GO sheets are partly filled by coated polymers. Zhang et al. (L. Zhang et al., 2011) compared the drug loading efficacy of PEI–GO generated by a non-covalent adsorption technique versus

PEI–GO prepared by a covalent method. Their results were expected, demonstrating that the former is less stable than the latter.

1.6.3 Stability information

Surface chemistry, lateral dimension, layer number, surface area, and purity are all features of graphene nanomaterials that are important for biological and drug delivery applications. Graphene has a surface area of 2600 m^2g^{-1}, four times larger than any other nanocomposites studied for drug delivery (K. Yang et al., 2010). A graphene monolayer is an exceptional case wherein every atom on the interface is exposed, resulting in a much higher drug loading capacity than other nanostructures. For a myriad of purposes, the number of layers and thickness of graphene and GO sheets is critical. A higher layer count reduces surface area while increasing the stiffness of graphene nanomaterials (GNMs) nanocarriers, which is necessary for cell penetration. Although the lateral dimensions of GNMs have minimal impact on effective surface area or drug loading, they may have size limits that affect renal clearance, blood-brain-barrier trafficking, biological degradation, cell uptake, and other biological processes. Even the cytotoxicity and cellular uptake of 2-D plate-like nanomaterials are not well known; the lateral dimensions and form of the nanomaterials may have a significant impact on toxicity. According to prior studies on nanoparticles and carbon nanotubes, the uptake and connection of nanocarriers with cells/macrophages are influenced by a variety of essential features such as shape, size, charge, and surface chemistry. Graphene and GO have a distinct 2-D structure with planar geometry rarely observed in biological systems; hence, the shape is important. Another important structural feature for maintaining the structural integrity of drug delivery carriers is rigidity; however, if the graphene and GO structures are excessively stiff, the cell may get damaged. To minimize this effect, it's crucial to lower the stiffness of graphene and GO sheets, which might be a roadblock for drug delivery applications. In terms

of surface chemistry, pure graphene is very hydrophobic and weakly dispersible in water; therefore, any biological uses will need the help of surfactants or surface modification.

On the other hand, GO is hydrophilic and may form stable colloids when distributed in the water. Many impurities, such as residues from nitrates, peroxide, sulfates, borohydride surfactants, permanganates, hydrazine, and some lower-molecular-weight oxidative debris, could be produced during GNM production, all of which could have negative biological effects and significantly influence their toxicity (Pumera, 2011). In general, the effective design of graphene and GO-based drug delivery applications necessitates resolving the many difficulties already mentioned. The first question is what changes must be made in order to create an efficient nano-carrier with optimal drug-loading capacity. Before conducting pre-clinical and clinical research, the second step is to validate or enhance their biocompatibility and toxicity. The third step is to create a system that can release medications in a controlled manner at an optimal dose at a particular spot necessary for effective treatment. In recent years, significant progress in addressing these difficulties essential for creating novel drug delivery systems has been reported, including *in vivo* experiments with promising outcomes.

1.6.4 Mechanism of targeting

1.6.4.1 Passive Targeting

Tumor-bearing blood vessels are naturally leaky, allowing nanocarriers to readily pass through the endothelium barrier and into the interstitial space. Tumor endothelial cell linings vary in size from 100 to 700 nm, fifty to seventy times bigger than the normal and distinct endothelium. Furthermore, tumors have a poor lymphatic drainage system, leading to a lack of vascular repatriation of extravascular particles, causing nanocarrier agglomeration at the tumor tissue. This is known as the enhanced permeability and retention (EPR) effect, and it's thought to be an excellent way to target tumors effectively (V. Torchilin, 2011)**.** Nanocarriers containing low molecular weight drugs, on the other hand, reenter the bloodstream due to diffusion and hence

cannot remain at the tumor site for a lengthy amount of time. The pathophysiological and immunochemical properties of tumor tissues determine the targeting impact of such drugs, which is also known as "passive targeting" **(Fig. 1.6)** (Karki et al., 2020; V. Torchilin, 2011). The utilization of nanocarriers not only increases drug circulation in the body but also enhances tumor cell specificity by leveraging the EPR effect. To achieve long-term drug retention, researchers use a variety of approaches, including stimuli-sensitive polymeric-based nano-carrier systems. Passive targeting is further aided by the diverse and different microenvironment around tumor cells compared to normal cells. Tumors that spread quickly and are hyperactive have a very high metabolic ratio. As a result, the available oxygen and nutrients are insufficient, enabling tumor cells to get additional energy via glycolysis, resulting in an acidic environment (V. P. Torchilin, 2007).

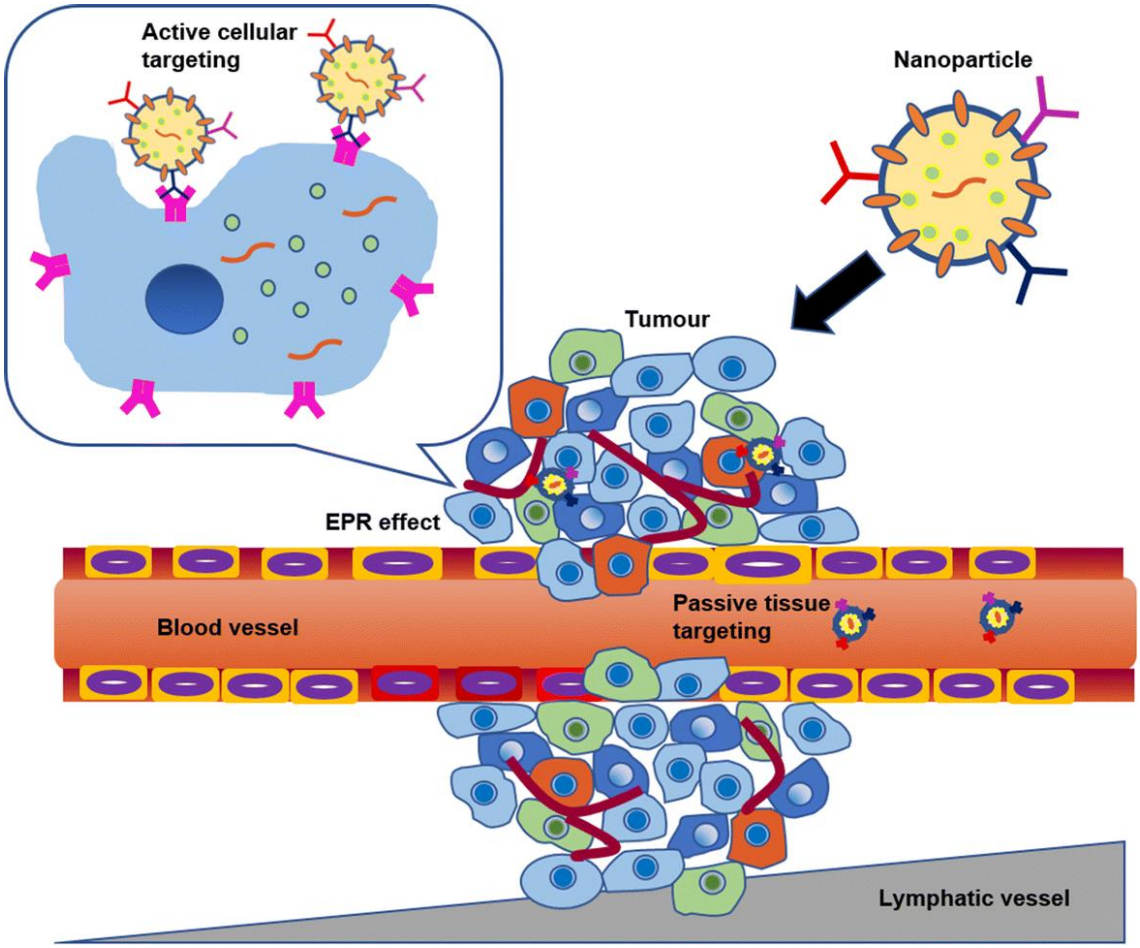

Figure 1.6. Schematic illustration of active targeting vs passive targeting of nanoparticles.

Additionally, tumor cells secrete specific enzymes, such as metalloproteases, that are linked to their mobility and survival (Pelicano et al., 2006). Various nanocarriers, such as polymers, liposomes, NPs, antibodies, and micelles, were employed to target this unique tumor microenvironment. A number of approaches for passive and active drug targeting to cancer cells and endothelial cells and enhanced drug transport have also been developed and clarified (Deryugina & Quigley, 2006). In this field, significant progress has been made, with a large number of nanomedicines with passive tumor-targeting mechanisms receiving FDA clearance for clinical usage. Exaggeration or misinterpretation of the EPR effect, differences between the animal model and human patients, and reduced penetration of the nanomaterials into the targeted tissue and tumors are the most severe limitations of passive tumor targeting that cannot be neglected.

The effectiveness of GO-based delivery is predicated on its capacity to improve tumor localization and accumulation. For example, increased tumor accumulation is caused by increased absorption, which is passively mediated by the enhanced permeability and retention effect. In a study, Yang et al. developed ultra-small, reduced graphene oxide coupled with PEG by non-covalent linkage with sheet diameter >30 nm and examined how surface chemistry and sizes impact the *in vivo* behaviors of graphene. The *in vivo* studies demonstrated complete tumor elimination from the mice following exposure to 808 nm NIR laser radiations. The efficacy of graphene-based DDS in photothermal cancer therapy was significantly enhanced because of the EPR effect and highly efficient tumor passive targeting (K. Yang et al., 2012). In another study, Yang et al. (K. Yang et al., 2011) demonstrated that nano-GO chemically modified with PEG mostly concentrates in the reticuloendothelial system after intravenous injection, including the spleen and liver, and may be progressively eliminated, most likely through both faecal and renal excretion. Further, *in vivo* investigations discovered several extremely intriguing behaviours of Nano-GO-PEG nanoparticles administered intravenously,

including highly effective passive tumor targeting and comparatively poor retention in reticuloendothelial systems. They continued to investigate *in vivo* phototherapy in the NIR region, and the findings indicated that I.V injection of modified nano-GO followed by low-power NIR laser irradiation on the tumor effectively ablates tumors (K. Yang et al., 2010). Blood biochemistry, haematological analysis, and histological investigations of the treated mice showed no signs of major toxicity at the tested dosages, (K. Yang et al., 2010, 2011) which indicates the strong potential of produced materials in the treatment of cancer.

1.6.4.2 Active Targeting

The active targeting of specific cancerous tissue is enabled by the surface functionalization of nanomaterial with site-specific targeting ligands (**Fig. 1.6**) (Karki et al., 2020). The targeting agents may interact with specific receptors upregulated by cancerous cells or tumor vessels. Small molecules, peptides (arginyl glycyl aspartic acid [RGD]), vitamins (folic acid), nucleic acids, glycoproteins (transferrin), antibodies and antibody fragments, and growth factors are some of the specific targeting ligands typically utilized to boost the site-specificity of nanocarriers. Nanocarriers having a high surface area to volume ratio may be able to attach multiple targeting groups effectively, facilitating better tumor cell localization. Active tumor targeting is a technique for reducing chemotherapeutic agent off-target administration while avoiding the drawbacks of passive tumor targeting and overcoming multidrug tolerance (Danhier et al., 2010). The selected target receptor must be produced uniformly in all target tissues for efficient active targeting. The selected targeting agent must preferentially attach to a receptor upregulated by cancer cells. Active targeting is used to target tumor cells or the tumor microenvironment/vasculature using a ligand-decorated nano-carrier. Both of these cellular targets have recently received much attention in active targeting to increase the effectiveness of chemotherapeutic drugs and lessen their adverse effects. The active targeting of tumor cells employs ligand-receptor interactions to target overexpressed cell surface

receptors with ligand-anchored nanocarriers (Patil et al., 2009). Following that, receptor-mediated endocytosis (internalization) enhances nano-carrier absorption by cancer cells, resulting in increased intracellular drug concentration with little or minimal tumor formation (Allen, 2002). Transferrin receptor (TfR), folate receptor (FR), and epidermal growth factor receptor (EGFR) are the most common upregulated cellular receptors on cancer cells in diverse types of malignancies (Pirollo & Chang, 2008). On the cellular surface of a distinct malignant tumor, a few of these tumor markers may be abundantly expressed, e.g., folate-modified nanomaterials could be exploited to target lung, breast, colorectal, and ovarian cancer cells because FR is upregulated in these tumor cells (Danhier et al., 2010). Transferrin may be employed as a substrate for targeted delivery of anticancer drugs into the brain since TfRs are abundantly present on the surface of endothelial cells of the blood-brain barrier (Sudimack & Lee, 2000). In contrast to the aforementioned technique, actively targeting the tumor vasculature (tumor endothelium) instead of tumor cells has several benefits. Targeting the tumor vasculature entails the elimination of tumor vascular endothelial cells, which block oxygen and nutrition delivery to tumor cells, resulting in tumor cell death (Gan & Feng, 2010; Neri & Bicknell, 2005). Active tumor vascular targeting might be enabled using ligand binding nanomaterials by targeting a range of components in the vascular system, including vascular cell adhesion molecules (VCAMs), vascular endothelial growth factors (VEGFs), αv β3 integrin's, and matrix metalloproteases (MMPs). Here are a few instances of active tumor targeting using different nanocarriers that have been surface-functionalized with targeted ligands (Martínez-Carmona et al., 2015; Neri & Bicknell, 2005). Choi and Park developed docetaxel-loaded nanocrystals with transferrin surface functionalization, resulting in active site-specific targeting characteristics in the human lung cancer cell line A549. Transferrin-modified docetaxel nanocrystals demonstrated higher cellular retention and toxicity than docetaxel nanocrystals and standard drugs (J. S. Choi & Park, 2017). In a separate study,

apatinib-loaded liposomes were surface engineered with the targeting ligand cyclic arginyl glycyl aspartic acid (cRGD) to target the αvβ3 integrin in the human colon HCT116 cancer cell line to compare non-targeted liposomes with targeted liposomes. The cRGD anchored liposomes demonstrated enhanced cellular internalization and tumor growth inhibition (Z. Song et al., 2017). In addition, Wu et al. designed folate-functionalized paclitaxel-loaded micelles to target a human esophageal cancer cell line (EC9706) which demonstrated higher cytotoxicity, better cellular internalization, and significant tumor growth suppression than free paclitaxel (W. Wu et al., 2012)**.** The commonly used targeted moiety by GO for the delivery of drugs in cancer are given below:

1.6.4.3 Tumor microenvironment targeting

Targeting the tumor microenvironment is an attractive strategy for the treatment of solid tumors. Luis Augusto Visani de Luna et al. reported that GOAg nanocomposite significantly enhanced ROS production relative to pristine silver nanoparticles (AgNP) and was more toxic for both macrophages than AgNP and pristine GO(de Luna et al., 2016). The polarization state of tumor-associated macrophages (TAMs) is crucial for the development and spread of tumors. Xiangyu Deng et al. demonstrated that M2 macrophage polarization might be reduced by photothermal treatment. In order to determine its anti-tumor efficacy *in vitro* and *in vivo*, they have employed GO coupled with PEG as the photothermal material and modulated their antitumor capability (X. Deng et al., 2020).

In general, cancer cells have the capacity to move across sites attributable to the intricate process of cytoskeletal reorganization. Integrins on pseudopodia, in particular, modulate intracellular signaling pathways that affect cell adherence to the extracellular matrix and cytoskeletal structure for movement. Honglan wang et al. have developed iRGD-modified GO nanosheets for effective cancer therapy. The synergistic disturbance of cytoskeleton remodeling caused by iRGD-specific binding to integrins and photothermal treatment results

in impaired metastasis and cell motility (H. Wang et al., 2021). Zhou et al. demonstrated the combination of integrin $\alpha_V\beta_3$ mono-antibody functionalized graphene oxide (GO) and pH-responsive charge-reversal polyelectrolyte as a carrier system for the active targeting and sustained release of DOX into tumor cells.

Albumin shows active tumor targeting via their interaction with gp-60 and SPARC proteins abundant in the tumor-associated endothelial cells and the tumor microenvironment. Wentao Deng et al. reported the development of photothermally triggered, VEGF-targeted, biocompatible paclitaxel nano drugs on dual-carriers made of albumin and graphene oxide that showed high biosafety and *in vivo* study indicated the effective tumor-reduction ability of the dual-targeted NPs, which increased their survival (W. Deng et al., 2018).

1.6.4.4 Receptor-mediated internalization

In order to boost the anticancer effect and treatment possibilities of GO-based drug delivery carriers, biological recognition ligands, such as folic acid (FA), transferrin, Biotin, Lectins, peptides, tumor-specific antibodies, or other potential targeting molecules, may be attached to GO. This results in the active targeting of drug candidates to tumor tissues. Yuan-Yong Song et al. reported a unique, multifaceted probe that combines photoacoustic imaging (PA), chemo-photothermal treatment, and actively targeted fluorescence imaging (FL) for malignancies (Y.-Y. Song et al., 2018). A delivery system (QD@Si-D/GO-FA) for active specific target dual-mode imaging and synergistic chemo-photothermal for tumor cells was efficaciously achieved by coating core-shell silver sulfide@mesoporous silica (QD@Si) with targeting molecule folate (FA) modified graphene oxide (GO), which was then mounted with anticancerous drug doxorubicin by electrostatic adhesion. These findings demonstrated the probe's significant potential for use in cancer, where it is anticipated to support the early detection and management of malignancies (Y.-Y. Song et al., 2018). In an interesting study performed by Zhang et al. designed folic acid (FA) covalently conjugated to nano graphene oxide (nGO)

loaded with camptothecin (CPT) and DOX molecules actively targeted human breast cancer MCF-7 cells and produced a much greater level of cytotoxicity compared to the nGO loaded with either DOX or CPT alone. It was determined that the FA-armed nGO delivery system that was loaded with DOX and CPT might have broad biomedical applications (L. Zhang et al., 2010). In a study, Chunzhi Huang et al. developed a nano-based drug delivery system (GO/PP-SS-DOX/PEG-FA) for effective cancer therapy. mPEG-PLGA (PP) and doxorubicin (DOX) were coupled through a disulfide link to produce the redox-sensitive PP-SS-DOX prodrug. PEG-FA offered specific targeting properties for the developed drug delivery system. Targeting nanohybrids were substantially more cytotoxic *in vitro* than non-targeting nanohybrids. According to *in vivo data*, targeted nanohybrids exhibited a potent anticancer impact while having almost little systemic adverse effects in mice with B16 tumors (C. Huang et al., 2018). Following the conjugation of GO with PEG and FA, siRNA was loaded onto the GO using 1-pyrenemethylamine hydrochloride through π–π stacking. This allowed for the specific intracellular delivery of hTERT siRNA. According to *in vitro* studies it was discovered that the transfected hTERT siRNA could effectively decrease the mRNA level and protein expression level in the HeLa cells (X. Yang et al., 2012).

Guodong Liu et al. reported the development of transferrin-conjugated Pegylated-nGO (Tf-PEG-GO-Dox) for loading and glioma-targeting delivery of the anticancer drug doxorubicin (Dox) using transferrin (Tf), an iron-transporting serum glycoprotein, as the ligand binds to the overexpressed receptors at the surface of cancer cells (G. Liu et al., 2013). The *in vitro* cell study results indicated successful cancer cell targeting, significant cellular internalization, and cytotoxicity in transferrin-overexpressing glioma cell lines than free DOX. The *in vivo* study indicated the effective tumor-reduction ability of the dual-targeted NPs, which increased their survival (G. Liu et al., 2013). In contrast to normal cells, tumor cells also have an overexpression of the biotin-specific receptors, which is necessary for tumor development.

Vinothini et al. synthesized DOX-loaded k-carrageenan conjugated GO for specific targeted drug delivery in cervical cancer. The results demonstrated pH-sensitive drug release, significant cytotoxicity, and induced greater DNA damage in HeLa cells compared to free Dox (Vinothini et al., 2019). This drug delivery system could be a promising therapeutic approach to cervical cancer treatment.

In a study, Qiu et al. developed nanosheets (FU/GO-PEG-GE11) made of graphene oxide (GO) that were functionalized with GE11, an effective ligand for the epidermal growth factor receptor (EGFR), and loaded with the anticancer drug 5-fluorouracil (5-FU). The targeting nanosystem was substantially more cytotoxic *in vitro* than non-targeting nanohybrids. According to *in vivo data*, targeted nanocomposites exhibited a potent anticancer impact while having almost little systemic adverse effects in mice with subcutaneous cervical cancer (Qiu et al., 2020).

1.6.4.5 Organelle specific Targeting

The cell's mitochondria, popularly known as the "powerhouse," regulates metabolism, biosynthesis, signaling, and bioenergetics. As a result, it has evolved into an unconventional target for cancer therapies, but a significant obstacle still exists in the specific targeting of mitochondria in the intracellular milieu in tumor cells (F. Wang et al., 2010). To solve this, Mallick et al. designed a positively charged, polyethyleneimine-coated, self-assembled graphene oxide nanoparticle (PEI-GTC-NP) that also contains cisplatin and topotecan and simultaneously. At 6 h, these PEI-GTC-NPs efficiently settled into the mitochondria of HeLa cervical cancer cells. This mitochondrial dysfunction caused the production of reactive oxygen species, which afterward significantly increased tumor cell death (Mallick et al., 2019). This technology may be utilized to target certain subcellular organelles for potential cancer treatments in the future. In another study, magnetic graphene oxide (GO) nanocarriers that target mitochondria were developed to effectively impair cancer cell mitochondria. The

magnetic-Fe_2O_3 was grafted onto the surface of GO, and then mitochondrion targeting peptide (MitP) was covalently modified to produce the 2D GOMNP-MitP nanosheets. GOMNP-MitP nanosheets demonstrated a high capability for loading chemotherapeutic drug mitoxantrone (MTX) and targeting specific cancer cell mitochondria. The GOMNP-MitP released MTX into the mitochondria with the help of an alternating magnetic field (AMF), substantially compromising mitochondrial activities such as attenuating ATP synthesis, decreasing mitochondrial membrane potential (MMP), and further culminating in the induction of apoptosis (H. Zhu et al., 2021). In this work, 2D nanosheets were used to provide very effective mitochondrion-targeting drug delivery for cancer chemotherapy.

Zhang et al. have also developed a glycyrrhetinic acid functionalized GO carrier system loaded with DOX for effective targeted delivery into mitochondria. According to the thorough *in vitro* and *in vivo* mechanistic investigation, GA-functionalized GO lowers the MMP and activates the MMA pathway. Comparing the GA-functionalized drug delivery system to the non-GA-functionalized nanocarrier delivery system, the former shows significantly increased apoptosis induction capability and anticancer effectiveness (C. Zhang et al., 2018). The GA-functionalized nanocarrier exhibits minimal toxicity as well, indicating the potential for it to be a beneficial drug delivery method.

Zeng et al. designed a lysosome-targeted delivery system (NGO-PEG-BPEI) to improve photodynamic treatment (PDT) of a photosensitizer (Ce6) by using pegylated GO and branched polyethyleneimine (BPEI) (Zeng et al., 2015). The effectiveness of PDT is considerably increased as a result of the particular organelle photo-damage that results from exposure to radiation because the photosensitizers particularly aggregate in certain organelles (such as lysosomes, endoplasmic reticulum, late endosomes, or the mitochondria) (Kessel et al., 2012). The developed system demonstrated enhanced cellular absorption, higher loading capability, targeted deposition of Ce6 in lysosomes, and therefore stronger ROS generating capacity of

the NGO-PEG-BPEI-Ce6, and significantly boosted photodynamic effectiveness (Kessel et al., 2012).

Contrarily, mitochondrial, and nucleus-targeted therapies have drawn more attention than Golgi apparatus, lysosome, and endoplasmic-targeted nanodrugs. Mostly because the targeting processes are yet uncertain, and it is currently difficult to synthesize relevant nanomaterials.

1.6.5 Multifunctional graphene oxide applications

1.6.5.1 Cancer-targeted graphene oxide

To build a GO drug delivery system for anticancer therapy, we can load anticancer drugs like Doxorubicin (DOX), Paclitaxel (PTX), and methotrexate (MTX), etc. on the surface of GO or immobilize it with graphene (J. Liu et al., 2013). Cell-type-specific nanoparticles as drug carriers could be used to target cells in lower dosage form successfully. For example, to specifically target one of the human breast cancer cell lines MCF-7, aptamer conjugated magnetic graphene oxide nanocarriers were synthesized and found to be an ideal drug carrier of anticancer targeted drug delivery systems (Hussien et al., 2018). In one study, Graphene oxide was successfully copolymerized with β-cyclodextrin, which was loaded with both hydrophobic drug methotrexate (MTX) and hydrophilic drug (DOX) showed excellent performance in killing cancer cells (Pooresmaeil & Namazi, 2018).

1.6.5.1 Bioimaging/theranostic applications

Instead of using metal ion chelates and stabilizing agents in the synthesis of GO, in a study, non-toxic GO nanoparticles were synthesized by conjugating with PLA and were found to be biocompatible and showed no toxicity toward human vascular smooth muscle cells. They were also found to be photo-stable in the biological milieu and hence can be used as a tool for bioimaging (Yogesh et al., 2020). Transferrin functionalized gold nanoclusters can be used as a NIR fluorescent probe for bioimaging of cancerous cells and has excellent water solubility, stability, and negligible cytotoxicity (Y. Wang et al., 2013). GO-ICOSAN is a carbon-based material that was found to be successfully internalized by the cells and accumulates in the

cytoplasm. This conjugate also shows a pretty good distribution profile, hence having the potential to be a theranostic agent for bioimaging (Ferrer-Ugalde et al., 2021). The GO and branched polyethyleneimine hybrid have electrical and optical properties; therefore, it facilitates sensing and bioimaging (H. Kim et al., 2011). Due to the high tissue penetration effect, NIR light can be used in fluorescence tracking. In a study, researchers synthesized nanometer-sized reduced GO-derived quantum dots, superior to other nanomaterial imaging platforms (Hasan et al., 2021).

1.6.5.2 Chemo-photothermal therapy

Conventional chemotherapy has various off-target site side effects and accumulation in the tumor tissue. Photothermal therapy (PTT) is a novel approach to treating tumors because of its non-invasiveness and high selectivity. This treatment involves transforming absorbed high NIR radiation into heat and is used in combination with chemotherapy (C. Huang et al., 2019). In a study, GO nanosheets were synthesized via a controllable approach by making a hydrogel of carboxymethyl cellulose, polyethylene glycol, and chitosan along with the anticancer drug DOX. This hydrogel can be potentially used as a chemo-photothermal agent due to its pH sensitivity, drug release behaviors, and substantial NIR absorption property (W. Liu et al., 2019). PEGylated GO loaded with DOX can also be used in photothermal treatment and chemotherapy, destroying the tumor without weight loss to the patient and preventing recurrence of the tumor (W. Zhang et al., 2011). PEGylated GO which is reduced to an ultra-small size, can be promised for ultra-effective photothermal treatment. Surface chemistry and size are important factors and critical to optimize while designing photo therapies for cancer (K. Yang et al., 2012). The surface characteristics, especially the functional groups attached to the GO, help in recognition of molecules and also increase the photothermal conversion efficiency. In one study, both the chemo and photothermal efficiency were enhanced by coating GO with $Cu_2{-}xSe$ nanoparticles and folic acid, which increased the photothermal efficiency

and then loaded with DOX to increase the anticancer effect (Zhen et al., 2018). For further surface modification, (GO) nanosheets with rich carboxyl groups were synthesized as the supporter for hyaluronic acid−methotrexate prodrug modification via an adipic dihydrazide cross-linker to enhance blood compatibility and photothermal therapeutic effect (H. Zhang et al., 2019). In another study, tea polyphenol-reduced and functionalized graphene oxide were conjugated with an anti-PDL1 antibody, and DOX was used to develop one single nanoplatform for synergistic targeted photo-chemotherapy (Hao et al., 2020). In most cases, the DOX loading can be enhanced by coating it with mesoporous silica (Shao et al., 2017). The addition of dopamine hydrochloride in oil-water biphasic reaction and mesoporous silica can act as a multifunctional drug carrier system for photothermal therapy of cancer (R. Liu et al., 2019). The nano-reduced GO sheets with NIR light absorbance properties are more biocompatible and less costly compared to other NIR photothermal agents like gold nanomaterial and carbon nanotubes (Robinson et al., 2011).

1.6.5.3 Chemo-photodynamic therapy

Photodynamic therapy is a non-invasive therapy for cancer that generates reactive oxygen species (ROS). The combination of chemotherapy and PDT along with PTT is a novel and efficient strategy for enhanced tumor eradication (X. Huang et al., 2020). Tumor cells are pathologically featured with hypoxic conditions, and hence ROS generation creates a toxic environment for them. To relieve tumor hypoxia by self-oxygenation, a nanosystem was developed consisting of GO doped with MnO_2, Ce6, and anticancer drug Cisplatin, which resulted in enhanced cell toxicity and tumor growth inhibition (P. Liu et al., 2021). Instead of individual photothermal, photodynamic, or chemotherapy, a synergistic therapy nanoplatform results in highly efficient antitumor activity (Liang et al., 2019). In a study, GO hollow nanoparticles were synthesized by using silicon dioxide and loading protoporphyrin in the structure. This conjugation is applied to induce high PTT and PDT when irradiated with NIR

and visible light (Jang et al., 2017). mPEG modified nGO can be synthesized as a photosensitizer (PS) carrier for photodynamic therapy of cancer as it exhibits pronounced phototoxicity in the cells under Xe light radiation (H. Dong et al., 2010). GO, and Titanium dioxide (TiO_2) hybrid can be used to generate ROS after visible light irradiation and enhance the visible-light-driven photodynamic activities (Z. Hu et al., 2012).

1.6.5.4 Drug/gene delivery applications

Because of its versatility, GO could be used as a targeted drug delivery system for gene therapy in cancer treatment. It can be used as a non-toxic vehicle for gene transfusion and siRNA delivery which can be further combined with PTT and PDT along with chemotherapy (Qu et al., 2019). In a study, it was proved that nanoscale graphene oxide sheets protect the oligonucleotides like a molecular beacon from enzymatic cleavage and deliver these oligonucleotides into the cells very efficiently. The nanoscale GO improves the transfection efficiency of oligonucleotides as a carrier; therefore, it is an excellent tool for gene therapy (C. H. Lu et al., 2010). In a study, GO was conjugated with PEI polymers by non-covalent electrostatic interactions, which has high stability in physiological pH and reduced cell toxicity. DNA can bind with the GO-PEI complex for gene delivery with high transfection efficiency (L. Feng et al., 2011). It is reported that GO can absorb ssRNA or ssDNA but not dsDNA, so it cannot be used as a gene carrier. To overcome this drawback, a nanoparticle (NP) system made of GO coated with cationic lipids with suitable physicochemical properties can be used for the development of surface-modified GO hybrid gene vectors (Di Santo et al., 2019). For human breast cancer treatment, GO and hydroxyapatite complexes loaded with Ganciclovir were made, which serve as a gene delivery vector for cancer treatment. They inhibit proliferation and induce cell apoptosis in cancerous cells (Cheang et al., 2018).

1.7 Doxorubicin as anticancer agent

Doxorubicin (Dox), a natural anthracycline antibiotic, is one of the most efficient chemotherapy medications used in the treatment of several cancer types against tumours. It is thought to bind with DNA by intercalation, like other anthracyclines, although the mechanism remains unknown. One of the mechanisms proposed to explain the effect of doxorubicin on malignant cells is the intercalation into DNA, which would impede DNA repair and be mediated by topoisomerase II. Doxorubicin inhibits topoisomerase II, which overwinds DNA during transcription, preventing recombination of the DNA double strand and, as a result, inhibiting DNA replication. Another possibility is the production of free radicals, which might damage DNA and cause cell death (Thorn et al., 2011). There is additional evidence that doxorubicin increases nucleosome turnover around promoters, which is ascribed to its intercalation characteristic. These changes in nucleosome assembly are thought to impact cell killing processes after chemotherapy. Different concentrations of doxorubicin have been tested on various types of cancer cell lines and cell models. The responses of different types of cells at transcriptional level show variations. Doxorubicin was found to play role in some additional cellular processes, including ceramide metabolism and cell cycle arrest (Taymaz-Nikerel et al., 2018).

1.7.1 Physicochemical properties of doxorubicin

Dox ($C_{27}H_{29}NO_{11}$); molecular weight: 543.52 g/mol), is an anthracycline antibiotic with antineoplastic activity. It is isolated from the bacterium Streptomyces peucetius var. caesius. Sold under the brand name DOXIL®, it is a fine, orange-red crystalline powder. It is soluble methanol, aqueous alcohols. Aqueous solutions are yellow orange at acid pHs, orange red at neutral pH, and violet blue at pH > 9. Aqueous solution is stable at neutral pH but degrades at acidic pH. Dox melts at ~ 230°C and has a log P ~1.27, with the UV absorption maxima at 481 nm. The chemical structure of Dox is shown in **Figure 1.7** ("National Center for Biotechnology Information, PubChem Compound Database; CID=31703)

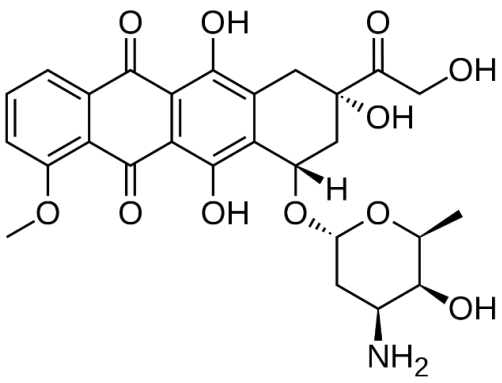

Figure 1.7 Chemical structure of doxorubicin

IUPAC Name: (7S,9S)-7-[(2R,4S,5S,6S)-4-amino-5-hydroxy-6-methyloxan-2-yl] oxy-6,9,11-trihydroxy-9-(2-hydroxyacetyl)-4-methoxy-8,10-dihydro-7H-tetracene-5,12-dione.

1.8 Oxaliplatin as anticancer agent

The 3rd-generation Pt compound known as oxaliplatin (depicted in **Fig. 1.8**) was engineered to surmount resistance observed in response to carboplatin and cisplatin. When utilized in conjunction with folinate and 5-fluorouracil, oxaliplatin serves as a highly effective therapeutic regimen for adjuvant and metastatic colorectal cancer. Notably, this treatment demonstrates significant efficacy in cases where the cancer inherently exhibits insensitivity to cisplatin (Wheate et al., 2010). Oxaliplatin is a Pt coordination molecule that consists of the (1R,2R)-1,2-diaminocyclohexane (DACH) ligand with oxalate as its leaving group. The inclusion of the bidentate oxalate ligand is of utmost importance in mitigating the reactivity of oxaliplatin, hence limiting its propensity to induce peripheral sensory neuropathy and associated deleterious side effects (Wheate et al., 2010). It is worth mentioning that the DACH ligand demonstrates more lipophilicity, leading to increased passive absorption of oxaliplatin in comparison to cisplatin and carboplatin. The utilisation of alternative cellular entry channels by oxaliplatin, beyond those employed by first- and second-generation medicines, may be attributed to its increased lipophilicity. The organic cation transporters OCT1 and OCT2 have been identified as potential facilitators of oxaliplatin absorption. Overexpression of these

transporters has been found to significantly increase the intracellular accumulation of oxaliplatin, a behaviour that is not observed with cisplatin or carboplatin. Colorectal cancer cells exhibit an elevated expression of organic cation transporters, potentially elucidating the effectiveness of oxaliplatin in treating this specific cancer type (S. Zhang et al., 2006). However, the therapeutic implications of these transporters remain ambiguous. Elevated expression of OCT2 has been found to be correlated with prolonged progression-free survival in patients suffering from metastatic colorectal cancer, as observed in certain clinical studies (Tashiro et al., 2014). In contrast, the levels of OCT2 mRNA demonstrated limited expression in nine cell lines associated with colorectal cancer, as well as among patients diagnosed with ovarian cancer (Martinez-Balibrea et al., 2015). Regarding CTR1, the available evidence indicating its involvement in promoting the absorption of oxaliplatin is comparatively less substantial when compared to cisplatin. However, there have been recorded cases of oxaliplatin resistance that are linked to the downregulation of CTR1. Additionally, a reduced level of the β1-subunit of Na+, K+-ATPase was seen in cells that showed resistance to oxaliplatin. Copper efflux transporters also seem to significantly influence the sensitivity to oxaliplatin. A significant association was seen between decreased ATP7B levels and a positive prognosis in individuals diagnosed with colorectal cancer (Martinez-Balibrea et al., 2015). Like cisplatin, oxaliplatin predominantly generates interconnections within the neighbouring guanine bases or between adenine and guanine in DNA, albeit to a lesser degree. Nevertheless, oxaliplatin-DNA complexes exhibit enhanced efficacy in impeding DNA replication. This heightened effectiveness can be attributed to the larger DACH ligand in oxaliplatin, which induces distinct structural deformations in DNA. DACH's considerable size and lipophilic nature are regarded as factors contributing to the distinct handling of oxaliplatin-DNA adducts. Remarkably, these oxaliplatin-DNA adducts are not identified or acknowledged by the Mismatch Repair (MMR) proteins. Intriguingly, this absence of recognition does not result in reduced cytotoxicity;

instead, it renders oxaliplatin's anti-tumor activity independent of the MMR system. Furthermore, previous research findings have indicated that there is no clear correlation between the cytotoxic effects of oxaliplatin and the increase in replicative bypass, which refers to DNA synthesis bypassing Pt-DNA adducts (Holford et al., 1998). These factors contribute to the drug's distinct activity spectrum compared to cisplatin or carboplatin. Ongoing clinical trials are being conducted to evaluate the therapeutic efficacy of oxaliplatin in the management of non-small cell lung malignancies, breast, gastric, and pancreatic cancer (Wheate et al., 2010).

Pt(IV) prodrugs represent an emerging category of compounds with the potential to enhance the pharmacokinetic attributes of the existing Pt(II) anticancer agents. These Pt(IV) complexes are distinguished by supplementary ligands in the axial positions, enabling additional chemical alterations and fine-tuning of their characteristics. Pt(IV) complexes exhibit substitution inertness, rendering them more stable in blood circulation by reducing interactions with plasma proteins. The Pt(IV) prodrugs undergo activation through reduction mechanisms to transform into square planar Pt(II) complexes. Glutathione and ascorbate have been identified as possible reducing agents, and it has been found that cellular proteins also play a crucial role in this reduction process (Wexselblatt & Gibson, 2012). The removal of axial ligands during the activation process of prodrugs might result in the acquisition of advantageous pharmacological characteristics, such as the augmentation of cellular uptake. On the other hand, the cytotoxicity of Pt(IV) compounds is significantly influenced by the characteristics and arrangement of equatorial ligands. Pt(IV) complexes present various advantages compared to their Pt(II) counterparts. Firstly, they demonstrate remarkable stability, enabling their administration through oral means. Secondly, they contribute to the reduction of side effects by minimising protein interactions. Lastly, their axial ligands can be modified to enhance pharmacological properties, such as facilitating the targeting of the Pt component to the tumour site.

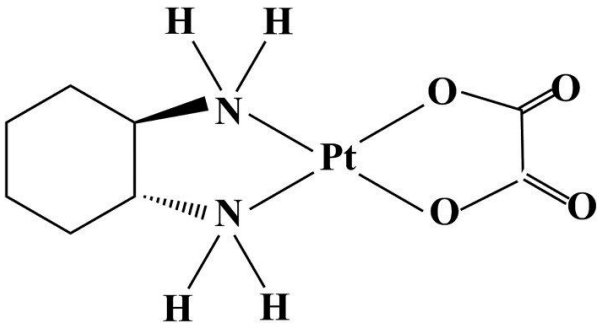

Figure 1.8 Chemical structure of Oxaliplatin (Diaminocyclohexane Oxalatoplatinum).

IUPAC Name: (1R,2R)-cyclohexane-1,2-diamine;oxalate;platinum(2+)

1.8.1 Physicochemical properties of Oxaliplatin

Oxaliplatin ($C_8H_{14}N_2O_4Pt$); molecular weight: 397.294 g/mol), is a Pt coordination molecule that consists of the (1R,2R)-1,2-diaminocyclohexane (DACH) ligand with oxalate as its leaving group, it is a fine white powder. It is soluble in water (4.6 g/L), very slightly soluble in methanol, and practically insoluble in ethanol and acetone. Oxaliplatin melts at ~ 230°C and has a log P ~0.19, with the UV absorption maxima at 255 nm. The chemical structure of oxaliplatin is shown in **Figure 1.8** ("National Center for Biotechnology Information, PubChem Compound Database; CID=9887054).

Objectives

Objective 1. Oxaliplatin delivery via chitosan/vitamin E conjugate micelles for improved efficacy and MDR-reversal in breast cancer.

Specific aims:

i. To synthesize (Ch/VES) copolymer and prepare oxaliplatin loaded chitosan/vitamin E conjugate micelles.
ii. To perform the physicochemical characterization of the chitosan/vitamin E conjugate (Ch/VES) and OXPt@Ch/VES micelles using ^{1}H NMR, particle size, zeta potential, encapsulation efficiency, drug loading, FTIR, SEM, GPC analysis, XPS, XRD spectroscopy, TGA/DSC analysis, CMC analysis and *in vitro* drug release study.
iii. To evaluate micelles *in vitro* against the breast cancer cells.
iv. To perform *in vivo* pharmacokinetic studies using Wistar rats.
v. To evaluate the therapeutic efficacy of the micelles in tumor-bearing mice.

Objective 2. Polymeric Graphene Oxide Nanoparticles Loaded with Doxorubicin for Combined Photothermal and Chemotherapy in Triple Negative Breast Cancer.

Specific aims: :

i. To synthesize GO via modified Hummer's method, mPEG-PLA by ring-opening polymerization reaction, and conjugation of GO with mPEG-PLA (GO(mPP)) via an esterification reaction.
ii. To prepare and optimize doxorubicin loaded polymeric Graphene Oxide Nanoparticles.
iii. To perform thorough physicochemical characterization of graphene oxide nanoparticles using UV, FTIR, NMR and Raman spectroscopy, particle size, surface charge, rate of drug release, NIR laser-mediated photothermal effect
iv. Evaluation of therapeutic efficacy *in vitro* against the breast cancer cells.

v. To evaluate the therapeutic efficacy of DOX@GO(mPP) NPs in tumor-bearing mice.

Objective 3. Biotinylated platinum(IV)-Conjugated Graphene Oxide Nanoparticles for Targeted Chemo-Photothermal Combination Therapy in Breast Cancer

Specific aims:

i. To develop tumor microenvironment sensitive graphene oxide nanoparticle formulation for the delivery of oxaliplatin in breast cancer.

ii. To develop actively targeted graphene oxide formulation (GO(OX)PB NPs) in breast cancer therapy utilizing over expressed receptors such as biotin receptors.

iii. To perform thorough physicochemical characterization of graphene oxide nanoparticles using UV, FTIR, NMR and Raman spectroscopy, particle size, surface charge, rate of drug release, NIR laser-mediated photothermal effect, XPS, XRD spectroscopy, TGA/DSC analysis,

iv. Evaluation of therapeutic efficacy *in vitro* against the breast cancer cells.

v. To evaluate the therapeutic efficacy of the GO(OX)PEG NPs and GO(OX)PB NPs in tumor-bearing mice

Chapter 2

Oxaliplatin delivery via chitosan/vitamin E conjugate based nanoassembly for improved efficacy and MDR-reversal in breast cancer.

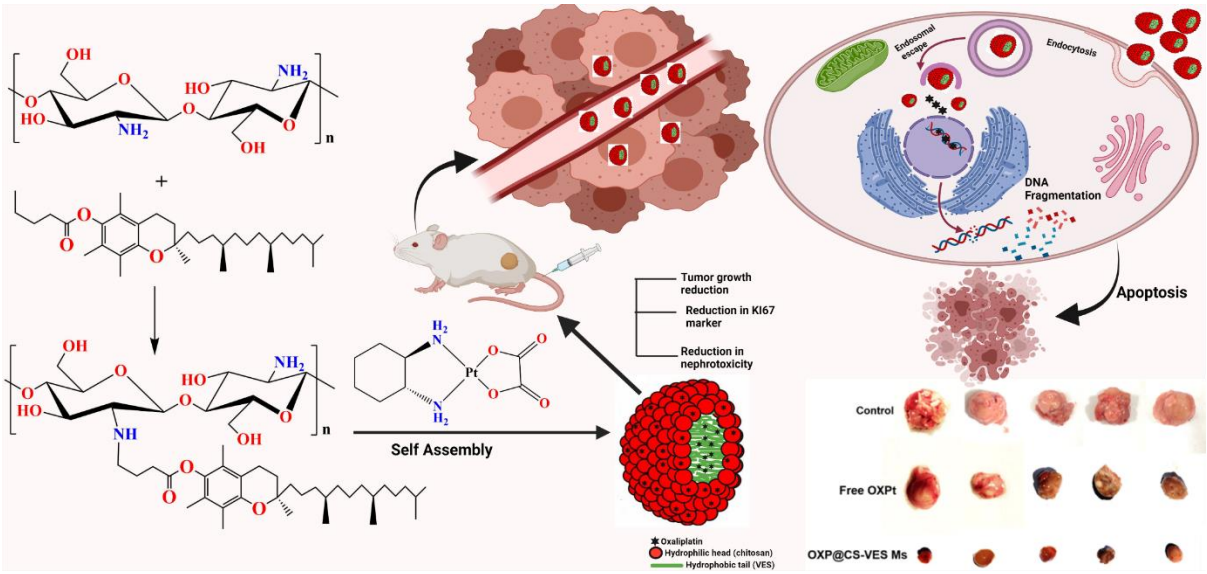

2.1 Introduction

Breast cancer is highly prevalent, being the second among all the cancers causing deaths in women (Libson & Lippman, 2014; J. Yin et al., 2017)**.** In the single year of 2020, 2.3 million women were diagnosed with breast cancer, and 6,27,000 women died globally (a report by World Health Organization (WHO) on breast cancer**)** (Jain et al., 2020b). Genetic profiling revealed the heterogeneity of the disease, and several breast cancer subtypes such as luminal A, luminal B, triple-negative/basal-like, HER2-enriched, and normal-like were identified (Greish et al., 2018). Luminal A breast cancer (estrogen receptor (ER)-progesterone receptor (PR)-positive and human epidermal growth factor receptor 2-negative (ER/PR+, and HER2 –ve)) is the most slow-growing breast tumor among all subtypes with a low anti-apoptotic protein Ki-67 expression. Luminal B (ER/PR+, HER2, + or –ve) has a high Ki-67 expression. Triple-negative breast cancer is a hormone-receptor-negative subtype (ER/PR/HER2 –ve) associated with Breast Cancer gene 1 (BRCA1) gene mutations. Tumors of HER2 enriched subtype (ER/PR –ve, HER2 +ve) grow faster than luminal cancers and are associated with poor prognosis (Chalakur-Ramireddy & Pakala, 2018; Haberman et al., 2019)**.** However, this type of tumor is successfully treated with HER2-targeted antibody therapy using Herceptin (trastuzumab). The other subtype, normal-like breast cancer (ER/PR+, and HER2 –ve), is similar to luminal A with a slightly worse prognosis.

Triple-negative, the most aggressively proliferative form of breast cancer subtype, is predominant in women under 40 and is diagnosed in approximately 5-20 % of breast cancer patients (Morris et al., 2007). Triple-negative breast cancer (TNBC) is associated with a high recurrence rate, metastasis, poor diagnosis, and prognosis (Chalakur-Ramireddy & Pakala, 2018; Jain et al., 2020b). As TNBC lacks the expression of ER/PR/HER-2 receptors, HER2-targeted hormone/drug therapy is not effective in this cancer. The genetic expression profile of TNBC patients reveals the presence of 6-subtypes of TNBC, basal-like (BL1 and BL2),

mesenchymal (M), mesenchymal stem-like (MSL), immunomodulatory (IM), and luminal androgen receptor (LAR), which are treated strategically with different chemotherapeutic agents depending on their enzyme-expression profiles (Lehmann et al., 2011; L. Yin et al., 2020)**.** Bevacizumab, a recombinant humanized monoclonal antibody with the potential to bind/inhibit vascular endothelial growth factor (VEGF), has been combined with chemotherapeutic agents, including poly(ADP-ribose) polymerase (PARP) inhibitors, cisplatin for BL1 subtype and mammalian target of rapamycin (mTOR) inhibitors (lapatinib, cetuximab, gefitinib) for BL2 subtype (Gibson et al., 2005). However, the survival rate of patients did not improve significantly. The M subtype has a high cell migration capability and is prone to develop resistance towards chemotherapeutic agents following neoadjuvant chemotherapy (Lehmann & Pietenpol, 2014). The resistance development in TNBC could be due to chromosomal instability, resulting in the amplification of myeloid cell leukemia-1 (*MCL-1),* Janus Kinase 2 gene (*JAK2),* and myelocytomatosis (*MYC), PIM1* proto-oncogenes, acting as a driving force for adaptation (Wein & Loi, 2017)**.**

Oxaliplatin (OXPt), a third-generation platinum-based chemotherapeutic agent, has been approved in combination with fluorouracil and leucovorin (Folfox) to treat primary/advanced colorectal cancer (Selim et al., 2014). Liposomal OXPt has been indicated to treat orphan designated ovarian cancer, colorectal carcinoma, cholangiocarcinoma, and pancreatic adenocarcinoma (Doi et al., 2019; C. Yang et al., 2011). Few clinical trials on OXPt are conducted in breast cancer patients (J. Liu et al., 2015; Recchia et al., 2007; Zelek et al., 2002). The results of some of these studies are still pending. Off-label use of OXPt in pretreated women with metastatic breast cancer showed little worth (Levêque, 2008). In phase II clinical trial, oxaliplatin-fluorouracil combination demonstrated a high safety profile in patients resistant to anthracycline and taxane (Zelek et al., 2002). Gemcitabine-oxaliplatin combination, administered to anthracycline and taxane pretreated patients with metastatic breast cancer,

offered some benefits (Caruba et al., 2007). Bevacizumab and Folfox6 combination, the standard regimen for breast cancer, has been tested in heavily pretreated Her2/neu-negative breast cancer patients (T. Li et al., 2015). The combination has significant antitumor activity and a good safety profile. Further, the clinical trials on OXPt reported several side effects such as neuropathy, hematological, nephron, and gastrointestinal tract toxicity (Grothey, 2005; Pasetto et al., 2006; Yaghobi Joybari et al., 2014). However, the extent of nephrotoxicity is much lower compared to cisplatin (Yaghobi Joybari et al., 2014).

Nanomedicine has emerged as a potential non-classical formulation for poorly soluble/absorbable anticancer agents, improving the drug's solubility, absorption, and local delivery via active/passive tumor targeting effect (Paraskar et al., n.d.; G. Wang et al., 2021). Unlike conventional OXPt, the nanoparticles-bound OXPt could demonstrate higher tumor accumulation, tissue penetrability, and reduction of side effects (Shahlaei et al., 2020). OXPt is a third-generation platinum compound with less toxicity and greater efficacy than other platinum drugs (Saldanha-araújo et al., 2019). The drug, alone or in combination, has shown effectiveness in treating colon, bladder, lung, liver, ovarian, head and neck, cervical, testicular, and breast cancers (Espinosa et al., 2005; Shahlaei et al., 2020). Recent studies used various nano-platforms to load physically entrapped or chemically conjugated OXPt (as Pt (IV) prodrugs) to increase the treatment efficacy (Abu Lila et al., 2012; J. Guo et al., 2020; Tummala et al., 2017; Q. Zhu et al., 2021). Chitosan (Ch), a deacetylated form of the naturally occurring polysaccharide chitin, has been an excellent choice for drug delivery or other biomedical applications (Kumar et al., 2004; Lian et al., 2013; Mu et al., 2019). The versatility of Ch as a biomaterial is due to its muco-adhesivity and absorption enhancing potential through the epithelial layer due to its cationic nature. Many accessible -OH and -NH_2 groups on the surface allow surface modification with hydrophobic groups or other tumor-targeting ligands (Mathew et al., 2010; Muddineti, 2017; Muddineti et al., 2018). Ch NPs were used to load OXPt and

investigated their therapeutic efficacy in oral and breast cancer (Saldanha-araújo et al., 2019; Vivek et al., 2014). Our study developed and used a Chitosan/vitamin E-based OXPt delivery system in breast cancer therapy. Ch(low/high molecular weight. 15/300 KDa) was conjugated to vitamin E (1:4 mol ratio), and the OXPt was physically entrapped at the various drug to polymer ratios. Thorough physicochemical characterization was carried out to establish the formation of a stable OXPt-loaded micelle system. The *in vitro* therapeutic efficacy was determined using ER+/PR+/HER2-, and triple-negative (ER-/PR-/HER2-ve) sensitive/resistant cell lines, MCF-7 and MDA-MB-231, respectively. The *in vivo* study used mouse mammary tumor cell line luciferase-expressing (4T1-Luc) tumor-bearing mice to evaluate the anticancer activity and treatment-mediated nephrotoxicity.

2.2 Materials and methods

2.2.1 Materials

Chitosan (Ch) (M Wt.= 15KDa; 300KDa), Vitamin E succinate (VES), Acridine orange (AO), N, N-dimethyl formamide (DMF), 4′,6-Diamidino-2-phenylindole dihydrochloride (DAPI), 6-trinitrobenzene sulfonic acid solution (TNBS), dimethyl sulfoxide (DMSO), N-hydroxysuccinimide (NHS), N-(3, Dimethylaminopropyl)-N′-ethyl carbodiimide hydrochloride (EDC), Tetrahydrofuran (THF), Triethylamine (TEA), paraformaldehyde, Propidium iodide (PI), Rhodamine B (Rh-B), Dichloro-dihydro-fluorescein diacetate (DCFH-DA), were procured from Sigma-Aldrich (Bangalore, India). Oxaliplatin (OXPt) was obtained from Neon Laboratories Ltd. Mumbai as a free sample. Dialysis membrane was purchased from Spectrum Laboratories, Inc. (the USA), GSure® DNA genomic isolation kit was procured from GCC Biotech Pvt. Ltd. (India), 5, 5′, 6, 6′-Tetrachloro-1, 1′, 3, 3′-tetraethylbenzimidazolocarbocyanine iodide (JC-1 Dye) was procured from Sigma-Aldrich (USA). Trypan blue solution, Methylthiazolyldiphenyl-tetrazolium bromide (MTT), and

Fluoromount-G were procured from Himedia Labs (India). TACS® Annexin V-FITC Apoptosis Detection Kit was obtained from R&D systems (Minneapolis, USA).

Cell lines:- Human breast adenocarcinoma cells (MDA-MB-231), human breast cancer cells (MCF-7) cells, and mouse mammary tumor cell line luciferase-expressing (4T1-Luc) were procured from the American Type Culture Collection (ATCC, USA) and the National Centre for Cell Science (NCCS, Pune, India). Himedia Labs (India) supplied the Penicillin Streptomycin, Minimum Essential Medium Eagle (MEM), Dulbecco's Modified Eagle Medium (DMEM), Trypsin-EDTA, and fetal bovine serum (FBS).

Animals:- Male Wister rats used in the pharmacokinetic studies and blood collection for hemolysis studies were obtained from Sainath Agency, Hyderabad, India. Female BALB/c mice (18−22 g, 6-8-week-old) were obtained for antitumor efficacy study from National Centre for Laboratory Animal Sciences, National Institute of Nutrition, Hyderabad, India. The study was approved and conducted with approval from the Institutional Animal Ethics Committee of BITS-Pilani, Hyderabad. The animals were caged in standard mouse/rat cages (no. 5/cage) kept in an air-conditioned room (23-24 °C, relative humidity 50-60 %) at 12 h light/dark circle *ad libitum* access to food and water.

2.2.2 Methods

2.2.2.1 Synthesis and characterization of Chitosan-Vitamin E succinate (Ch/$(VES)_4$) conjugates

The Ch/$(VES)_4$ copolymer was synthesized by conjugating the –COOH group of α-tocopheryl succinate to the -NH_2 groups of Ch (15, 300 KDa) due to the existence of EDC and NHS. The molecular structure of Ch/$(VES)_4$ conjugate is demonstrated in **Fig. 2.1A**. In a nutshell, to 1 % acetic acid and DMF solution (1: 1) ratio, Ch (50 mg) was added, and VES (7.07 mg) was added in 1 mL of DMF, followed by an appropriate amount of EDC (3.79 mg), NHS (2.29 mg),

and 20 µL of TEA. To remove hydrophilic byproducts, the product was dialyzed in distilled water pH 5.5 with a cellulose acetate membrane with a molecular weight cutoff [MWCO] = 2KDa, then freeze-dried or lyophilized. Proton nuclear magnetic resonance spectroscopy ^{1}HNMR (Bruker spectrometer-300 MHz, Bruker, USA) was used to examine the conjugate's chemical structure in DMSO-D6 solution at 25°C shown in (**Fig. 2.1B)**. The infrared (IR) spectrum was recorded using FTIR (Jasco-4200, USA) following the previously reported KBr pellet method (Fanelli et al., 2018)**.** The FTIR spectrum of Ch/$(VES)_4$ copolymer was observed by scanning the pellet over a broad IR region of 400 to 4000 cm^{-1} **(Fig. 2.1C)**. The Ch/$(VES)_4$-Rh-B conjugate was synthesized for the cellular uptake study is demonstrated in **Fig. 2.2.**

The conjugation efficiency of Ch and VES was estimated by size exclusion chromatography (GPC) (waters Corporations, USA), installed with a refractive index detector, ultra-hydrogel™ linear (7.8 × 300 mm column). The mobile phase was 1% acetic acid solution (1 mL/min). The number of amino groups substituted during Ch and VES conjugation was assessed by TNBS (2, 4, 6-Trinitrobenzene Sulfonic Acid) method. A calibration curve was plotted for Ch and Ch/$(VES)_4$ within a specific 200-1000 µg/mL concentration range. Measured absorbance of the solution at 335 nm and determined concentration of primary amines by calculation from the extinction coefficient or by comparison to standard. The following equation was used to estimate the level of substitution:

$$DS = \left(1 - \frac{K_{Ch-VES}}{K_{Ch}}\right) X100 \qquad \textit{Equation 2.1}$$

$K_{Ch\text{-}VES}$ and K_{Ch} are the slope rates of Ch/$(VES)_4$ and Ch.

As mentioned earlier, the polymer's critical micelle concentration (CMC) was measured utilizing pyrene as a fluorescent probe (Kumari et al., 2017)**.** In the condition of pyrene, Ch/$(VES)_4$ copolymer concentrations ranging from 1 to 150 µg/mL in water were shaken for 12 h in an orbital shaker (Heidolph, Titramax 1000). The test samples were filtered and

analyzed using Spectramax ™ multiplate reader (Molecular Devices, US) at Ex 339 nm/ Em 339 nm wavelengths, respectively.

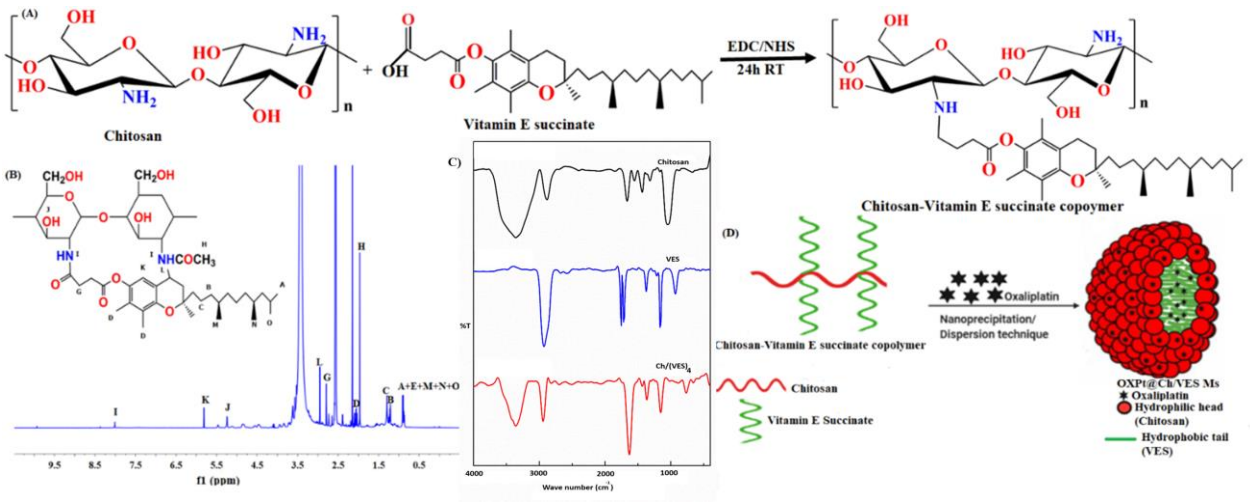

Figure 2.1 Synthetic scheme of Ch/(VES)4 conjugates (A); 1H NMR spectrum of Ch/(VES)4 conjugate (B); FTIR spectra of Ch (15 KDa), VES and Ch/(VES)4 conjugate (C); Illustration of supramolecular micellar nanoaggregates formed by Ch/(VES)4 copolymer (D).

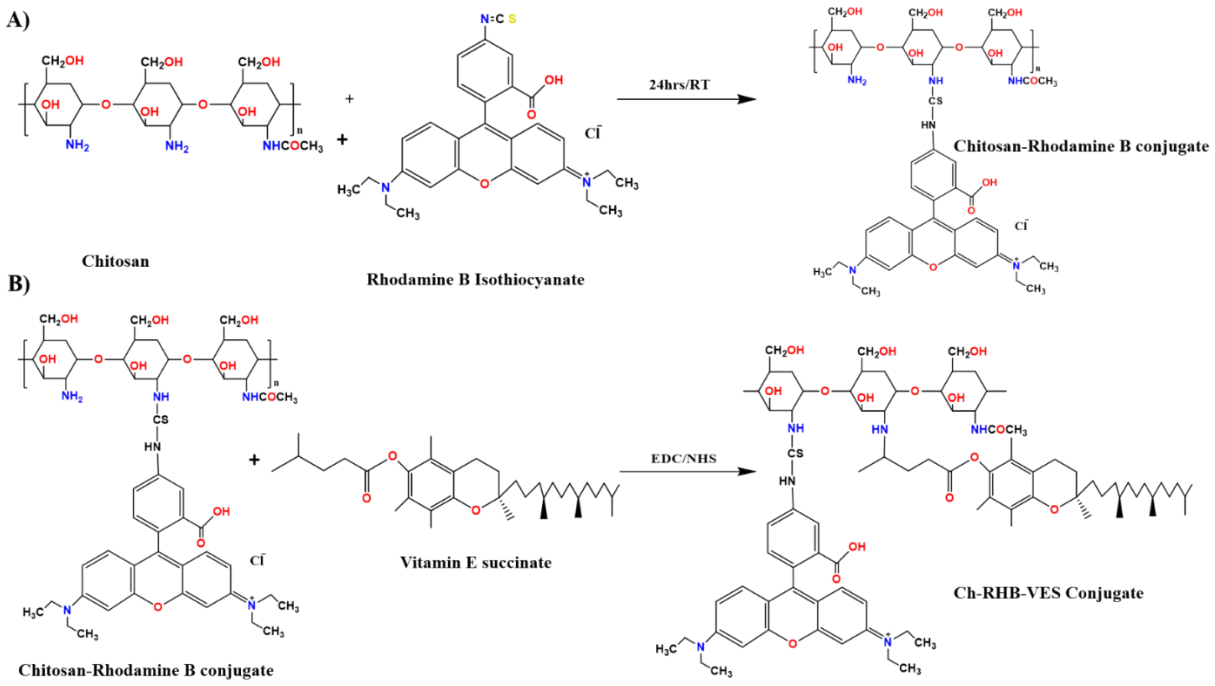

Figure 2.2 Synthetic scheme of chitosan rhodamine B vitamin E succinate conjugate.

2.2.3 Preparation and characterization of OXPt@Ch/VES micelles

2.2.3.1 Preparation of OXPt@Ch/VES micelles

The dispersion/ nanoprecipitation approach, incorporating the ultrasonic probe-type method, was used to prepare oxaliplatin-loaded micelles. In Brief, 8 mg of Ch/$(VES)_4$ copolymer was added in 5 mL of 1% acetic acid, OXPt was solubilized in 100% methanol, and then drop by drop OXPt solution was added to the Ch/$(VES)_4$ solution in the ratios of 1:1, 1:1/2, and 1:1/4 were made. The organic solvents were then evaporated by stirring the mixture overnight at room temperature. Using a probe-type sonifier (Sonics Vibra cell), the resultant solution was then sonicated for 5 minutes at 200 W, 35 amplitude; in 3-second intervals, the pulse was cycled off for 2 seconds. The sonication procedure was performed in an ice bath to keep the temperature low. To eliminate any unloaded drugs, centrifuged the micelle solution for 20 minutes at 3500 rpm. The supernatant micelles have been filtered using a 0.8μm syringe filter to discard impurities before being preserved at 4 °C.

2.2.3.2 Physico-chemical characterization of OXPt@Ch/VES micelles: size, surface charge, morphology, drug loading (DL), and entrapment efficiency (EE)

The zeta sizer (Nano ZS 90, Malvern Instruments Ltd., UK) was used to estimate the size distribution, average particle size, and zeta potential of OXPt@Ch/VES Ms at 25°C. Before measuring the size of micelles, they were adequately diluted in Milli-Q water. The polydispersity index (PDI), representing the width of the frequency-size distribution curve, was calculated. The hydrodynamic diameter of OXPt@Ch/VES Ms was determined at different pH (2, 3, 5, 6.8, 7.4 & 9).

A UV–Visible spectrophotometer was used to determine the OXPt content in Ch/(VES) Ms at a maximum wavelength of 255 nm. The surface morphology was assessed using a Field Emission Scanning Electron Microscope (Apreo Lo Vac, FEI, USA). Lyophilized micelles

were deposited on carbon tape and sputter-coated with a gold-palladium alloy for 30 minutes at a thickness of 10 mm. The images were taken at a resolution of 500 nm with an accelerating voltage of 20 kV.

The OXPt@Ch/VES Ms were diluted with methanol to release the drug from the Micelles before determining EE and DL (Ms). The following equations were used to quantify the formulation's entrapment efficiency (EE) and drug loading (DL).

$$\% \text{ EE} = \frac{Weight\ of\ OXPt\ present\ in\ supernatant}{Weight\ of\ OXPt\ added\ initially} \times 100 \qquad \textit{Equation 2.2}$$

$$\% \text{ DL} = \frac{Weight\ of\ OXPt\ present\ in\ supernatant}{Weight\ of\ the\ OXPt\ added\ initially + weight\ of\ polymer\ added} \times 100 \qquad \textit{Equation 2.3}$$

2.2.3.3 Kinetic stability Analysis

The zeta sizer (Nano ZS 90, Malvern Instruments Ltd., UK) was used to evaluate the average particle size of OXPt@Ch/VES Ms for 21 days at 25°C. A UV–Visible spectrophotometer set to λmax 255 nm was used to determine the % drug content of the sample. The particle size was measured to determine the particle's stability under physiological circumstances.

2.2.3.4 Differential scanning calorimetry (DSC)

A Differential Scanning Calorimeter (DSC 60, Shimadzu, Japan) was used to perform the thermo-analytical evaluation of micelles. To summarize, OXPt, Ch, VES, Ch/$(VES)_4$, and lyophilized OXPt@Ch/VES Ms were kept in standard aluminum pans, the flow rate was set 20ml/min, and dry nitrogen was fed through the system. The reference was an empty aluminum pan. The samples have been handled at a fixed rate of 10 °C/ min over a 30-600 °C range.

2.2.3.5 X-ray diffraction (XRD)

The XRD properties of the free OXPt and the OXPt@Ch/VES Ms were analyzed by an X-ray diffractometer (ULTIMA-IV, Rigaku). The scanned angle was adjusted at 2-theta from 0° to 50°, and the voltage was 40 kV, with a continuous scanning current of 30 mA.

2.2.3.6 X-ray photon electron spectroscopy (XPS) Analysis

K-Alpha X-ray Photoelectron Spectroscopy (Thermo-Fischer, USA) was used to analyze the chemical composition on the surface of the Ch, Ch/$(VES)_4$ copolymer and OXPt@Ch/VES Ms. Under 10^{-6} torr vacuum pressure, an X-ray source (1375 eV) was employed. The pass energy was set at 200 eV and 50 eV for broad and narrow scanning, respectively, with a 568° electron take-off angle. Advantage software (version 4.88) evaluated the collected XPS data. A Smart type background and a Gaussian peak shape with 35 % Lorentzian character were used to deconvolute all HR XPS spectra.

2.2.4 *In-vitro* release study

The *in vitro* OxPt release from OXPt@Ch/VES micelles was tested by the dialysis method (Muddineti, 2017). 1 mL of the formulation was sealed in dialysis membrane and was maintained in a phosphate buffer solution of 100 mL (pH 7.4, pH 6.5, or pH 5.5) in a beaker, shaken at 100 RPM/min, and maintained at 37 ˚C (Vivek et al., 2014). At predetermined intervals, solutions from every flask were periodically withdrawn and replenished at the same volume with a fresh buffer. The UV spectrophotometer was used to measure the amount of OXPt released at λmax 255 nm. By fitting the collected data into the zero-order, Higuchi, first order, Korsmeyer Peppas, Hixson Crowell model, and Weibull model, mathematical models were used to explore the release behavior of OXPt from the formulations. The experiments were repeated three times, and the data are reported as an average of the acquired results (Mean SD; n=3).

2.2.5 Hemolysis test

The compatibility of Ch/$(VES)_4$ conjugate was evaluated by collecting blood from the rat and centrifugation at 3500 g for 10 minutes to isolate the erythrocytes from the blood. Cells were resuspended in physiological saline following centrifugation to get a 5 % volume fraction suspension. RBC suspension (100µl) was added to different concentrations of polymer solution 0.025, 0.05, 0.100, 0.200, 0.250 and 0.900 mL. Positive control was achieved by mixing Triton-X 100 (0.5 mL) with 4.5 mL of RBC's and similarly, a negative control was prepared by combining RBCs with normal saline. The formulations were applied to the erythrocyte suspension of 5% and held residual for two h with moderate shaking and centrifugation at 3500 g for 20 minutes. The quantity of hemoglobin (Hb) in the supernatant was then measured to assess the hemolysis. Spectramax^{TM} multiplate reader (Molecular Devices, US) was used to quantify hemoglobin (at 576nm), and the formula indicated below was used to compute it:

$$\text{Hemolysis (\%)} = \frac{Ab_{Sample} - Ab_{(-)Control}}{Ab_{(+)Control} - Ab_{(-)Control}} X100 \qquad \textit{Equation 2.4}$$

Where Ab_{sample} = the sample's absorbance, and $Ab_{(+)}$ = Triton-X 100 absorbance and $Ab_{(-)}$ = PBS solution absorbance.

2.2.6 Cell culture

2.2.6.1 Cellular uptake

MCF-7 and MDA-MB-231 cells were seeded at a density of 50,000 per well on a 12-well polystyrene tissue culture plate. OXPt@ Ch/$(VES)_4$-Rh-B Ms formulation was added to the cells at doses of 10 and 20 µg/mL for 1 and 4 h, respectively, in a serum-free medium. Washed the cells with PBS three times, labeled them with DAPI, and then fixed them in 4% paraformaldehyde for 20 min. Fluoromount G was used to mount the cells on a glass plate and examined them under a confocal microscope. Flow cytometry experiments were conducted

using cells grown in a 12 well plate (0.2 x 10^6 cells/well). The cells were handled the next day in the same way as in the confocal microscopy experiment. After treatment, cells were rinsed in PBS, trypsinized, centrifuged, rinsed, and resuspended in PBS, pH 7.4. The cellular internalization was determined using a flow cytometer (BD FACS Area III) and the rhodamine channel (ex/em. 540/570 nm) to measure the fluorescence of 10,000 live cells.

2.2.6.2 *In vitro* cytotoxicity study

The cell viability experiment was carried out to verify the cellular toxicity of the established formulation blank Ch, Ch/$(VES)_4$, Free OXPt, and OXPt@Ch/VES MS MDA-MB-231 sensitive cells, MCF-7, and MDA-MBA-231 resistant cells. In short, the cells were grown in the DMEM complete media. 10,000 cells were grown per well in a 96-well plate during the growth phase. Next, the cells were treated with blank Ch, $Ch(VES)_4$, Free OXPt, and OXPt@Ch/VES MS for 24, 48 h and 4 h followed by 24 h incubation (max OXPt concentration up to 100 µg/ mL). After 24 and 48 h of incubation, each well-received 50µl of MTT and incubated for another 4 h before the media was withdrawn. 150 µl of DMSO were added to each well to solubilize the formazan crystals formed. Next, we measured the absorbance using (SpectramaxTM, Molecular Devices) at 570 nm. Control cells were those that were not given any treatment. Each sample was tested three times on each plate. The half-maximal dose (IC_{50}) was determined using Graph pad Prism 9.0.2 software.

Cell viability (%) = $\frac{Ab_{Sample}}{Ab_{Control}}$X100 ***Equation 2.5***

2.2.6.3 Annexin V assay

A 12-well plate was seeded and cultured for 24 h with MDA-MB-231 and MCF-7 cells. The cells were then treated at a dose of 6 µg/mL with free OXPt, OXPt@Ch/VES Ms. the cells were collected after they had been in culture for 24 h, and then they were rinsed three times

with cold PBS. Pellets that had been centrifuged were resuspended in Annexin-V-FITC/PI buffer, and they were kept in the dark for 15 mins. Cells were analyzed on a flow cytometer cytometry (FACS Aria III, BD Biosciences, and the USA) by gating 10,000 live cells. Only single cells were gated for fluorescence analysis. The data were plotted as Annexin V-FITC vs. PI with quadrant gating.

2.2.6.4 Cell cycle analysis

Cancer cells seeded appropriately were incubated with free OXPt, OXPt@Ch/VES Ms at a 6 µg/mL concentration for 24h. Next, the cells were collected by centrifugation, washed, fixed with ethanol (70 %) for 24 h. After being fixated, the cells were harvested by centrifugation, rinsed, and reconstituted in 500 µl of PBS containing 200 µg/ml RNAase. PI (20 µg/mL in PBS) was used to tint the cellular DNA maintained at room temperature for 30 minutes in the dark. A flow cytometer (BD Biosciences, USA) was used to quantify the DNA content for these experiments. The FCS Express 7 Flow Cytometry Software was used to calculate the proportion of cells in the G1, S, and G2/M cycles.

2.2.6.5 DNA fragmentation assay

In 6 well tissue culture plates, 50,000 cells/well of MDA-MB-231 and McF-7 cells were seeded and kept in incubation at 37°C for about 24 h. After a 24-h incubation period, the cells were given treatment with free OXPt, OXPt@Ch/VES Ms at a 50 µM OXPt concentration, then incubated for another 24 h period. The cells' DNA was extracted and fixed on a 1.5 % agarose gel with ethidium bromide (0.5 µg/mL) using the GSure® DNA genomic isolation kit. The fragments were then examined utilizing the gel doc technique.

2.2.6.6 Nuclear Staining assay

Fifty thousand breast cancer cells of MCF-7 and MDA-MBA-231 were seeded on 6-well plates/well, incubated for 24 h, and fed with IC50 concentrations of free OXPt and OXPt@Ch/VES Ms for 24 h. After being rinsed two times with PBS at each stage, the cells were harvested by trypsinization. The cells were then fixed for 20 minutes in 4 % paraformaldehyde, rinsed, and stained with acridine orange (0.1 mg/mL) for 20 minutes and DAPI (10 µg/mL) 5 minutes in the dark at 37°C. The excess stain was rinsed with PBS, and plates were then focused on detecting any nuclear structural changes induced by Free OXPt and OXPt@Ch/VES Ms using fluorescence microscopy. Acridine orange was detected in the green channel (480-490 nm), while DAPI was detected in the blue channel (358 nm).

2.2.6.7 ROS detection assay

According to an earlier approach, DCFH-DA was employed as a fluorescent probe to measure ROS production in MCF-7 and MDA-MBA-231 breast cancer cells (X. Zhu et al., 2021). MCF-7 and MDA-MBA-231 cells were grown onto 12-well plates with or without glass cover slides, grown for 24 h, and afterward treated independently for 24 h with free OXPt and OXPt@Ch/VES Ms at IC_{50} concentrations. The cells were treated with DCFH-DA (5 µM), incubated at 37 °C for 20 minutes, stained with DAPI, and photographed using a fluorescent microscope in the green channel (Ex/Em: 492–495/517–527 nm).

2.2.6.8 Mitochondrial membrane potential study

The JC-1 stain was used to assess mitochondria membrane potential qualitative change. JC-1 accumulates in polarized mitochondria (normal cells) and forms J-aggregates with a high red fluorescence luminosity (Ex/Em. 560/595 nm). JC-1, on the other hand, remains as monomers in depolarized mitochondria displaying green fluorescence (Ex/Em. 485/535nm) (Vivek et al., 2014). MCF-7 and MDA-MBA-231 cells were treated with free OXPt, OXPt@Ch/VES Ms

(10 µM) for 24 h in 6 well plates. Cells were stained with 5 mM JC-1 for 30 minutes at 37 °C and rinsed after treatment. Finally, the cells were viewed under a fluorescence microscope.

2.2.6.9 Generation of OXPt-resistant cells

A low-concentration (continuous) treatment method-built drug resistance in MDA-MB-231 cells by gradually raising the drug concentration. Cells were first cultured in T-25 flasks supplemented with free OXPt (1 µM). The OXPt concentration was slowly increased to 10 µM over 6 months of continuous culturing.

2.2.6.10 Platinum content in the cell

A fixed number of cells (10^6 cells/ well) in a 6-well plate were seeded and cultured for 24 h with MDA-MB-231 sensitive and resistant cells and treated with Free OXPt and OXPt@Ch/VES Ms with OXPt concentration of 10 µM in the culture medium and then incubated for 0.5 or 2 h after treatment at 37°C. Rinsed and lysed the cells with PBS and cell lysis buffer. The Pt content in the cells was quantified using atomic absorption spectrometry (AAS), Pt levels in cells were measured in ng of Pt/10^6 cells.

2.2.6.11 Anti P-glycoprotein efficacy studies

Phycoerythrin-labeled anti–p-glycoprotein antibody was used to assess Pgp activity in MDA-MB-231(S) and MDA-MB-231(R) cells. For 30 minutes, cells were grown with phycoerythrin-labeled anti–p-glycoprotein antibody (5µl). After that, the cells were trypsinized, harvested, and rinsed several times using PBS. The pellet was resuspended using PBS, and flow cytometry (BD FACS Aria III) was used to analyze them at a wavelength of ex 488 nm. An antibody-labeled cell's fluorescence was measured, and data was recorded thrice from 10,000 cell population occurrences.

2.2.7 *In vivo* study

2.2.7.1 Pharmacokinetic study

Nine Overnight starved Wistar rats (male, 180-220 g) were utilized to investigate the effect of OXPt@Ch/VS Ms formulation on the pharmacokinetics of OXPt after intravenous (IV) administration. Rats were arbitrarily split into three groups and given a single dose of 5mg/kg of Free OXPt and OXPt@Ch/VS Ms by venous injection. Heparinized tubes were used to collect blood samples (0.5 mL) from the retro-orbital vein at 0, 1, 3, 6, 12, 24, and 48 h after IV injection. The blood was centrifuged at 3,000 g for 10 minutes to remove plasma. Plasma samples were kept frozen at -20°C until they were analyzed. The plasma samples were tested for OXPt content using RP-HPLC on a C18 (150nm 4.4nm, 5m) column at λ_{max} 255nm. The mobile phase composition: 5:95= acetonitrile: water, pH adjusted with orthophosphoric acid to 3.5 (85 %). The oven temperature and flow rate were adjusted to 25°C and 1 mL/min. The pharmacokinetic parameters were computed using the pK solver software. The statistical significance was determined using the Student's t-test. P> 0.05 was regarded statistically significant, whereas P > 0.01 was deemed significant.

2.2.7.2 Determination of Therapeutic efficacy *in vivo*

The anticancer activity of free OXPt, OXPt@Ch/VES Ms was tested in a tumor-bearing mice model. 100 µl of 1.5 x 10^6 cells 4T1-Luc cells were injected into the dorsal flank area of female BALB/c mice caused the development of a subcutaneous tumor. The mice were watched for 10-14 day, and the tumor's development was noted. A Vernier caliper was used to determine the tumor volume [(length ×width^2)/2]. The mice were segregated randomly into three groups (n=5) when the tumor volume reached approximately 50 mm^3; free OXPt, OXPt@Ch/VES Ms were administered intravenously at a dosage of 5 mg/kg, whereas the control group received normal saline. For 21 days, alternating days, the mice were injected. Every alternative day

throughout the trial, tumor volume and body weight were assessed. The tumor masses were extracted and weighed separately, and the survival curve was examined by Kaplan-Meier analysis (Martínez-García et al., 2018).

2.2.7.3 *In vivo* Fluorescence imaging analysis

Further, *in vivo* tumor accumulation of free OXPt, OXPt@Ch/VES Ms were observed by *in vivo* imaging system IVIS® Lumina III, PerkinElmer, USA (Yuan et al., 2018). Free OXPt and OXPt@Ch/VES MS were injected into BALB/c mice harboring breast cancer tumors through the tail vein. The BALB/c mice were categorized into three groups (n=2) when tumor volume reached 150-200 mm^3. Group one was taken as control; group two was supplied with OXPt@Ch/VES Ms and group three with free OXPt solution at a dose of 5 mg/kg of OXPt equivalents. Mice were given 150 mg/kg D-luciferin intraperitoneally 10–15 minutes before imaging to track 4T1 growth using bioluminescence. The tumor accumulation profiles were investigated at various time intervals (7days, 14days, and 21days) post-injection by acquiring images with IVIS® using an excitation filter at 620 nm and emission at 780 nm.

2.2.8 Immunohistochemistry

2.2.8.1 TUNEL Assay in Tumor Cryosections

TUNEL assay (Terminal deoxynucleotidyl transferase-mediated nick end labeling) was used to assess the level of apoptosis in tumor tissue and kidney (Biswas et al., 2013). The tumors were collected from mice and sectioned by cryostat (Leica biosystems, Germany) at a thickness of 5 µm. For the evaluation of cell apoptosis, the apoptosis detection kit for the tumor tissue terminal deoxynucleotidyl transferase dUTP nick end tagging (TUNEL) (FragEL DNA Fragmentations Detection Kit, Merck, Darmstadt, Germany) was used to stain sections of the tumor tissue as per the manufacturer's protocol. Blue and green filters were used to observe the

stained tumor sections under a fluorescent microscope. The images were processed and analyzed utilizing Image J software.

2.2.8.2 ROS Production in Tumor Tissues

A DCFH-DA fluorescent probe was used to assess ROS generation in malignancies (Mohammed et al., 2019). When the tumor growth reached ~50 mm^3, free OXPt and OXPt@Ch/VES Ms were given intravenously into tumor-bearing mice at an OXPt equivalent dose of 5 mg/kg. After 24 h of post-injection with the DCFH-DA probe (50 µL, 25 µM), the tumors were injected intratumorally. The mice were sacrificed after 30 minutes, and the tumors were separated, sectioned by cryostat (Leica biosystems, Germany) at a thickness of 5 µm and examined under a fluorescence microscope.

2.2.8.3 Immuno-histochemical analysis of Ki67

To examine cell proliferation, an immuno-hist Ki67 immuno-histochemical examination of the tumor was done (H. Chen et al., 2020). The tumor-bearing mice were sacrificed and fixed for 24 h in 4 % paraformaldehyde following the treatment protocol. With the help of microtome, 5 µm slices were cut from the embedded tumor tissues for Ki67 immunohistochemical analysis. At 4°C, tumor slices were treated overnight with Ki67 (catalog #9129S) at a 1:500 dilution. After that, the sections were rinsed with PBS and incubated for 2 h with Alexa Fluor® 488 conjugate secondary antibody. Finally, tissue sections were rinsed in PBS, covered with a coverslip, and examined under a fluorescence microscope. Microscopic images of the tissues were obtained using a microscope (Leica).

2.2.8.4 H & E staining

H&E staining was done on tissues obtained from tumor-bearing animals. Following therapy, main organs such as the liver, kidney, heart, spleen, and lung were removed, fixed, and slices of 5 µm thickness were cut. The manufacturer's protocol was followed to stain the sections

with Harris's haematoxylin−eosin (H and E) reagent. The sections were observed under the light microscope for histological studies (Muddineti, 2017)**.**

2.2.9 Statistics

All of the tests were done in triplicate, and the results are indicated as mean and standard deviation (mean SD). GraphPad Prism software was used to assess the significance of differences between all groups using t-test and one-way ANOVA. The analysis was statistically significant at p-values were less than 0.05. The symbols *, **, *** represents p-values <0.05, 0.01 and 0.001, respectively.

2.3. Results & Discussion

2.3.1. Physicochemical Characterization of the Ch/$(VES)_4$ conjugate and OXPt@Ch/VES Ms

Ch/$(VES)_4$ copolymer was effectively produced through the conjugation of VES to the Ch backbone utilizing EDC as a reaction catalyst. A strong ^1H peak of vitamin E Succinate (at 1–2.5 ppm) appeared at about 2.5 ppm **(Fig. 2.1B)**. The infrared spectrum provided additional confirmation of the generation of the Ch/$(VES)_4$ conjugate, as shown in **Fig. 2.1C**. The N-H (3292 cm^{-1}), C-H (2928 cm^{-1}), O-H (3352cm^{-1}), C=O (1619 cm^{-1}), C-N (1416 cm^{-1}), C-O-C (1158 cm^{-1}) and C-O (1001 cm^{-1}) further confirmed the Ch/$(VES)_4$ structure. The result was in accordance with the previously published literature (B. Wei et al., 2019). The degree to which amino groups have been substituted, as determined by the TNBS method, was 15.65 % for Ch/$(VES)_4$ (15KDa) and 17.75 % for Ch/$(VES)_4$ (300KDa), suggesting that the conjugate was effectively synthesized. Size exclusion chromatography (SEC) was used to determine the increase in the molecular weight of the Ch 15KDa after each conjugation. GPC analysis revealed that 4 moles of VES were attached to Ch polymer at the specified reaction condition **(Fig. 2.3, Table 2.1).** Pyrene was utilized as a fluorescent probe to determine the CMC of the

Ch/(VES) copolymer of Ch 15KDa and 300KDa. The CMC value was calculated to be 12.6µg/mL for Ch/(VES) 15KDa and 9.25µg/ml for 300KDa **(Fig. 2.4).** The reduced critical micelle concentration value showed that the Ch/$(VES)_4$ copolymer might readily develop a core-shell structure in an aqueous environment and keep the micellar structure intact *in vitro* and *in vivo* under diluted circumstances.

The OXPt@Ch/VES Ms were prepared by infusing the OXPt solution into the Ch/$(VES)_4$ solution while stirring mechanically, and after that, ultra-probe sonication was done. The micelles were characterized physiologically using zeta potential measurements, particle size analysis, X-ray diffraction spectroscopy (XRD), DSC analysis, drug loading, and encapsulation efficiency. The blank Ch/$(VES)_4$ micelles displayed particle size of 217 ± 2.3nm, which increased after drug loading to 255.5 ± 1.5, 263.6±2.1, and 282.7±2.5 for micelles of the drug to polymer weight ratios of 1:1, 1:1/2, 1:1/4 in case of Ch(15KDa) micelle formulation represented in **Table 2.2.** In contrast**,** 300KDa nanomicelle formulation displayed a particle size of 251.5 ± 2.3nm, 282.2±2.5nm, and 292.5nm. **Fig. 2.5A** shows a representative particle size distribution curve obtained from Malvern Zetasizer for Ch/$(VES)_4$ (15KDa) micelles (1:1 DTP ratio). The representative scanning electron micrograph of OXPt@Ch/VES Ms (DTP-1:1) reported a significant association with DLS data as shown in **Fig. 2.5A**. The micelles with a narrow polydispersity index of 0.2–0.35 and a positive zeta potential were found. The zeta potential values for blank and OXPt@Ch/VES Ms (1:1 DTP ratio) were 47.4 ± 2.12 and 31± 1.23 mV **(Fig. 2.5B) (Table 2.2).** The Ch (15KDa) conjugate with a DTP weight ratio of 1:1 had the maximum OXPt loading, and encapsulation efficiency represented in **Table 2.2**.

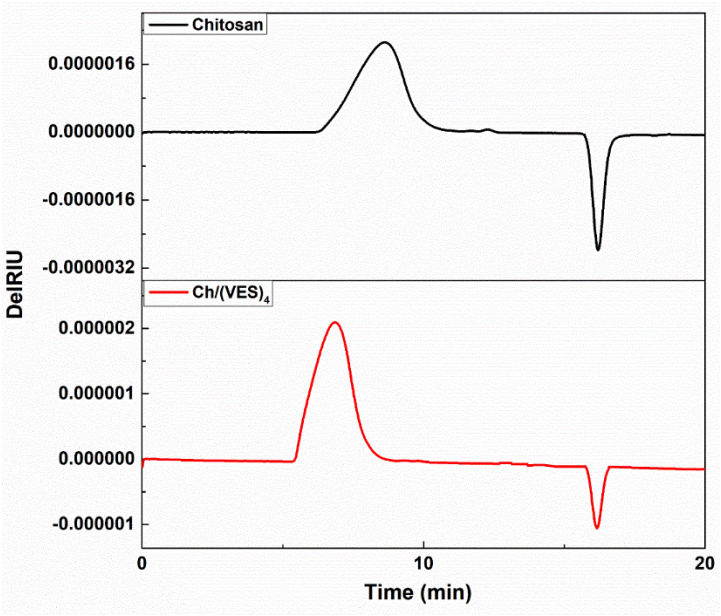

Figure 2.3 GPC analysis of chitosan (15KDa) and chitosan vitamin E succinate conjugate in 1 % acetic acid used as mobile phase.

Table 2.1 Relative molecular weight of each conjugate and estimation of the number of VES and attached to each chitosan molecule by SEC analysis.

Conjugates	**Molecular weight (Da)**	**PDI**	**Approximated No. of molecules attached to each Chitosan molecule**
Chitosan	14993	1.07	-
Chitosan-Vitamin E succinate Conjugate	17205	1.23	4.17

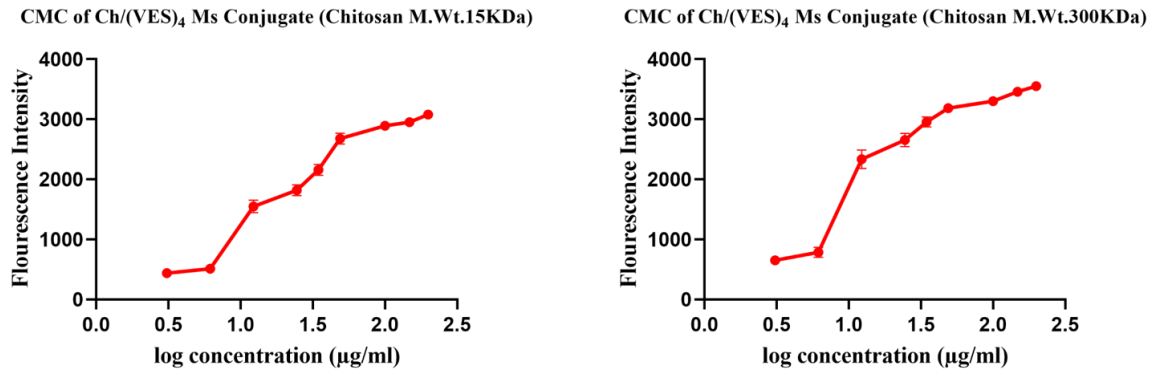

Figure 2.4 CMC of Chitosan-Vitamin E succinate conjugate of chitosan Molecular weight 15KDa and 300KDa.

The size of the micelles directs a low degree of reticuloendothelial system (RES) internalization, minimal renal excretion, and retention in solid tumors due to the EPR effect. The morphology of micelles was spherical, with low polydispersity, as determined by SEM **(Fig. 2.5A).** To see how the Ch solution pH affected the hydrodynamic diameter, OXPt@Ch/(VES) Ms were made using Ch solution at different pH values (2–9.0; **Fig. 2.5F, I**). Chitosan's hydrodynamic size is determined by the repulsive interaction between its free -NH_2 groups and in acidic conditions free -NH_2 groups are protonated, while in basic conditions, the surface protonation decreases, resulting in weak solubility of Ch and an increase in particle size due to particle-particle interactions being heightened (Gokce et al., 2014; Hajdu et al., 2008; Nallamuthu et al., 2015). Thus, the majority of the amino groups in Ch/(VES) were in an unprotonated state at high pH values (6.8–9.0), imparting no effect on micellar surface charge. At low pH, however, most of the NH_2 groups on Ch/(VES) were protonated, imparting a net positive charge. The mean hydrodynamic diameter of the co-loaded micellar system, on the other hand, did not change considerably in Ch solutions within the 3.0 to 5.0 pH range. The mean particle size of the co-loaded OXPt@Ch/VES micellar system rose significantly in Ch solutions with pH 6.8 to pH 9.0. Particle agglomeration due to the reduced repulsive potential might be responsible for the increase in particle size of the co-loaded micellar system (Avadi

et al., 2010; Hussain et al., 2013). DSC thermograms were plotted simultaneously for thermal analysis of newly formed OXPt@Ch/VES Ms along with OXPt, and blank micelles have been shown in **Fig. 2.5D.** Ch, VES, Ch/$(VES)_4$, Free OXPt and OXPt@Ch/VES Ms exhibited endothermic melting peaks at 95.3°C, 98.7°C, 110°C, 298.2°C, and 95.5°C, respectively. In XRD analysis, free OXPt showed peaks at 2-theta (°) values of 7.8, 15.5, 17.8, 25.9, 32.9, 37.2, and 41.8. Peaks associated with free OXPt disappeared in lyophilized drug-loaded nanoformulation **(Fig. 2.5E)**.

The chemical state of the surface elements in Ch, Ch/$(VES)_4$, and OXPt@Ch/VES Ms formulation was determined quantitatively by X-ray photoelectron spectroscopy. The complete survey and core-level spectra of Ch, Ch/$(VES)_4$, and OXPt@Ch/VES Ms samples are shown in **Fig. 2.6,** respectively. The elements C, N, and O are predominated in the Ch and Ch/$(VES)_4$ samples, while the elements C, N, O, and Pt(iv) predominated in the OXPt@Ch/VES Ms. **(Table 2.3)** C1s, O1s, and N1s binding energies for Ch, Ch/$(VES)_4$, and OXPt@Ch/VES Ms formulation were calculated using a deconvolution method of corrected XPS spectra. The C1s core level spectra of Ch, Ch/$(VES)_4$ and OXPt@Ch/VES Ms samples are shown in **Fig. 2.6.** feature three peaks at binding energies of 284.24, 285.71, 287.13 eV (for Ch), 284.40, 285.91, 287.31 eV (for Ch/$(VES)_4$), 284.41,285.90,287.31 eV (for OXPt@Ch/VES Ms), these peaks were connected with (C-H/C-C), alcohol/ether/amine (C-OX) and acetal (O-C-O) group. The N1s area in XPS spectra of Ch, Ch/$(VES)_4$, and OXPt@Ch/VES Ms samples are displayed in **Fig. 2.6.** The results demonstrated that the peaks at 397.84, 399.29 eV (for Ch), 339.19, 401.64 and 402.49 eV (for Ch/$(VES)_4$) and 399.15, 401.27, 402.18 eV (for OXPt@Ch/VES Ms) corresponding to the peaks of -C-OH,-C-N; O=C-N; and –NHx groups, respectively. These results indicated that blending the Ch with VES produced the conjugate with a reduced amino group number. The O1s region contains peaks at 531.12, 532.19, 533.54 eV (for Ch), 531.19, 532.23, 534.55 eV (for Ch/$(VES)_4$), 531.23, 532.30, 534.48 eV (for OXPt@Ch/VES Ms)

assigned to O-C-O; -C-OH, C-N; and H_2O molecule adsorbed on the polymer surface. The C1s, N1s, and O1s peaks in the spectra of Ch/$(VES)_4$ and OXPt@Ch/VES Ms lyophilized samples have comparable morphologies, indicating that the origins and patterns of the most prevalent surface species in both materials are identical and are most likely dependent on surface morphology. These findings corroborate the spectroscopic findings, which pointed to the production of the Ch/$(VES)_4$ conjugate.

Table 2.2 Determination of percent Drug loading, Encapsulation efficiency, Particle size and Zeta potential (Ch=15KDa).

S.No.	**Formulation [Ch/$(VES)_4$-OXPt)]**	**Particle Size (nm)**	**PDI**	**Zeta potential (mV)**	**% Entrapment efficiency**	**% Drug loading**
1	OXPt Loaded micelle(1:1)	255.5	0.31	+31	32.67	16.33
2	OXPt Loaded micelle(1:1/2)	263.6	0.42	+28.7	15.35	5.11
3	OXPt loaded micelle(1:1/4)	282.7	0.31	+20.8	26.4	5.28

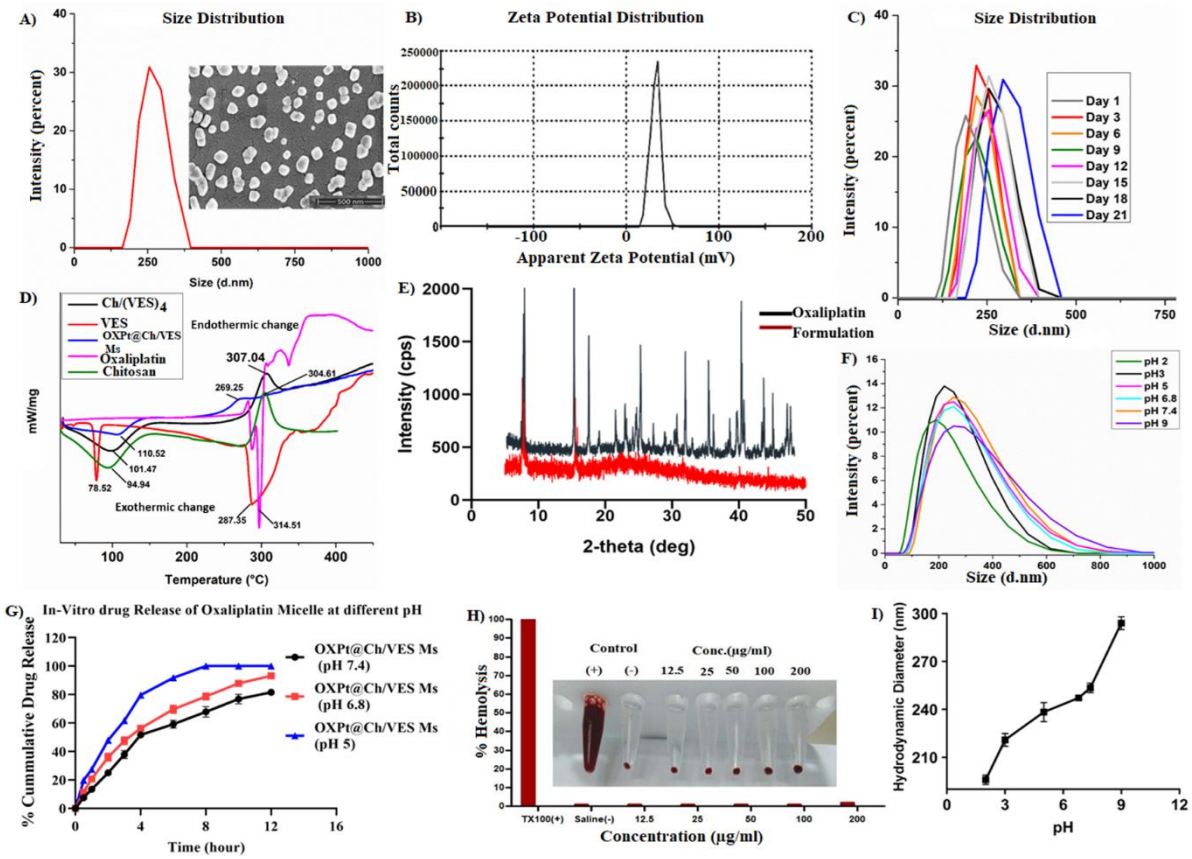

Figure 2.5 Physicochemical characterization of OXPt@Ch/VES Ms formulation. Particle size and SEM image of OXPt@Ch/VES Ms with cryoprotectant (A); zeta potential (B); 21days stability study of OXPt@Ch/VES Ms at 4 °C (C); DSC thermogram (D); XRD analysis of OXPt and OXPt@Ch/VES Ms (E); hydrodynamic diameter of the OXPt@Ch/VES Ms at various pH (F, I); *in vitro* drug release of OXPt@Ch/VES Ms at pH 7.4, pH 6.8 and pH 5 (G); *in vitro* hemolysis study of $Ch/(VES)_4$ (H).

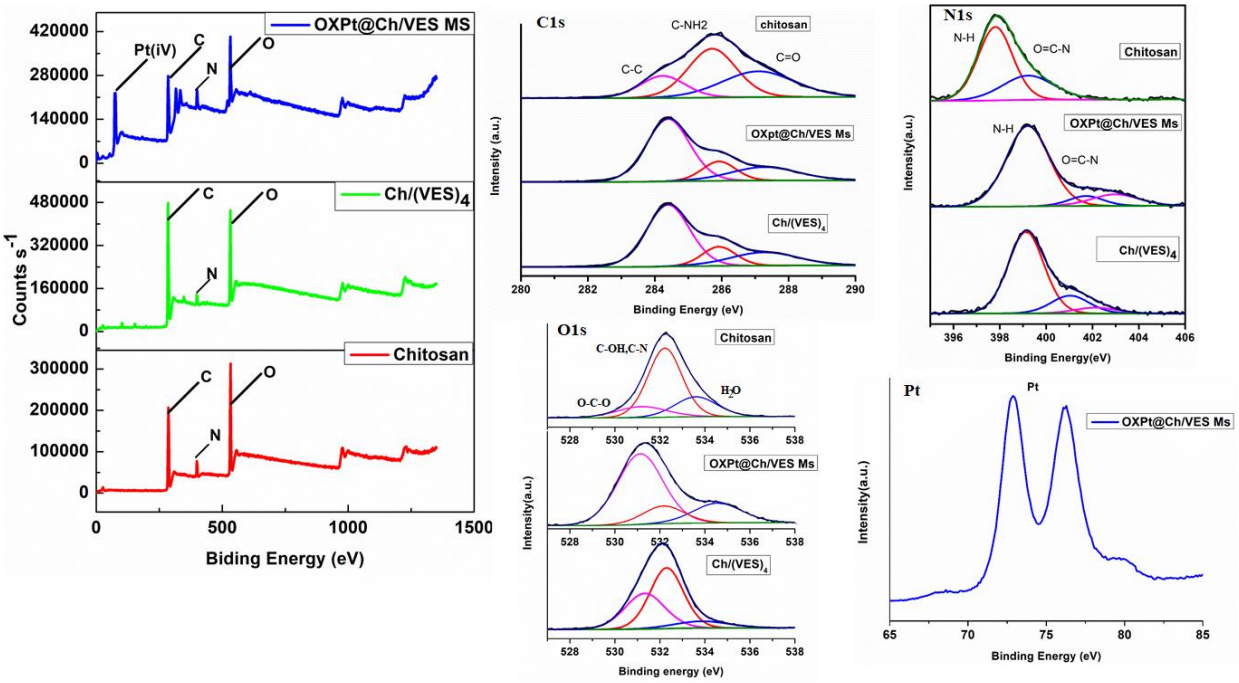

Figure 2.6 Survey spectra analysis and Deconvoluted XPS spectra analysis of O1s, N1s, and C1s and Pt (IV) of chitosan, Chitosan vitamin E succinate conjugate and OXPt@Ch/VES Ms formulation.

Table 2.3 C1s, O1s and N1s binding energies evaluated from a deconvolution procedure of corrected XPS spectra for chitosan, chitosan vitamin E succinate and Oxaliplatin micelle formulation.

	Binding energy/eV **High resolution spectra**				
Chitosan (Ch)	C1s 284.24 285.71 287.13	O1s 532.19 531.12	N1s 397.84 399.29	Pt(iv) - - - - -	Species C-C/C-H -C-OH, C-N O=C-N

		533.54		- -	O-C-O, C=0 H_2O
Chitosan Vitamin E succinate copolymer Ch/$(VES)_4$	284.40 285.91 287.31	532.23 531.19 534.55	399.19 401.64 402.49	- - - - - -	C-C/C-H -C-OH, C-N -C-OH, C-N O=C-N O-C-O -NHx H_2O
OXPt@Ch/VES Ms	284.41 285.90 287.31	532.30 531.23 534.48	399.15 401.27 402.18	- - - - - - 72.82, 76.28	C-C/C-H -C-OH, -C-N O=C-N O-C-O -NHx Pt H_2O

The drug release studies for the OXPt@Ch/VES Ms formulation were carried out at 37°C with PBS pH 7.4, 6.8, and 5. The amount of OXPt released was determined using UV spectroscopy.

OXPt released from the Ch/$(VES)_4$ showed a statistically significant difference. The crucial aspect of any delivery method relies on the carrier's ability to efficiently release the cargo at the specified spot. **(Fig. 2.5G)** strongly depicts the release of OXPt from Ch/$(VES)_4$ micelle formulation in phosphate buffer pH 5, pH 6.8, and pH 7.4. This implies that OXPt release was greater in acidic pH 5.0 than at alkaline pH 7.4. Because the ingestion of drug-loaded nanomicelle via endocytosis results in exposure to an acidic environment, this pH-dependent release may aid in improving OXPt efficacy (Rim et al., 2011). The higher surface area of Ch due to a smaller size at low pH could also be the reason for the faster release of drug from OXPt@Ch/VES Ms, as confirmed by the particle size measurement at various pH environments. An increased cytotoxic activity against tumor cells would arise from such efficient release. Penetration, hydration, dissolution, and ultimately diffusion were the usual steps in drug release from any formulation. This typically happens when a drug has to be released from a matrix; in our instance, Ch served as the matrix, assisting in the sustained release of OXPt from the OXPt@Ch/VES Ms formulation. As a result of this process, a polymer's erosion and swelling are additional variables that influence drug release and kinetics. The OXPt release behavior from our designed nanoformulation was investigated, appropriately fitting with various comparable mathematical release models such as zero and first order, Korsmeyer–Peppas, Hixson–Crowell, Higuchi model, and Weibull model. The kinetic models of the releasing behavior with regression coefficient (R^2) and the relevant release kinetics are presented in **Table 2.4**. The findings are best suited to the Weibull model at pH 7.4, pH 6.8, and pH 5 with a linear regression coefficient of 0.993 (**Fig. 2.7)**.

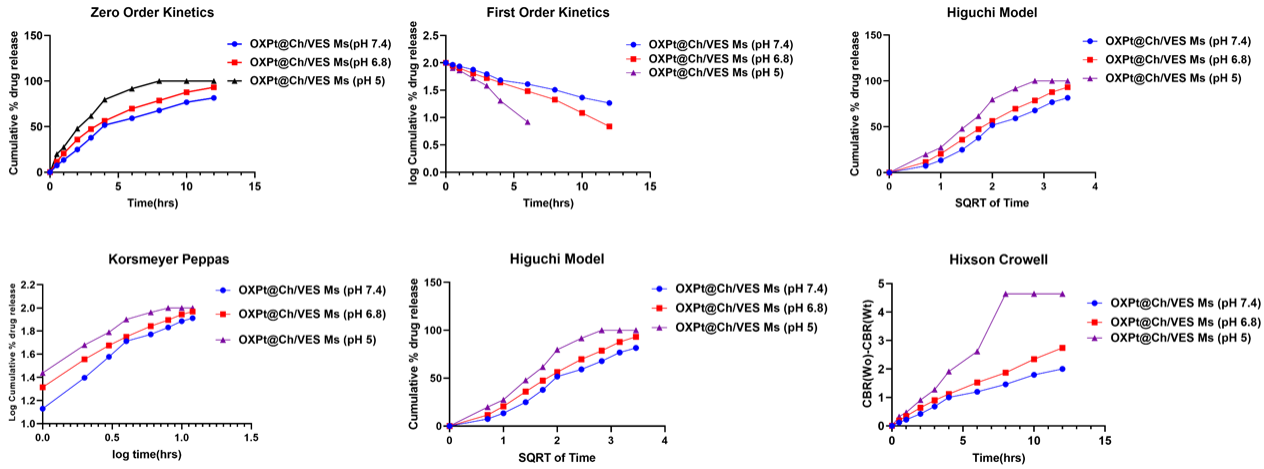

Figure 2.7 Kinetic release mathematical models of OXPt@Ch/VES Ms formulation at various pH's.

Table 2.4 kinetic models of the releasing behaviour with regression coefficient (R^2).

OXPt@Ch/VES Ms (pH)	**Zero order**	**First order**	**Higuchi model**	**Korsmeyer Peppas**	**Hixson Crowell model**	**Weibull Model**	**Best fit model**
7.4	y = 6.8059 x + 10.44 R^2 = 0.9249	y = -0.0616 x + 1.9867 R^2 = 0.9928	y = 26.155 x - 6.9717 R^2 = 0.978	y = 1.343x - 1.5766 R^2 = 0.9652	y = 0.1685 x + 0.1063 R^2 = 0.9791	y = 0.9855 x - 1.8728 R^2 = 0.9945	Weibull model

6.5	y = 7.4616 x + 15.421 R^2 = 0.9172	y = -0.0925 x + 2.0044 R^2 = 0.9932	y = 28.986 x - 4.2534 R^2 = 0.9911	y = 1.6478x - 2.2303 R^2 = 0.9825	y = 0.222x + 0.1342 R^2 = 0.9933	y = 0.9496 x - 1.4715 R^2 = 0.9976	Weibul model
5	y = 8.0132 x + 25.546 R^2 = 0.8091	y = -0.1947 x + 2.0347 R^2 = 0.9437	y = 32.451 x + 1.9374 R^2 = 0.95	y = 1.7714x - 2.6284 R^2 = 0.9262	y = 0.438x + 0.1065 R^2 = 0.9478	y = 0.9944 x - 0.9995 R^2 = 0.9754	Weibul model

Though since supramolecular micellar aggregates are typically ingested through the intravenous route, a hemocompatibility test was required to determine if the new Ch/$(VES)_4$ would cause hemolysis. After stirring, the erythrocyte pellets in the Ch/$(VES)_4$ copolymer samples were readily disseminated, and no clumps were detected. As demonstrated in **Fig. 2.5H,** there was no discernible change between the Ch/$(VES)_4$ copolymer and the negative control. In the positive control samples, full hemolysis was also detected, and the solution was distinctly red-colored. These findings indicate that at the maximum dosage of 0.2 mg/mL at 37°C, the Ch/$(VES)_4$ copolymer did not trigger hemolysis or erythrocyte agglutination, suggesting that it is a suitable nanocarrier for delivery of drug to tumors. A similar trend was observed in the previously reported literature (Jamil et al., 2016; Y. Zhou et al., 2015).

2.3.2. *In vitro* assays

2.3.2.1 Cellular uptake

Confocal microscopy and flow cytometry were explored for qualitative and quantitative cellular uptake. MCF-7 and MDA-MB-231 were used for all *in-vitro* cell-based studies. The bright red fluorescence of OXPt@Ch/VES Rhodamine B conjugated micelle formulation was increased from 1 to 4 h, indicating its time-dependent cellular uptake for all the two cell lines. As indicated in **Fig. 2.8A, B**, the red fluorescence intensity of OXPt@Ch/VES MS was significantly increased for 20µg/mL concentration compared to 10µg/mL in all the tested cells, which was further quantified by flow cytometry experiments. As depicted in **Fig. 2.8C, D**, the flow cytometer's histograms revealed a rise in the mean fluorescence value of OXPt@Ch/VES Ms (20µg/mL) compared to OXPt@Ch/VES Ms (10µg/mL), which were plotted as a bar graph. For MCF-7 cells, the geometric mean of OXPt@Ch/VES Ms (20µg/mL) was increased from 1500.2±64.06 to 2355.5±49.27 from 1 to 4 h and that of OXPt@Ch/VES Ms (10µg/mL) were increased from 290.4±9.7 to 1090.7±12.25 respectively depicted in **Fig 2.8F**. The same trend was observed for MDA-MB-231 cells. The intensity of fluorescence increased in a time-dependent manner. For MDA-MB231 cells, the geometric mean of fluorescence was 1450.3±125.8 (20µg/mL) and 310.4±18un 20.2 (10µg/mL) in 1h, which was increased to 2756.1.±137.6 (20µg/mL) and 1210.6±142.5 (10µg/mL) after 4h of incubation with OXPt@Ch/VES Ms depicted in **Fig. 2.8E**. The micellar uptake is an energy-dependent endocytosis process, whereas free OXPt moves within cells by diffusion. The stable micellar system of OXPt@Ch/VES Ms internalized more effectively and resulted in the time-dependent increase of intracellular OXPt-signal. Micelles were found to be widely dispersed in both the cytoplasm and the nucleus of both cell lines. Micelles seemed to have fragmented the cell membrane and nuclear membrane, as depicted in **Fig. 2.9A.** The characteristic is due to Chitosans high hydrophilicity of hydroxyl groups, its vast number of main amino groups, and

the polymer chain's flexible shape (Y. Xu et al., 2011). The majority of these drugs are hydrophilic and have a large molecular weight, limiting their ability to penetrate biological barriers. Since the absorption of drug-loaded Ch micelles via endocytosis results in exposure to an acidic environment, the pH-dependent release may assist in enhancing OXPt effectiveness in the current research (Bareford & Swaan, 2007).

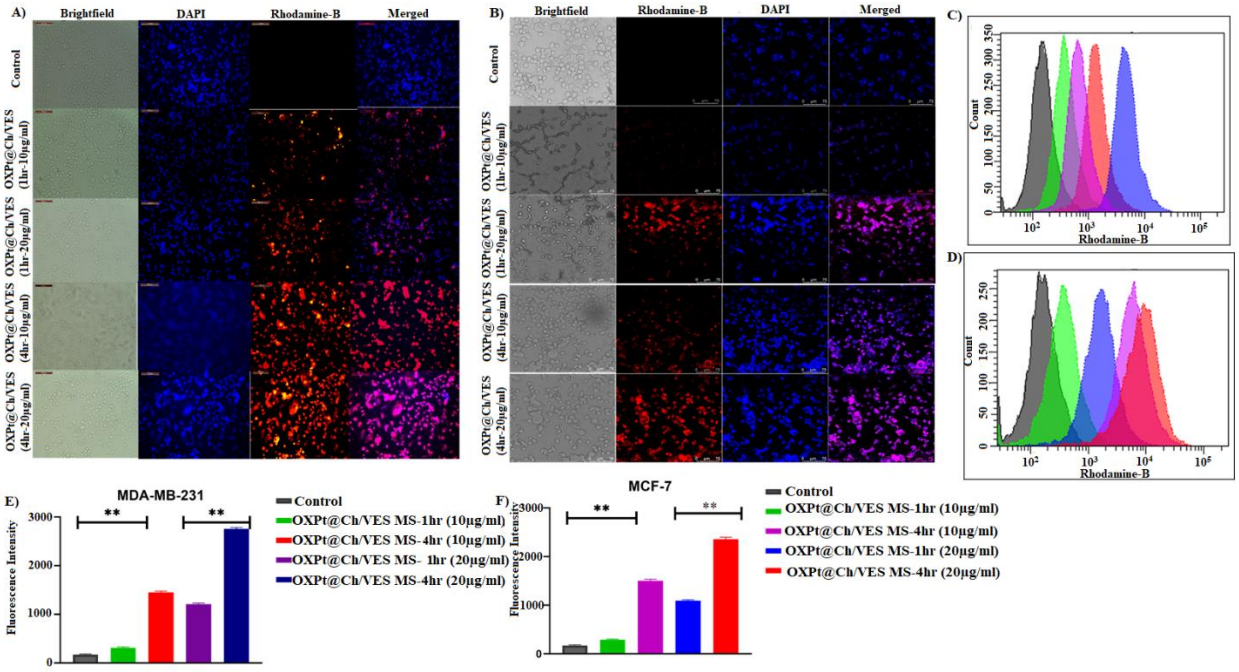

Figure 2.8 Cellular uptake study. Fluorescence microscopy images of MDA-MBA-231cells (A) and MCF-7 cells (B) treated with OXPt@Ch/VES Ms at OXPt concentration of 10 and 20µg/mL after 1h and 4h incubation; illustrative histogram plot achieved from statistics calculation by flow cytometer and assessment of the geo mean of fluorescence of the MDA-MBA-231cells (C) & (E) and MCF-7 cells (D) & (F). The data represents mean ± standard deviation, calculated from three sets of experiments. The significance of difference was assessed by Student t-test, *, **&*** indicates $p < 0.05$, $p < 0.01$ and $p < 0.001$ respectively.

2.3.2.2 *In vitro* cytotoxicity

MTT assay was used to evaluate cell viability after 24, 4-24h and 48 h, using MCF-7 cells, MDA-MB-231 cells, and MDA-MB-231(R) at 37°C to evaluate the cytotoxicity of

OXPt@Ch/VES nanomicelles formulation, and the results are shown in **Fig 2.9D.** In general, the cytotoxicity of the drug encapsulated in Ch/$(VES)_4$ nanomicelles increased when the drug concentration and incubation duration were increased. The cell viability decreased significantly with the OXPt@Ch/VES treatment compared with Free OXPt and Ch/$(VES)_4$. The $Ch(VES)_4$ Ms demonstrated cell viability of 76.62 % (24 h), 83.80% (4-24 h), 71.59% (48 h), Free OXPt 22.45% (24 h), 43.54% (4-24 h), 13.49% (48 h) and OXPt@Ch/VES 12.70% (24 h), 34.51% (4-24 h), 5.98% (48 h) in MCF-7 cells while in MDA-MB-231 cells $Ch(VES)_4$ Ms demonstrated cell viability of 69.32 % (24 h), 82.58% (4-24 h), 70.49% (48 h), Free OXPt 15.32% (24 h), 46.32% (4-24 h), 16.59% (48 h) and OXPt@Ch/VES 9.02% (24 h), 38.02% (4-24 h), 5.02% (48 h) respectively and in MDA-MB-231 R Resistant cells $Ch(VES)_4$ Ms demonstrated cell viability of 79.49 % (24 h), 85.33% (4-24 h), 74.21% (48 h), Free OXPt 32.21% (24 h), 47.70% (4-24 h), 27.27% (48 h) and OXPt@Ch/VES 29.20% (24 h), 41.33% (4-24 h), 21.72% (48 h) respectively at the OXPt concentration of 100µg/mL. A cell viability investigation revealed that the OXPt-CS-VES micelle formulation promoted greater cellular internalization and resulted in lower cell viability when compared to free OXPt. Another rationale for cytotoxicity in OXPt@Ch/VES would be the anticancer effect of VES.

The cytotoxicity of Ch/$(VES)_4$ Ms, free OXPt, and OXPt@Ch/VES Ms was compared using IC-50 values, as shown in **Fig. 2.9D**. Cells incubated for 4 h followed by 24 h had a higher IC50 value than cells incubated for 24 h continuously. Further, IC50 values were found to be decreased for 48 h. When compared to free OXPt tested cell lines, the anti-proliferative activity of OXPt@Ch/VES Ms was the highest. The decrease in IC50 values from 24 to 48 h suggested that the cytotoxicity was time dependent. This could be due to retention of associated OXPt in micelles intracellularly, and when compared to free OXPt, this compound had higher cytotoxicity, as the intracellular OXPt concentration lowered due to its exit out of the cells via diffusion.

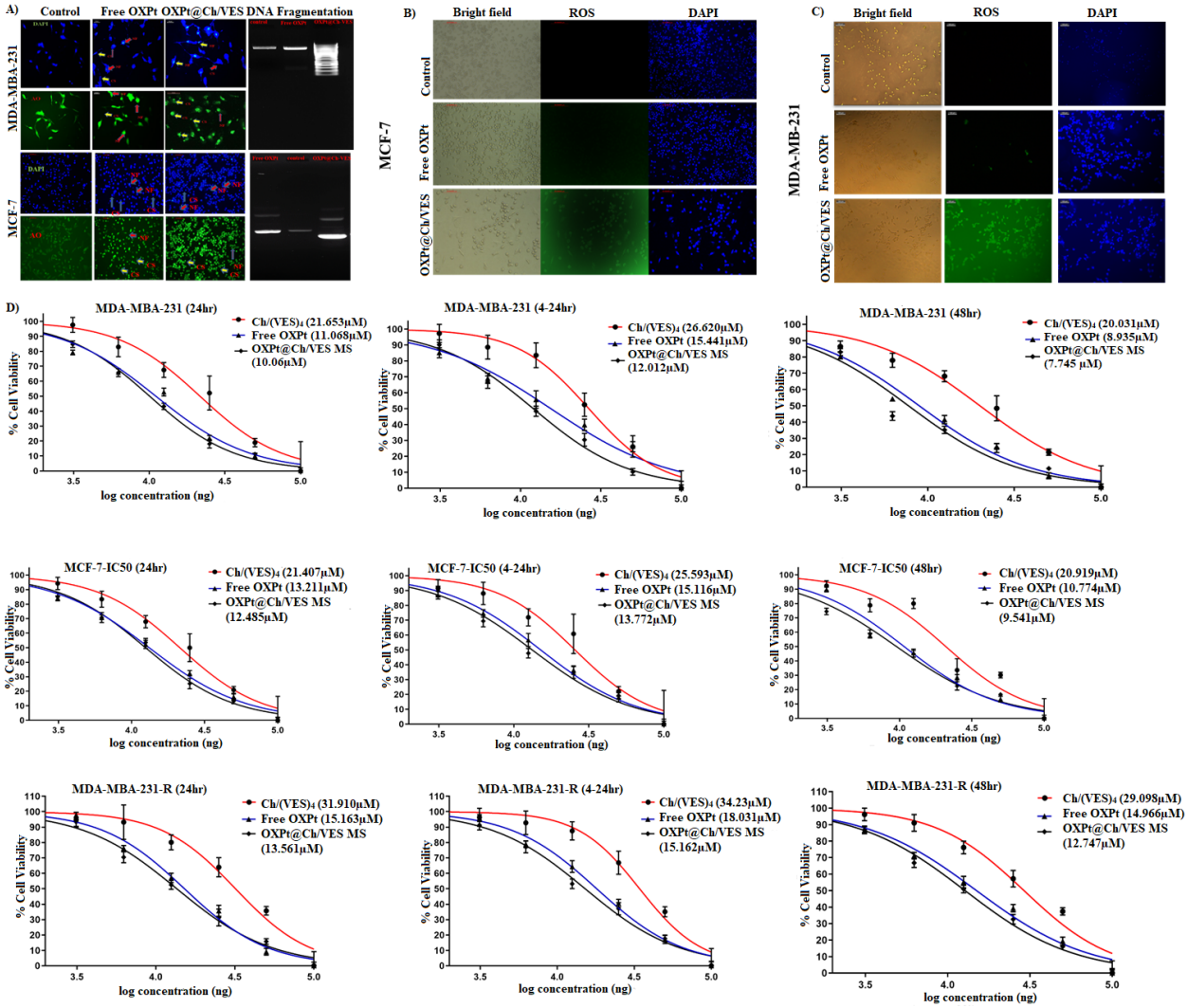

Figure 2.9 Nuclear staining (left) and DNA fragmentation (right) treated with free OXPt and OXPt@Ch/VES Ms formulation at OXPt concentration of 50 μM (A); Study on the generation of ROS in MCF-7 and MDA-MBA-231 cells for 24 h (B, C); Anticancer activity of free OXPt, OXPt@Ch/VES micelle and Ch/$(VES)_4$ copolymer by MTT assay. MCF-7 and MDA-MB-231 cells were treated with OXPt at a concentration range of 3.5 to 100μg/ml (n=3). The IC 50 values of free OXPt, OXPt@Ch/VES micelle, and Ch/$(VES)_4$ for cultured MCF-7, MDA-MB-231-S, and MDA-MBA-231-R cancer cells at 24 h, 4 h followed by 24 h incubation, and 48 h (D); The significance of difference was assessed by ANOVA, $^{**}p < 0.01$.).

2.3.2.3 Apoptosis assay

The Annexin V test was used to assess the degree of apoptosis caused by OXPt. Following therapy, phosphatidylserine (PS), an early apoptotic marker, was transported from the inner plasma membrane to the outer plasma membrane, drawing macrophages. As a result, the phenomenon triggered the development of phagocytized apoptotic bodies. The triggering of apoptosis was calculated by observing the fluorescence of FITC, which has a strong affinity for PS. Propidium iodide (PI), which specifically binds to necrotic bodies, quantifies necrotic cells simultaneously. As indicated in **Fig. 2.10A**, MDA-MB-231 and MCF-7 cells were treated for 18 h with free OXPt and OXPt@Ch/VES Ms at 10 µg/mL OXPt concentration. MCF-7 and MDA-MBA-231 cells were both treated with free OXPt exhibited total apoptosis of 16.6±1.3 % and 16±1.47 %, respectively, whereas OXPt@Ch/VES Ms produced total apoptosis of 36.3±1.57% and 33.9±1.35% in MCF-7 and MDA-MBA-231 cells. OXPt@Ch/VES Ms triggered more apoptosis than free OXPt, and this may be due to the nanocarrier systems' enhanced cellular uptake of OXPt.

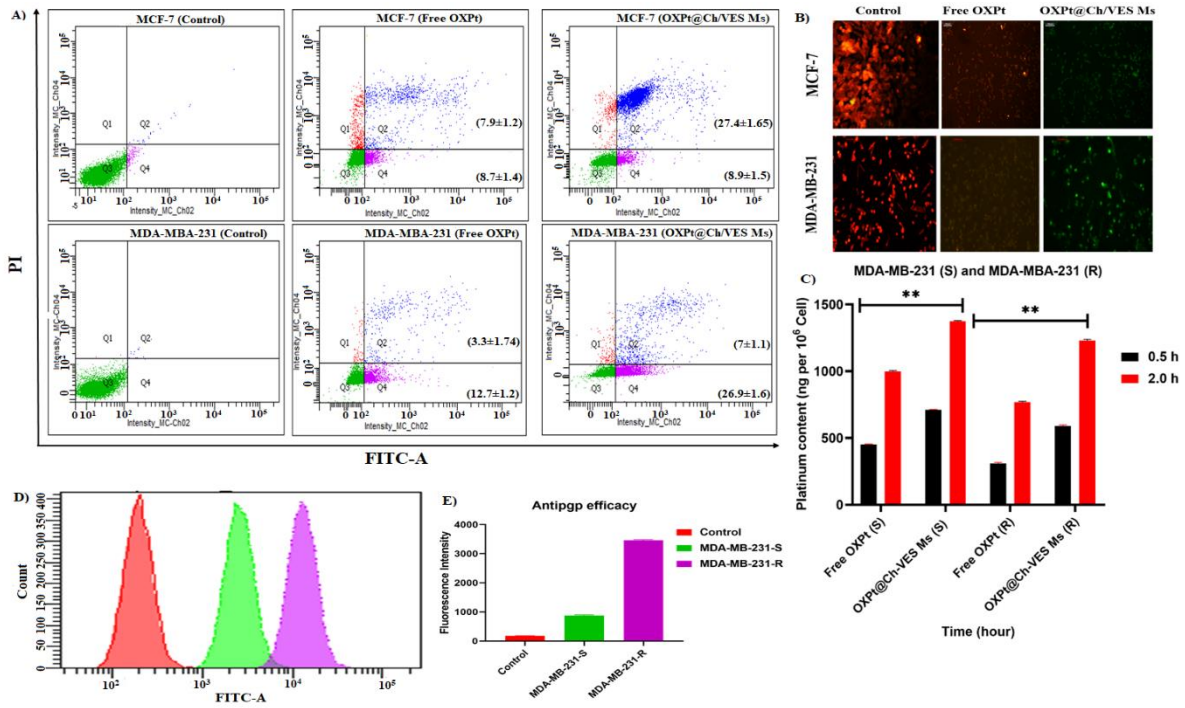

Figure 2.10. Quantitative assessment of Apoptosis in MCF-7 and MDA-MB-231 cells induced by untreated- control, Free OXPt and OXPt@Ch/VES micelle formulation at Oxaliplatin concentration of 10µg/ml (A); Change in mitochondria membrane Potential, fluorescence microscopy images of MDA-MB-231 and MCF-7 cells treated with free OXPt and OXPt@Ch/VES Ms followed by incubation of cells with mitochondria depolarization indictor JC-1 dye (B); Pt uptake (ng of Pt per 10^6 cells) by MDA-MB-231 (S) and MDA-MB-231 (R) cancer cells after 0.5 and 2 h incubation with free OXPt and OXPt@Ch/VES micelles measured by AAS (mean ± SD, n = 3) (C); Flow cytometry data of MDA MB-231-S and MDA MB 231-R cell lines treated with anti-P-gp antibody. The cells were seen in dual filters using FITC (ex/em 495/520) (D); Geo mean fluorescence is depicted in triplicates as mean ± SD (E).

2.3.2.4 Cell cycle analysis

Treatment with the free OXPt and OXPt@Ch/VES Ms at OXPt concentration of 10µg/mL caused the arrest of the cell population in G2/M in MCF-7, MDA-MB-231, and MDA-MB-231(R) tested cell lines. The arrest was much higher in OXPt@Ch/VES Ms treated cells than

in free OXPt treatment in these cell lines**. (Fig. 2.11A, C, E)** indicates the number of cell populations in different phases following treatment. The arrested breast cancer cells in the G2 cell division cycle were ~4.50 fold compared to untreated, and Free OXPt treated cells, respectively (Liao et al., 2018). The OXPt@Ch/VES Ms treatment resulted in the lowest number of cells in the G1 population due to the shifting of the cells to the G2 phase **(Fig. 2.11B, D, F).**

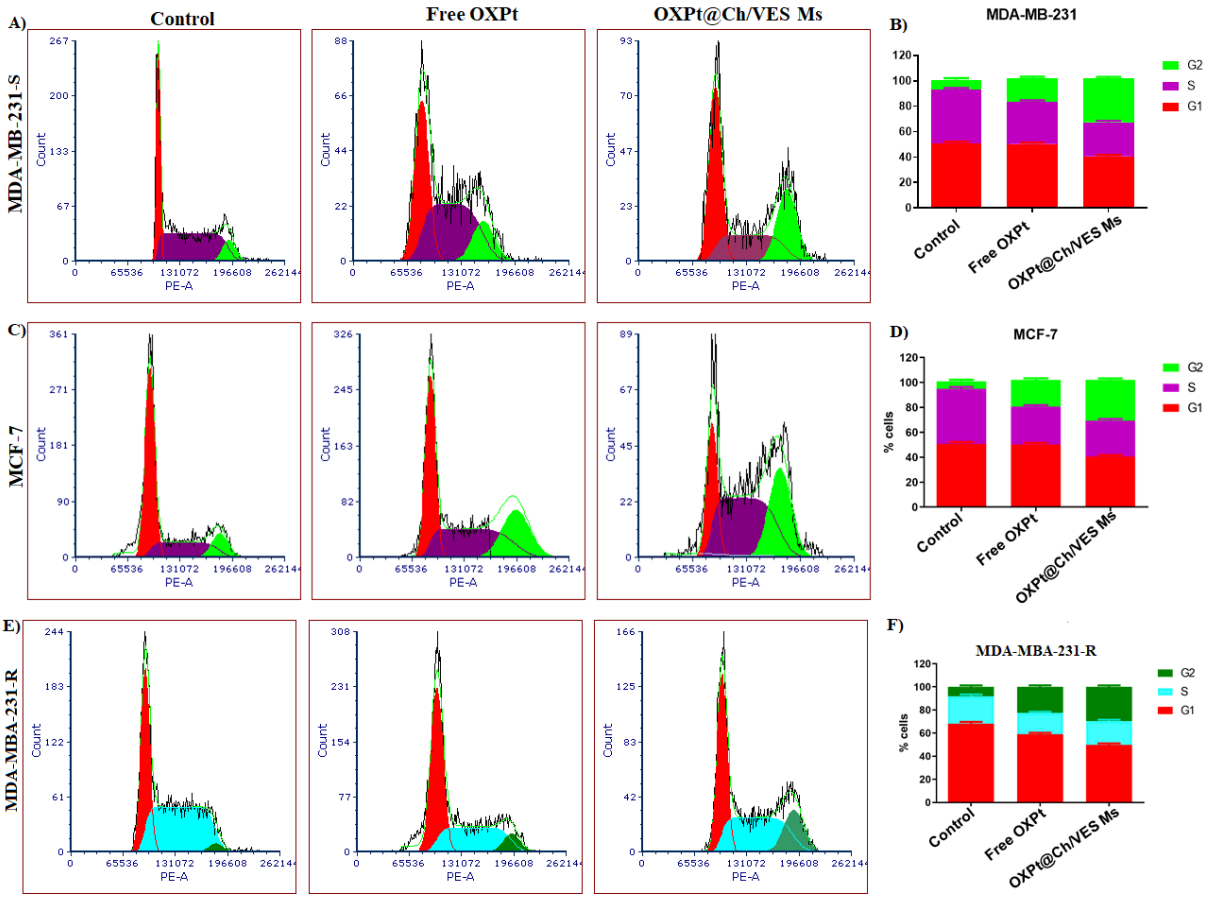

Figure 2.11 Cell cycle analysis of MCF-7 cells, MDA-MBA-231-S and MDA-MBA-231-R after 24h of treatment with free OXPT and OXPt@Ch/VES Ms Formulation (A, C, E); the bar graph represents the percent cells in G1, S, and G2 phase (B, D, F).

2.3.2.5 DNA fragmentation study and nuclear staining

Gel electrophoresis was performed to assess the extent of DNA damage. When compared to Free OXPt, OXPt@Ch/VES Ms treated cells; the OXPt@Ch/VES Ms treated cells showed more DNA fragmentation with a ladder-like pattern **(Fig. 2.9A left)**. The control DNA was undamaged and showed no signs of deterioration. After treatment, nuclear labeling with DAPI and acridine orange (AO) was used to examine apoptotic cells' proportion and cellular characteristics **(Fig. 2.9A right).** Nuclear fragmentation, cell blebbing, and shrinkage were detected in apoptotic cells. When comparing free OXPt to OXPt@Ch/VES micelles (1:1), confocal microscopy revealed that OXPt@Ch/VES micelles (1:1) caused cell shrinkage, chromatin condensation, and cell blebbing extensively than free OXPt treatment. A similar observation was noted in earlier studies (Thangam et al., 2012; Vivek et al., 2012).

2.3.2.6 Mitochondria membrane potential (MMP) and ROS detection assay

The control cells generated red JC-1 fluorescence, which diffuses to yellow in free OXPt-treated cells owing to the coupled localization of red and green signals. The cells treated with OXPt@Ch/VES Ms emitted a bright green fluorescence **(Fig. 2.10B).** MMP fluctuation has been linked to mitochondrial malfunction and apoptosis. JC-1 (carbocyanine cationic dye) clumps at high concentrations in the electronegative core of mitochondria and produces a red fluorescence (~590 nm). The quantity of dye accumulating in mitochondria reduces as mitochondria are depolarized; the dye stays in monomer form and exhibits green fluorescence (~529 nm). The fluorescence intensity of DCFH-DA, an indication of reactive oxygen species production, was evaluated in the reactive oxygen species detection assay. Compared to free OXPt treatment, cells treated with OXPt@Ch/VES Ms (1:1) produced substantially more ROS **(Fig. 2.10B, C).** Increased ROS levels may cause mitochondrial damage via depolarization of the mitochondrial membrane, leading to cell apoptosis as a result (Y. Xu et al., 2011).

2.3.2.7 Anti P-glycoprotein efficacy study and platinum content in the cell

AAS was used to assess the Pt content of MDA-MB-231(S) and MDA-MB-231(R) cell lysis solutions. Pt levels in cells were expressed as ng of Pt/10^6 cells, as shown in **Fig. 2.10C**. The results show that the Pt absorption by the OXPt@Ch/VES Ms inside the cell is substantially higher than that of free OXPt and that the OXPt@Ch/VES Ms is capable of delivering and releasing the OXPt. As demonstrated in **Fig. 2.10D**, the intensity of fluorescence in resistant (MDA MB-231-R) cells administered with anti-P-gp antibody was greater than in sensitive cells. MDA-MB-231R has shown >4 fold higher (Geo means of fluorescence 3458 ± 25) than MDA-MB-231-S (Geo means of fluorescence 875 ± 27) **(Fig. 2.10E).** Blocking drug resistance by inhibiting P-gp-mediated drug efflux and/or causing tumor cell death has emerged as a prominent hotspot in drug resistance. VES has been shown in recent trials to have strong anticancer efficacy in various malignancies. OXPt@Ch/VES Ms operates by decreasing the activity of the P-gp ATP enzyme and downregulating P-gp protein expression, hence overcoming P-gp-mediated drug efflux and suppressing MDR in triple-negative breast cancer cells (Thangam et al., 2012).

2.3.3 Pharmacokinetic study

Fig. 2.12H and Table 2.5 present the plasma concentration of OXPt versus time curve and pharmacokinetic parameters of free OXPt solution and OXPt@Ch/VES Ms-treated rats groups following a bolus dose (OXPt dose equivalent. 5 mg/Kg). $AUC_{(0\text{-}48\ h)}$ (µg/ml*h) of OXPt@Ch/VES Ms (741.70 µg/mL*h) was ~4.8-fold higher than the free OXPt solution (154.18 µg/mL*h) ($P < 0.05$). The half-life ($t_{1/2}$) and mean residence time (MRT) of OXPt@Ch/VES Ms treated groups were 9.39 h, 13.4 h compared to 1.18 h, 1.34 h, respectively in free OXPt solution-treated groups. The ~8-fold increase in the $t_{1/2}$ and ~10 fold increase in MRT indicated the sustained release of OXPt from the OXPt@Ch/VES Ms, supporting the *in*

vitro drug release profile (Vivek et al., 2014). The decrease in the *in vivo* clearance of OXPt in OXPt@Ch/VES Ms treated group (by ~4.8-fold) was observed compared to OXPt solution groups. The slow clearance could be due to the improved stability of the micelles-entrapped OXPt than free OXPt with a short elimination half-life (Ito et al., 2012; W. Zhang et al., 2008).

Table 2.5 The table represents the pharmacokinetic parameters of the free oxaliplatin and OXPt@Ch/VES micelle formulation. Note: Each point represents the mean ± SD of three rats.

PK Parameters	**Free OXPt**	**OXPt@Ch/VES MS formulation**
Lambda-z (1/h)	0.5888	0.0738
t1/2(h)	1.1774	9.3945
T0.5(h)	0.5	0.5
C0.5(µg/ml)	72.4276	60.0807
AUC 0-48 h (µg/ml*h)	154.1845	741.7012
AUC 0-inf_obs (µg/ml*h)	157.9569	760.2291
MRT 0-inf_obs(h)	1.3436	13.4008
Vz_obs (mg/kg)/(µg/ml)	0.0538	0.0892
Cl_obs (mg/kg)/(µg/ml)/h	0.0317	0.0066

2.3.4 *In vivo* study

2.3.4.1 Tumor Inhibition Study.

The intravenous treatment with OXPt@Ch/VES Ms reduced tumor development considerably more (>4-fold) than the control group, free OXPt in the tumor inhibition experiment **(Fig. 2.12E).** The OXPt@Ch/VES Ms, owing to its nanosize, demonstrate increased tumor accumulation, biodistribution, and cytotoxicity due to passive targeting (EPR effects). Additionally, the formulations showed no systemic toxicity in mice, as shown by insignificant body weight change during the study duration (**Fig. 2.12C).** The tumor weight in the OXPt@Ch/VES Ms treated group was considerably lower than in the control group.

Furthermore, live animal optical imaging demonstrated that compared to the treatment groups, tumors in the control group had the highest BLI intensity **(Fig. 2.12F and Fig. 2.13)**. The results revealed a progressive growth in tumor volume in all groups, with the control group increasing at a significantly faster rate than the treatment groups, correlating with the tumor volume inhibition trial **(Fig. 2.12A)**. The survival study was also carried out post-resection of the tumor for 21 days. The mice treated with the higher dose of OXPt@Ch/VES Ms lived significantly longer than the Free OXPt treated animals, while the lowest survival data was obtained for untreated/control animals. The percentage survival of the treated and control group mice was represented with the Kaplan-Meier curve in **Fig. 2.12D**. These findings showed that OXPt@Ch/VES Ms therapy not only dramatically decreased tumor growth but also enhanced the survival length of the treated mice three weeks after tumor removal. Overall, the new potent and OXPt@Ch/VES Ms showed considerable anticancer therapeutic efficacy *in vivo*. A similar pattern was noticed in the previously mentioned literature (Liao et al., 2018).

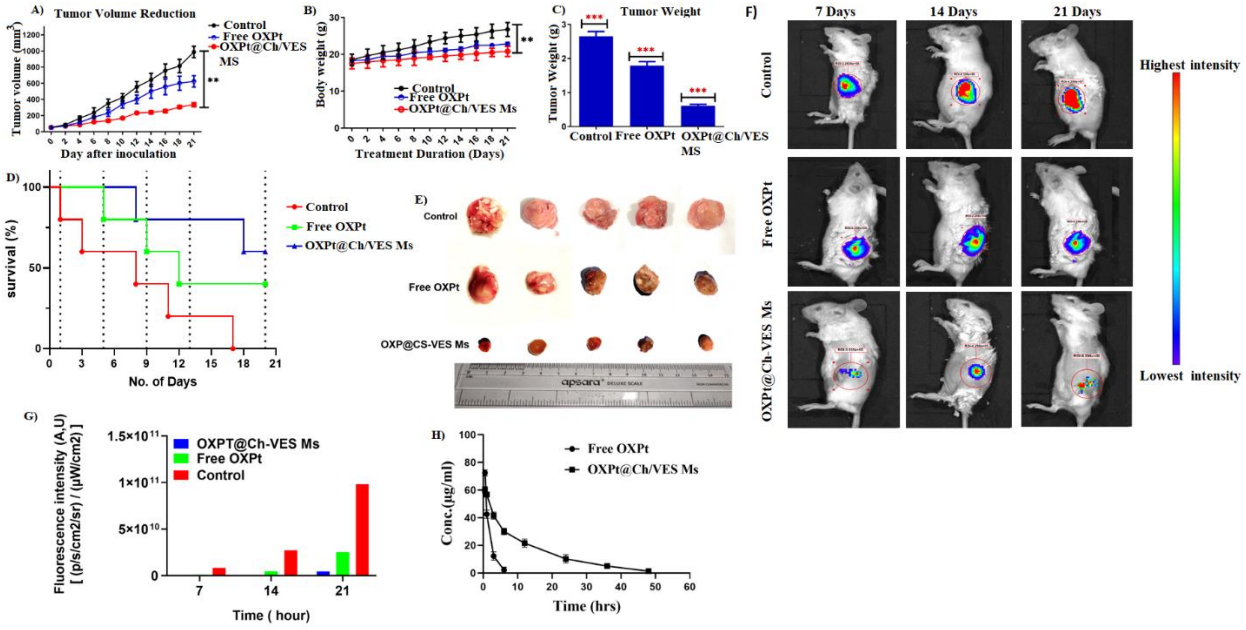

Figure 2.12 Assessment of Therapeutic efficacy of free OXPt and OXPt@Ch/VES micelle formulation in 4T1-LUC tumor-bearing BALB/C mice. Graphical representation of Tumor volume vs. days during treatment (A); measurement of body weight during the treatment (B); the average weight of tumors isolated from various treatment groups (C); survival rate graph (D); and representative tumors isolated from mice post-treatment (E); Analysis of in-vivo biodistribution by IVIS imaging of 4T1 LUC Tumor-bearing mice after the I.V administration of free OXPt and OXPt@Ch/VES Ms formulation at OXPt concentration of 5mg/kg, images captured at predetermined post-injection time periods (F); graphical representation of fluorescence intensity vs. time (G); and mean plasma concentration-time profiles of OXPt after IV administration of a single 5mg/kg dose of free OXPt and OXPt@Ch/VES Ms to rats (H).

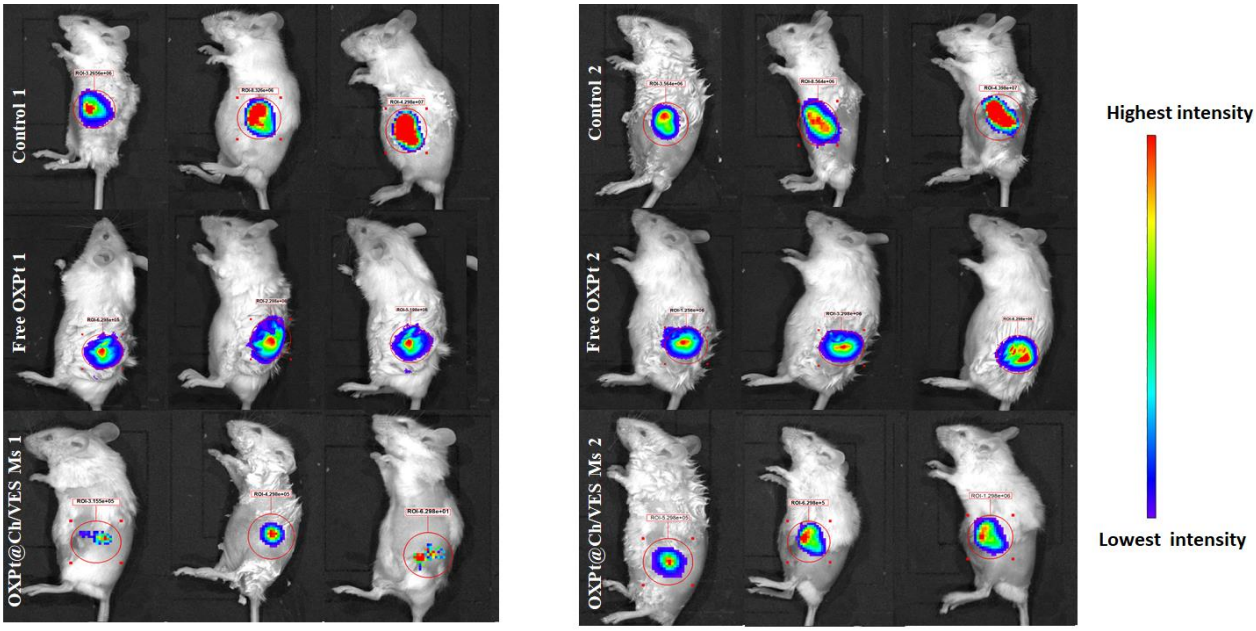

Figure 2.13 Analysis of in-vivo biodistribution by IVIS imaging of 4T1 LUC Tumor bearing mice after the I.V administration of free OXPt and OXPt@Ch/VES Ms formulation at OXPt concentration of 5mg/kg, images captured at predetermined post injection time periods.

2.3.5 Immunohistochemistry

2.3.5.1 TUNEL Assay on Tumor Cryosections.

The TUNEL test was predicated on the idea that nucleases (started by caspases) break nuclear DNA, resulting in cell death. Terminal deoxynucleotidyl transferase (TdT), which binds tagged dUTP to the DNA, recognizes the nicked ends of fragmented DNA. Fluorescence or color of apoptotic cells was produced by dUTP that had been tagged with a chemical entity. In the tumor sections, there were considerably more apoptotic bodies (indicated by a bright green fluorescence) following OXPt@Ch/VES Ms treatment compared to other treatment groups, whereas in kidney sections, decreased green fluorescence intensity was seen in OXPt@Ch/VES Ms treatment group compared to free OXPt and untreated group, indicating less nephrotoxicity in OXPt@Ch/VES Ms treatment group **(Fig. 2.14A, E).**

2.3.5.2 ROS Production in Tumor Tissues

Chemotherapeutics can induce apoptosis and cancer cell arrest by increasing intracellular ROS. The release of cytochrome C due to increased mitochondrial oxidative stress leads to caspase activation and ultimately apoptosis and cell death. The DCFH-DA dye diffuses into the cell and is deacetylated to a non-fluorescent molecule by cellular esterases before being oxidized to the highly fluorescent 2', 7'- dichlorofluorescein (DCF) (Figueroa et al., 2018)**.** As a result, the treated tumor-bearing mice were tested for ROS generation using Dichloro-dihydro-fluorescein diacetate (DCFH-DA) as a probe. After 30 minutes of DCFH-DA injection, the treated mice were sacrificed, and the tumor sections were examined under fluorescence microscopy, which demonstrated a substantial increase in green fluorescence in OXPt@Ch/VES Ms compared to free OXPt. Thus, the inclusion of VES in OXPt in OXPt@Ch/VES Ms as the core-forming moiety caused more significant ROS generation (**Fig. 2.14B)**. As previously reported, VES induced apoptosis in various cancer cell lines (Muddineti et al., 2017).

2.3.5.3 Immuno-histochemical analysis of Ki67

Ki-67 is a highly effective biological marker for determining proliferation. Ki-67 protein was found in all active phases of the cell cycle but was not found in the resting phase. Immunohistochemical analysis was used to investigate the rise in Ki-67 cellular content. The tumor sections were treated with a Ki-67 antibody, followed by Alexa Fluor® 488 secondary antibody, and green signals were seen using a fluorescence microscope. As shown in **Fig. 2.14C**, the control tumor area had the greenest fluorescence, indicating the most growth. Tumor sections from mice treated with OXPt@Ch/VES Ms had fewer green signals, indicating decreased cell proliferation than the control group. Ki-67 labeling revealed the following expression in various treated tumors: Saline (control) > free OXPt > OXPt@Ch/VES Ms; a similar trend was seen with tumor volume reduction.

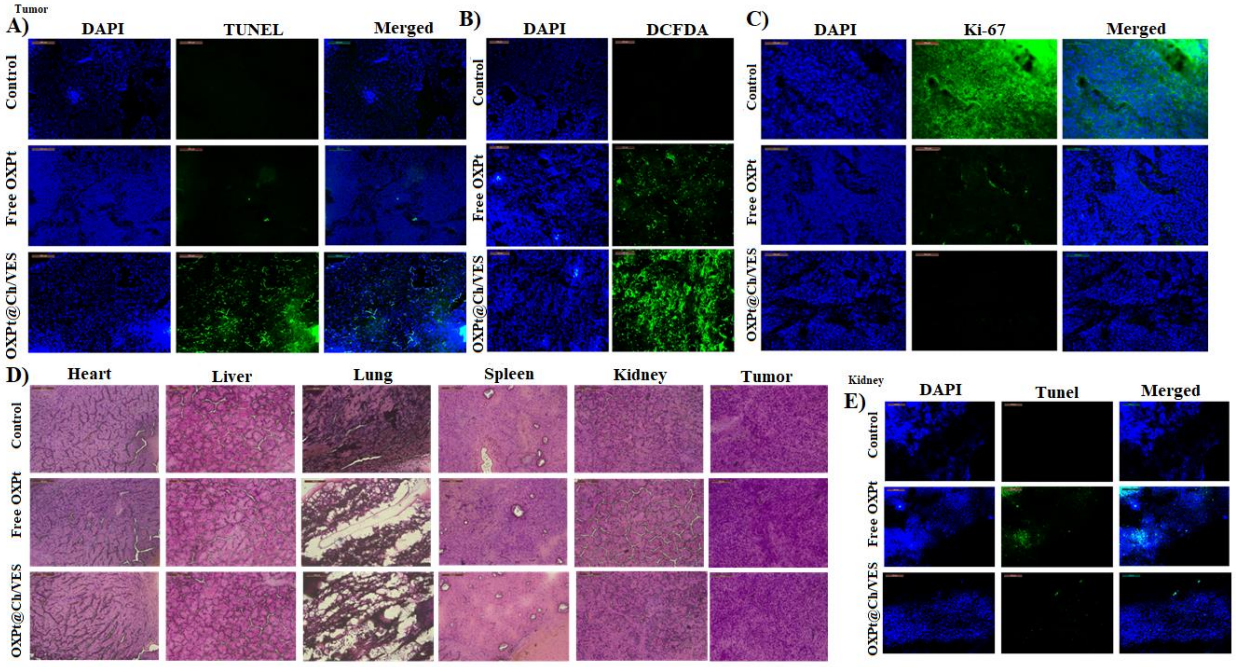

Figure 2.14 Detection of apoptosis by TUNEL assay in tumor and Kidney cryosections visualized by a fluorescence microscope. Magnification, 20X (A, E); study on the generation of ROS in 4T1-LUC tumor-bearing mice using the fluorescence probe, DCFH-DA (B); histological analysis of tumors from different treatment groups immunostained with KI67 (C): histopathological analysis of frozen mice organ sections (6 µm) using haematoxylin and eosin (nucleus: purple, and cytoplasm: pink) (D). Scale bar. 100 µm. The data represented as mean ± SD.

2.4. Conclusion

A novel Ch self-assembled nanomicellar system using VES as the hydrophobic core and Ch as the hydrophilic shell was developed for drug delivery by conjugating four molecules of Vitamin E succinate and entrapping OXPt. The system was physiochemically studied and revealed several intriguing characteristics, including size, zeta potential, encapsulation efficiency, high drug loading, and drug-release profile. The anticancer effect was proven in MCF-7, MDA-MB-231 (S), and MDA-MB-231 (R). The ability of OXPt@Ch/VES Ms to suppress the tumor progression was judged using 4T1 Luc-tumor-bearing mice. The

OXPt@Ch/VES Ms were stable, biocompatible, and released the loaded drug in a sustained manner. The micelles were taken up by tumor cells in the *in vitro* cell-based studies, demonstrating a better cell-killing impact than the free drug. The highest tumor volume suppression in tumor-bearing mice has been observed for the OXPt@Ch/VES Ms. The immune histopathological analysis indicated that the OXPt@Ch/VES Ms therapy caused significantly higher apoptosis induction than free OXPt treatment. These findings indicated that the Ch(15 KDa)-$(VES)_4$ supramolecular micellar nanoaggregates have great potential as nanocarriers for anticancer drug delivery with the ability to reverse the drug resistance. Therefore, the developed OXPt@Ch/VES Ms could be an effective treatment modality for breast cancer.

2.5 Acknowledgment

Prof. Swati Biswas acknowledges the Department of Science and Technology-Science and Engineering Research Board (DST-SERB) for providing research support through the core research grant (CRG/2018/001065). Mr. Asif Mohd Itoo is thankful to the BITS-Pilani Hyderabad campus and Lady Tata Memorial Trust for providing fellowship. The authors sincerely acknowledge the DST FIST [SR/FST/LS-II/2018/210] for the *in vivo* real-time optical imaging facility

Chapter 3

Polymeric Graphene Oxide Nanoparticles Loaded with Doxorubicin for combined Photothermal and Chemotherapy in Triple Negative Breast Cancer

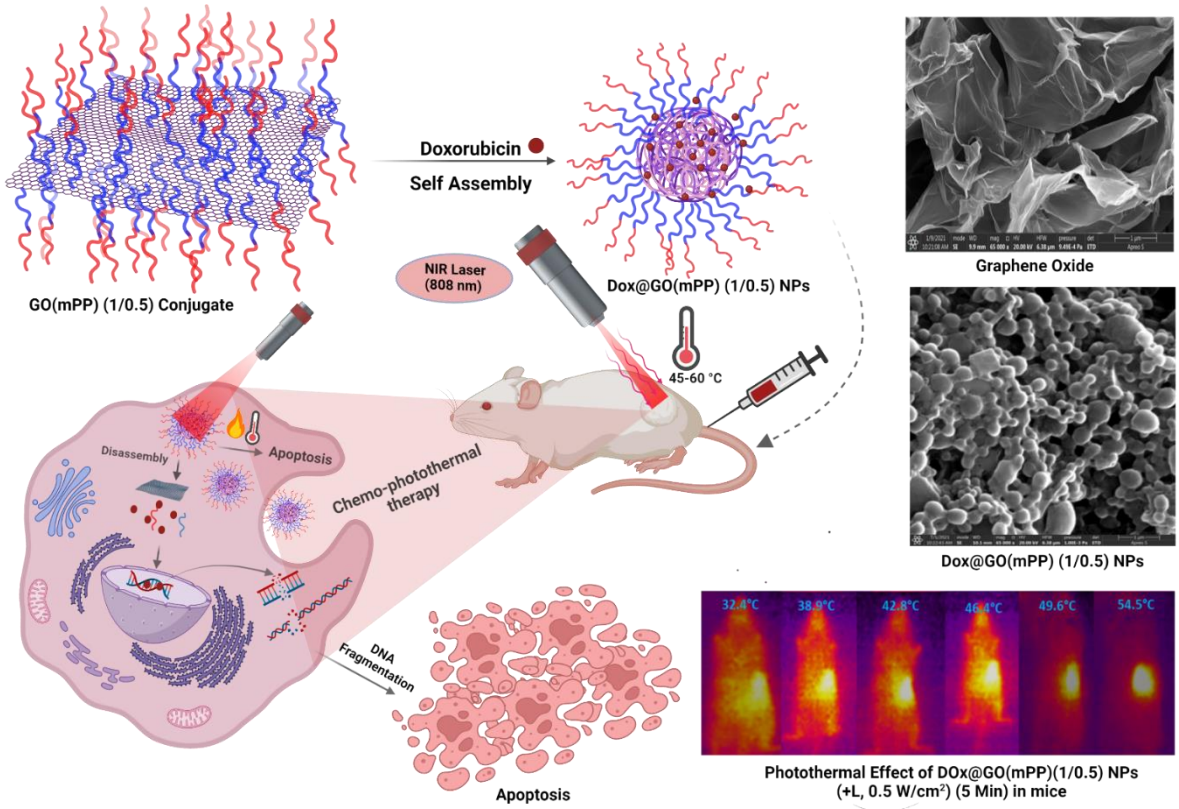

3.1 Introduction

Cancer is one of the most concerning diseases, especially in nations with a high standard of living. Nearly 8 million people die each year from cancer, contributing significantly to the global burden of morbidity and mortality associated with cancer (Itoo, Paul, Padaga, et al., 2022; Parmanik et al., 2022; Paul et al., 2022a). Breast cancer is the second most common malignancy to cause mortality among women in the US (Watkins, 2019). Triple Negative Breast Cancer, TNBC, a particularly aggressive and invasive kind of breast cancer, is distinguished by the absence of overexpression of the human epidermal growth factor receptor 2 (HER2), and lack of expression of the progesterone receptor (PR), and estrogen receptor (ER) (Bianchini et al., 2017; Foulkes et al., 2010). It is a heterogeneous group of tumors with varying histology, molecular peculiarities, and therapeutic responses, presenting a significant clinical challenge because of its high malignancy and dismal prognosis (Johnson et al., 2013). Currently, the only clinically proven therapy for TNBC is chemotherapy. However, it has several drawbacks, including substantial damage to normal tissues, limited tumor tissue accumulation, poor selectivity, and drug resistance (Waks & Winer, 2019). Photothermal therapy (PTT) has gained attention as an emerging treatment strategy due to its spatiotemporal specificity, synergistic effect, and minimum invasiveness. When exposed to an external light stimulus, it causes irreparable destruction. It actively encourages the thermal extirpation of cancer cells locally by converting light energy into heat using photothermal conversion agents (Rajani et al., 2020; Zou et al., 2016). PTT is less damaging and has fewer negative effects on healthy tissues than chemotherapy since it is safe, non-invasive, and better regulated. It offers advantages over other therapies by sparing healthy tissues through precise targeting and localized heat delivery. PTT can be performed non-invasively, reducing the need for surgery

and associated complications and minimizing systemic side effects and toxicity. Additionally, PTT can be repeated without accumulating long-term damage, making it suitable for recurring tumors or chronic conditions. Moreover, investigations have demonstrated that PTT is far more effective than chemotherapy for treating superficial lesions, such as those found in breast cancer (J. Liu et al., 2020; Miao et al., 2013; Rajani et al., 2020; Z. Xu et al., 2014). Recently, a wide variety of nanomaterials with excellent photothermal conversion and therapeutic efficacy have been designed for the unique features of PTT. Therefore, selecting a top-notch photothermal agent is crucial for the effective therapy of cancer.

Graphene oxide (GO) is recently being investigated extensively as a potential photothermal agent for drug delivery in cancer for its endocytosis, large specific surface area, good biocompatibility, and other functional biomolecules (S.-Y. Lee et al., 2022; Y.-J. Lu et al., 2014; Luo et al., 2020; B. Ma et al., 2021; Mohd et al., 2022a; J.-J. Shi et al., 2022; Q. Wu et al., 2016; X. Zhu et al., 2023). GO has a substantially larger loading capacity than conventional drug carriers, enabling the loading of numerous drugs onto the GO surface through π–π stacking interactions, hydrogen bonding, electrostatic attraction, van der Waals forces (Goenka et al., 2014; J. Liu et al., 2013; K. Yang et al., 2013)**,** and efficiently improves drug transport into cells (D. Chen et al., 2012; Di Santo et al., 2019). More crucially, GO is one of the prospective nanoscale materials capable of heating up to a high temperature and inducing hyperthermia, which would eventually cause cancer cells to be destroyed thermally (Chang et al., 2016; W. Jiang et al., 2018; Shao et al., 2017). As demonstrated earlier, the bloodstream rapidly removed carrier systems with high negative or positive charges (Aoki et al., 1997; Yamamoto et al., 2001). However, it's worth noting that the previously described GO surface has a strong negative charge, limiting its potential as a drug delivery carrier (dos Santos et al., 2018; B. Wang et al., 2018). As a result, adding cationic drugs or targeting ligands to the surface of GO enhances its tumor penetration, surface potential, and cellular uptake. It suits multimodal

synergistic therapeutic applications and specific targeted drug delivery (Iyer et al., 2006). Although GO may be evenly distributed in water, it immediately forms clumps when exposed to electrolyte solutions such as buffered saline (Z. Liu et al., 2008a). To overcome the agglomeration problem, polyethylene glycol (PEG) molecules have been covalently bound to GO (Z. Liu et al., 2008a; Miao et al., 2013)**;** alternatively, amphiphilic PEG copolymers may be physically attached to GO (Zu & Han, 2009). The GO dispersions in aqueous environments are sterically stabilized by the flexible, hydrophilic PEG chains.

Doxorubicin (Dox) is one of the chemotherapeutic drugs that is now employed most often in clinical applications due to its high antitumor effectiveness against a variety of solid tumors (T. Feng et al., 2014). Dox was therefore chosen as the model drug. However, clinical use of Dox has been severely constrained due to the widespread distribution of Dox throughout the body and potential side effects to normal cells, including multidrug resistance, nephrotoxicity, myelosuppression, and dose-dependent cardiotoxicity (J. Liu et al., 2016). Therefore, it was urgently necessary to build an appropriate drug delivery system for the release of Dox.

Herein, the present work developed a novel 2D carbon nanomaterial graphene-based multifunctional nanoplatform that converted to 3D colloidal spherical structures upon functionalization with an amphiphilic block copolymer, methoxy-poly(ethylene glycol)-poly-(lactide) (mPP). The FDA-approved copolymer mPEG-PLA was chosen due to it is biodegradability and biocompatibility (Hrkach et al., 2012; K. S. Lee et al., 2008). The GO was successfully prepared by a modified Hummers method and then conjugated with mPEG-PLA to form GO/mPEG-PLA copolymer (GO(mPP)). The capacity of the GO(mPP) copolymer to load the chemotherapeutic drug Dox through hydrophobic, electrostatic attractions, and/or π–π stacking interactions was excellent. The polymeric GO NPs combine chemo and photothermal therapies as an effective therapeutic strategy for TNBC. Overall, the novelty of our work lies in developing a graphene oxide-based polymeric self-assembled nanoplatform that combines

chemo- and photothermal therapy by physically encapsulating Dox. The NPs were thoroughly characterized physicochemically, and their therapeutic efficacy was evaluated in the *in vitro* and *in vivo* assay systems using metastatic TNBC models.

3.2. Materials and methods

3.2.1 Materials

Graphite, dimethyl aminopyridine, Stannous octoate, methoxy polyethylene glycol, N, 4′, 6-Diamidino-2-phenylindole dihydrochloride (DAPI), Propidium iodide (PI), DL-Lactide, dimethyl sulfoxide (DMSO), paraformaldehyde, N,N'dicyclohexyl carbodiimide, Acridine orange (AO), and Tetrahydrofuran (THF), were received from Sigma-Aldrich (Bangalore, India). Dialysis membrane was sourced from Spectrum Laboratories, Inc. (the USA). GSure® DNA genomic isolation kit was provided by GCC Biotech Pvt. Ltd. (India). Himedia Labs (India) provided Trypan blue solution, Methylthiazolyldiphenyl-tetrazolium bromide (MTT), and Fluoromount-G. R&D systems (Minneapolis, USA) provided the TACS® Annexin V-FITC Apoptosis Detection Kit and utilized without further purification. Doxorubicin HCl was received from Sun Pharma Ltd. (India) as a free sample.

Cell lines:- Mouse mammary gland luciferase-expressing adenocarcinoma cells (4T1-Luc), Human breast adenocarcinoma cells (MDA-MB-231), and Mouse mammary gland adenocarcinoma cells (4T1) cells were sourced from the American Type Culture Collection (ATCC, USA), and National Centre for Cell Science (NCCS, Pune, India). Fetal bovine serum (FBS), Trypsin-EDTA, Minimum Essential Medium Eagle (MEM), Dulbecco's Modified Eagle Medium (DMEM), Streptomycin, and Penicillin were provided by Himedia Labs (India).

Animals:- The Sainath Agency, and National Centre for Laboratory Animal Sciences at the National Institute of Nutrition in Hyderabad, India provided male Wistar rats, and BALB/c mice (Female, 17−21 g, 5-8-week-old) employed in hemolysis experiment, pK and anticancer

studies. The Institutional Animal Ethics Committee (IAEC) at BITS-Pilani in Hyderabad approved the study and allowed it to be executed. The rodents were kept in standard rat/mouse cages (five per cage) with a 12-h light/dark cycle, unrestricted access to water and food, and a temperature and humidity range of 23-24 °C and 50-60 % RH.

3.2.2 Methods

3.2.2.1 Synthesis of Graphene oxide

Graphene oxide was synthesized using a modified version of Hummer's process (SreeHarsha et al., 2019). In this procedure, graphite flakes (1g) were treated with 46 mL of concentrated H_2SO_4. Next, 1 g of sodium nitrate was added to this reaction mixture and agitated for 30 minutes, and the reaction condition was regulated using an ice bath. In order to halt the process, 6 grams of potassium permanganate ($KMnO_4$) were added. After that, the $KMnO_4$-containing reaction mixture was placed in a water bath at 35 °C and agitated for 1 h at 400 rpm. Following that, 92 mL of distilled water was gently poured into the mixture while the temperature was maintained below 100 °C with the use of an ice bath. Next, the flask was heated to 100 °C in an oil bath., where the reaction was kept for 15 min. A bright yellow dispersion was obtained by treating the mixture with 5 mL of 30% H_2O_2 solution and 150 mL of distilled water. The synthesis of GO is shown by the color shift from black to brilliant yellow. Finally, GO was rinsed with deionized water until the supernatant had a neutral pH indicating that acid traces had been removed, and the solution was lyophilized for future studies.

3.2.2.2 Synthesis of mPEG-PLA di-block copolymer

As described earlier, the ring-opening polymerization reaction was carried out to synthesize mPEG-PLA di-block copolymers (Kumbham et al., 2020). In a dry polymerization tube, 0.4 g of pure D, L-Lactide (144.13 Da), and 1 g of mPEG (5000 Da) were introduced. The reaction mixture included stannous octoate (0.008% w/w) in toluene as a catalyst. The reactants were

heated for a short period until they became liquid. The tube was hermetically sealed with a vacuum, and the copolymerization was carried out at a temperature of 160 °C for 6 h. Next, The copolymer was digested in THF and separated with cold diethyl ether. The precipitate was allowed to dry, dispersed in deionized water, dialyzed on a semipermeable acetate cellulose dialysis bag (MWCO. 3.5 KDa) and freeze-dried.

3.2.2.3 Synthesis and characterization of GO(mPP) Conjugate

The GO(mPP) conjugate was synthesized by the esterification reaction. In this reaction, GO reacted with mPEG-PLA in three different ratios (1/0.5, 1/1, and 1/2) under DCC and DMAP in DMF at room temperature for 24 h. The reaction mixture underwent evaporation, dialysis, rehydration with deionized water, and freeze-dried.

The Fourier transform infrared (FTIR) spectroscopic analysis of GO, mPEG-PLA, and GO(mPP) conjugate were investigated employing the potassium bromide (KBR) pellet technique (Itoo, Paul, Ghosh, et al., 2022), and the FTIR (Jasco-4200, USA) spectrophotometer was used to collect the spectra across a broad IR range of 400 to 4000 cm^{-1}. The gel permeation chromatographic (GPC) method was used to assess the conjugation efficiency mPEG-PLA conjugate. In the GPC system, refractive index detector is employed, specimens were eluted using an Ultra-hydrogel^{TM} linear exclusion column that was 7.8 mm x 300 mm in size. Water was used as the mobile phase operated at a flow rate of 1 mL/min. The chemical structure of the mPEG-PLA (D_2O) solution was characterized using ^{1}H-NMR spectroscopy (Bruker spectrometer-300 MHz, Bruker, USA, at ambient temperature. Thermogravimetric analysis (TGA) was performed in a nitrogen environment using a thermogravimetric analyzer (Shimadzu, Japan) at 10 °C/min from 50 to 800 °C.

3.2.3 Preparation and characterization of Dox@GO(mPP) NPs

3.2.3.1 Preparation of Dox@GO(mPP) NPs

To induce loading, Doxorubicin (Dox) was incubated in GO(mPP) for 24 h. In a nutshell, 10 mg of the GO(mPP) nanocarrier was dispersed in 10 mL of distilled water, ultra-probe sonicated (Ultrasonic Processor 500 Watt, 20 kHz, 35 A) for 3 h. The hydrodynamic diameter and PDI were measured after being centrifuged for 10 minutes at 3000 rpm. Next, Dox (1 mg/mL) was mixed with the GO(mPP) dispersion solution and stirred continuously for 12 h at ambient temperature. The unbound Dox was eliminated from the solution by dialyzing against deionized water for 24 h. Further, centrifugation was performed on the solution at 3000 rpm for 5 min. The pellet was collected and resuspended in PBS to get the Dox@GO(mPP) NPs.

3.2.3.2 Physico-chemical characterization of Dox@GO(mPP) NPs

A dynamic light scattering approach was used to investigate the zeta Potential (ζ), size distribution, and particle size at 25 °C utilizing a Nano ZS 90 from Malvern Instruments Ltd,. United Kingdom. Before particle size measurement, Dox@GO(mPP) NPs were mixed with double distilled or Milli-Q water to reduce opalescence for better measurement. The examination was performed three times, and the polydispersity index was calculated based on the width of the size distribution (PDI). PDI is a metric that measures the average homogeneity of a particle solution. The amount of Dox in Dox@GO(mPP) NPs was quantified by using a UV-visible spectrophotometer (Jasco UV-670, Japan) set to wavelength 480 nm. The surface topography of graphite, GO, Dox@GO(mPP) NPs was assessed by the Field Emission Scanning Electron Microscope (Apreo Lo Vac, FEI, USA). After being lyophilized, the NPs were mounted on carbon tape, and a gold-palladium alloy was used to sputter them for 30 minutes at a thickness of 10 mm. At an accelerating voltage of 20 kV, the photographs were taken at a resolution of 500 nm. A further investigation of the GO sample morphology was

carried out using an atomic force microscope (AFM) (Seiko Instrument, Japan). The specimens were laid out on a copper grid wrapped with a porous carbon sheet and a silicon wafer that had been coated, both of which had been processed in a vacuum at 45 °C. In order to conduct stability tests, the Dox@GO(mPP) NPs were kept both at room temperature and 4 °C. The Dox@GO(mPP) NPs samples were tested for % drug loading content, and particle size at specified time intervals for 30 days. Using a UV-vis spectrometer (Jasco UV-670, Japan) set to ambient temperature, the effectiveness of stimulated release pattern, drug loading, and drug encapsulation of Dox@GO(mPP) NPs were examined. The formulas below were used to determine the drug loading DL (%), and entrapment efficiency EE (%) of Dox@GO(mPP) NPs:

$$\text{EE (\%)} = \frac{Weight\ of\ Dox\ present\ in\ NPs}{Weight\ of\ Dox\ added\ initially} \times 100 \qquad \textit{Equation 3.1}$$

$$\text{DL (\%)} = \frac{Weight\ of\ Dox\ present\ in\ the\ NPs}{Weight\ of\ the\ \text{Dox@GO(mPP) NPs.}} \times 100 \qquad \textit{Equation 3.2}$$

3.2.3.3 Kinetic stability analysis

An experiment was conducted to study the kinetic stability of Dox within Dox@GO(mPP) NPs for 21 days by using a UV–VIS–NIR Spectrophotometry technique. Both Dox@GO(mPP) NPs and free Dox were dissolved in either methanol or distilled water at a constant concentration of 5 µg/mL. The absorbance spectra of Dox were then measured by scanning the solutions with a UV–visible spectrophotometer (Jasco UV-670, Japan).

3.2.3.4 Differential scanning calorimetry (DSC) and thermogravimetric analysis (TGA)

A DSC calorimeter (DSC 60, Shimadzu, Japan) and thermogravimetric analyzer were employed to conduct DSC/TGA on powder samples of graphite, GO, GO(mPP), and Dox@GO(mPP) NPs. DSC/TGA analyses were performed between 60 to 500 °C at a heating

rate of 10 °C/min under a dynamic nitrogen environment. The weights of the powder samples were maintained the same (5–10 mg) in all measurements for effective comparison.

3.2.3.5 XRD analysis

The X-ray diffraction (XRD) examination of graphite, GO, GO(mPP), and Dox@GO(mPP) NPs were done using Cu Kα radiations on a piece of ULTIMA-IV Rigaku equipment (Japan) at a voltage of 40 kV and a current of 200 mA. The finely powdered materials refraction data were recorded for 2θ angles ranging from 3 to 55°.

3.2.3.6 X-ray photoelectron spectroscopy (XPS) analysis

The chemical composition of Graphite, GO, GO(mPP), and Dox@GO(mPP) NPs were examined using an XPS instrument (Thermo-Fisher, USA). Avantage software was used to evaluate the collected XPS data. The C1s peak of adventitious carbon at 284.8 eV was used as a standard to calibrate the binding energy values of XPS lines.

3.2.3.7 Photothermal heating effect.

The photothermal heating effect of GO, GO(mPP), and Dox@GO(mPP) NPs were examined by exposing the aqueous dispersions of the given solutions to NIR laser-808 nm (MR.FCL.808.T2.2W.MM-OEM, Shanghai MRTRADE International Co., LTD.) radiations in sample cells for 5 min at a power density of 0.25 W/cm^2. Dox@GO(mPP) NPs were also examined using different concentrations and laser power densities (0.25, 0.5, 1.0, and 2.0 W/cm^2) to analyze the effects of concentrations and various laser power densities on photothermal heating and the real-time temperature. Infrared thermal images of the solution were captured using an IR camera at 10 s intervals. The experiment was repeated three times.

3.2.3.8 *In vitro* drug release study

The NIR laser and pH dual-responsive release behavior of Dox from Dox@GO(mPP) NPs was examined under various pH conditions (pH 7.4, 6.8, and 5) using the dialysis technique (L.

Guo et al., 2016; Patel et al., 2023; Paul et al., 2023). Briefly, 2 mL of Dox@GO(mPP) NPs were poured into a cellulose acetate dialysis bag and submerged in PBS (100 mL) with magnetic stirring at 60 rpm (37 °C) and exposed to 808 nm laser irradiation at a power density of 0.25 W/cm^2 for 5 min. The released buffer in the tube was changed with new PBS (1 mL) at predefined intervals of time after every 1 h to maintain sink conditions. The released Dox content was estimated using the UV-vis spectrometer at 480 nm. The collected data were fitted into various mathematical models like the Weibull model, Korsmeyer-Peppas, Higuchi kinetics models, Hixson Crowell, first order, and zero-order kinetic model to examine the release mechanism of Dox from Dox@GO(mPP) NPs. The experiments were carried out in three repetitions, with the findings being reported as an average of the acquired results (Mean S.D; n=3).

3.2.3.9 Hemolysis study

A hemolysis test based on red blood cells (RBCs) was used to explore the effectiveness and biocompatibility of the GO and GO(mPP) conjugate for use *in vivo*. In brief, Wistar rat blood stabilized with EDTA was collected in heparinized tubes. Then, centrifugation at 3500 g for 10 min (4 °C) was used to separate the serum from the blood, and the RBCs were then rinsed five times in a sterile isotonic NaCl solution. Following the final wash, the cells were diluted to 1/10 of their original volume in sterile isotonic PBS solution and made to 5 % v/v suspension (Itoo, Paul, Ghosh, et al., 2022). The diluted RBS suspension was mixed with Triton-X 100 (1% solution) as a positive (+) control, 0.9 % w/v NaCl solution as a negative (-) control, and GO(mPP) conjugate at concentrations ranging from 0.0125- 0.2 mg/mL, respectively. After that, the mixtures were vortexed and allowed to rest for 2 h at ambient temperature. After that, all the mixtures were centrifuged for 5 min at 2500 rpm, and the absorbance of the uppermost supernatants was recorded using a UV-vis spectrometer at 540 nm. Herein, the hemolytic ratio (HR) was calculated as follows:

Hemolysis (%) = $\frac{Ab_{Sample} - Ab_{(-)Control}}{Ab_{(+)Control} - Ab_{(-)Control}}$X100 ***Equation 3.3***

The data are represented as the mean ± the standard deviation (SD), and the measurement was repeated in triplicate for each of the samples.

3.2.3.10 Cyclic voltammetry

A microcomputer-based electrochemical analyzer was used to conduct the studies. First, deionized water was used to disseminate GO, free Dox, Dox@GO NPs, and Dox@GO(mPP) NPs. The concentrations of GO and Dox were kept the same in Dox@GO NPs, and Dox@GO(mPP) NP solutions, respectively. The solution was then deposited onto a glassy carbon (GC) electrode with a diameter of 4 mm. The electrochemical tests were performed in phosphate buffer pH 7.4 (50 mM) using a reference electrode of Ag/AgCl and a counter electrode of platinum (X. Yang et al., 2008).

3.2.4 Cell culture studies

3.2.4.1 *In vitro* cell cytotoxicity assay

MDA-MB-231 and 4T1 cells were selected for the cytotoxicity experiment. The cells were cultured in 96-well plates for 24 h at a concentration of 10000 cells/well to facilitate cell adhesion. Then, the GO, GO(mPP), free Dox, and Dox@GO(mPP) (1/0.5) NPs were administered to the cells at various doses of 3.125-100 µg/mL for 24 h and 48 h. After 12 h of treatment, the cells in the 96-well plate were irradiated with 808 nm NIR laser radiation (±L, 0.25 W/cm^2) from 0 to 300 seconds and then left for 12, 36 h incubation. After incubation, the media was removed from the cells, and the cells were subjected to 50 µL of MTT in DMEM for an additional 4 h in the darkness. Next, the MTT solution was taken out and each well was supplied with 150 µL of DMSO to solubilize the formazan crystals. The absorbance of these specimens was recorded at a wavelength of 570 nm using a SpectramaxTM multiplate

reader (Molecular Devices, US). Additionally, varied irradiation durations (0–10 min) and power densities (0.25-2 W/cm^2) were examined for their *in vitro* cytotoxic effects on MDA-MB-231 and 4T1 cells. The following formula was used for quantification (Ch et al., 2023):

$$(\%)\ \text{Cell viability} = \frac{Abs_{Sample}}{Abs_{Control}} \text{X } 100 \qquad \textit{Equation 3.4}$$

Graph pad Prism 9.0.2 software was used to calculate the half-maximal dosage (IC-50). The outcomes of each test were averaged after being performed in triplicate.

3.2.4.2 Cellular uptake studies

The way in which the cells of MDA-MBA-231 and 4T1 take in both Free Dox and Dox@GO(mPP) (1/0.5) NPs was evaluated quantitatively and qualitatively using a flow cytometer and a confocal microscope. In brief, 50,000 cells of MDA-MBA-231 and 4T1 were grown in 12-well plates and incubated overnight at 37°C. Afterwards, the media was replaced with new media containing Dox and Dox@GO(mPP) (1/0.5) NPs at a Dox concentration of 6 µg/mL for 1-4 h. The cells were then exposed to an 808 nm laser (0.25 W/cm2) for five minutes, and then incubated at 37 °C for different periods of time, before being evaluated by a flow cytometer (BD FACS Area III) (10,000 gated cells). The cells were also observed qualitatively using a confocal microscope to observe internalization of the cells at 1 and 4 h. After discarding the media, washed the cells with cold PBS, fixed for 15 min at ambient temperature with 4 % paraformaldehyde, and labeled with DAPI. After that, rinsed the cells with PBS and monitored using a fluorescence microscope (Leica, Germany), following Dox_{ex} 480 nm and Dox_{em} 590 nm.

3.2.4.3 Annexin V assay

The TACS® Annexin V-FITC Apoptosis Detection Kit was employed to determine apoptosis caused by Free Dox and Dox@GO(mPP) (1/0.5) NPs in MDA-MBA-231 and 4T1 cells. In

brief, the cultured cells maintained on the incubator in a 12-well cell culture plates were treated with free Dox and Dox@GO(mPP) (1/0.5) NPs for a period of 12 h at a constant Dox concentration of 6 µg/mL before being exposed to an 808 nm NIR laser for 5 minutes at a power density of 0.25 W/cm^2. After that, the cells were washed carefully with PBS buffer, trypsinized, and reconstituted in 1X binding buffer. After that, Annexin V-FITC conjugate was introduced to each of the cell suspensions, and they were incubated at ambient temperature for 10 min while being protected from light. The cells were then treated for 5 min with propidium iodide (PI) solution at a concentration of 1 µg/mL (Ghamkhari et al., 2021; Kumbham et al., 2020). Thereafter, the samples were examined employing a BD FACS Area III flow cytometer. Apoptotic cells were found to be stained solely with the Annexin V-FITC conjugate when a gated cell population was used to determine the percentage of apoptotic cells.

3.2.4.5 Cell cycle analysis

The percentage of cells in the S, G0/G1, and G2/M phases of the cell cycle following DNA-specific labeling can be determined by performing cell-cycle analysis employing flow cytometry. Propidium iodide (PI) dye was used to examine the cell cycle. The analysis depends on the capacity of PI to stoichiometrically label cellular DNA. The level of staining determines the quantity of DNA in the cell (Itoo, Paul, Ghosh, et al., 2022). MDA-MB-231 and 4T1 cells were grown and maintained in 12 well plates as previously described, with free Dox and Dox@GO(mPP) (1/0.5) NPs with or without 808 nm NIR laser radiations and incubation for 12 h prior to analysis at fixed Dox concentration. The cells were trypsinized, centrifuged (1200 rpm for 5 min), rinsed with 1X PBS, and recentrifuged following proper incubation. After that, chilled ethanol was used to induce a fixation of the cellular specimens and kept for 3 h at a temperature of -20 °C before being centrifuged at 2500 rpm and rinsed with 1X PBS. Next, each sample was treated with RNase (50 µL) and left to stand for 15 min. It was then provided with 50 µL of PI (stock: 1 mM) and kept in the dark for an additional 20 minutes. The

experiment was carried out on a flow cytometer system (BD Biosciences, USA) using suitable compensation and threshold settings and analyzed using FCS Express 7 Flow cytometry software.

3.2.4.6 Reactive oxygen species (ROS) assay

The redox-sensitive fluorogenic probe 2′,7′-dichlorodihydrofluorescein diacetate (DCF-DA) was employed to assess ROS generated in 4T1 and MDA-MB-231 cells after treatment with Dox@GO(mPP) (1/0.5) NPs and free Dox, and subjected to 808 nm NIR laser radiations (±L) for 5 min. The non-fluorogenic probe DCF-DA is transformed into the highly fluorescent 2′,7′-dichlorofluorescein (DCF) via intracellular esterases and oxidation (Kumbham et al., 2022). The MDA-MB-231 and 4T1cells were seeded, cultured in 12-well plates, and administered independently with free Dox and Dox@GO(mPP) (1/0.5) NPs at IC-50 concentrations for 24 h. After treatment, cells were rinsed with PBS, incubated with DCF-DA dye at 37 °C for 30 min, labeled with DAPI, and images were captured using a fluorescence microscope (Leica, Germany) in the green channels at excitation (492-495 nm) and emission wavelength of 517-527 nm).

3.2.4.7 Mitochondrial membrane potential (MMP) Study

The cell stress and early apoptosis are indicated by a disturbance in the MMP (ΔΨm). In a potential-dependent way, the JC-1 dye is capable of forming reversible clusters in the mitochondrial membrane. JC-1 is responsible for the production of the j-monomer at a low ΔΨm which emits green fluorescence at 530 nm within the cytosol. At higher ΔΨm potentials, it causes the formation of the j-aggregate complex, which emits a red luminous light in the mitochondrial membrane. The degree of mitochondrial membrane depolarization is proportional to the green-to-red fluorescence emission ratio. Early apoptotic cells have a disturbed ΔΨm, so JC-1 dye may well be employed as an early apoptotic marker (Mallick et

al., 2019). Cultured MDA-MB-231 and 4T1 cells were administered independently with free Dox and Dox@GO(mPP) (1/0.5) NPs at IC-50 concentrations and subjected to 808 nm NIR laser radiation (0.25 W/cm^2) for 5 min. After 24 h, the cells were trypsinized, centrifuged, washed with PBS, and stained with JC1-dye (1 L/mL) for 15 min. For quantitative analysis, the examination was performed employing a flow cytometer (BD FACS Area III) at excitation (485 nm) and emission wavelength of 590 nm with proper compensation and threshold. A fluorescence microscope (Leica, Germany) was used to take the photographs for qualitative analysis.

3.2.4.8 Nuclear staining assay

DAPI staining was employed to assess nuclear morphological alterations (fragmented nuclei and condensed chromatin) in free Dox and Dox@GO(mPP) (1/0.5) NPs treated 4T1 and MDA-MB-231 cells with or without exposure to 808 nm NIR laser radiations. DAPI dyes both live and preserved cells because of their strong affinity for adenine-thymine-rich DNA regions (Kowsalya et al., 2021). 1x10^5 cultured cells of MDA-MB-231 and 4T1 in 12 well plate were introduced with free Dox and Dox@GO(mPP) (1/0.5) NPs for 24 h. Following an incubation period of 24 h, the cells were rinsed with PBS and then preserved using 4% paraformaldehyde for 20 minutes at 37 °C, and stained with DAPI (10 µL, 0.5 µg/mL) for 5 min, and acridine orange (AO) (0.1 mg/mL) for 20 min. After that, the cells were washed once more with PBS to eliminate the excess stain and visualized in the green (AO, 480-490 nm) and blue channels (DAPI, 358 nm) under a fluorescence microscope (Leica, Germany).

3.2.5 *In vivo* studies

3.2.5.1 Pharmacokinetic (pK) study

The pK analysis of free Dox, Dox@GO, and Dox@GO(mPP) (1/0.5) NPs was performed in male Wistar rats (220 ± 20 g). The animals were housed in an environment that provided them

with natural light, unfettered access to food and drink, at a RH of 55%, and a temperature of 25 °C. Prior to injection, the rats were randomly segregated into 4-groups (control, free Dox, Dox@GO, and Dox@GO(mPP) (1/0.5) NPs, n=3) and starved for 10 h but given free access to water. Each group of rats received the same quantity of Dox (5 mg/kg) via the tail vein. Subsequently, blood samples of about 0.5 mL each were withdrawn from the retro-orbital plexus at predetermined time periods into heparinized tubes. Plasma was obtained using centrifugation at 10,000 rpm for 5 min and stored at -20 °C for further examination. To determine the Dox concentration, 200 µL of frozen rat plasma was taken, put in a 1.5 mL plastic tube, and vortexed for 10 min with triple volume cold acetonitrile to separate plasma protein, followed by centrifugation. Afterward, supernatant (20 µL) was taken and examined for chromatographic analysis employing a HPLC system (Shimadzu) with a mobile phase of o-phosphoric acid/acetonitrile (pH 2.6) (75/25, v/v) and a reverse phase C18 Phenomenex column (150 nm ×4.4 nm, 5 µm) at a column oven temperature of 40 °C and eluted at a flow rate of 0.6 mL/min. The pK solver software was used to calculate the pharmacokinetic parameters, and the student's t-test was used to establish the statistically significant difference.

3.2.5.2 Determination of *in vivo* therapeutic efficacy, *in vivo* fluorescence imaging, and biodistribution analysis

The combination chemo-photothermal treatment impact of free Dox and Dox@GO(mPP) (1/0.5) NPs were examined *in vivo* in 4T1-Luc tumor-bearing mice when the tumor volume had grown to 50 mm^3. The tumor was developed by administering 100 µL of 4T1-Luc cells into the right flank of each female BALB/c mice at a concentration of 1.5 million cells under anesthetic conditions. After that, the mice were divided up into five groups, with a total of five mice in each group: control (PBS), free Dox, Dox@GO(mPP) (1/0.5)NPs (-L), Dox@GO(mPP) (1/0.5) NPs (+L, 0.25 W/cm^2), and Dox@GO(mPP) (1/0.5) NPs (+L, 0.5 W/cm^2). After drug administration (IV), the 4T1-Luc tumor-bearing mice were subjected to

808 nm NIR laser radiation (0.25 W/cm^2 and 2 W/cm^2) for 5 min at 12 h. During the laser therapy, thermal camera was employed for the collection of temperature images as well as changes in the tumor area. Tumor volume and body weight were measured every alternate day during the experiment. The tumor masses were removed and weighed independently, and in order to evaluate the survival curve, the Kaplan-Meier method was used (Martínez-García et al., 2018). After the survival study, the mice were euthanized, and lung tissue was removed from all of the different groups and imaged. The number of macroscopic metastatic nodules per lung was counted to determine the inhibitory action of nanoparticle formulations on breast cancer lung metastasis. In addition, the *in vivo* imaging system IVIS® Lumina III, PerkinElmer, USA, detected the *in vivo* tumor accumulation of free Dox and Dox@GO(mPP) (1/0.5) NPs (Yuan et al., 2018). Bioluminescence was used to monitor 4T1 development in mice after they had been administered with D-luciferin (150 mg/kg) intraperitoneally, 10–15 min before imaging. Several distinct time periods were analyzed in terms of the tumor accumulation trends (5, 10, 15, and 21 days) after injection, employing IVIS® with a 620 nm excitation filter and a 780 nm emission filter. In mice, the biodistribution of free Dox and Dox@GO(mPP) (1/0.5) NPs was studied for 36 h. The fluorescent signal of Dox were collected at 1, 3, 6, 12, 24, 36 h post injection. Following the completion of the *in vivo* imaging, the mice were killed, and their tumors as well as other primary organs (liver, heart, spleen, kidney, lung) were removed for imaging and immunohistochemistry.

3.2.6 Immunohistochemistry

3.2.6.1 TUNEL assay

The TUNEL assay was used to determine the apoptotic effect in frozen tumor sections following the manufacturer's instructions after treatment with free Dox and Dox@GO(mPP) (1/0.5) NPs with or without laser. The tumor cryo-sections of a thickness (5 µm) were obtained

using a cryotome (Leica, Germany) and placed on super frost plus slides. The cryosections of the tumor were fixed in a solution containing 4% paraformaldehyde for 10 min while they were kept at room temperature. The TUNEL test was then performed using the TUNEL detection kit on the tissue slices obtained from the tumor in accordance with the manufacturer's instructions (FragEL ^{TM} DNA Fragmentation Detection Kit, Merck, Darmstadt, Germany). Tumor slices were examined for the presence of apoptotic cells' green fluorescence and cell nuclei's blue fluorescence. The fluorescent microscope (Leica, Germany) was used to acquire and capture the images.

3.2.6.2 Immuno-histochemical analysis for hematoxylin & eosin (H&E) staining and Ki-67

H & E staining is the fundamental basis for morphological examination of preserved, processed, embedded, and sectioned tissues. Thirty-five days later, mice administered with free Dox and Dox@GO(mPP) (1/0.5) NPs were euthanized. Main organs (heart, kidney, spleen, lung, liver, and tumor) were isolated, preserved in 4% paraformaldehyde solution, and samples were subsequently fixed in paraffin for H&E staining to assess the possible organ toxicity and cancer cell apoptosis. An immuno-hist Ki67 analysis of the tumor was also performed to assess cell proliferation. The Ki-67 protein (nuclear antigen) is produced throughout the active cell cycle (M, G2, S, and G1 phases) except during the resting phase (G0). The Ki-67 protein may be utilized as a marker for cell proliferation. Following the treatment protocol, the tumor cryo-section slices were incubated with a 1:500 dilution of Ki67 (catalog #9129S) at 4 °C. The slices were then washed in PBS and treated with Alexa Fluor® 488 conjugated secondary antibody for 2 h. Finally, tissue slices were washed in PBS and viewed under a fluorescence microscope (Leica, Germany) after being covered with a coverslip.

3.2.6.3 ROS production in tumor tissues

In order to measure the level of ROS activity within the tumor, mice were given a 50 µL injection of DCFH-DA (25 µM) directly into the tumor, 24 h after receiving either free Dox or Dox@GO(mPP) NPs. Next, 30 minutes later, the mice were killed and the tumors were isolated, spliced using a cryostat (Leica Biosystems, Germany), and observed using a fluorescence microscope.

3.2.7 Statistics

The data was processed by determining the average, then using statistical methods such as one-way ANOVA and t-test through the use of Prism 8.0 software (GraphPad). Results were considered statistically significant if the p-value was less than 0.05, with significance levels denoted as *** for $p<0.001$, ** for $p<0.01$ and * for $p<0.05$.

3.3.0 Results and Discussion

3.3.1 Physiochemical characterization of Dox@GO(mPP) NPs

The novel pH and photothermal responsive 2D carbon nanomaterial-based multifunctional nanoplatform (Dox@GO(mPP) NPs) that combines photothermal and chemotherapy as an effective treatment strategy for TNBC breast cancer therapy was developed following the steps, as illustrated in **Scheme 3.1,** which comprised: synthesis of GO via modified Hummer's method followed by ultra-probe sonication of GO to obtain nano GO (35 W, 3 h). Next, mPEG-PLA was synthesized by ring-opening polymerization reaction followed by conjugation with GO via an esterification reaction between the –OH groups of mPEG-PLA and –COOH groups of GO to obtain GO(mPP) conjugate, and upon functionalization of GO with amphiphilic copolymer mPEG-PLA its form changed from 2D to 3D colloidal nanostructure because of its flexible structure. Finally, loading of Dox onto GO(mPP) conjugate through electrostatic interactions, hydrophobic interactions, or π–π stacking between Dox and GO(mPP) to prepare

Dox@GO(mPP) NPs (**Figure 3.1**). Herein, the carboxylation of graphene oxide is useful for further targeted modification and increasing GO solubility. The newly synthesized GO, mPEG-PLA copolymer, GO/mPEG-PLA conjugate was physiochemically characterized by XRD analysis, ^{1}H NMR, FTIR spectroscopy, UV absorption, GPC analysis, DSC/TGA analysis, cyclic voltammetry, and XPS analysis.

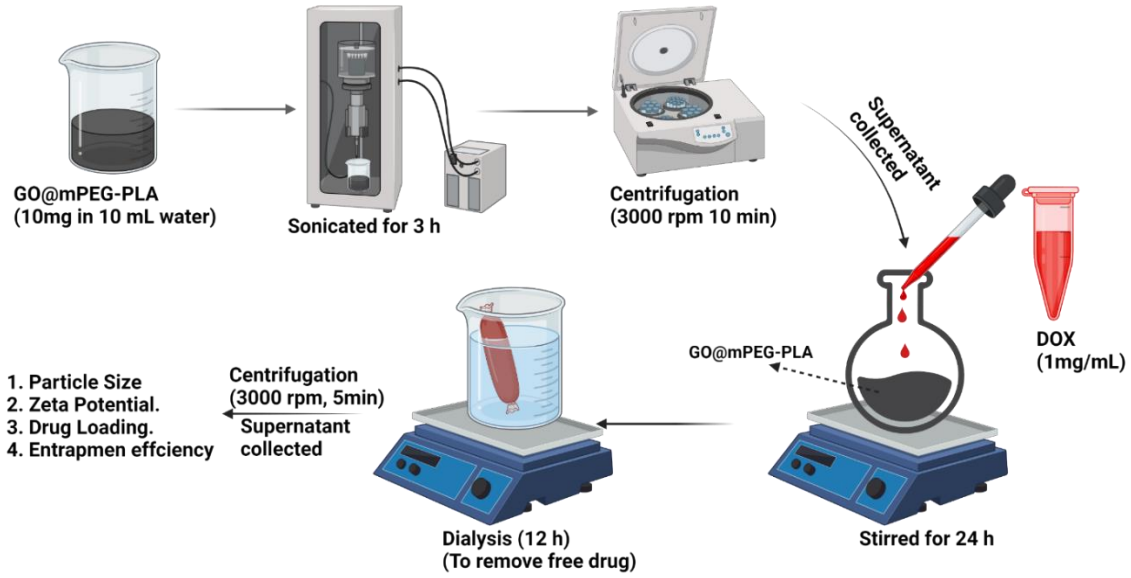

Figure 3.1 Schematic illustration for the preparation of Dox@GO(mPP) NPs.

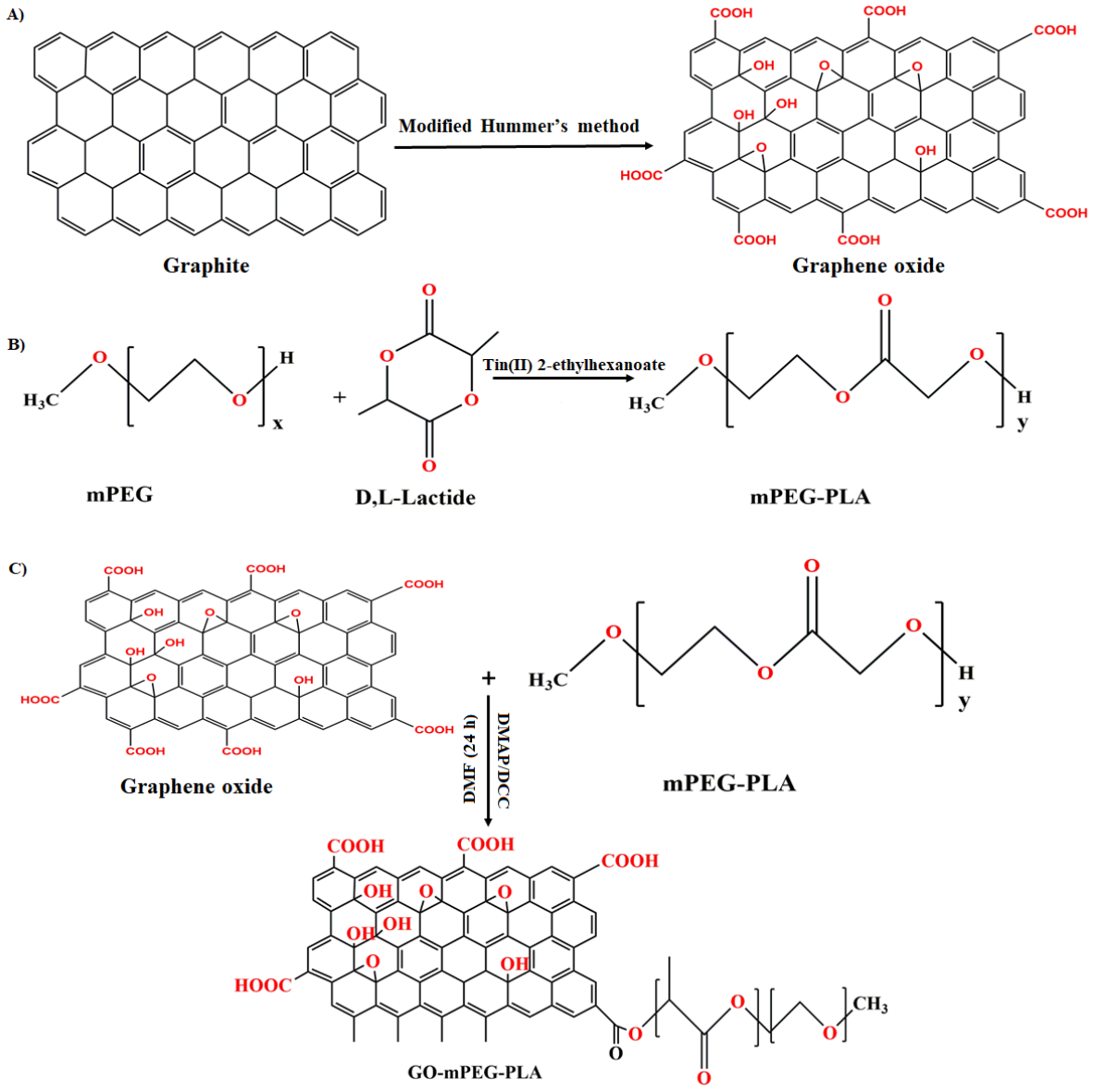

Scheme 3.1. Synthetic schematic illustration of Graphene oxide (GO) (A); mPEG-PLA (B); and GO-mPEG-PLA [GO(mPP)] conjugate (C).

3.3.1.1 XRD analysis

Figure 3.2A shows the XRD patterns of GO and graphite. Graphite in its purest form has a very high diffraction peak at 2θ=26.7, which belongs to the diffraction of the (002) plane with an interplanar distance of d_{002} = 3.34 Å. In the XRD pattern of GO obtained via modified Hummer's method, the (002) reflection of graphite vanishes after oxidation to GO, and a diffraction peak at 2θ= 11.787 is visible, corresponding to the diffraction of the 001 crystal

plane (d_{001} = 7.502 Å), which is typical for GO and indicating effective graphite oxidation and the generation of oxygen-containing groups that are distributed randomly across the graphene sheet's basal plane and edges (Z. Zhang et al., 2019). The XRD examination of free Dox displayed prominent peaks at 2θ values of 12.97, 14.79, 16.50, 18.32, 19.18, 20.46, 22.50, 23.25, 24.96, 26.35, 29.99, 30.95, 32.98, and 38.44 °. In the lyophilized drug-loaded nanoformulations, the peaks connected to free Dox vanished (**Figure 3.3A**).

3.3.1.2 FTIR analysis

Contrary to graphite, an IR-inactive solid, the FTIR spectra of GO show several peaks that might be attributable to the oxygen-containing functional groups of GO **(Figure 3.3B)**. The broad band at 3422 cm^{-1} corresponds to the stretching vibrations of –OH groups, the band at 2920 cm^{-1} ,1720 cm^{-1} corresponds to –CH, –C=O stretching, the bands at 1065 cm^{-1} and 1217 cm^{-1} assigned to -C=O stretching and the peak at 967.52 cm^{-1} to epoxy groups. Lastly, the tiny band at 825 cm^{-1} results from the bending of -C≡O in carboxylic groups. Both the FTIR and XRD results demonstrated that the pure graphite was successfully oxidized to produce GO. ^{1}H NMR, GPC, XRD, and FTIR spectroscopy were used to establish the identification and purity of the synthesized mPEG-PLA copolymers. **Figure 3.3C** depicts the ^{1}H NMR spectrum of mPEG-PLA copolymer, identified by the appearance of a peak at 3.64, 3.38 ppm attributable to the methylene and methyl protons of the PEG units and peaks at 5.25 ppm, and 1.55 ppm belongs to the methylene ($-CH_2$) and methyl ($-CH_3$) protons of PLA, respectively. The prominent peaks in the FTIR spectra of mPEG-PLA **(Figure 3.3B)** are as follows: -C-O-C- stretching vibration of PEG are associated with the peaks at 1108 cm^{-1} and 1348.70 cm^{-1}, -C=O stretching vibration are responsible for the peaks at 1752 cm^{-1} in PLA, the peak at 2363 cm^{-1} is attributed to the stretching vibrations of -C=C- and the peak at 2897 cm^{-1} corresponds to -C-H stretching of PEG. The prominent peaks at 1753 cm^{-1} and 1262 cm^{-1}, which correspond to the ester bonds (O-C=O), proved that GO and mPEG-PLA were successfully conjugated

(**Figure 3.3D**). Further supporting the conjugation of GO to mPEG-PLA were vibration frequencies at 1262 cm^{-1} (-C-O-C), 1753 cm^{-1} (-C=O), 1632 cm^{-1} (-C=C stretch), 2887 cm^{-1} (-CH stretching), and 3476 cm^{-1} (-OH stretching). The prominent peaks in the FTIR spectra of Dox@GO(mPP) NPs are represented in **Figure 3.2E**. SEC analysis was used to assess how the molecular weight of the mPEG-PLA conjugate increased after conjugation and demonstrated that under the stated reaction conditions shown in **Table 3.1**, 9 moles of PLA were covalently bonded to the mPEG polymer.

Table 3.1 GPC analysis of mPEG-PLA.

Polymers	**Observed relative molecular weight (Da)**	**Approximated No. of ligands attached**
mPEG	4986	-
mPEG-PLA	6283	9

3.3.1.3 XPS analysis

Moreover, the GO and GO(mPP) structure was also confirmed by XPS analysis. The core-level and complete survey spectra of graphite, GO, and GO(mPP) are shown in **Figure 3.2B, F.** After deconvolution, it is clearly evident from **Figure 3.2C** that the C1s spectrum of graphite contains two peaks at 284.70 eV and 289.9 eV, corresponding to the sp^3- hybridized carbon (C-C) and a shake-up satellite peak (π-π^*). The GO C1s spectra (**Figure 3.2D**) showed a high degree of oxidation, as shown by the presence of multiple oxygen groups: peaks at 284.6 eV, 286.6 eV, and 288.5 eV were assigned to carbon atoms in sp^2 carbon (C-C), the epoxide (C-O-C), and the carboxyl functional groups (C=O), respectively (Johra et al., 2014). The core-level

spectra of O1s of GO are shown in **Figure 3.2E**. When oxygenated functions are present, they are found as C=O, C=O/O-H/C-O-C at peaks 531.39 eV and 532.5 eV, respectively. After GO functionalization with mPEG-PLA (**Figure 3.2F**), the XPS core level Spectra of GO(mPP) conjugate showed a shift in the binding energy and a significant decrease in the intensity of peaks. The C1s spectrum showed peaks at 284.73 eV, 285.95 eV, 286.61 eV, and 288.79 eV corresponding to carbon atoms in sp^2 carbon (C-C), C-OH group, the epoxide (C-O-C), and the carboxyl functional groups (C=O), respectively (**Figure 3.2G**). The O1s region contains peaks at 532.5 eV, 533.56 eV attributed to oxygen atoms in C=O/O-C=O and C-O-C=O (ester group) (**Figure 3.2H**). The XPS analysis results confirmed that mPEG-PLA had been successfully grafted onto GO.

3.3.1.4 UV analysis

The GO(mPP) conjugate is projected to have a maximum loading content of drugs through electrostatic, π-π stacking, or hydrophobic interactions due to its huge poly-aromatic surface area (X. Xu et al., 2016). Herein, Dox was effectively loaded onto the GO(mPP) copolymer after being stirred overnight. The effective loading of Dox onto the Dox@GO(mPP) NPs was investigated by fluorescence spectra analysis, UV-vis spectra analysis, and cyclic voltammetry. The fluorescence intensity of Dox after loading on the Dox@GO(mPP) NPs was substantially less than that of free drug with the same Dox concentration, as shown in **Figure 3.4A**, which might be due to the fluorescence quenching effect demonstrating that there is strong π-π stacking interaction between Dox and GO. According to the UV data **(Figure 3.2I)**, the GO has a maximum absorption peak at 235 nm, which is the typical absorption peak of C=O and corresponds to π-π* transitions of the remaining sp^2 C=C bonds (Johra et al., 2014; R. Li et al., 2021). GO(mPP) conjugate has a maximum absorption peak at 255 nm after mPEG-PLA functionalization due to the gradual reduction of GO, which also increases π-conjugation. As the π-conjugation increases, the transition requires less energy, resulting in the apparent shift

of absorption peak to the longer wavelength region. In the UV analysis of Dox@GO(mPP) NPs, Dox has shown an absorption peak at 480 nm, demonstrating the successful loading of Dox onto GO(mPP) conjugate. Electrochemistry is one of the methods used rather often to explore the behavior of electron transport in nanohybrids that combine carbon nanotubes with electroactive substances.

3.3.1.5 Cyclic voltammetry

The cyclic voltammetry curves are shown in **Figure 3.2J** employing the Dox@GO(mPP)-modified GC electrode, the Dox@GO electrode, and the control electrodes of GO- and Dox-modified GC electrodes in various ratios. The anode and cathode peak potentials of 0.512 and 0.318 V, respectively, were found to represent the usual redox pair of peaks for Dox. This finding may be explained by the fact that the quinone part of the molecule undergoes a redox reaction, which gives rise to the distinctive peaks of Dox. The redox peak of the Dox@GO(mPP)-modified GC electrodes are significantly enhanced at corresponding places compared to the redox peak of the Dox@GO and Dox-modified GC electrodes. The synergistic effect brought on by the π-π stacking between Dox and GO may help explain why the Dox@GO(mPP)-modified electrode and Dox@GO exhibit larger redox reaction currents. It has been shown that the relationship between the two components present in homogenous NPs effectively increases the amount of electron transit.

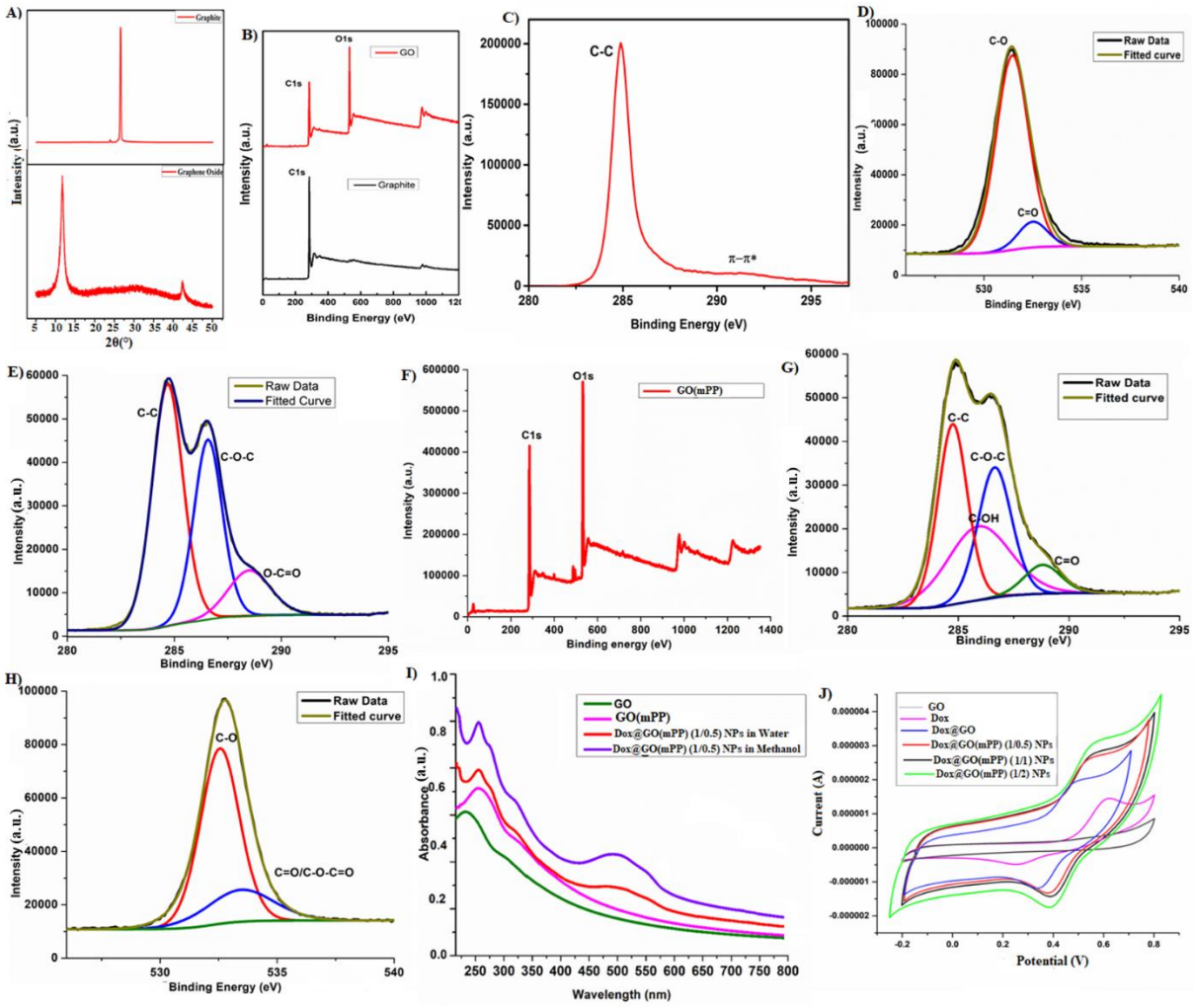

Figure 3.2 XRD patterns of Graphite and Graphene oxide (GO) (A); XPS survey spectra of graphite and GO (B); C1s survey spectra of graphite (C); O1s survey spectra of GO (D); C1s survey spectra of GO (E); XPS survey spectra of GO(mPP) (F); C1s survey spectra of GO (mPP) (G); O1s survey spectra of GO(mPP) (H); UV-vis spectra of GO, GO(mPP) and Dox@GO(mPP) (1/0.5) NPs in water and methanol (I); Cyclic voltammetry analysis (J).

3.3.1.6 Entrapment efficiency (% EE) and drug loading (% DL)

The entrapment efficiency (% EE) and drug loading (% DL) capacity of GO(mPP) copolymer for the chemotherapeutic drug Dox are represented in **Table 3.2**. The drug loading capacities ranged from 3 % to 6.3 %, and entrapment efficiencies between 33.07 % to 70 % were obtained for the different GO(mPP) ratios. The higher GO(mPP) (1/1, 1/2) copolymer ratio resulted in

somewhat reduced drug loading, most likely because the higher molecular weight mPEG-PLA chains occupied a larger fraction of the GO surface, offering a stronger hurdle to Dox attachment on the GO(mPP) surface. The GO(mPP) (1/0.5) conjugate with a drug-to-polymer weight ratio (1:10) demonstrated maximum Dox encapsulation efficiency and loading and was investigated for further studies.

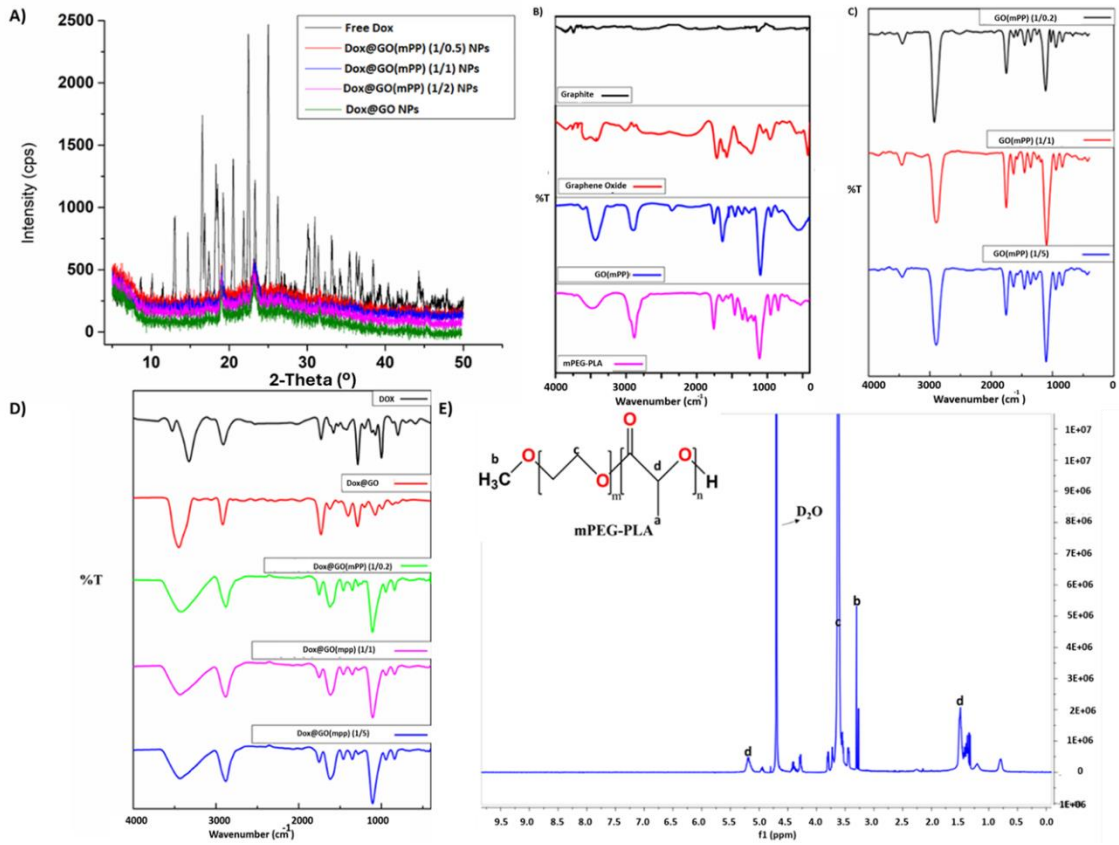

Figure 3.3 XRD analysis of free Dox, Dox@GO, and Dox@GO(mPP) NPs in various ratios (A). FTIR spectra analysis of graphite, graphene oxide, GO(mPP), and mPEG-PLA using the KBR pellet technique (B); 1H-NMR spectrum of mPEG-PLA (C); FTIR spectra analysis of GO(mPP) conjugates in various ratios using the KBR pellet technique (D). FTIR spectra analysis of Dox@GO(mPP) NPs in different ratios using the KBR pellet technique (E).

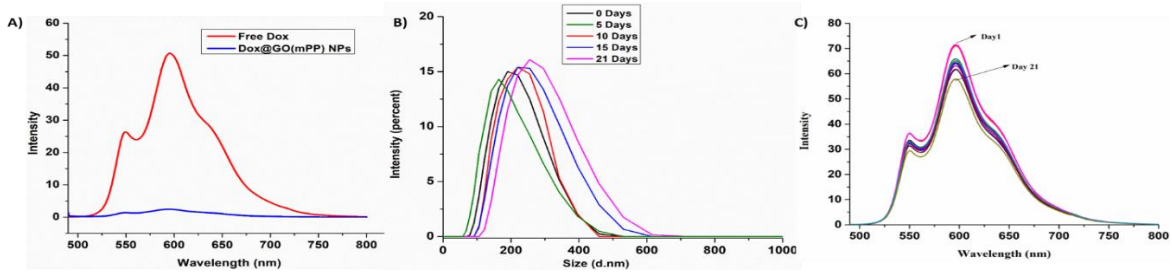

Figure 3.4 Fluorescence Spectra analysis of free Dox and Dox@GO(mPP) (1/0.5) NPs (A). Particle size analysis of Dox@GO(mPP) (1/0.5) NPs for 21 days (B). Fluorescence spectra analysis of Dox@GO(mPP) (1/0.5) NPs for 21 days (C).

Table 3.2 Physiochemical characterization of Dox@GO(mPP) NPs

S.No.	**Formulation (DTP, 1:10)**	**Particle Size(nm)**	**PDI**	**Zeta Potential**	**%Drug Loading**	**%Entrapment efficiency**
1	GO(mPP)(1/0.5)	147.2±5	0.28	-	-	-
2	Dox@GO(mPP) (1/0.5)	161.0±4	0.32	-28.2	6.3	70
3	GO(mPP) (1/1)	162.4±5	0.26	-	-	-
4	Dox@GO(mPP) (1/1)	188.2±3	0.44	-24.8	4.19	46.15
5	GO(mPP) (1/2)	160.3±2	0.22	-	-	-
6	Dox@GO(mPP) (1/2)	195.9±6	0.26	-22.1	3.00	33.076
7	Dox@GO	184±2	0.32	-30.4	2.65	29.2

3.3.1.7 Particle size and zeta potential

The particle sizes of the blank (GO) and Dox@GO(mPP) NPs (1/0.5) were measured by DLS and found to be 147.2±5 nm and 161.0±4 nm, with PDI 0.28, 032, respectively (**Figure 3.6A**).

The zeta potential for blank and Dox@GO(mPP) NPs was found to be -30.2 ± 1.34 and -28.2 ± 1.14 mV indicating the good colloidal stability of the nanocarrier system, represented in **Table 3.2, Figure 3.6B**. Additionally, after 21 days of storage at 4 ℃, the Dox fluorescence intensity, drug loading (%), and particle size in Dox@GO(mPP) (1/0.5) NPs were all investigated. As shown in **Figure 3.4B,** the size of the Dox@GO(mPP) (1/0.5) NPs did not grow much and kept their original size of ~161 nm while being stored at 4 ℃ is evidence that the NPs are stable. . Additionally, the fluorescence intensity of Dox (**Figure 3.4C**) was little diminished after being stored at 4 ℃, and the amount of drug loading was also discovered to be steady (**Figure 3.5A**). The morphology of graphite (**Figure 3.6C**), GO (**Figure 3.6D**), and Dox@GO(mPP) (1/0.5) NPs was investigated thoroughly by SEM and AFM. The AFM measurements demonstrated that GO sheets are between 0.8 and 2 nm thick and that a typical GO layer is roughly 0.8 nm thick, which implies that the specimen is largely made up of single graphene monolayers and a few layers of graphene nanosheets(**Figure 3.6E**). Moreover, SEM images demonstrated that the generated Dox@GO(mPP) (1/0.5) NPs were spherical and nanosized **(Figure 3.6A),** with a 3D shape that differed significantly from that of the GO sheet because of its flexible structure. The size of a biomaterial is a key element to consider when determining whether it is suitable for IV administration and the introduction of drugs to tumor tissues via passive targeting.

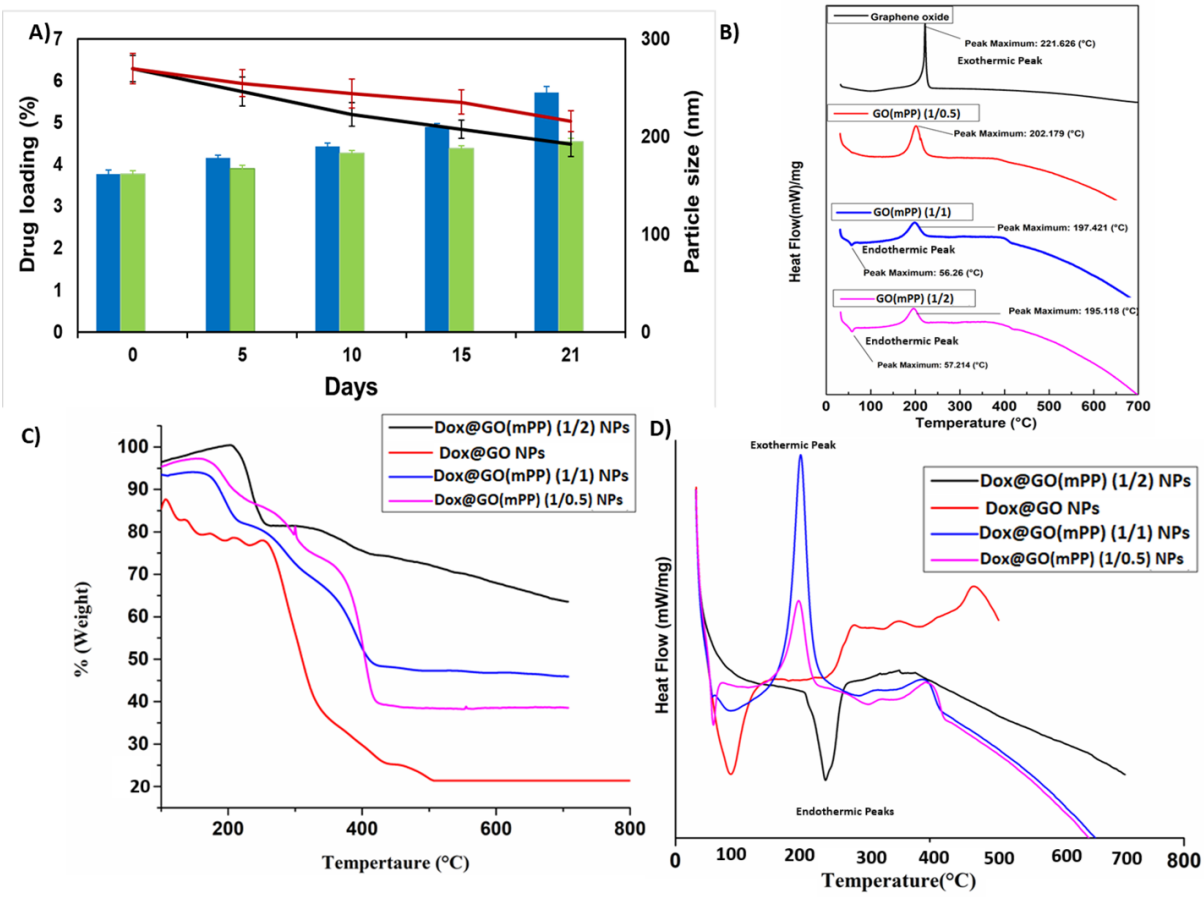

Figure 3.5 Kinetic stability Study (A). TGA thermogram of Dox@GO(mPP) NPs in various ratios (B). DSC thermogram of GO and GO-mPEG-PLA in various ratios (C). DSC thermogram of Dox@GO(mPP) NPs in various ratios (D).

3.3.1.8 DSC and TGA analysis

The DSC and TGA analysis were performed for thermal analysis of newly formed GO, GO(mPP), and Dox@GO(mPP) NPs. **Figure 3.6F** depicts TGA graphs for GO, GO(mPP), and Dox@GO(mPP) NPs. The thermal degradation of GO began below 150 °C due to the evaporation of water held in the π--stacked layered structure, indicating that it was thermally unstable. Mass loss was noticeably increased in the 165–250 °C range due to the decomposition of labile oxygen-containing groups. When mPEG-PLA was coupled with GO, the loss of mass of the resulting GO(mPP) conjugate was substantially increased from 350 °C, which was almost 180 °C higher than that of GO. This aptly demonstrated that conjugation of GO with

mPEG-PLA was highly effective in enhancing GO's thermal stability. An intermediate weight loss profile between that of mPEG-PLA and GO was observed in Dox@GO(mPP) NPs **(Figure 3.5B)**. The thermal characteristics of the produced composites were also investigated using DSC measurements. According to DSC curves, GO decomposed and exhibited a high-intensity exothermic peak at 221.44 °C, GO-mPEG-PLA exhibited an exothermic peak at 202.179 °C, and Dox@GO (mPP) (1/0.5) NPs exhibited an exothermic crystallization point in the range of 145.74 °C to 232.71 °C, with a peak maxima at 190.59 °C and endothermic melting point in the range of 53.29 °C to 69.35 °C with a peak minima at 60.85 °C (**Figure 3.5C**). After the π-π interaction of Dox with GO(mPP), the peak's position and shape changed. The DSC measurements of other composites are represented in **Figure 3.5D**.

3.3.1.9 *In vitro* drug release

Next, we measured Dox release from Dox@GO(mPP) (1/0.5) NPs at pH 5, 6.8, and 7.4 with or without exposure to NIR laser irradiation (±L). The Dox@GO(mPP) (1/0.5) NPs showed controlled *in vitro* Dox release over many hours. The quantity of Dox liberated from the Dox@GO(mPP) (1/0.5) NPs had a laser irradiation-dependent and pH-dependent release behavior, as shown in **Figure 3.6G**. The photothermal impact of Dox@GO(mPP) (1/0.5) NPs, which might impair the interactions between DOX and GO(mPP), could reflect the increased Dox release during NIR laser irradiation. These findings showed that when chemotherapy was combined with photothermal treatment, chemotherapy could greatly boost effectiveness. The drug release rate was reduced when the amount of mPEG-PLA in the GO(mPP) nanocomposites was raised, most likely because both of these adjustments enhanced the drug diffusion barrier created by the existence of copolymer chains on the GO surface. On the basis of the r^2 values, a model for drug release kinetics that provides the best match was developed is demonstrated in (**Table 3.3**) (**Figure 3.7**). The drug release from Dox@GO(mPP) (1/0.5) NPs at various pHs showed regression values of 0.9826 (pH 7.4, -L), 0.9606 (pH 7.4, +L),

0.9869 (pH 6.8, -L), 0.9861 (pH 6.8, +L), 0.9977 (pH 5, -L) and 0.9865 (pH 7.4, +L). The Dox release from Dox@GO(mPP) (1/0.5) NPs at pH 5 and 6.8 (±L) followed the Korsmeyer Peppas kinetic model, while at pH 7.4 (±L) followed the Higuchi model. The 'n' values of the Korsmeyer–Peppas equation for Dox@GO(mPP) (1/0.5) NPs suggested that the drug release mechanism model was Fickian diffusion at pH 5 and pH 6.8.

3.3.1.10 Hemolysis study

In this study, the hemocompatibility of GO and GO(mPP) (1/0.5) was assessed in terms of hemolysis using female Wistar rat blood. The hemolytic effect of GO and GO(mPP) (1/0.5) nanocarriers were examined at varying concentrations (25-200 µg/mL) employing PBS as negative and Triton-X 100 as positive controls, respectively. **Figure 3.6H** shows that after 2 h of incubation with nanocarriers, the hemolytic ratio was less than 5 % for all tested doses. According to ISO/TR 7406, samples having hemolytic rates of less than 5% (the necessary, safe hemolytic ratio for biomaterials) are classified as non-hemolytic, implying that Dox@GO(mPP) (1/0.5) NPs are blood compatible (Ourique et al., 2015).

3.3.2 Photothermal heating effect

The photothermal effects of GO, GO(mPP) (1/0.5), and Dox@GO(mPP) (1/0.5) NPs were investigated, and concurrently temperature changes were recorded at 20 s intervals under 808 nm laser irradiation. The solution temperature of GO reached 36 °C, GO(mPP) (1/0.5) (43.8 °C), and Dox@GO(mPP) (1/0.5) NPs (48.6 °C) under the 808 nm laser irradiation (0.25 W/cm^2) within 5 min at the same GO concentration, respectively represented in **Figure 3.6I, J**. The temperature of pure water rose slightly to 26.9 °C, demonstrating that the GO, GO-mPEG/PLA, and Dox@GO-mPEG/PLA NPs had outstanding photothermal properties under 808 nm laser irradiation.

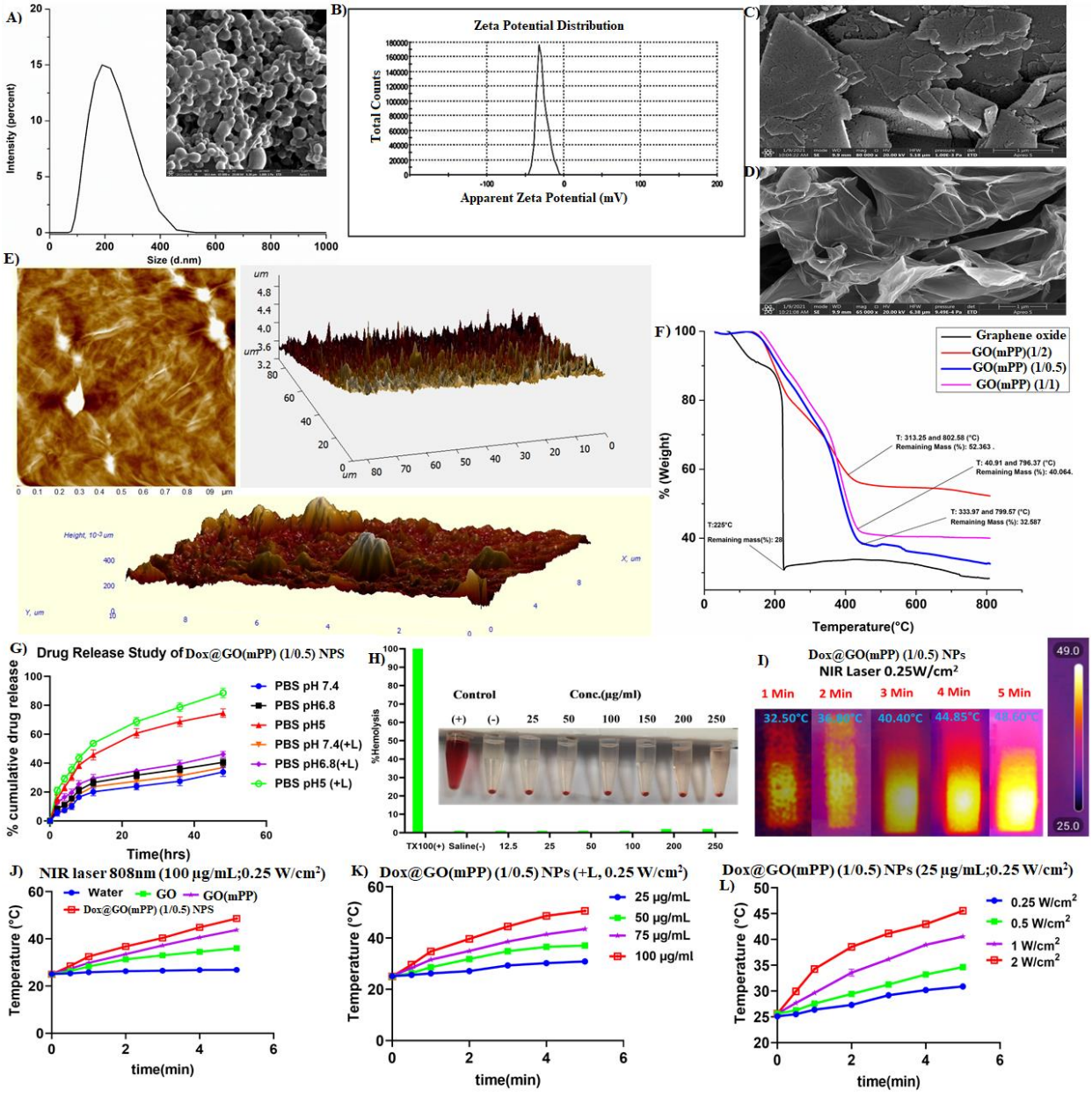

Figure 3.6 Physiochemical characterization of Dox@GO(mPP) NPs. Particle size and SEM image (inset) of Dox@GO(mPP) (1/0.5) NPs with cryoprotectant (A); Zeta Potential (B); SEM images of Graphite (C) and GO (D); Atomic force microscopy (AFM) image for GO (E); DSC thermogram (F); Drug release study of Dox@GO(mPP) (1/0.5) NPs at various PHs (G); *in vitro* hemolysis study of GO(mPP) (1/0.5) polymer (H); Thermal images of Dox@GO(mPP) (1/0.5) NPs exposed to 808 nm Laser (0.25 W/cm^2) for 5 min (I); Temperature variation curves of pure water, GO, and GO(mPP) (1/0.5) polymer exposed to 808 nm Laser (0.25 W/cm^2) for

5 min (J); Temperature variation curves of various concentrations of Dox@GO(mPP) (1/0.5) NPs exposed to 808 nm Laser (0.25 W/cm^2) for 5 min (K)**;** Temperature variation curves of Dox@GO(mPP) (1/0.5) NPs (25 µg/mL) exposed to various power intensities for 5 min (L).

Conversely, it was determined that temperature is laser power and concentration-dependent **(Figure 3.6K, L),** and the temperature of the Dox@GO(mPP) (1/0.5) NPs solution (25 µg/mL) elevated significantly with an increment in power density from 0.25-2 W/cm^2 or concentration from 25-100 µg/mL irradiation due to the significant photothermal conversion effectiveness of Dox@GO(mPP) (1/0.5) NPs. A temperature of around 45 °C or higher is sufficient to ablate malignant cells through hyperthermia (Cells, 2020), which may be achieved by adjusting the substrate concentration and irradiation intensity.

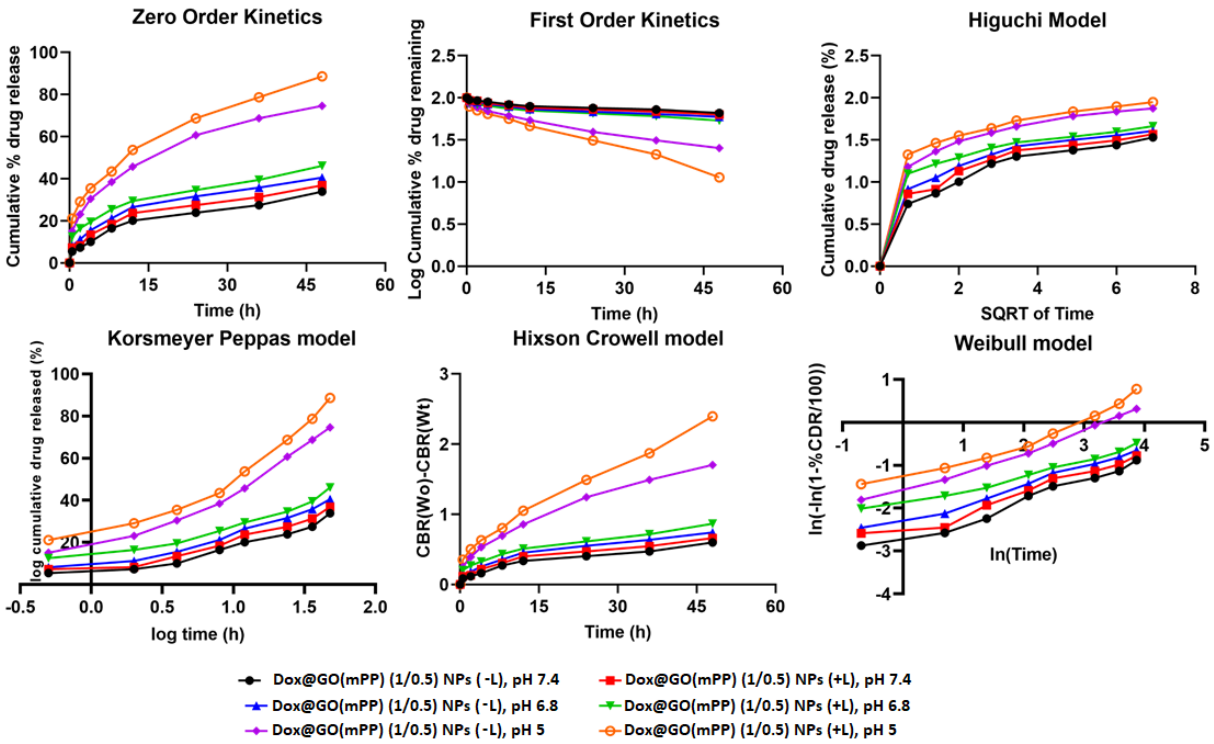

Figure 3.7 Release kinetic study of Dox@GO(mPP) (1/0.5) NPs in different pHs.

Table 3.3 Release kinetic study of Dox@GO(mPP) (1/0.5) NPs in different pHs with or without laser.

S.No.	pH	Zero order	First order	Higuchi model	Korsmeyer Peppas model	Hixson Crowel model	Weibull model	Best-Fit model
1	pH 7.4 (-L)	y = 0.6084 x + 6.9938 R^2 = 0.8792	y = -0.0033 x + 1.9692 R^2 = 0.9115	y = 4.6458x + 1.5075 R^2 = 0.9826	y = 0.4168x + 0.8093 R^2 = 0.9736	y = 0.0108 x + 0.1098 R^2 = 0.9012	y = 0.4536x - 2.7171 R^2 = 0.972	Higuchi -model
2	pH 7.4 (+L)	y = 0.6553 x + 8.7312 R^2 = 0.8519	y = -0.0036 x + 1.9608 R^2 = 0.8926	y = 5.066x + 2.6277 R^2 = 0.9757	y = 0.3835x + 0.9107 R^2 = 0.9606	y = 0.0119 x + 0.1386 R^2 = 0.8795	y = 0.4242x - 2.4746 R^2 = 0.9604	Higuchi - model
3	pH 6.8 (-L)	y = 0.7184 x + 10.454	y = -0.0041 x + 1.9525	y = 5.5968x + 3.629	y = 0.3659x + 0.9918	y = 0.0134 x + 0.1674	y = 0.4119x - 2.2796	Korsmeyer Peppas model

		R^2 = 0.839	R^2 = 0.888	R^2 = 0.9758	R^2 = 0.9869	R^2 = 0.8723	R^2 = 0.9854	
4	pH 6.8 (+L)	y = 0.7516 x + 13.615 R^2 = 0.8181	y = -0.0046 x + 1.9371 R^2 = 0.8841	y = 5.8762x + 6.4087 R^2 = 0.9583	y = 0.2882x + 1.1504 R^2 = 0.9861	y = 0.0145 x + 0.2204 R^2 = 0.8635	y = 0.336x - 1.8914 R^2 = 0.9791	Korsmeyer Peppas model
5	pH 5 (-L)	y = 1.3412 x + 19.629 R^2 = 0.8473	y = -0.0115 x + 1.9133 R^2 = 0.9547	y = 10.424x + 6.9647 R^2 = 0.9807	y = 0.3594x + 1.2724 R^2 = 0.9977	y = 0.0323 x + 0.3131 R^2 = 0.9253	y = 0.4754x - 1.6065 R^2 = 0.9871	Korsmeyer Peppas model
6	pH 5 (+L)	y = 1.5369 x + 23.594 R^2 = 0.8569	y = -0.0174 x + 1.9109 R^2 = 0.9816	y = 11.867x + 9.3249 R^2 = 0.9791	y = 0.3223x + 1.3834 R^2 = 0.9865	y = 0.0438 x + 0.3569 R^2 = 0.9594	y = 0.48x - 1.3432 R^2 = 0.948	Korsmeyer Peppas model

3.3.3 *In vitro* assays

3.3.3.1 Cellular uptake study, intracellular ROS generation, and MTT assay

Confocal fluorescence imaging and flow cytometry were used to evaluate the cellular internalization of free Dox and Dox@GO(mPP) (1/0.5) NPs both qualitatively and quantitatively in MDA-MB-231 and 4T1 cells. In both cell lines, the clear, bright red fluorescence was observed in the cytoplasm and nuclei in Dox@GO(mPP) (1/0.5) NPs targeted cells, suggesting quick internalization of Dox@GO(mPP) (1/0.5) NPs. For MDA-MB-231 (**Figure 3.8A**) and 4T1 cells (**Figure 3.8B**), the red fluorescence intensity of free Dox and Dox@GO(mPP) (1/0.5) NPs increased from 1 to 4 h, indicating time-dependent cellular absorption. In addition, Dox@GO(mPP) (1/0.5) NPs with Laser (+L) had much higher red fluorescence intensity than free Dox and Dox@GO(mPP) (1/0.5) NPs without laser (-L), showing laser dependent cellular uptake in both cell lines. Moreover, Flow cytometry studies were performed further to validate the photothermally increased internalization and intracellular release depicted in **Figure 3.8C, D.** The mean fluorescence intensity values for Dox@GO(mPP) (1/0.5) NPs and free Dox were shown to increase from 1 to 4 h in the flow cytometer's histogram, which was displayed as a bar graph **(Figure 3.8E, F))**. Flow cytometry analysis demonstrated time and laser-dependent increase in fluorescence intensity in both the tested cell lines. The findings on cellular uptake and intracellular release showed that the increase in temperature generated by NIR light exposure enhanced cell membrane permeability and drug release. This resulted in an effective Dox intracellular drug delivery that may be employed in photothermal therapy to treat cancer.

The DCFH-DA dye as an intracellular sensor was used to observe the ROS formation of Dox@GO(mPP) (1/0.5) NPs in both the tested cell lines. As indicated in **Figure 3.12C, D**, 4T1, and MDA-MBA-231 cells treated with the Dox@GO(mPP) (1/0.5) NPs + 880 nm (0.25 W/cm^2, 5 min) laser exhibited considerable green fluorescence; however, no substantial green

fluorescence was observed in the absence of laser irradiation. The phenomena above suggested that both the tested cell lines treated with NPs produced higher intracellular ROS when exposed to laser radiations. As a result, the phenomenon demonstrated that Dox@GO(mPP) (1/0.5) NPs might be advantageous in improving chemo-photothermal combinational treatment results and killing cancer cells.

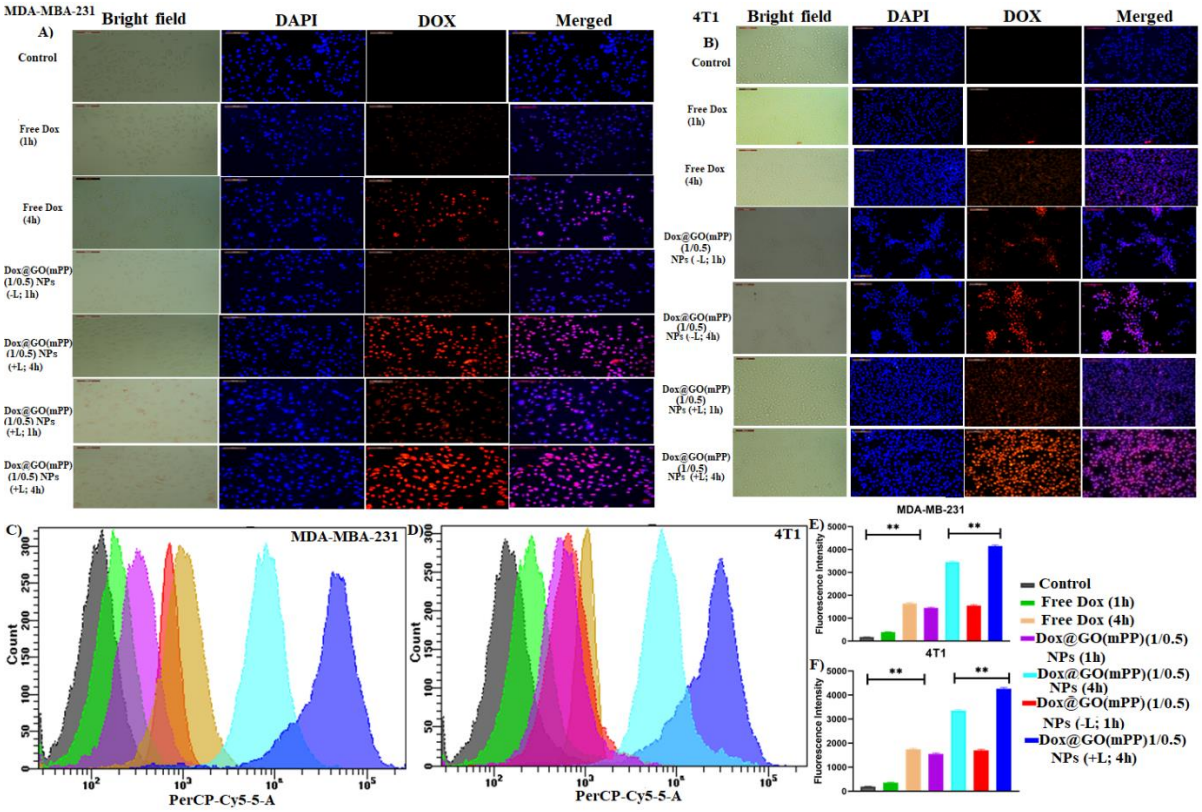

Figure 3.8 Cellular internalization study of free Dox and Dox@GO(mPP) (1/0.5) NPs (± L) (0.25 W/cm2) in MDA-MB-231 (A) and 4T1 (B) cells and the results were observed after 1 and 4 h of incubation. The histogram and a bar graph were used to demonstrate the amount of NPs taken up by MDA-MB-231 (C, E) and 4T1 (D, F) cell lines using flow cytometry, with a statistical significance of $p < 0.01$.

Furthermore, the cytotoxic effect of free Dox, GO(mPP) conjugate, Dox@GO(mPP) (1/0.5) NPs with or without laser (±L) (0.25W/cm^2) on MDA-MB-231 and 4T1 cells was assessed *in*

vitro using the MTT test for 24 and 48 h. **Figure 3.10** demonstrates that the positive control group (+L alone) had comparable cell survival to the negative control group (PBS, -L), suggesting that laser irradiation alone was not harmful. Consequently, the laser-irradiated cells exhibited a more significant amount of cell death than the laser-non-irradiated cells in both of the time periods (24 and 48 h). When laser intensity, dose, and duration of Dox@GO(mPP) (1/0.5) NPs were increased, the number of surviving cells decreased, demonstrating a dosage, time, and laser-dependent relation (**Figure 3.9E**). The Dox release might be responsible for the strong inhibitory action of Dox@GO(mPP) (1/0.5) NPs without laser. The inhibitory effect of Dox@GO(mPP) (1/0.5) NPs was enhanced further after laser irradiation, indicating that PTT paired with chemotherapy might boost therapeutic effectiveness (Liang et al., 2019). A cell viability study demonstrated that the Dox@GO(mPP) (1/0.5) NPs induced more cellular absorption, leading to reduced cell viability as compared to free Dox.

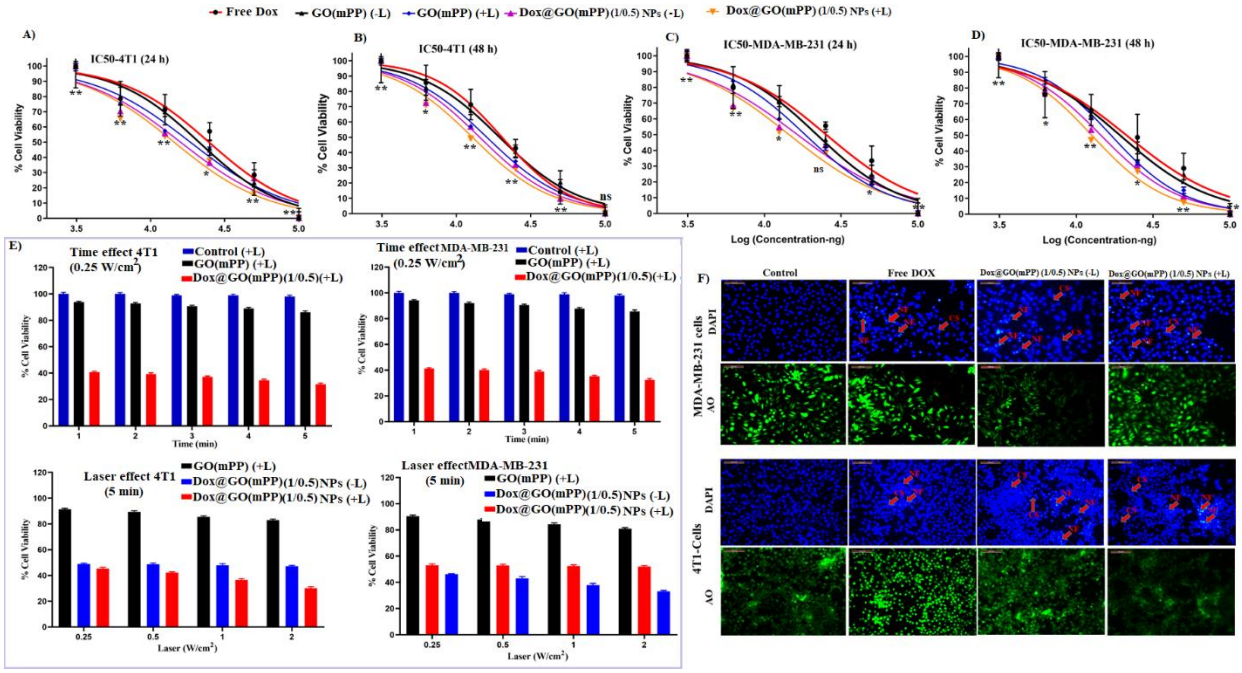

Figure 3.9 Anticancer activity of free Dox, Go(mPP) (± L), and Dox@GO(mPP) (1/0.5) NPs (± L) (0.25 W/cm2) by MTT assay. MDA-MB-231 and 4T1 cells were treated with Dox at a concentration range of 3.5 to 100 µg/mL (n=3). The IC50 value of free Dox, Go(mPP) (± L),

and Dox@GO(mPP) (1/0.5) NPs (± L) for cultured 4T1 (A, B) and MDA-MB-231 (C, D) cells at 24 h and 48 h; Effect of Time and laser on the cytotoxicity of MDA-MB-231 and 4T1 cells (E); Nuclear staining (F). The significance of the difference was assessed by ANOVA, **P<0.01, *P<0.05.

The cytotoxic effect of free Dox, GO(mPP) conjugate, Dox@GO(mPP) (1/0.5) NPs with or without laser (±L) (0.25W/cm^2) on MDA-MB-231 and 4T1 cells was compared using IC-50 values, represented in **Figure 3.9A, B, C, D** and **Table 3.4**. Cells treated for 24 h exhibited a higher IC-50 value than cells incubated continuously for 48 h. When compared to free Dox and Dox@GO(mPP) (1/0.5) NPs (-L) in tested cell lines, Dox@GO(mPP) (1/0.5) NPs (+L) had the strongest anti-proliferative activity, indicating that photothermal combined with chemotherapy has improved treatment efficacy. The fact that the IC-50 values lowered from 24 to 48 h showed that the cytotoxicity was time-dependent.

Table 3.4 IC-50 value of Free Dox, GO(mPP) –L, GO(mPP) (+L), Dox@GO(mPP) (1/0.5) NPs (–L), and Dox@GO(mPP) (1/0.5) NPs (+L) in 4T1 and MDA-MB-231 cells.

Compound	**4T1**		**MDA-MB-231**	
	IC-50 (24 h) (µM)	**IC-50 (48h) (µM)**	**IC-50 (24 h) (µM)**	**IC-50 (48h) (µM)**
Free Dox	18.56	16.03	18.56	16.86
GO(mPP) (-L)	24.79	20.25	25.26	21.24
GO(mPP) (+L)	21.24	19.52	21.95	19.28
Dox@GO(mPP) (1/0.5) NPs (-L)	15.95	14.36	16.41	14.48
Dox@GO(mPP) (1/0.5) NPs (+L)	14.42	12.83	14.47	12.63

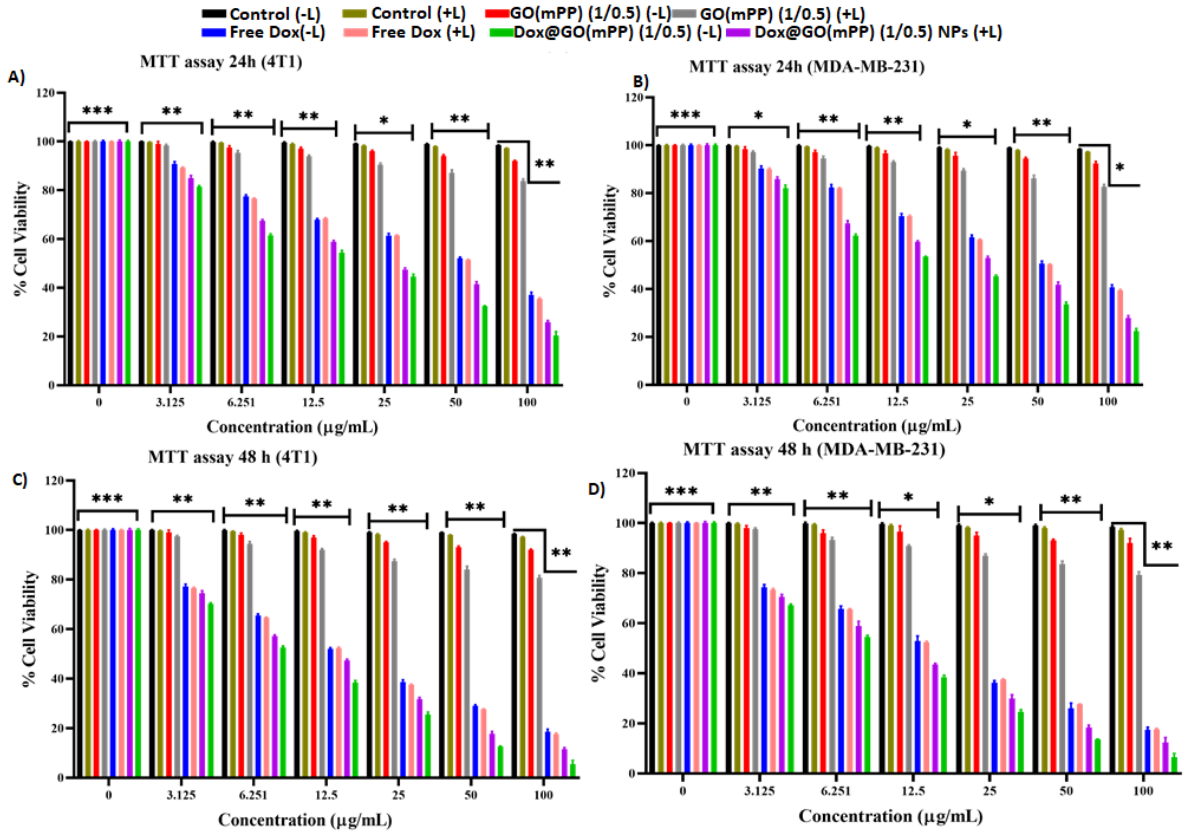

Figure 3.10 Cytotoxicity study of Free Dox, GO(mPP) (–L), GO(mPP) (+L), Dox@GO(mPP) (1/0.5) NPs (–L), and Dox@GO(mPP) (1/0.5) NPs (+L) in 4T1 and MDA-MB-231 cells.

3.3.3.2 Nuclear staining assay

4',6-diamidino-2-phenylindole (DAPI) is a fluorescent stain that binds strongly to A–T rich DNA regions and helps visualize chromatin condensation or nuclear damage. It differentiates between living and apoptotic cells by coloring the distinctive condensed nuclei of the latter brilliant blue(Khan & Akhtar, 1982). As a result, this staining approach was used to identify apoptosis induction by free Dox and Dox@GO(mPP) (1/0.5) NPs (±L) in MDA-MBA-231 cells and 4T1 cells, respectively. **Figure 3.9F** shows that control cells (without NPs) had intact nucleus structure, but tested cells treated with Dox@GO(mPP) (1/0.5) NPs (+L) had horseshoe-shaped, condensed, or shattered nuclei, respectively, than free Dox and Dox@GO-

mPEG/PLA NPs (-L). This was further confirmed by staining nuclei with acridine orange, and the undamaged cell membrane allows AO to infiltrate and dye the nuclei green. The control cells looked normal and were green in color, as shown in **Figure 3.9F**. MDA-MBA-231 and 4T1 cells treated with Dox@GO(mPP) (1/0.5) NPs (+L) displayed morphological alterations as membrane blebbing, cell shrinkage, and chromatin condensation, indicating that it triggered more apoptosis in both the tested cell lines than free Dox and Dox@GO(mPP) (1/0.5) NPs (-L).

3.3.3.3 Annexin V-FITC/propidium iodide apoptosis assay

Annexin V–FITC/PI labeling was used to assess viable cell apoptosis. The proportion of normal cells (bottom left quadrant) in the control group (without NPs) was around 98.8±1.2 %, and the proportion of viable cells was drastically reduced when the cells were co-incubated with free Dox and Dox@GO(mPP) (1/0.5) NPs (±L). As shown in **Figure 3.11A**, cells fed with free Dox displayed total apoptosis of 27.14±2.6 % in MDA-MBA-231 cells and 31.4±2.3 % percent in 4T1 cells, respectively, Dox@GO(mPP) (1/0.5) NPs (-L) displayed total apoptosis of 49.56±2.56 % in MDA-MB-231 cells, and 51.3±3.15% in 4T1 cells, whereas Dox@GO(mPP) (1/0.5) NPs (+L) exhibited total apoptosis of 65.15±4.1 % and 64.12±3.4 % in MDA-MBA-231 cells and 4T1 cells. Dox@GO(mPP) (1/0.5) NPs with laser-induced greater apoptosis than free Dox and Dox@GO-mPEG/PLA NPs without laser might be attributed to the nanocarrier system's increased cellular absorption of Dox.

3.3.3.4 Cell cycle analysis and mitochondria membrane potential (MMP) study

Cell cycle analysis was conducted on 4T1 and MDA-MBA-231 cells using a flow cytometer to see whether cell growth suppression was linked to cell cycle arrest **Figure 3.11B**. Following treatment with Dox@GO(mPP) (1/0.5) NPs, the percentage of cell populations in the G2/M phase rose from 20.81 to 38.2 % (-L) and 44.68 % (+L), respectively. Following this increase,

the percentages of cell populations in the G1 and S cells decreased. **Figure 3.11C, D** depicts the greatest arrest in the G2/M phase for Dox@GO(mPP) (1/0.5) NPs (+L) against free Dox and Dox@GO(mPP) (1/0.5) NPs (–L), confirming Dox mechanism of action (Meiyanto et al., 2011), which arrests the cell in the early G2/M phase. The results confirmed earlier cytotoxicity findings that the Dox@GO(mPP) (1/0.5) NPs treatment (+L) was more effective than free Dox and Dox@GO(mPP) (1/0.5) NPs (-L) treatments in terms of therapeutic impact.

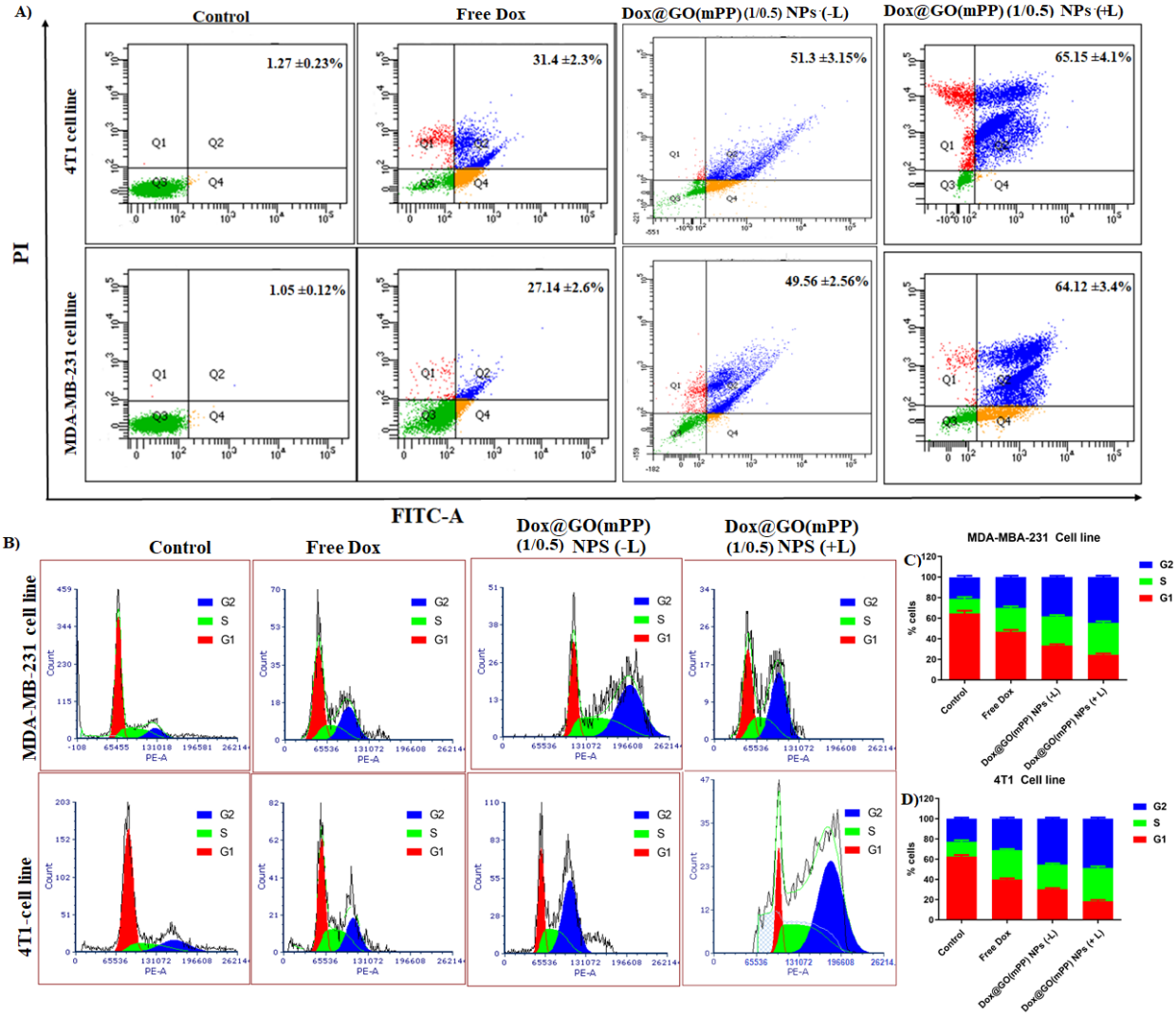

Figure 3.11 Annexin V assay (A) and cell cycle analysis (B). The level of cell death due to apoptosis was measured by analyzing the behavior of 4T1 and MDA-MB-231 cells that were exposed to free Dox, and Dox@GO(mPP) (1/0.5) NPs (± L) (0.25 W/cm2), after being

incubated for 24 h. The data was collected using flow cytometry, with the Q3 and Q4 quadrants representing early and late stages of apoptosis respectively. The effect of the free Dox and Dox@GO(mPP) (1/0.5) NPs (± L) on cell cycle progression with histogram plots and a representative bar graph showing the distribution of cells in various stages of the cell cycle in both MDA-MB-231 (C) and 4T1 cells (D).

Mitochondrial damage is exacerbated by producing reactive oxygen species (ROS), leading to cell apoptosis. Thus, we examined the impact of free Dox and Dox@GO(mPP) (1/0.5) NPs (±L) treatment on MMP in 4T1 and MDA-MB-231 cells. The cationic JC-1 dye particularly indicates mitochondrial depolarization. This dye accumulates in mitochondria in a potential-dependent way, as indicated by a shift in fluorescence emission from red (590 nm) to green (529 nm) when the mitochondrial membrane is disrupted (Mallick et al., 2019). When compared to untreated cells, which look red (aggregated-form of the dye), Dox@GO(mPP) (1/0.5) NPs (+L) treated cells exhibited a higher green intensity (monomer-form of the dye) than Free Dox (red-green merged) and Dox@GO(mPP) (1/0.5) NPs (-L) treated cells (**Figure 3.12A**). These findings demonstrated that Dox@GO(mPP) (1/0.5) NPs caused mitochondrial membrane damage, lowering membrane potential. Flow cytometry analysis demonstrated that 4T1 and MDA-MB-231 cells treated with Dox@GO(mPP) (1/0.5) NPs (+L) exhibited more mitochondria membrane potential disruption, as shown in **Figure 3.12B**.

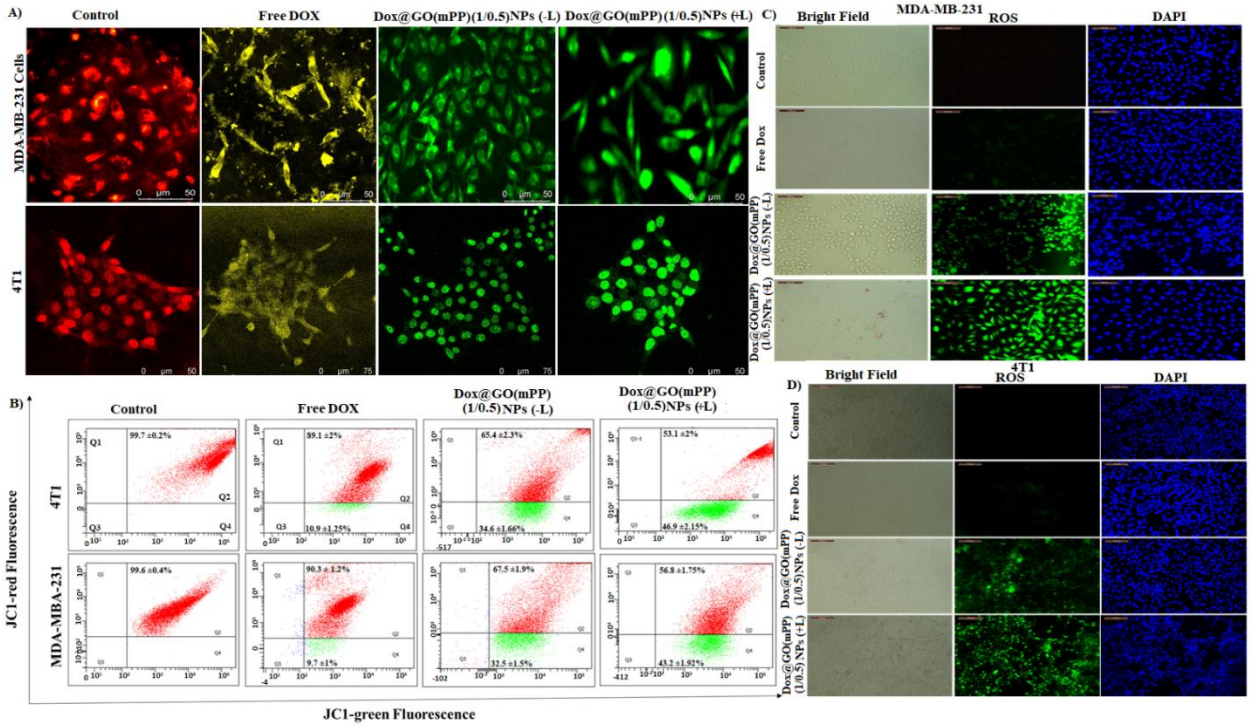

Figure 3.12 Qualitative and quantitative assessment of MMP in MDA-MB-231 and 4T1 cells treated with free Dox and Dox@GO(mPP) (1/0.5) NPs (± L) (0.25 W/cm2) by fluorescence microscopy (A), and flow cytometry (B). Intracellular ROS generation in MDA-MB-231 and 4T1 cells treated with free Dox and Dox@GO(mPP) (1/0.5) NPs (± L) by fluorescence microscopy (C, D).

3.3.4 Pharmacokinetic Study

The pharmacokinetic (pK) characteristics were assessed by measuring drug concentrations at specific time points after IV injection of free Dox, Dox@GO, and Dox@GO(mPP) (1/0.5) NPs into the tails of female Wistar rats. (**Table 3.5 and Figure 3.13H, I)** represent the pK parameters and plasma Dox concentration-time curves. The findings revealed that the free Dox and Dox@GO NPs level in blood was rapidly removed, with a blood retention $T_{1/2}$ of 1.39 h and 3.52h. The Dox@GO(mPP) (1/0.5) NPs, on the other hand, had a blood retention $T_{1/2}$ of 26.28 h, over 18.9 times higher than that of free Dox and 7.46 times than of Dox@GO NPs. As a result, the AUC values of the Dox@GO(mPP) (1/0.5) NPs rose to about 58.67 times those

of free Dox and 8.04 that of Dox@GO NPs. The PK data revealed that Dox@GO(mPP) (1/0.5) NPs had the greatest $t_{1/2}$, C_{max}, AUC, MRT, and lowest clearance compared to free Dox and Dox@GO NPs. The free dox is promptly cleared out of the systemic circulation. Meanwhile, Dox loaded onto Dox@GO(mPP) (1/0.5) NPs is not immediately accessible to the systemic environment, lowering drug clearance and, as a consequence, increasing NPs Dox plasma residence time (Z. Liu et al., 2017; C. Wang et al., 2018). Moreover, incorporating PEG into the nanoparticle system also allows the Dox to circulate for a longer period. PEGylation reduces opsonin protein interaction in systemic circulation. Unopsonized NPs have a longer half-life and residence time in the blood due to immune system evasion (Mohamed et al., 2019).

3.3.5 *In vivo* biodistribution

The free Dox, Dox@GO NPs, and Dox@GO(mPP) (1/0.5) NPs were intravenously injected into 4T1-Luc tumor-bearing mice to study the *in vivo* biodistribution of the nanocomposites. *In vivo*, we obtained the fluorescence distribution of Dox at 0, 0.5, 1, 3, 6, 12, 24, and 36 h **Figure 3.13A, B, and C** show that 30 min after the injection, free Dox, Dox@GO NPs, and Dox@GO(mPP) (1/0.5) NPs treated groups had a prominent fluorescence signal from the liver, which might be attributable to the liver's high macrophage uptake. The fluorescence intensity at the tumor site of the Dox@GO(mPP) (1/0.5) NPs treated group steadily rose up to 12 h post-injection, but the free Dox, Dox@GO NPs treated group had a considerably lower signal, showing that the Dox@GO(mPP) (1/0.5) NPs may gradually clump at the tumor site. The tumor in the Dox@GO(mPP) (1/0.5) NPs treated group still has a strong fluorescence signal 24 h after injection, indicating that the Dox@GO(mPP) (1/0.5) NPs have high targeting and retention capacity. **Figure 3.13D, E, and F** depict *ex vivo* fluorescence pictures of dissected tissues taken 24 h after injection. The tumor fluorescence in the Dox@GO(mPP) (1/0.5) NPs treated group is much greater than in the free Dox group, and the Dox@GO NPs group shows

that the Dox@GO(mPP) (1/0.5) NPs may efficiently accumulate in the tumor location (**Figure 3.13G**). Additionally, both groups detected no significant fluorescence signals in the lungs, heart, or spleen. However, mild fluorescence signals in the kidney and liver were observed in both groups, potentially due to effective renal elimination (**Figure 3.13H**).

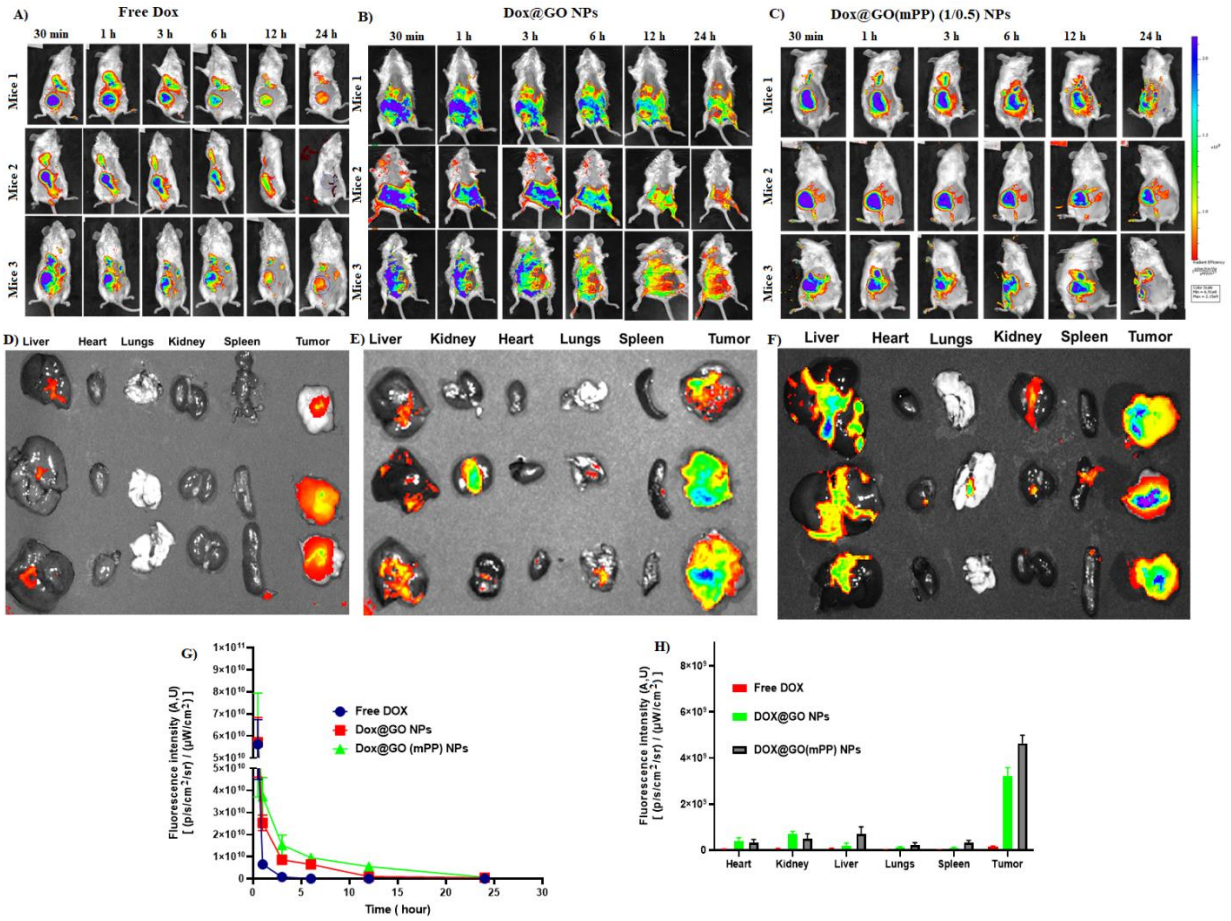

Figure 3.13 Examination of *in vivo* biodistribution of a free DOX, Dox@GO, and Dox@GO(mPP) NPs in 4T1-LUC tumor-bearing mice using a technique called IVIS imaging at Dox dose of 5 mg/kg. Pictures taken at specific intervals after the injection (A, B, C); graph showing the relationship between fluorescence intensity vs time (G); measurement of Dox level in vital organs at 24 h post-injection (D, E, F) and bar graph of fluorescence intensity of Dox signals in various organs (H). The data is shown as the average value ± SD.

Table 3.5 Mean plasma concentration-time profiles of Dox after IV administration of a single 5 mg/kg dose of free Dox, Dox@GO, and Dox@GO(mPP) (1/0.5) NPs to rats.

Parameter	**Unit**	**Free Dox Value**	**Dox@GO Value**	**Dox@GO(mPP) (1/0.5) NPs Value**
Lambda_z	1/h	0.498	0.197	0.0264
$t_{1/2}$	h	1.395	3.53	26.282
$C_{0.5}$	μg/mL	4.125	27	44.08
C0	μg/mL	5.472	37.385	61.305
AUC 0_t	μg/mL*h	11.577	84.372	678.921
AUC 0-inf_obs	μg/mL*h	12.092	90.471	942.936
MRT 0-inf_obs	h	1.810	3.594	36.707
Vz_obs	(mg/kg)/(μg/mL)	0.832	0.281	0.202
Cl_obs	(mg/kg)/(μg/mL)/h	0.414	0.056	0.006

3.3.6 *In vivo* antitumor activity of Dox@GO(mPP) (1/0.5) NPs

We investigated the *in vivo* anticancer potential of Dox@GO(mPP) (1/0.5) NPs after being encouraged by the remarkable *in vitro* combined chemo-photothermal therapeutic activity of Dox@GO(mPP) (1/0.5) NPs. The PBS, free Dox, and Dox@GO(mPP) (1/0.5) NPs were administered intravenously into 4T1-Luc tumor-bearing mice (100 mm^3). The tumor regions of the mice in the Dox@GO(mPP) (1/0.5) NPs groups were exposed to 808 nm NIR laser irradiation (0.25 or 0.5 W/cm^2) for 5 min. The thermal images of the tumor region in mice

administered with Dox@GO(mPP) (1/0.5) NPs and exposed to an 808 nm laser are shown in **Figure 3.16H.**

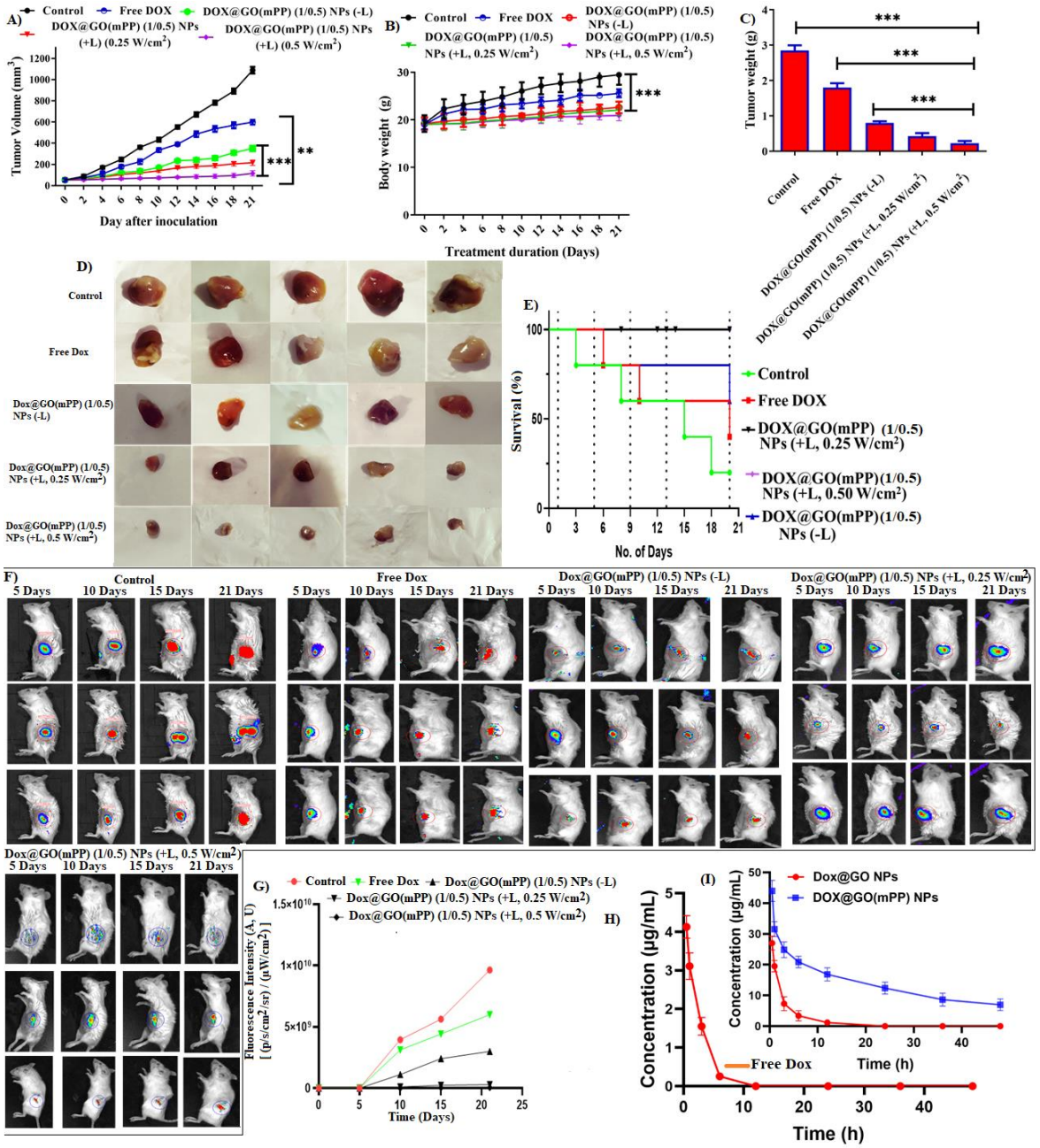

Figure 3.14 Evaluating the effectiveness of free Dox and Dox@GO(mPP) (1/0.5) NPs (± L) (0.25, 0.5 W/cm2) (808 nm) in treating 4T1-LUC tumor bearing BALB/C mice. A graph showing tumor volume change over time during treatment, with days on x-axis and tumor volume on y-axis (A); evaluation of body weight gain or loss as a result of therapy (B); the

mean tumor mass for each treatment group (C); post-treatment mice tumors (D); survival rate graph (E); and IVIS imaging of 4T1 LUC tumor-bearing mice following IV injection of free Dox and Dox@GO(mPP) (1/0.5) NPs formulation at 5 mg/kg Dox dosage, pictures acquired at preset post-injection time intervals. (F); a graph showing the relationship between fluorescence intensity vs time (G); average plasma concentration-time profiles of free Dox following IV delivery of a single 5 mg/kg dose (H), Dox@GO, and Dox@GO(mPP) (1/0.5) NPs to rats (I). The data is represented as mean ± SD.

The mean temperature of the tumor site immediately increased to 54.5 °C and 46.8 °C, respectively, after being irradiated with the 808 nm laser at 0.5 W/cm^2 and 0.25 W/cm^2, respectively (**Figure 3.16I**). This temperature is sufficiently high for PTT and to trigger the release of Dox. Following laser irradiation, the tumor area of the PBS-treated mice increased by 2 °C, and no change in the temperature of the surrounding tissue was observed without exposure to NIR laser radiation. The tumor development of the Dox@GO(mPP) (1/0.5) NPs group was significantly suppressed by the laser at 0.5 W/cm^2 due to the outstanding combined photothermal and chemotherapy property of Dox@GO(mPP) (1/0.5) NPs (**Figure 3.14A, D**). Moreover, chemotherapy alone Dox@GO(mPP) (1/0.5) NPs (-L) also suppressed tumor development, although not as well as the combinational therapy group. Photothermal heating might promote drug release from Dox@GO(mPP) (1/0.5) NPs, resulting in an increased chemotherapeutic action, which could explain the outstanding combinational therapeutic effect. On the other hand, photothermal heating has been shown in a number of prior investigations to considerably enhance nanomaterial internalization by increasing cell membrane permeability (L. Feng, Yang, et al., 2013; Tian et al., 2011). These findings demonstrated that when Dox@GO(mPP) (1/0.5) NPs were coupled with NIR laser irradiation, an effective combinational chemo-photothermal treatment effect for anticancer therapy could be achieved. **Figure 3.14A** shows the tumor progression over 21 days in different treatment

groups. The growth in tumor volume was faster in PBS-treated control animals than in other treated groups, while Dox@GO(mPP) (1/0.5) NPs (+L) exhibited the slowest rate of increase in tumor volume. The average tumor volumes post 21 days were 1088 ± 96 mm^3, 598 ± 37 mm^3, 350 ± 26 mm^3, 215 ± 17 mm^3, 115 ± 12 mm^3 for control, Free Dox, Dox@GO(mPP) (1/0.5) NPs (-L), Dox@GO(mPP) (1/0.5) NPs (+L, 0.25 W/cm^2) and Dox@GO(mPP) (1/0.5) NPs (+L, 0.5W/cm^2), respectively. Moreover, the mice's body weights were likewise recorded. **Figure 3.14B** shows that the body weight of mice in all experimental groups did not change significantly, indicating good biocompatibility and biosafety of Dox@GO(mPP) (1/0.5) NPs *in vivo* application. The tumor weight in the Dox@GO(mPP) (1/0.5) NPs (+L, 0.25, 0.25 W/cm^2) treated group was significantly reduced When compared to the control group, free Dox and Dox@GO(mPP) (1/0.5) NPs (-L) (**Figure 3.14C**).

3.3.6.1 *In vivo* fluorescence imaging

Furthermore, the bioluminescence imaging (BLI) indicated that tumors in the control group had the highest BLI intensity compared to the other treatment groups. **Figure 3.14F, G** shows the acquired BLI intensities around the region of interest. Dox@GO(mPP) (1/0.5) NPs (+L, 0.5W/cm^2) group showed lowest BLI intensity followed by Dox@GO(mPP) (1/0.5) NPs (+L, 0.25W/cm^2), Dox@GO(mPP) (1/0.5) NPs (-L), and free Dox. The findings demonstrated that tumor volume increased over time in all groups, with the control group growing significantly higher than the treatment groups, which correlated to the tumor volume inhibition study. When the tumor volume in the PBS-injected mice reached about 1100 mm^3, all mice were anesthetized and removed the tumor. The tumor weight was significantly lower in the Dox@GO(mPP) (1/0.5) NPs (+L, 0.5 W/cm^2) treated group compared to the other groups **(Figure 3.14D)**. In **Figure 3.14E**, the Kaplan-Meier curve was used to depict the percentage survival of the Dox@GO(mPP) (1/0.5) NPs (±L) treated, free Dox, and control group mice.

Mice treated with Dox@GO(mPP) (1/0.5) NPs and laser (0.5 W/cm^2 or 0.25 W/cm^2) irradiation lived for more than 21 days without dying and showed a 100 % survival rate compared to free Dox and Dox@GO(mPP) (1/0.5) NPs mice group without laser. These results demonstrated that PTT suppresses tumor growth and enhances the laser-treated mice's percentage survival.

3.3.6.2 Immuno-histochemical analysis

The therapeutic effect of treatments was further examined by staining the tumor tissues with DCFDA dye, the terminal deoxynucleotidyl transferase-mediated dUTP nick end labeling (TUNEL) assay, and Ki-67, which allow immunohistochemically detection of proliferating and apoptotic cells, respectively (**Figure 3.15**). In the ROS and TUNEL assays (**Figure 3.15B, D**), more bright green fluorescence was observed in tumor samples following treatment with Dox@GO(mPP) (1/0.5) NPs (+L, 0.5 W/cm^2) compared to other treatment groups confirmed more apoptotic bodies and significant production of ROS. In the Ki-67 assay (**Figure 3.15C**), more cell proliferation was observed in the control group (greenest fluorescence) and least in Dox@GO(mPP) (1/0.5) NPs (+L, 0.5 W/cm^2) treatment group indicated Ki-67 positive tumor cells were nearly completely absent in Dox@GO(mPP) NPs (+L) treatment group, confirming the least tumor growth. The organ damage in treatment groups was further evaluated by hematoxylin and eosin (H&E) staining, as shown in **Figure 9A**. One of the serious adverse effects of DOX-mediated chemotherapy is cardiotoxicity (J. Liu et al., 2016). As a result, H&E staining was used to examine the cardiac tissues of mice groups that had been given free Dox or different formulations. The cardiac segment of the Dox-treated mice group shows evident neutrophil accumulation when compared to that of the PBS group, indicating severe cardiotoxicity of free Dox. Surprisingly, when delivered with Dox@GO(mPP) (1/0.5) NPs (+L, 0.25 or 0.5 W/cm^2), it is conceivable that localized dox release and reduced dox diffusion from the primary tumor to the heart are accountable for the considerable reduction in the

cardiotoxicity caused by Dox . There was no histological damage to the other organs, such as the kidney, lungs, spleen, and liver, confirming the formulation's low toxicity.

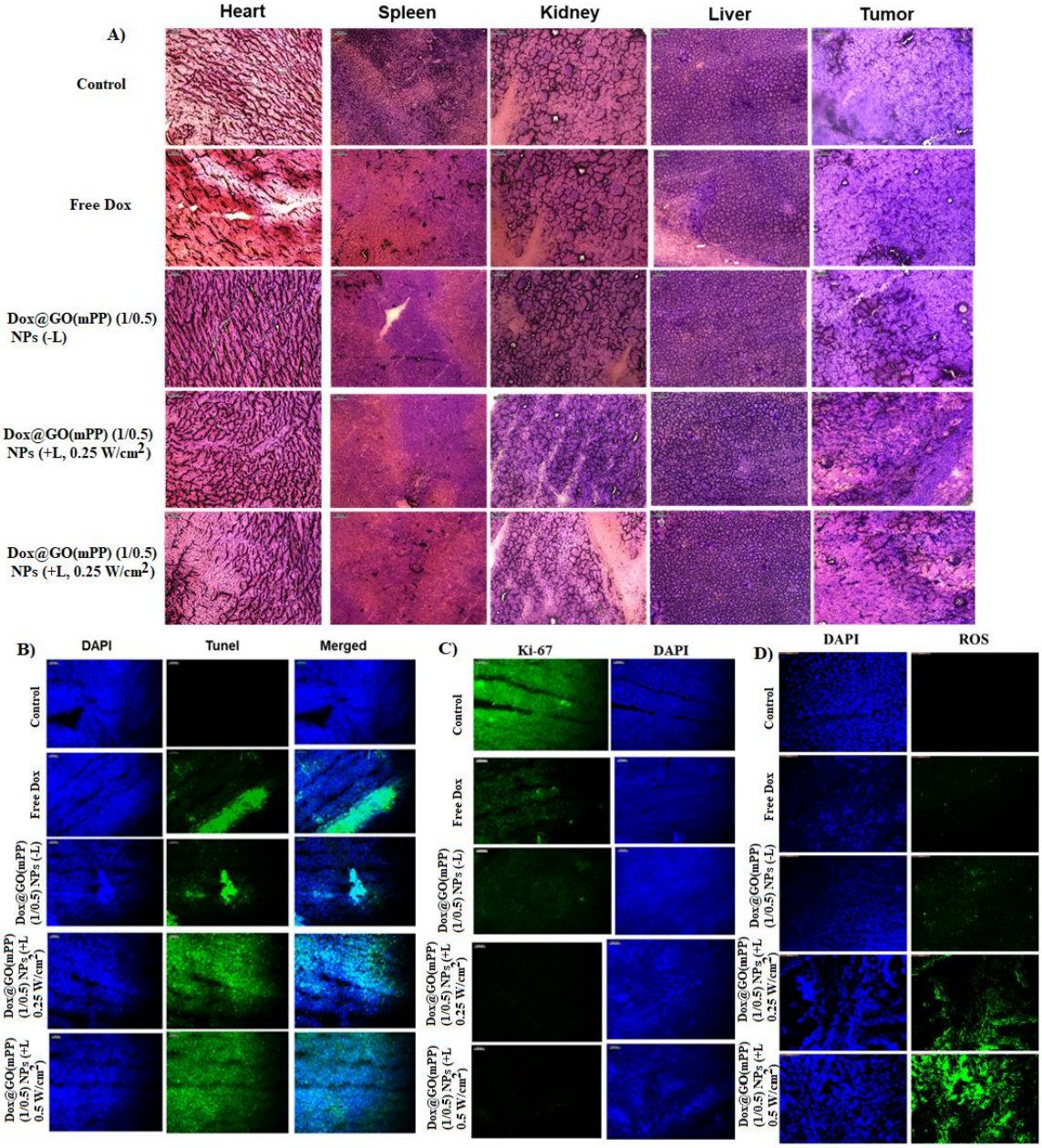

Figure 3.15 Histology examination of frozen mice organ slices (6 µm) utilizing hematoxylin and eosin (cytoplasm: pink, and nucleus: purple) (A). Scale bar. 100 µm. TUNEL test in cryosections of tumor tissue examined under a fluorescence microscope, magnification-20X (B); examination of the histology of tumors immunostained with KI-67 from various treatment

groups (C); an investigation on the production of ROS in 4T1-LUC tumor-bearing mice utilizing the fluorescent probe DCFH-DA (D). The data is represented as mean ± SD.

3.3.6.3 Metastasis study

The delayed and late stages of cancer development are characterized by spontaneous metastasis (Moreno-Smith et al., 2010). The lung organs were taken after the anticancer study and investigated using bioluminescence (BLI) measurement following luciferin treatment to demonstrate the effectiveness of Dox@GO(mPP) (1/0.5) NPs + laser-treated animals to inhibit lung metastasis of 4T1 breast tumor. The greatest BLI signals were shown in the lung of the PBS and Free Dox treated groups in the photographic pictures showing exceptional metastasis of 4T1 cancer cells from the original tumor to the lung (**Figure 3.16A, C, and E**). The lung metastasis of Dox@GO(mPP) (1/0.5) NPs (-L) treated group was somewhat inhibited, which may be related to the reduction of tumor development caused by Dox. The metastatic lesions in the lungs were significantly decreased by Dox@GO(mPP) (1/0.5) NPs (+L, 0.25 or 0.5 W/cm^2) treated group. The lung metastasis of mice was quantified by monitoring the number of pulmonary metastasis nodules. **Figure 3.16B, F** demonstrates that there are hardly any metastatic nodules visible in the mice group treated with Dox@GO(mPP) (1/0.5) NPs (+L, 0.25 or 0.5 W/cm^2) than the lung tissue of the PBS, free Dox, and Dox@GO(mPP) (1/0.5) NPs (-L) group. The weight of the lungs has also grown due to the presence of metastatic nodules; it was greatest in the tumor-bearing untreated control group and lowest in the group that received treatment with Dox@GO(mPP) (1/0.5) NPs (+L, 0.25 or 0.5 W/cm^2) (**Figure 3.16D**). This suggested that Dox@GO(mPP) (1/0.5) NPs + laser group had the strongest antimetastatic effectiveness, which was also supported by H&E staining of the lung tissue (**Figure 3.16G**).

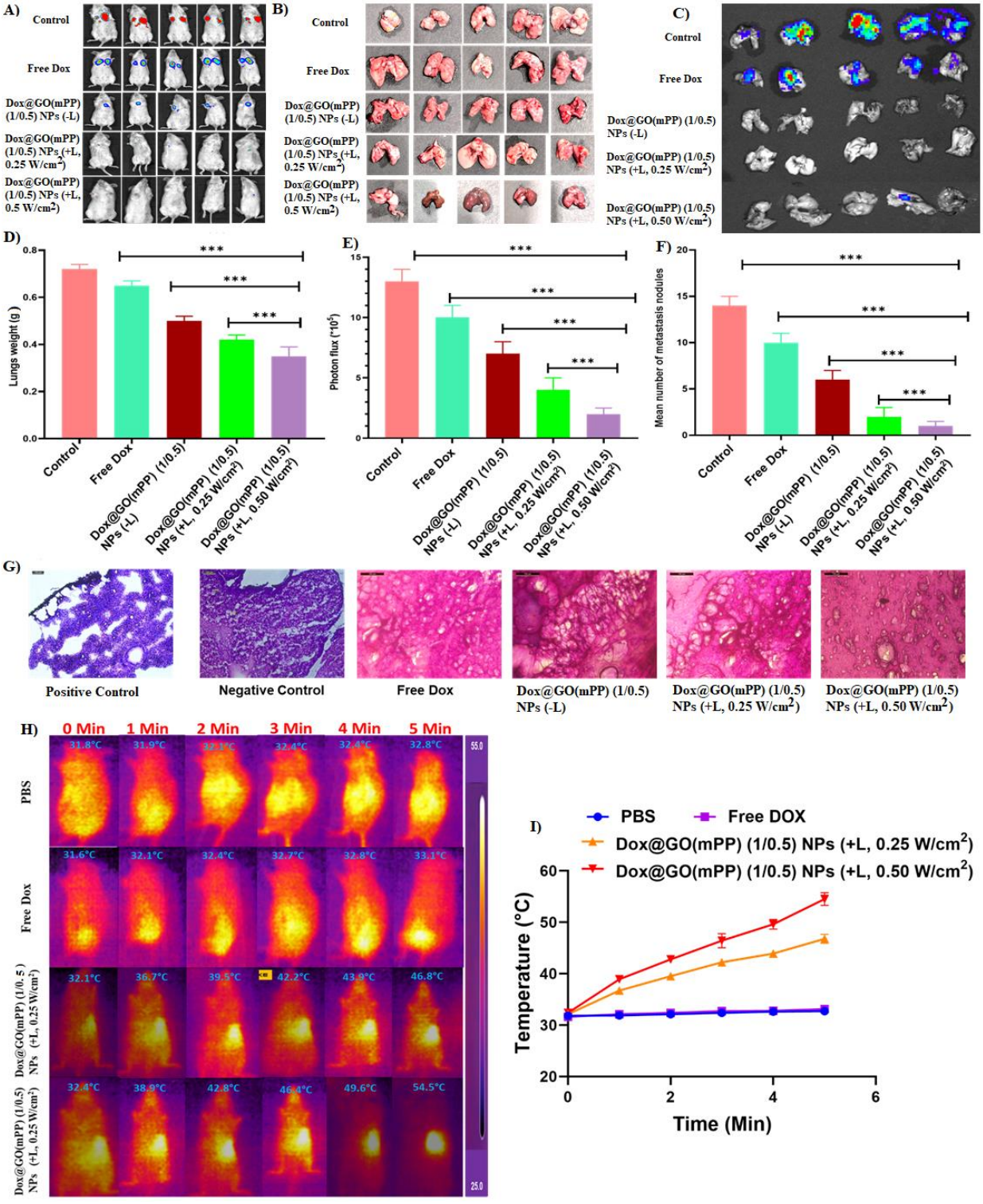

Figure 3.16 Reduction of metastasis of 4T1-Luc cells in lungs by Dox@GO(mPP) (1/0.5) NPs (± L) treatment (power density 0.25, 0.5 W/cm2). Imaging of live mice to evaluate metastases on day 7 after surgery (n=5) and the bioluminescence bar graph (A); visual representation of lungs of free dox, and Dox@GO(mPP) (1/0.5) NPs (± L) (0.25, 0.5 W/cm^2) mice groups to

examine the growth of metastatic nodules of 4T1 cells (B) and lungs/nodules in the free Dox, and Dox@GO(mPP) (1/0.5) NPs (± L) (0.25, 0.5 W/cm^2) treatment groups are shown in a bar graph (F); Intensities of ex-vivo bioluminescence in lung tissues of free Dox, and Dox@GO(mPP) (1/0.5) NPs (± L) (0.25, 0.5 W/cm^2) (C, E) and bar graph representation of lung weight (D). Tumor metastasis in lung sections was detected using hematoxylin and eosin staining. Scale bar.100 µm (G). IR thermal images of PBS, free Dox, and Dox@GO(mPP) (1/0.5) NPs (± L)-injected 4T1-Luc tumors after laser illumination (0.25, 0.5 W/cm^2) (H). The photothermal effect of free Dox and Dox@GO(mPP) (1/0.5) NPs (± L) in 4T1 tumor-bearing mice *in vivo* (I). The significance of the difference was analysed by paired t-test (*** $p < 0.001$). According to the histopathological results, the lungs of the tumor-bearing untreated mice showed a dense tissue population indicative of metastatic sites. On the other hand, the lung histology of the Dox@GO(mPP) (1/0.5) NPs laser-treated group was comparable to that of normal, non-tumor implanted animals. Similar findings have also been observed in other places (F. Wang et al., 2016). These findings confirmed the efficacy of Dox@GO(mPP) (1/0.5) NPs in combination with 808 nm NIR laser irradiation in suppressing tumor metastasis.

3.4. Conclusion

Herein, we innovatively synthesized GO-based NPs system GO(mPP), demonstrating a structural change of GO sheets to a stable nanosized 3D colloidal spherical structure, which is amenable for drug delivery and tissue penetration. Among various tested GO: mPP ratios, Dox@GO(mPP) (1/0.5) NPs were selected for its smallest size, superior drug carrying capacity. A thorough physicochemical characterization was performed followed by *in vitro* studies using TNBC cells, and *in vivo* studies using TNBC-bearing mouse model to assess the therapeutic effectiveness. The results demonstrated that the NPs treatment with laser was highly efficient in inducing apoptosis, significant cytotoxicity, mitochondrial membrane

depolarization, and ROS generation leading to a higher proportion of cell death than free Dox and Dox@GO(mPP) NPs without laser. Furthermore, the pK study following administration of an intravenous bolus dose of doxorubicin indicated that the Dox@GO(mPP) (1/0.5) NPs had higher AUC, extended $t_{1/2}$, and more MRT with slower clearance than free Dox and Dox@GO NPs. *In vitro*, we realized the GO-mediated photothermal effect upon irradiation using NIR (808 nm) in the cancer cells, and *in vivo*, we observed the effect in tumors. The *in vivo* anticancer potential of Dox@GO(mPP) (1/0.5) NPs in 4T1-Luc tumor-bearing mice showed that the combination of Dox@GO(mPP) (1/0.5) NPs and targeted laser irradiation could concurrently slow the development of the main tumors and inhibit their distant metastasis. The developed colloidal nanoplatform could be a potential treatment option for TNBC by the combined chemo-photothermal therapeutic strategies.

3.5 Acknowledgments

Prof. Swati Biswas acknowledges the support from Department of Science and Technology-Science and Engineering Research Board (DST-SERB), India (Grant no. CRG/2018/001065). The authors also sincerely acknowledge the use of *in vivo* imaging facility, which is supported by the DST-FIST research grant [SR/LS-II/2018/210]. The Central Analytical Laboratory, Birla Institute of Technology and Science (BITS), Pilani, Hyderabad Campus, India, is thoroughly gratified by the authors for providing the instrumentation facilities like Confocal microscope, UV, and Fluorescence spectrophotometer, XPS, XRD, DSC, FACS, and SEM instrument for different characterizations. Mr. Asif Mohd Itoo thanks Lady Tata Memorial Trust, India, for the junior research fellowship.

Chapter 4

Biotinylated graphene oxide-conjugated platinum (IV) prodrug nanoparticles for targeted and chemophotothermal combination therapy in Breast cancer

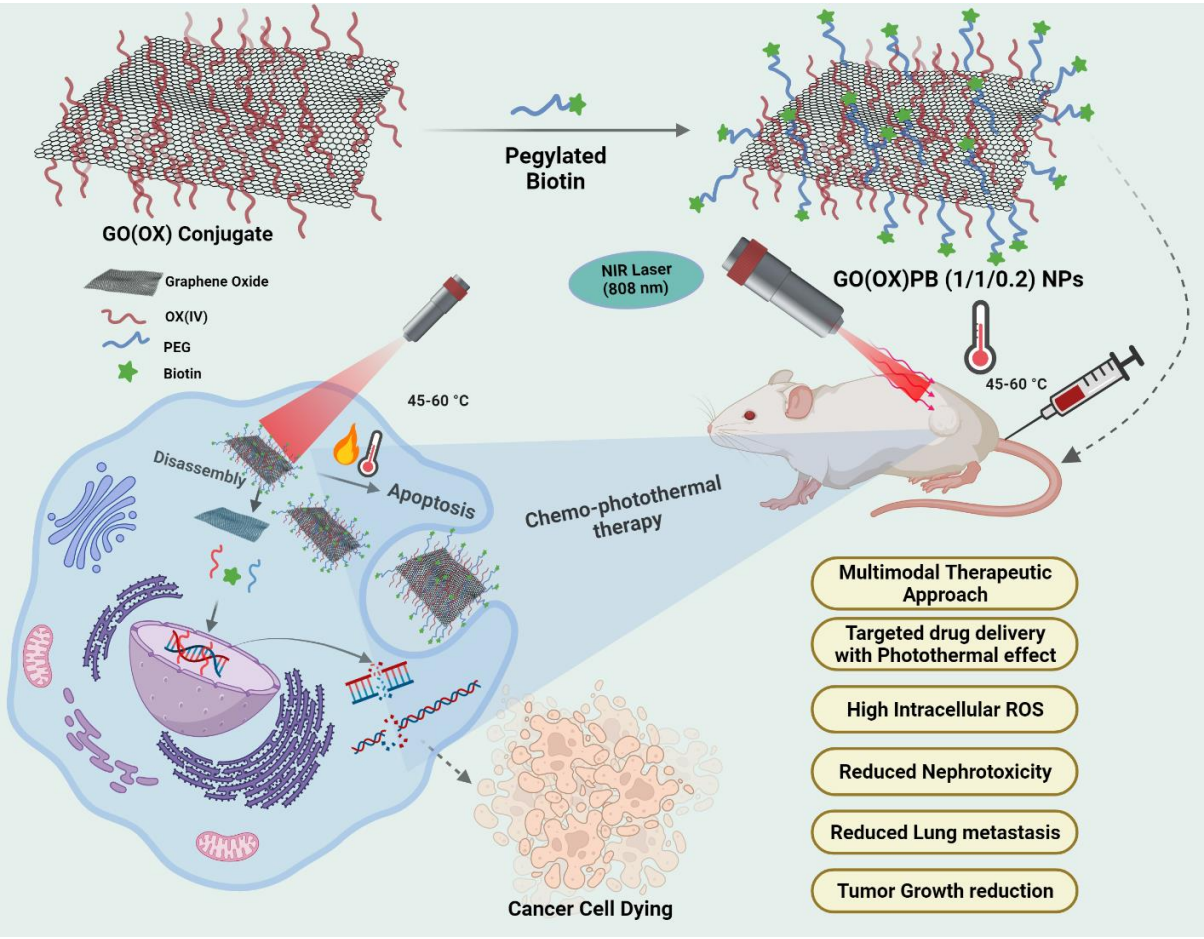

4.1 Introduction

Breast cancer (BC) is the most prevalent form of cancer in women globally, accounting for 266,120 new cases and 40,920 fatalities per year (V. Thakur & Kutty, 2019). The prevalence of BC poses a notable public health issue, anticipating that approximately 12.5% of women in the United States will experience the onset of invasive BC over the course of their lives (Alkabban & Ferguson, 2019). In 2023, the United States had 55,720 newly diagnosed instances of *in situ* BC and 297,790 newly diagnosed cases of invasive BC, as per recent estimates (Alkabban & Ferguson, 2019; Giaquinto et al., 2022; Siegel et al., 2023). Metastatic BC has a significantly high death rate and a pessimistic prognosis, as indicated by a 5-year relative survival rate of 29% (Giaquinto et al., 2022). Therefore, early detection and efficient treatment of BC, particularly in cases of metastatic-stage cancers, are crucial for extending the survival of patients. Presently, BC is commonly treated through a variety of methods, including surgical intervention, hormonal therapy, radiation therapy, chemotherapy, immunotherapy, and targeted therapies (Giaquinto et al., 2022; Siegel et al., 2023). The process of targeted drug delivery entails the utilization of specialized carriers, including antibodies, vitamins, and peptides, to convey drugs to tumor sites with precision while simultaneously reducing the exposure of healthy tissues to the drugs. (Zhong et al., 2014). Vitamin-based drug targeting is a promising idea since some vitamins, such as riboflavin, biotin, vitamin B12, and folic acid, are selective targeting agents for overexpressed cancer cell receptors (Vinothini et al., 2019). Biotin, also referred to as Vitamin H or B-7, has been scientifically demonstrated to have a significant impact on the growth and spread of tumors by disrupting essential cellular processes. Moreover, research has demonstrated that cancer cells exhibit a greater abundance of biotin receptors on their cellular membrane compared to normal cells, highlighting the significance of biotin in the development of tumors (Mauro et al., 2015).

Among the highly targeted, selective, and successful anticancer therapies, photothermal therapy (PTT) is another therapeutic modality that uses photothermal conversion agents to convert light energy into heat, resulting in the localized killing of cancer cells. Because of its specificity in both place and time, as well as its synergistic benefits and low invasiveness, this method has attracted attention as an innovative treatment option (Rajani et al., 2020; Zou et al., 2016). PTT has demonstrated reduced harm and fewer adverse impacts on healthy tissues in comparison to chemotherapy due to its safety, non-invasive nature, and enhanced regulation. Moreover, research has shown that PTT is superior to chemotherapy in the treatment of superficial malignancies, including those found in BC (J. Liu et al., 2020; Rajani et al., 2020). Recently, there has been significant progress in the development of diverse nanomaterials for PTT, exhibiting outstanding capabilities in converting light into heat and delivering effective therapeutic outcomes. Hence, the choice of an optimum photothermal agent is pivotal for the effective management of cancer. Graphene and its derivatives are currently being extensively studied as prospective drug carrier systems for precise and controlled delisvery in cancer therapy, leading to a surge in interest.

Graphene oxide (GO) is a 2D-carbon atom with hydrophilic groups, including epoxide, carboxyl, and hydroxyl groups, spread across its extensive surface. It can be effortlessly mixed with water and modified using both non-covalent and covalent methods (Goenka et al., 2014; J. Liu et al., 2013; Mohd et al., 2022b; K. Yang et al., 2013). GO has been thoroughly investigated as a promising photothermal agent for delivering drugs in cancer treatment due to its ability to be taken up by cells, its huge surface area, excellent biocompatibility, and the presence of other functional biomolecules (Y.-J. Lu et al., 2014; B. Ma et al., 2021; Mohd et al., 2022a; J.-J. Shi et al., 2022; Q. Wu et al., 2016). More significantly, GO is a promising nanoscale substance with the ability to reach elevated temperatures and induce hyperthermia, ultimately leading to the thermal destruction of cancer cells (Chang et al., 2016; W. Jiang et

al., 2018; Shao et al., 2017). Non-covalent interactions such as hydrophobic, π-π stacking, and electrostatic interactions are frequently used to modify GO with drug molecules. Additionally, the non-toxicity and excellent biocompatibility of GO make it a promising drug carrier when combined with various polymers, vitamins, and active pharmaceutical ingredients (Mauro et al., 2015; Pourjavadi et al., 2016). Utilizing targeting agents like biotin or folic acid to modify graphene oxide (GO) enables the selective targeting of breast cancer cells that have an overexpression of specific receptors. This modification enhances the ability of GO to penetrate tumors, increases its surface potential, and improves its cellular uptake. Consequently, GO becomes suitable for multimodal synergistic therapeutic applications and specific targeted drug delivery while minimizing the heating of healthy cells (Iyer et al., 2006). GO is a promising material for cancer nanomedicine due to its ability to enhance drug loading and release, as well as its ability to be activated by light for controlled drug release through photothermal processes. Recently, biodegradable polymers such as poly(lactic-co-glycolic) acid (PLGA), poly(lactic acid) (PLA), albumin, chitosan, and gelatin have been utilized to modify the surface of GO due to their ability to release continuously (Mohd et al., 2022b). Among the stabilizing agents, polyethylene glycol (PEG) is the most widely researched. The functionalization of graphene oxide to polyethylene glycol enhances the stability of the material in aqueous solutions and increases its biocompatibility, making it a suitable candidate for use in drug delivery systems.

Herein, the study presents the development of a novel therapeutic approach involving oxaliplatin (IV) prodrug, PEGylated graphene oxide, and PEGylated biotin (PB) in a single platform for BC treatment. This platform demonstrates promising prospects for targeted drug delivery and the synergistic application of photothermal-chemotherapy when exposed to NIR-laser irradiation. The synthesis of GO was successfully achieved through a modified Hummers method, followed by conjugation with various ratios of OX(IV) to form GO(OX)(IV). OX(IV) is a derivative of the chemotherapy drug oxaliplatin, offering potential advantages, such as

increased water solubility for consistent dosing, reduced toxicity, enhanced stability leading to prolonged and effective treatment, decreased neurotoxicity and nephrotoxicity, and greater specificity (J. Kim et al., 2015). The resulting GO(OX) (1/1) conjugate was further modified by conjugating it with PEG and pegylated biotin (PB), resulting in the formation of GO(OX)PEG (1/1/0.2) NPs and GO(OX)PB (1/1/0.2) NPs. These NPs underwent comprehensive physicochemical characterization, and their therapeutic efficacy was evaluated in both *in vitro* and *in vivo* experiments using metastatic triple-negative breast cancer (TNBC) models, enabling targeted drug delivery to tumors. The collective findings from both *in vitro* and *in vivo* studies demonstrated enhanced therapeutic efficacy while reducing the toxicity to the overall system, highlighting the excellent synergistic impact of the combined chemotherapeutic and photothermal effects of the GO(OX)PB (1/1/0.2) NPs.

4.2. Materials and methods

4.2.1 Materials

Graphite, succinic anhydride, Polyethylene glycol (PEG), N, N'dicyclohexyl carbodiimide (DCC), 4-Dimethylaminopyridine (DMAP), Dimethylformamide (DMF), hydrogen peroxide, potassium permanganate, biotin, dimethyl sulfoxide (DMSO), calcein AM, rhodamine B, and paraformaldehyde were purchased from Sigma-Aldrich (Bangalore, India). 5,5,6,6'-tetrachloro-1,1',3,3' tetraethylbenzimi-dazoylcarbocyanine iodide (JC-1) dye was purchased from ThermoFisher scientific. Fetal bovine serum (FBS), DMEM medium, trypsin, penicillin-streptomycin, and Methylthiazolyldiphenyl-tetrazolium bromide (MTT) were purchased from Himedia Labs (India). Annexin V-FITC/PI apoptosis and necrosis detection kit was obtained from R&D systems (Minneapolis, USA). All other reagents and solvents were provided by Sigma-Aldrich (Bangalore, India and used as received. Oxaliplatin was received as a free sample from Neon laboratories Ltd. (India).

Cell lines:- Human breast cancer cells (MCF-7), mouse mammary gland adenocarcinoma cells (4T1), and Mouse mammary gland luciferase-expressing adenocarcinoma cells (4 T1-Luc) were sourced from the American Type Culture Collection (ATCC, USA).

Animals: *In vivo* experiments adhered to CPCSEA guidelines (BITS-Hyd/IAEC/2021/26) approved by IAEC, Department of Pharmacy, BITS Pilani, Hyderabad. Male Wistar rats (220 g, 7–8 weeks) were used for pharmacokinetic studies, and female Balb/c mice (20–22 g, 6–8 weeks) were used for the tumor xenograft model. Animals were obtained from the National Centre for Laboratory Animal Sciences housed according to experimental needs in a controlled environment (23 ± 2 °C, 60 ± 10% humidity, 12h light/dark cycle).

4.2.2 Methods

4.2.2.1 Synthesis of Graphene oxide (GO)

The modified Hummer's approach was employed to synthesize GO from pristine graphite powder (B. Wang et al., 2018). The process entailed combining sulfuric acid (H_2SO_4) and phosphoric acid (H_3PO_4) in a volume ratio of 9:1, agitating for a brief period, and introducing graphite powder into the solution. Subsequently, potassium permanganate ($KMnO_4$) was gradually introduced into the solution, and the resulting mixture was agitated for a duration of 6 h until it acquired a deep green color. The surplus $KMnO_4$ was eliminated by introducing hydrogen peroxide (H_2O_2) and agitated for a duration of 10 min. Following the cooling of the exothermic reaction, hydrochloric acid (HCl) and deionized water were introduced into the solution, which was subsequently subjected to centrifugation (Zaaba et al., 2017). The liquid portion was extracted, and the remaining substances were rinsed repeatedly in a furnace prior to being dehydrated to generate the GO powder.

4.2.2.2 Synthesis of Oxaliplatin prodrug, OX(IV)

To initiate the reaction, OX (0.25 g, 0.63 mmol) was dissolved in 4 mL of 30% hydrogen peroxide. The reaction was permitted to occur at ambient temperature for a duration of 24 h.

The solution was subsequently concentrated using rotary evaporation to acquire the unprocessed product. The product was dissolved in methanol at a low temperature and then separated out by precipitation in ethyl ether at a low temperature. The obtained compound was subjected to two washes with cold ethyl ether and then dried under a vacuum. This process resulted in the formation of OX(IV)-OH, which was obtained as a white powder with a yield of 97 %. For the second step, a solution of OX(IV)-OH (0.215 g) in 3 mL of DMSO was prepared, and then succinic anhydride (0.050 grams) was added to it. The reaction was allowed to occur for 12 h at ambient temperature in the absence of light. The solution was subsequently precipitated in cold ethyl ether, subjected to two washes with cold ethyl ether, and dried under a vacuum. This process resulted in the production of OX(IV)-COOH, which was obtained as a white powder with a yield of 93%.

4.2.2.3 Synthesis of GO(OX)(IV) Conjugate

The synthesis of the GO(OX)(IV) conjugate was accomplished through an esterification reaction where GO was combined with OX(IV)-COOH in different ratios (1:1/2/5/10). The reaction took place in the presence of DCC and DMAP as catalysts, using DMF solvent at room temperature for a duration of 24 h. The combination obtained was subsequently dehydrated by evaporation, rehydrated with deionized water, purified by dialysis using a cellulose ester membrane with a molecular weight cut-off of 2 KDa, and ultimately freeze-dried. The masses of OX(IV)-OH and carboxylated OX(IV) were verified using LCMS (Shimadzu).

4.2.2.4 Synthesis of Pegylated Biotin (PB) copolymer

To produce PB conjugate, a solution was prepared by dissolving 100 mg of PEG-bis-amine in 1 mL of anhydrous DMSO and stirring it for a duration of 30 min. Subsequently, a quantity of Biotin (12.21 mg) was introduced into the PEG-bis-amine solution, and the resulting combination was agitated for the duration of one night. The resultant combination underwent filtration and was subsequently subjected to treatment with distilled water. It was then dialyzed

against deionized water for a duration of 48 h, using a molecular weight cut-off of 2000 Da. The ultimate solution was freeze-dried for subsequent use, and the chemical composition of the PB conjugate was examined using FTIR, 1H NMR spectroscopy, and MALDI-TOFF analysis.

4.2.2.5 Synthesis of GO(OX)PEG conjugate

The GO(OX)PEG conjugate was formed by linking the carboxyl group of GO(OX)(IV) to the amino groups of PEG bis amine using EDC and NHS as catalysts. The procedure entailed dissolving the GO(OX)(IV) (1/1) conjugate in DMF and subsequently introducing PEG at varying proportions. This was followed by the addition of EDC, NHS, and 20 µL of tri ethyl amine (TEA). The product was further purified using dialysis in water with a pH of 5.5, utilizing a dialysis membrane with a molecular weight cut-off (MWCO) of 2 kDa. Following purification, the product was either freeze-dried or lyophilized. The chemical structure of the conjugate was analyzed using Fourier Transform Infrared Spectroscopy (FTIR) and X-ray Photoelectron Spectroscopy (XPS).

4.2.2.6 Synthesis of GO(OX)PB conjugate

The GO(OX)PB conjugate was synthesised by connecting the carboxyl group of the GO(OX)(IV) (1/1) conjugate to the amine groups of PB utilising EDC and NHS as coupling agents. Specifically, a solution of 1 mg of GO(OX)(IV) (1/1) conjugate was prepared by dissolving it in DMF. This solution was then combined with different ratios (1:0.1/0.2/1:0.5) of PB, along with the relevant quantities of EDC, NHS, and 20 µL of TEA. The product underwent dialysis in distilled water with a pH of 5.5, using a cellulose acetate membrane with a molecular weight cutoff of 2 kDa. After that, it was either freeze-dried or lyophilized. The chemical structure of the conjugate was examined by FTIR and XPS investigation.

Fourier Transform Infrared Spectroscopy (FTIR) was used to identify the functional groups and analyze the interactions between functional groups on the surface of GO, OX(IV),

GO(OX)(IV) (1:1/2/5/10), PB, GO(OX)PEG (1:0.1/0.2/0.5) and GO(OX)PB (1:0.1/0.2/0.5) using the KBR pellet approach. The analysis was performed via an FTIR spectrometer (Jasco-4200, USA). The freeze-dried materials were combined with potassium bromide (FTIR grade) and subjected to scanning within the frequency range of 4000-400 cm^{-1} at a resolution of 4 cm^{-1}, with a total of 64 scans. This process was conducted to acquire the spectrum. Moreover, the ^{1}H Nuclear Magnetic Resonance spectroscopy of OX(IV)-OH, OX(IV)-COOH, and PB was performed using a Bruker spectrometer operating at 300 MHz. The specimens were dissolved in a deuterated D2O solution using TMS as an internal reference. An ultraflexTOF/TOF equipment was used to conduct a MALDI-TOF-MS analysis to estimate the molecular mass of the synthesized polymer (PB). The measurements were conducted using a positive linear mode within the m/z range of 2,000-100,000.

4.2.3 Preparation and characterization of GO(OX)PB NPs

4,2.3.1 Preparation of GO(OX)PB NPs

The GO(OX)PB conjugate was dispersed in DMF to a concentration of 5 mg/mL. It was then stirred for 5 h, and the solvent was eliminated using a rotary evaporator. The polymer film obtained was immersed in 1 mL of PBS pH 7.4 and kept at 37 °C for 2 h. After that, it was treated with ultra-probe sonication using an Ultrasonic Processor with a power of 500 watts, a frequency of 20 kHz, and a current of 35 A for a duration of 1 h. The NPs obtained GO(OX)PB NPs were subjected to centrifugation at a speed of 7,000 rpm for a duration of 10 min. The pellet was resuspended in PBS (pH 7.4), and subsequently freeze-dried using mannitol as a cryoprotectant.

4.2.3.2 Physico-chemical characterization of GO(OX)PB NPs

The average particle size, polydispersity index (PDI), and zeta potential of GO(OX)PB NPs were measured using a Zeta-sizer instrument (Nano ZS3600, Malvern Instruments Ltd, UK) at a temperature of 25°C and wavelength of 633 nm. The instrument utilizes dynamic light

scattering to obtain these measurements. The surface morphology of the optimized formulation GO(OX)PB was characterized using scanning electron microscopy (SEM). In preparation for SEM analysis, a dilution of the OX(IV)-loaded NPs was placed on a carbon tap, left to dry overnight in a desiccator, and then coated with a thin layer of gold. These samples were then examined using a field emission scanning electron microscope (Apreo Lo Vac, FEI, USA).

The entrapment efficiency and drug loading are two important parameters used to evaluate the performance of drug delivery systems such as NPs. The drug loading and entrapment efficiency of GO(OX)PB NPs were determined using an atomic absorption spectrophotometer (AA7000, Shimadzu). This technique allows for the quantification of the drug in the carrier system and in the supernatant, which can be used to calculate the entrapment efficiency and drug loading by the given formula below:

$$\text{EE (\%)} = \frac{Weight\ of\ OX(IV)\ present\ in\ NPs}{Weight\ of\ OX(IV)\ added\ initially} \times\ 100 \qquad \textbf{\textit{Equation 4.1}}$$

$$\text{DL (\%)} = \frac{Weight\ of\ OX(IV)\ present\ in\ the\ NPs}{Weight\ of\ the\ \text{GO(OX)PB NPs.}} \times 100 \qquad \textbf{\textit{Equation 4.2}}$$

In addition, a stability assessment of optimized GO(OX)PB NPs was performed over a 30-day period at two distinct temperature conditions (25 ± 2°C and 4 ± 2°C). At predetermined intervals (5, 10, 15, 20, 25, and 30 days), the mean particle size (Z-average), polydispersity index (PDI), and entrapment efficiency (EE%) of the NPs were analyzed, and the obtained results were compared to those of the freshly prepared NPs.

4.2.3.3 Thermal Analysis

The samples of GO, free OX, GO(OX)PEG NPs, and GO(OX)PB NPs were thermally analyzed using the differential thermal analysis/ thermal gravimetric analysis (DTG/TGA) (DTG-60, Shimadzu, Japan). 5 mg of each sample were placed in aluminum pans and the temperature

range for scanning was between 20-600°C with a scan rate of 10°C/min. The analysis was conducted in a nitrogen atmosphere.

4.2.3.4 X-ray Diffractometry (XRD) analysis

X-ray diffraction (XRD) analysis of graphite, GO, GO, OX, OX(IV), GO(OX)(IV), PB, GO(OX)PEG NPs and GO(OX)PB NPs were performed using the X-ray diffractometer (Rigaku, ULTIMA-IV). The samples were placed on glass substrates, and small-angle XRD measurements were acquired using a super-speed X-ray diffractometer equipped with a nickel filter and a copper radiation source (Cu Kα radiations, k = 0.15405 nm). The device was operated with a tube voltage of 40 kV and a tube current of 30 mA. The samples were scanned within a 2θ range of 2-60 °.

4.2.4.5 X-ray photoelectron spectroscopy

The functionalization of GO GO(OX)(IV), GO(OX)PEG NPs, and GO(OX)PB NPs was evaluated using X-ray photoelectron spectroscopy (XPS) with a monochromatic Al Kα source from Thermo-Fischer, USA. A vacuum pressure of less than 10^{-6} Torr was employed to utilize an X-ray source with an energy of 1375 eV. The pass energy was adjusted to 200 eV for wide scanning and 50 eV for narrow scanning, while the electron take-off angle was configured at 568°. The spectra were examined utilizing the Avantage program.

4.2.4.6 Raman Spectroscopy

The Raman spectroscopy analysis of GO, GO(OX)PEG NPs, and GO(OX)PB NPs was performed using the UniRAM 3300 micro-Raman mapping spectrometer. Prior to analysis, the instrument was calibrated using the crystalline silicon peak at 520 cm^{-1}. The acquisition process utilized an excitation laser with a wavelength of 532 nm, and 30 % of the laser power was employed for the acquisition. The sample was focused using a 50X objective, and the Raman shift center was set at 1600 cm^{-1}. Each laser exposure lasted for 1 second, and a total of 30 accumulations were utilized to collect the final signal.

4.2.4.7 *In vitro* drug release study

The dialysis method was used to evaluate the drug release behavior of GO(OX)PEG NPs and GO(OX)PB NPs, which are responsive to both NIR laser and pH (Paul et al., 2022b). The NP solution was encapsulated in a dialysis bag with a molecular weight cutoff of 2000 Da and immersed in PBS buffer solutions of varying pH (5, 6.8, and 7.4, 100 mL each). The complete arrangement was positioned on a magnetic stirrer, which was functioning at a temperature of 37 °C and a rotational speed of 150 rpm for a pre-established period. Throughout the experiment, a 1 mL sample of the release medium was collected, and an equivalent amount of fresh medium was introduced to uphold sink conditions. Following a duration of 12 h, the sample was subjected to NIR (near-infrared) light with a wavelength of 808 nm, at a power density of 0.5 W/cm^2, for a duration of 5 min. Before and after NIR irradiation, 1 mL of the release media was collected and substituted with a new medium. The quantification of the emitted OX was performed using atomic absorption spectrometry (AA7000, Shimadzu) at a wavelength of 266 nm. The current work entailed the integration of gathered data into various mathematical models, such as the zero-order kinetic model, Weibull model, Higuchi kinetics models, Hixson Crowell model, first-order kinetic model, and Korsmeyer-Peppas model. The aim was to examine the mechanism by which OX is released from GO(OX)PEG and GO(OX)PB NPs. The investigation was conducted with three repeats, and the results were reported as the mean and standard deviation of the recorded data (Mean S.D; n=3).

4.2.4.8 Hemolysis study

The efficacy and biocompatibility of the GO(OX)(1/1) conjugate for *in vivo* applications were investigated using a hemolysis test that relied on red blood cells (RBCs). Concisely, blood from Wistar rats was collected in tubes containing EDTA to stabilize it, and these tubes were also treated with heparin.

In the hemolysis experiment, 200 µL of concentrated red blood cells (RBCs) were mixed with 4 mL of phosphate-buffered saline (PBS) to achieve a hematocrit of 5%. Then, 0.2 mL of the diluted RBC suspension was combined with 0.8 mL of GO(OX) (1/1) suspensions in PBS at concentrations of 25-250 µg/mL. Positive and negative controls were prepared by incubating 1% solution of Triton-X 100 and PBS (0.8 mL) with 0.2 mL of diluted RBC solution, respectively. The mixes were gently agitated and kept at room temperature for a duration of 2 h. The mixes underwent centrifugation at a force of 345 g for a duration of 5 minutes. After that, the supernatant was put into a cuvette, and a UV-visible spectrometer was used to measure the absorbance at 541 nm (Itoo, Paul, Ghosh, et al., 2022). In this context, the hemolytic ratio (HR) was computed using the following formula:

$$\text{Hemolysis (\%)} = \frac{Ab_{Sample} - Ab_{(-)Control}}{Ab_{(+)Control} - Ab_{(-)Control}} \text{X100}$$

4.2.5 Photothermal effect

To examine the photothermal properties of GO, GO(OX) conjugate, GO(OX)PEG (1/1/10.2), and GO(OX)PB (1/1/10.2) NPs. The aqueous dispersions containing varying concentrations of samples were introduced into sample cells and subjected to irradiation (808 nm laser + .5 W/cm^2) for 5 min using NIR laser equipment (MR.FCL.808.T2.2W.MM-OEM, Shanghai MRTRADE International Co., LTD.). In this study, we aimed to examine the impact of distinct laser power densities on the photothermal heating of GO(OX)PB (1/1/10.2) NPs. To achieve this, we conducted experiments utilizing different laser power densities (0.25, 0.5, 1.0, 1.5, 2.0 W/cm^2) and monitored the temperature of the solution in real-time using an IR camera at 20-second intervals. Moreover, the photothermal stability of the GO(OX)PB (1/1/10.2) NPs solution at a concentration of 100 µg/mL was evaluated using an NIR light 808 nm and subjected to 5 laser on/off cycles. Moreover, the photothermal conversion efficiency (η) of the

GO(OX)PB (1/1/10.2) NPs was evaluated using the formula established in a prior study (X. Zhu et al., 2016), as delineated by the subsequent equation.

$$\eta = \frac{hA(T_{max}-T_{amb})-Q_0}{I(1-10^{-A_\lambda})} \qquad \textit{Equation 4.3}$$

Herein, the h denotes the heat transfer coefficient, A represents the container's surface area, T_{surr} stands for the ambient temperature, T_{max} signifies the peak temperature attained by the system during irradiation, Q_{dis} accounts for the energy garnered from light absorption by the sample cell, I denote the laser power, and A_λ corresponds to the absorbance of the GO(OX) PB (1/1/0.2) NPs at the wavelength of 808 nm.

In the process of calculating hA, the incorporation of a dimensionless parameter denoted as θ is enacted. The acquisition of the specific value of θ necessitates the utilization of equation 2, as stipulated within the subsequent equation:

$$\theta = \frac{T-T_{amb}}{T_{max}-T_{amb}} \qquad \textit{Equation 4.4}$$

Hence, the value of hA can be established in the subsequent manner:

$$hA = \frac{mC_p}{\tau} \qquad \textit{Equation 4.5}$$

The parameter τ can be determined by analyzing the linear time-dependent data plotted against the -ln(θ). This data is obtained during the cooling phase. The symbols m and Cp represent the mass and heat capacity of water, respectively.

4.2.6 *In vitro* cell culture studies

4.2.6.1 Combined chemo and photothermal therapy effects *in vitro*

The MTT assay was utilized to estimate the combined chemo and photothermal therapy effects *in vitro* in MCF-7 cells (Itoo et al., 2023; Itoo, Paul, Ghosh, et al., 2022). The experiment involved seeding cells in a 96-well plate at a density of 1 x 10^4 cells per well and

incubating with 100 µL of DMEM medium. Following a 24-h incubation period, the GO(OX)PEG NPs and GO(OX)PB NPs were introduced into the designated well and subjected to an additional 24-h incubation period at a temperature of 37°C, 5 % CO_2, to assess the potential for dark toxicity. In order to assess the phototoxicity induced by the NIR laser, the GO@OXPt(IV)/PEG and GO@OXPt(IV)/PEG-Biotin NPs were subjected to a medium replacement with fresh RMPI 1640 medium after a 12-h of incubation period. Subsequently, these wells were exposed to NIR laser irradiation (MR.FCL.808.T2.2W.MM-OEM, Shanghai MRTRADE International Co., LTD.). Each well was subjected to an 808 nm NIR laser with a power density of 0.5 W/cm^2 for a duration of 5 min. Following a 24 and 48-h coincubation period, 50 µL of MTT (5 mg/mL in PBS) was introduced to each well and allowed to incubate for an additional 4 h. Subsequently, the medium was extracted and replaced with 150 µL of DMSO to dissolve the formazan crystals. To estimate the relative cell viability, the absorbance at 570 nm (OD570) was measured using a Spectramax^{TM} multiplate reader (Molecular Devices, US). Moreover, we investigated the potential cytotoxic effects of different irradiation durations (ranging from 0 to 5 min) and power densities (ranging from 0.25 to 2 W/cm^2) on MCF- cells *in vitro*. The following formula is used to calculate % cell viability:

$$(\%)\ \text{Cell viability} = \frac{Abs_{Sample}}{Abs_{Control}} \text{X } 100 \qquad \textit{Equation 4.6}$$

The determination of the half-maximal dosage (IC-50) was carried out using GraphPad Prism 9.0.2 software. The results obtained from each trial were computed and averaged to obtain a representative value, following the execution of the experiment three times.

4.2.6.2 Cellular uptake study

The cellular uptake of GO(OX)PEG (1/1/0.2)-RhB NPs and GO(OX)PB (1/1/0.2)-RhB NPs was assessed by MCF-7 cells through a combined quantitative and qualitative analysis employing a flow cytometer and a confocal microscope. To elaborate, a population of 50,000

MCF-7 cells was cultivated within 12-well plates and subjected to an overnight incubation period at 37°C. Subsequently, the existing culture medium was substituted with fresh medium containing GO(OX)PEG (1/1/0.2)-RhB NPs and GO(OX)PB (1/1/0.2)-RhB NPs, maintaining an OX concentration of 10 μg/mL. This exposure was conducted over a time span of 1 to 4 h. Afterward, the cells underwent a 5 min exposure to an 808 nm laser (0.5 W/cm²) followed by incubation at 37°C for varying durations. Subsequently, analysis was performed using a BD FACS Area III flow cytometer on a gated subset of 10,000 cells. The cells were also subjected to qualitative examination using a confocal microscope to assess cellular internalization at 1 and 4 h. Following media removal, cells were rinsed with cold PBS, fixed for 15 min at room temperature using a 4% paraformaldehyde solution, and subsequently stained with DAPI. Subsequently, the cells were washed with PBS and positioned cell-side down on microscope slides coated with Fluoromount-G. They were subjected to monitoring using a confocal microscope (Leica, Germany), with observations conducted at wavelengths of the rhodamine channel (Ex/Em 540/570 nm). A series of z-stack images were also acquired through sequential imaging of x-y planes. This was achieved by adjusting the focal length of the specimen, enabling the capture of consecutive z-axes with a slice thickness of 1 μm.

The process of cellular internalization, specifically the mechanism of endocytosis, was investigated through the utilization of confocal imaging. In summary, MCF-7 cells were placed in 12 well tissue culture plates with a seeding density of 50000 cells per well. After 24 h, the cells were treated with chlorpromazine (an inhibitor of clathrin-mediated endocytosis), nystatin (an inhibitor of caveolae-mediated endocytosis), and Amiloride (an inhibitor of macropinocytosis-mediated endocytosis) at a concentration of 20 μg/mL for a duration of 1 h. After the incubation period, the medium was removed, and the cells were exposed to a formulation of RHB-loaded GO(OX)PB (1/1/0.2) NPs. The uptake of the formulation was then examined for a duration of 4 h. Following the necessary incubation period with the therapy,

the cells were handled in accordance with the protocol and examined using a confocal microscope.

4.2.6.3 Raman spectra analysis of GO inside cells

The cellular internalization of GO(OX)PB (1/1/0.2)-RhB NPs was also quantitatively evaluated by Raman spectra in MCF-7 cells using a UniRAM 3300 micro-Raman mapping spectrophotometer (J. Huang et al., 2012). The MCF-7 cells (5x 10^4) were seeded on circular cover glasses in 12-well tissue culture plates and treated with GO(OX)PB (1/1/0.2)-RhB NPs for 2, 4, 6, and 8 h in serum-free media. Subsequently, the cells were washed four times with PBS, fixed in 4% paraformaldehyde for 10 min, and mounted on microscopy slides using Fluoromount-G. Finally, the cells were observed for GO signal using the Raman spectrophotometer.

4.2.6.4 *In vitro* cell Platinum content

A fixed quantity of MCF-7 cells (10^6 cells/well) was initially seeded and cultured in a 12-well plate for 24 h (Itoo, Paul, Ghosh, et al., 2022). After incubation, the cells were treated with Free OX, GO(OX)PEG (1/1/0.2) NPs, and GO(OX)PB (1/1/0.2) NPs, with or without laser ($\pm$L) containing a concentration of 10 μM of OX. Following treatment, the cells were coincubated at 37 °C for either 0.5 or 2 h. To prepare the cells for analysis, they were washed and lysed using a combination of PBS and cell lysis buffer. The amount of Pt present in the cells was determined using atomic absorption spectrometry (AAS) (AA7000, Shimadzu), and the Pt levels were quantified as ng of Pt per 10^6 cells.

4.2.6.5 Live/Dead cell assay

The experiment followed a previously established protocol [23] to conduct the live/dead cell viability/cytotoxicity assay. Sterile coverslips with a thickness of 0.17 mm were positioned in a six-well plate. Subsequently, a cell suspension containing 50,000 cells in DMEM was introduced into each well. Following an initial incubation at 37°C with 5% CO_2 for 24 h, the

cells underwent treatment with different concentrations of GO(OX)PEG (1/1/0.2) NPs and GO(OX)PB (1/1/0.2) NPs, Subsequently, the cells were further incubated for 48 h. After the initial incubation, the cells were rinsed with sterile PBS and subjected to the application of Calcein-AM, a polyanionic dye, at a concentration of 5 μM. This dye generates a vibrant and intense green color when excited at 495 nm and emits light at 515 nm, specifically indicating the presence of live cells. Additionally, the cells were treated with propidium iodide at a concentration of 5 μM, which results in a vivid red coloration when excited at 495 nm and emits light at 635 nm, thereby indicating the presence of dead cells. Following the application of dyes, the cells were incubated at a temperature of 37 °C for a duration of 30 min. Subsequently, the stained cells were examined and evaluated using a confocal microscope (Eclipse TS100, Nikon, Japan).

4.2.6.6 Mitochondrial membrane potential (MMP) study and Reactive oxygen species (ROS) assay

The JC-1 dye is utilized to quantify the depolarization of mitochondria. This dye is cationic and can accumulate in mitochondria in a potential-dependent manner. This accumulation is shown by a change in fluorescence emission from red to green, which occurs when the mitochondria are injured and their membrane is lost. The cells were exposed to the IC-50 dose of free OX, GO(OX)PEG (1/1/0.2) NPs, and GO(OX)PB (1/1/0.2) NPs for a duration of 24 h. After 12 h of incubation the cells were exposed to NIR laser radiations (808 nm, 0.5 W/cm^2) for 5 min. Next, the cells were rinsed with phosphate-buffered saline (PBS) and exposed to a concentration of 10 μg mL−1 of JC-1 dye for 15 min at a temperature of 37 °C. The cells were subsequently examined using a confocal microscope (Leica, Germany). The quantitative assessment of the data in MMP involved employing a flow cytometer (BD FACS Area III). This device measured fluorescence at an excitation wavelength of 485 nm and an emission wavelength of 590 nm. To ensure accuracy, the instrument was fine-tuned with suitable compensation and threshold settings.

Reactive oxygen species (ROS) were quantified using the DCF-DA dye. The DCF-DA dye penetrates the cell and undergoes a reaction with reactive oxygen species, resulting in the formation of a green, fluorescent molecule called dichlorofluorescein (DCF). ROS quantification was conducted with both fluorometry and microscopy techniques. In summary, a concentrated solution of DCF-DA (10 mM) was diluted to a workable concentration of 100 μM. The MCF-7 cells were exposed to IC-50 concentrations of free OX, GO(OX)PEG (1/1/0.2) NPs, and GO(OX)PB (1/1/0.2) NPs, coupled with exposure to 808 nm NIR laser radiation (±L, 5 min) for a duration of 24 h. Next, the cells were rinsed with PBS and then treated with a 100 μM concentration of DCF-DA (working solution) for a duration of 30 minutes at a temperature of 37 °C. Subsequently, the cells underwent staining with DAPI, and images were captured utilizing a confocal microscope (Leica, Germany), specifically in the green channel. The excitation wavelength applied was 492–495 nm, and the emission wavelength ranged from 517 to 527 nm. The quantitative assessment of the data in ROS involved employing a flow cytometer (BD FACS Area III).

4.2.6.7 Annexin V assay

The quantification of apoptotic and necrotic cells by Free OX, GO(OX)PEG (1/1/0.2) NPs, and GO(OX)PB (1/1/0.2) NPs, in MCF-7 cells was performed using annexin V-FITC labelling (TACS®), coupled with exposure to 808 nm NIR laser radiation (±L, 5 min). Following the treatment, the cells were rinsed with PBS at a low temperature and then exposed to 100 μL of annexin binding buffer. An aliquot of Annexin V-FITC at a concentration of 2 μg/mL was introduced and incubated in a light-free environment at room temperature for a duration of 15 minutes. Next, 400 microliters of annexin binding buffer were introduced. Before doing FACS analysis, 5 mL of propidium iodide (PI) solution at a concentration of 1 μg/mL was introduced into each 100 μL cell suspension. After this, cell analysis was executed utilizing a flow cytometer (FACS Aria III, BD Biosciences, USA), where the examination focused on 10,000

viable cells within a defined gating strategy. Only individual cells were chosen for fluorescence analysis, and the data were visually represented by plotting Annexin V-FITC against PI using quadrant gating.

4.2.6.8 Cell cycle analysis

Cell cycle measurement in Free OX, GO(OX)PEG (1/1/0.2) NPs, and GO(OX)PB (1/1/0.2) NPs-treated cells was conducted using propidium iodide stain, coupled with exposure to 808 nm NIR laser radiation (±L, 5 min). Following the designated duration of treatment, the cells were collected and preserved by immersing them in 70% ethanol for a period of one night at a temperature of 4 °C. The following day, the cells were rinsed with a 1× PBS solution. To stain the cellular DNA, Propidium Iodide (PI) was used at a concentration of 20 μg/mL in PBS. A FACS instrument (FACS Aria III, BD Biosciences, USA) was used to analyze the cell cycles of the treated cells. The Flow Jo Software was then utilized to analyze the data and determine the distribution of cells within the G2/M, S, and G1 phases of the cell cycle.

4.2.7 *In vivo* studies

4.2.7.1. Pharmacokinetic (pk) study

The pK analysis of free OX, GO(OX)PEG (1/1/0.2) NPs, and GO(OX)PB (1/1/0.2) NPs was conducted in male Wistar rats (220 ± 20 g). Rats were housed under conditions of natural light and provided with food and water at 25 °C and 55% RH. Before injection, rats were divided into 4 groups (control, free OX, GO(OX)PEG (1/1/0.2) NPs, and GO(OX)PB (1/1/0.2) NPs, n = 3), fasted for 10 h, with access to water. All rat groups were administered an equivalent dose of OX (5 mg/kg) intravenously through the tail vein. Following this, blood samples of approximately 0.5 mL each were collected from the retro-orbital plexus using heparinized tubes at predetermined intervals. The Plasma was acquired through centrifugation at 10,000 rpm for 5 min and then preserved at −20 °C for subsequent analysis. For OX concentration measurement, 200 μL of frozen rat plasma was transferred to a 1.5 mL plastic tube. The plasma

was mixed with a triple volume of cold acetonitrile and vortexed for 10 min to facilitate the separation of plasma proteins. This mixture was then subjected to centrifugation. Subsequently, the resulting supernatant was isolated and subjected to pharmacokinetic (PK) analysis using an atomic absorption spectrophotometer (AA7000, Shimadzu). The analysis involved configuring the instrument with the following parameters: element Pt, Lamp Current Low (Peak) (mA): 14, Wavelength (nm): 265.9, Slit Width (nm): 0.7, and Lamp Mode: BGC-D2. The pk parameters were derived using the non-compartmental model within Phoenix 8.0 WinNonlin software (Pharsight Corporation, USA). The statistical significance of differences was determined by applying the student's t-test.

4.2.7.2. Nephrotoxicity study

The rats were rendered anesthetized through intraperitoneal administration of sodium pentobarbital (50 mg/kg). A single bolus dose of free OX, GO(OX)PEG (1/1/0.2) NPs, and GO(OX)PB (1/1/0.2) NPs was administered at an equivalent dose of OX (5 mg/kg) via the tail vein (Hanada et al., 2010). Following the rats' recovery from anesthesia, they were kept in a temperature-regulated setting and provided with unrestricted access to a standard laboratory pellet diet along with *ad libitum* access to water. Subsequently, blood samples of approximately 0.5 mL each were collected from the retro-orbital plexus using heparinized tubes at predetermined intervals, and the plasma was separated. The collected plasma was stored at -20 until blood urea nitrogen (BUN), creatinine level analysis, and other hematological parameters. BUN and creatinine levels were determined with a BUN and creatinine diagnostic kit. The kidneys from different experimental groups were also dissected and macroscopically examined for changes. They were then quickly placed in a 4% paraformaldehyde solution in saline for fixation. These samples were stained with hematoxylin and eosin (H&E) and analyzed using a light microscope to evaluate histological changes and capture images.

4.2.7.3 *In vivo* therapeutic efficacy, *in vivo* fluorescence imaging, and biodistribution analysis

The *in vivo* assessment of the synergistic chemo-photothermal therapeutic effects was conducted using free OX, GO(OX)PEG (1/1/0.2) NPs, and GO(OX)PB (1/1/0.2) NPs in a murine model with 4T1-Luc tumors. This assessment took place when the tumor volume reached 50 mm^3. Tumorigenesis was induced by subcutaneously inoculating a suspension of 4 T1-Luc cells, consisting of 1.5 x 10^6 cells in 100 μL volume, into the right flank of female BALB/c mice. The procedure was performed under anesthesia to ensure controlled conditions. Subsequently, the murine subjects were partitioned into six distinct cohorts, each comprising five mice. The categorizations were as follows: control (PBS treated), free OX, GO(OX)PEG (1/1/0.2) NPs (-L), GO(OX)PB (1/1/0.2) NPs (-L), and GO(OX)PEG (1/1/0.2) NPs (+L), and GO(OX)PB (1/1/0.2) NPs (+L). Following intravenous drug administration, the mice bearing 4 T1-Luc tumors underwent exposure to 808 nm near-infrared (NIR) laser irradiation at a power density of 1.0 W/cm^2 for a duration of 5 min each, occurring at the 12-h time point. Throughout the course of laser treatment, a thermal imaging system was utilized to capture temperature profiles and alterations in the tumor's spatial extent. Tumor dimensions were assessed every other day, along with monitoring of body weight over the experimental timeline. The tumor masses were excised and quantified individually, and subsequently, the survival curve was assessed using the Kaplan-Meier methodology. After the survival investigation, humane euthanasia was administered to the mice, followed by extraction of lung tissue across the distinct experimental cohorts for subsequent analysis. Enumeration of macroscopic metastatic nodules within the lung tissue was conducted as a metric to ascertain the inhibitory impact of nanoparticle compositions on the occurrence of breast cancer lung metastases. Furthermore, the *in vivo* tumor accumulation of free OX, GO(OX)PB (1/1/0.2) NPs, and GO(OX)PEG (1/1/0.2) NPs (±L) was identified using IVIS® Lumina III by PerkinElmer, USA. The bioluminescence was employed to observe the progression of 4T1 tumors in mice after the

intraperitoneal administration of D-luciferin (150 mg/kg), done 10-15 min prior to imaging. The various specific time intervals post-injection were examined to assess the patterns of tumor accumulation (5, 10, 15, and 21 days) utilizing the IVIS® system equipped with a 620 nm excitation filter and a 780 nm emission filter. The biodistribution analysis of GO(OX)PEG-RhB (1/1/0.2) NPs and GO(OX)PB-RhB (1/1/0.2) NPs was conducted in mice over a duration of 36 h. The fluorescence emitted by RhB was captured at time intervals of 1, 3, 6, 12, 24, and 36 h after injection. After the *in vivo* imaging sessions, the mice were euthanized, and their tumors, along with primary organs (liver, heart, spleen, kidney, and lung), were extracted for subsequent imaging and immunohistochemical analysis.

4.2.8 Immunohistochemistry

4.2.8.1 TUNEL assay

The TUNEL assay was performed to evaluate the extent of apoptosis in the tumor tissue using the terminal deoxynucleotidyl transferase-mediated nick end labeling kit (Merck, Darmstadt, Germany) (Paul et al., 2022b). The experiment was conducted according to the instructions provided by the manufacturer. Essentially, the tumor tissues were exposed to the terminal deoxynucleotidyl transferase (TdT) reaction solution for a duration of 15 minutes at a temperature of 37 °C. Afterward, the TdT reaction mixture, consisting of EdUTP, TdT enzyme, and equilibration buffer, was introduced to the preserved tumor tissue and allowed to incubate for 60 minutes at a temperature of 37 °C in the absence of light. The slides were subsequently cleansed using deionized water, followed by a 5-minute treatment with a solution containing 3% BSA and 0.1% Triton™ X-100 in PBS. The tissue sections were treated with DAPI for a duration of 5 minutes and thereafter seen using a fluorescence microscope from Leica, Germany.

4.2.8.2 ROS production and immune-histochemical analysis of Ki-67 in tumor tissue

The DCFH-DA fluorescent probe was utilized to evaluate the production of reactive oxygen species (ROS) in cancerous cells. When the tumor size reached approximately 75 mm^3, free OX, GO(OX)PB (1/1/0.2) NPs, and GO(OX)PEG (1/1/0.2) NPs (±L) were administered intravenously to mice with tumors at a dose comparable to 5 mg/kg of OX. The tumors were injected intratumorally after a 24-h post-injection period with the DCFH-DA probe (50 μL, 25 μM). After a duration of 30 min, the mice were euthanized, and the tumors were isolated. The tumors were then cut into sections using a cryostat machine (Leica biosystems, Germany) with a thickness of 5 μm. Finally, the sections were observed using a fluorescence microscope.

Moreover, an immunohistochemical analysis of the tumor was conducted to assess cell proliferation using the Ki67 marker. The tumor segment was treated with methanol to fix it, then blocked with a 3% BSA solution for 1 h. It was then incubated overnight at 4 °C with the Ki-67 primary antibody (Rabbit mAb #9129S) for Ki-67 evaluation. The next day, the tissue slices were rinsed with PBS and exposed to the secondary antibody Alexa Fluor® 488 for a duration of 2 h at room temperature in a dark environment. After a 2-h incubation period, the tissues were rinsed with phosphate-buffered saline (PBS), exposed to 4',6-diamidino-2-phenylindole (DAPI) for 5 minutes, and examined using a fluorescence microscope.

4.2.8.3 Hematoxylin and Eosin (H&E) staining

The tissue samples were obtained from tumor bearing mice and then underwent H&E staining (Itoo, Paul, Ghosh, et al., 2022). Following the treatment, the major organs, such as the liver, kidney, heart, spleen, and lung, were removed, conserved, and then cut into 5 μm thick slices. The sections were stained using the hematoxylin-eosin (H&E) reagent according to the manufacturer's instructions. The slices were scrutinized using a light microscope for histological examination.

4.2.9 Statistics

The data was analyzed by calculating the average and applying statistical methods (one-way ANOVA and t-test) using Prism 8.0 software (GraphPad). Statistical significance was determined based on a p-value threshold of 0.05, with significance levels indicated as *, **, or *** for $p<0.05$, $p<0.01$, and $p<0.001$, respectively.

4.3 Results and Discussion

4.3.1 Preparation and Characterization of GO(OX)PB (1/1/0.2) NPs

The pH and photothermal dual-responsive multifunctional targeted nanocomplexes, identified as GO(OX)PB (1/1/0.2) NPs, were synthesized through a comprehensive six-step synthetic process outlined in **Scheme 4.1, 4.2, and 4.3**. This synthetic route involved several crucial steps in the fabrication of pH- and photothermal dual-responsive nanocomplexes, including (i) the synthesis of graphene oxide using a modified Hummers method; (ii) the generation of nanoscale-GO through ultrasonication (35 W, 3 h); (iii) the synthesis of oxaliplatin prodrug OX(IV) via dihydroxyl derivatization, involving the reaction with hydrogen peroxide. Specifically, OX was initially oxidized to OX(IV)-OH using 30% H_2O_2, followed by modification with succinic anhydride on the axis ends of OX(IV)-OH; (iv) the creation of GO(OX) complexes through a classical ester reaction between the -OH groups of GO and -COOH groups of OX(IV) in different ratios; (v) the synthesis of pegylated biotin through amide bond formation; and (vi) the conjugation of GO(OX)(IV) complex with PEG and PEGylated-Biotin (PB) through carboxamide reaction in the presence of EDC and NHS, with varying ratios. The structure of these complexes was characterized by mass spectroscopy, ^{1}H-NMR, FTIR spectroscopy, DSC, TGA analysis, XPS analysis, and Raman spectroscopy. The ^{1}H-NMR spectra of the OX(IV)-OH, OX(IV)-COOH, and PB confirmed the correct identity of the product represented in **Fig. 4.1** and **4.2,** respectively. **Fig. 4.3** displays the ^{1}H-NMR spectra and corresponding chemical shift allocations of the PB copolymer. The characteristic peaks of the

PEG units are observed at around 3-4 ppm because of the methylene protons. The identification of the biotin group in PB copolymer was accomplished by observing two distinct peaks corresponding to the methane protons at 4.3 and 4.5 ppm. The molecular mass of OX(IV)-OH and OX(IV)-COOH was confirmed by LCMS and found to be 431.28 and 530 (m/z), respectively, represented in **Fig. 4.5**. The MALDI-TOF-MS spectrum analysis confirmed the successful synthesis of PB and showed an increase in molecular weight, as shown in **Fig. 4.6**. Upon calculating the molecular weights of the PB conjugate, and it can be inferred that approximately ~1 molecule of biotin was successfully conjugated to PB, with m/z values of 2244.6 for PB.

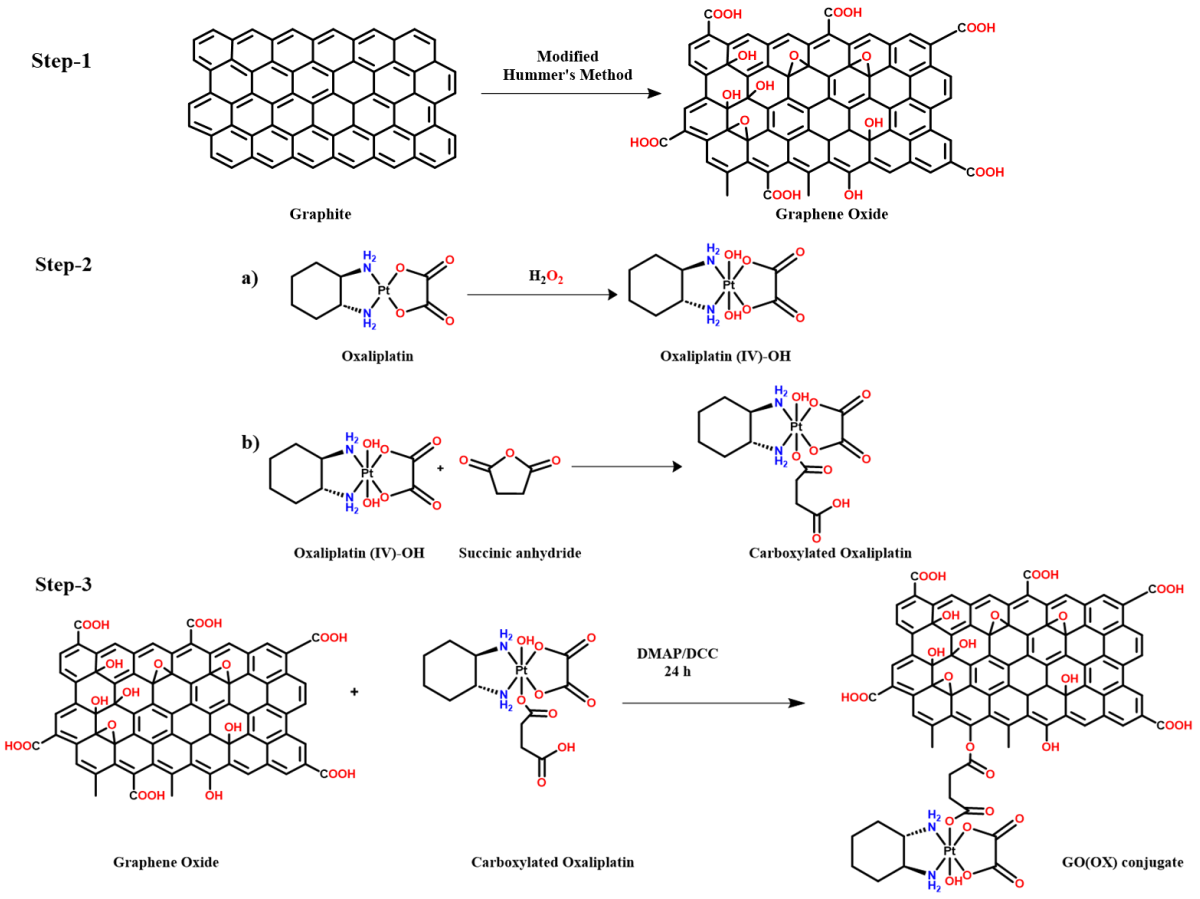

Scheme 4.1. Synthesis scheme for the preparation of Graphene oxide (GO), carboxylated oxaliplatin, and GO(OX) conjugate.

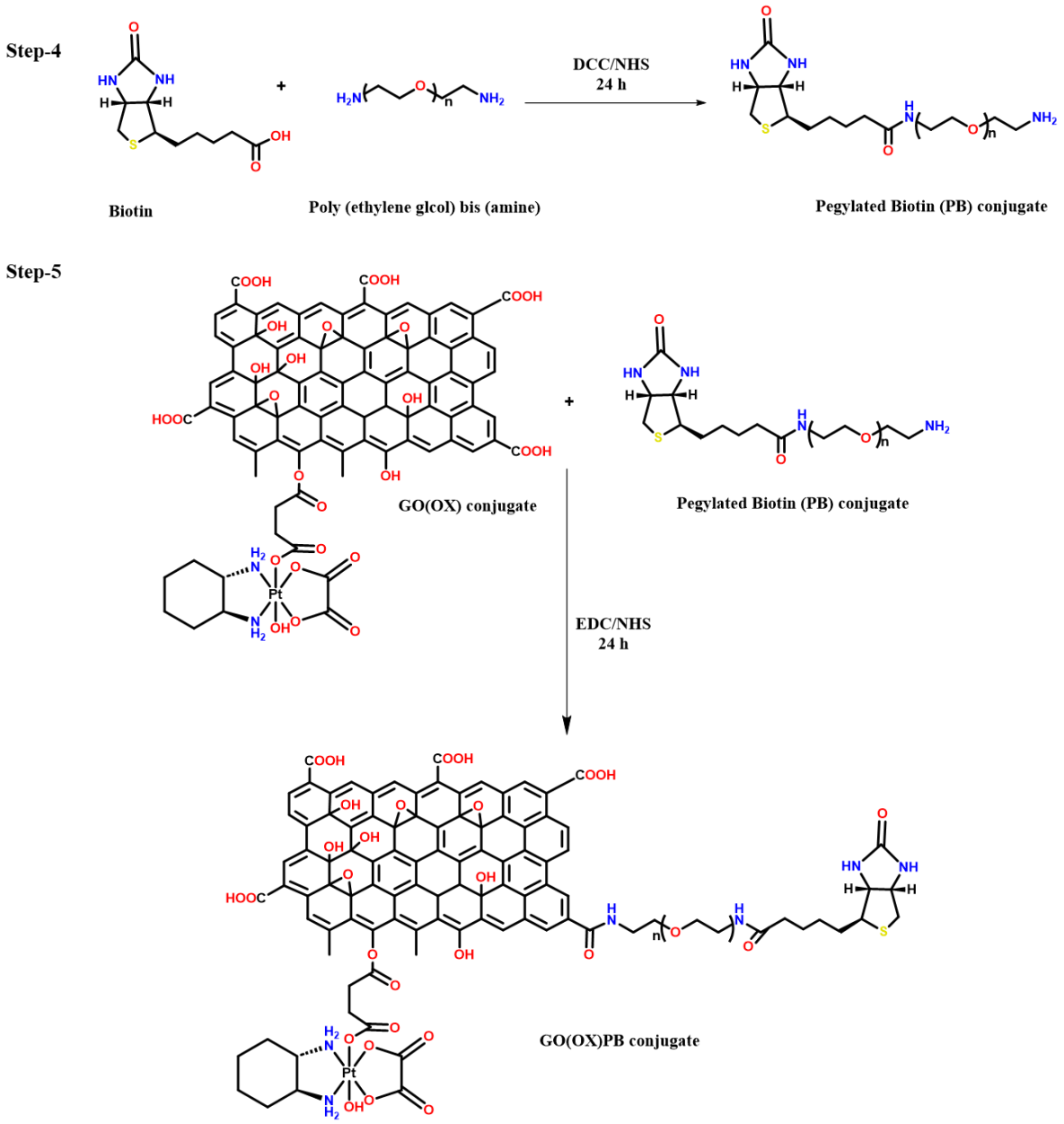

Scheme 4.2. Synthesis scheme for the preparation of PB conjugate and GO(OX)PB conjugate.

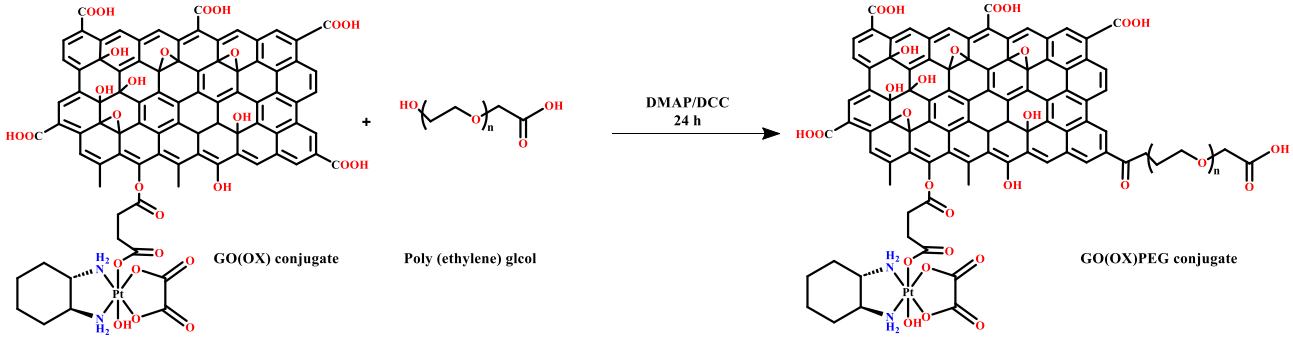

Scheme 4.3. Synthetic schematic illustration of GO(OX)PEG conjugate.

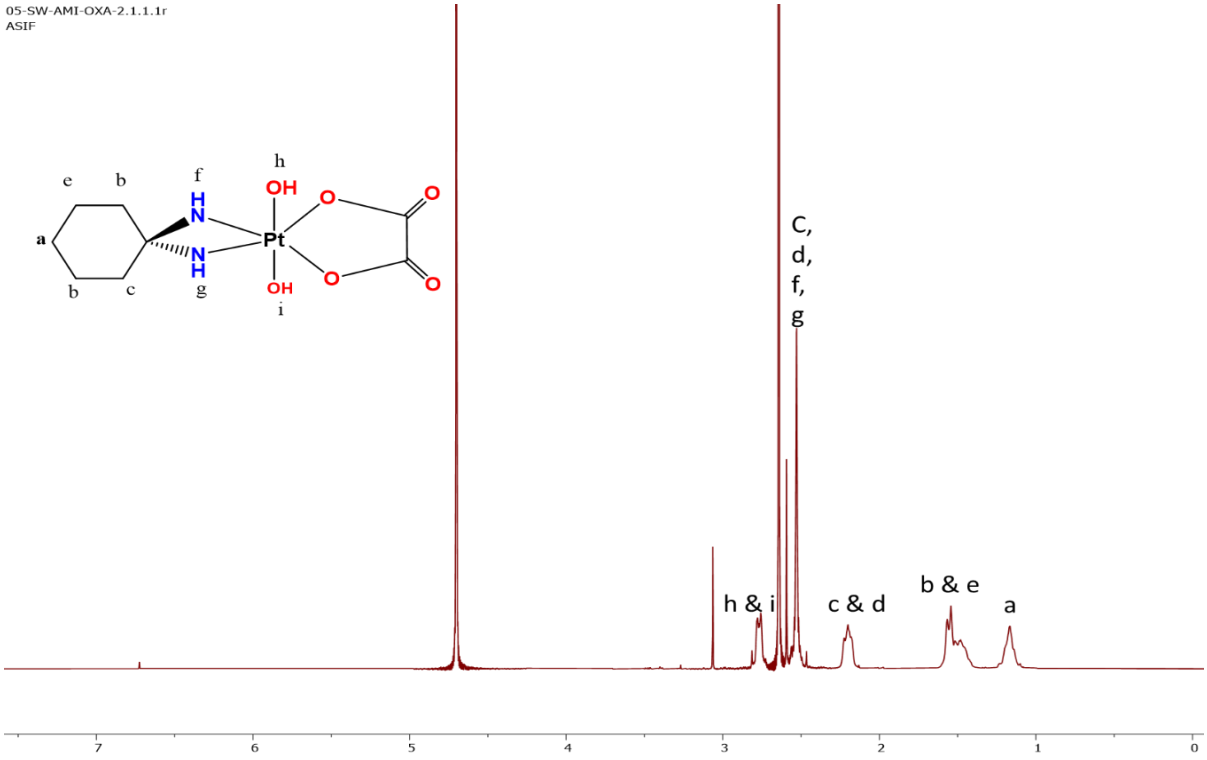

Figure 4.1 ^{1}H NMR spectrum of Dihydroxy oxaliplatin (IV).

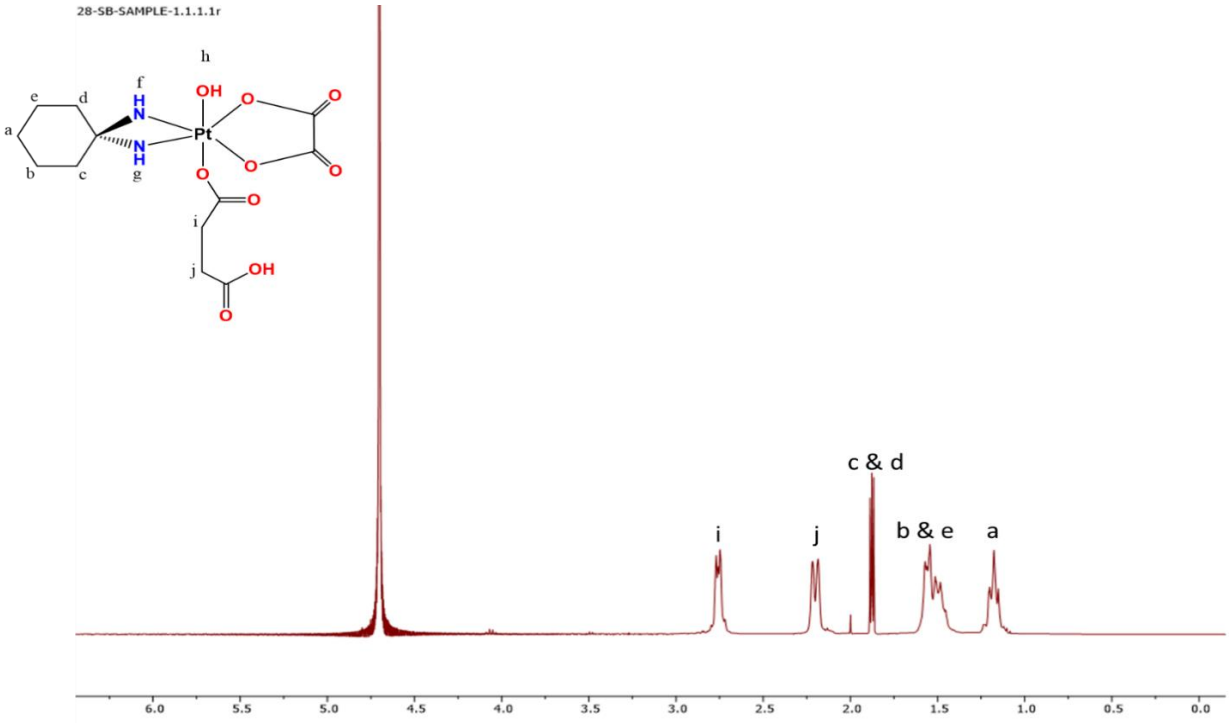

Figure 4.2 ^{1}H NMR spectrum of carboxylated oxaliplatin (IV).

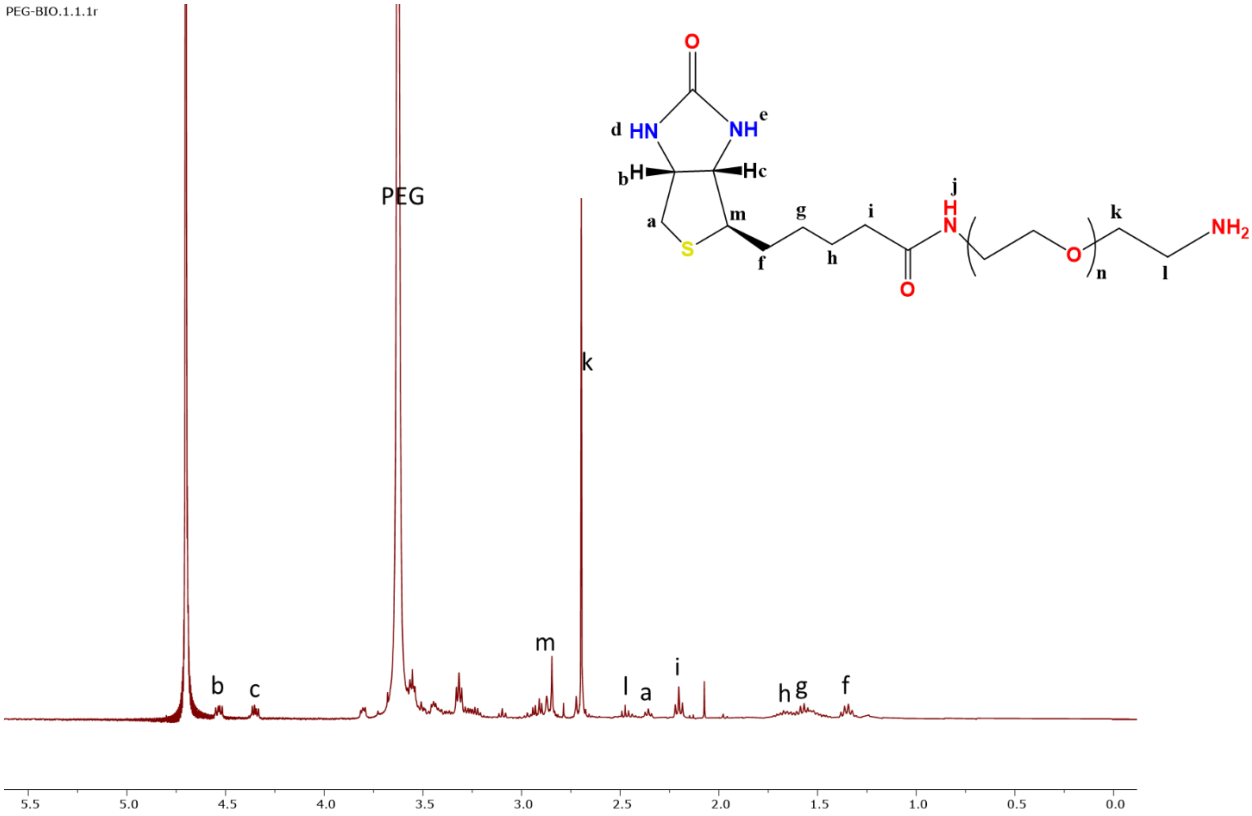

Figure 4.3 1H NMR spectrum of pegylated biotin (PB).

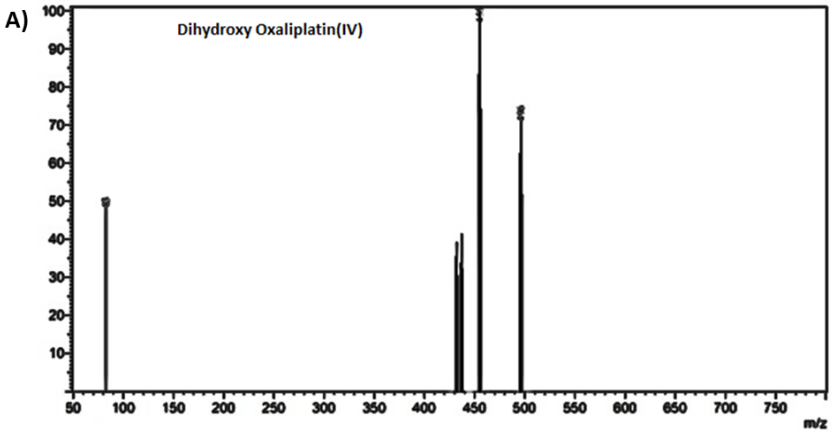

Figure 4.4 Mass spectrum of Dihydroxy Oxaliplatin(IV) (A).

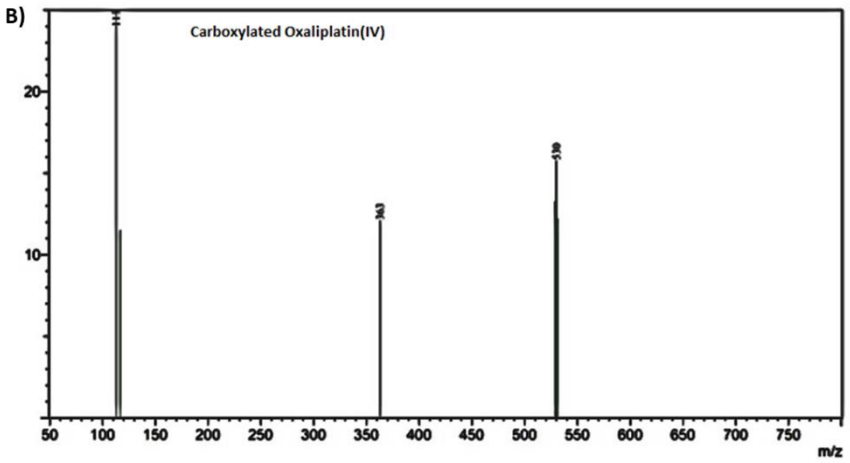

Figure 4.5 Mass spectrum of Carboxylated oxaliplatin(IV) (B).

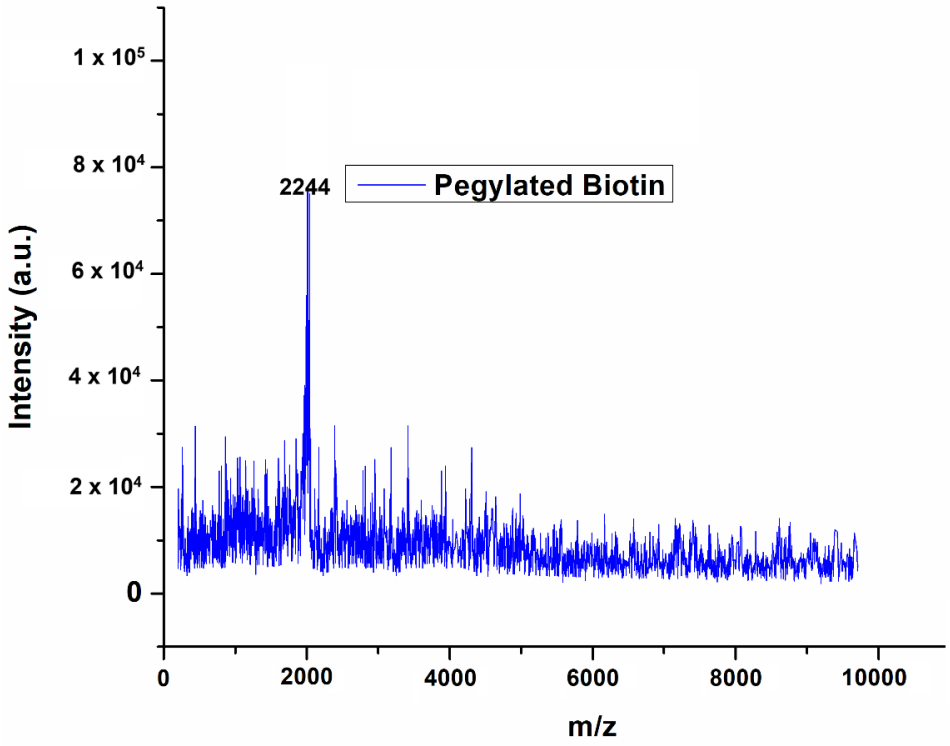

Figure 4.6 MALDI-Toff analysis of Pegylated biotin

Unlike graphite, which does not exhibit infrared activity, the FTIR spectra of GO display numerous peaks corresponding to the presence of oxygen-containing functional groups (**Fig. 4.7**). The FTIR spectra of GO exhibited a prominent and wide peak at around 3447 $cm^{-1,}$ which can be attributed to the presence of physically adsorbed water molecules and hydrogen bonds formed by the hydroxyl groups of GO. This observation serves as confirmation of the existence

of hydroxyl OH groups in the GO sample. Additionally, a signal observed at 1604 cm^{-1} indicated the existence of an aromatic C=C functional group in GO. The prominent peaks observed at 1049 and 1401 cm^{-1} were attributed to the presence of C-O (alkoxy) and >O- (epoxy) bonds, respectively. Upon examination of the chemical structure of PB, as depicted in **Fig. 1A**, it was noted that a distinct and broad peak region, spanning from 3235 to 3376 $cm^{-1,}$ was related to the presence of -NH and -OH groups. Moreover, a prominent peak at 1714 cm^{-1} was observed, which corresponds to the presence of the carboxylic acid (-COOH) functional group.

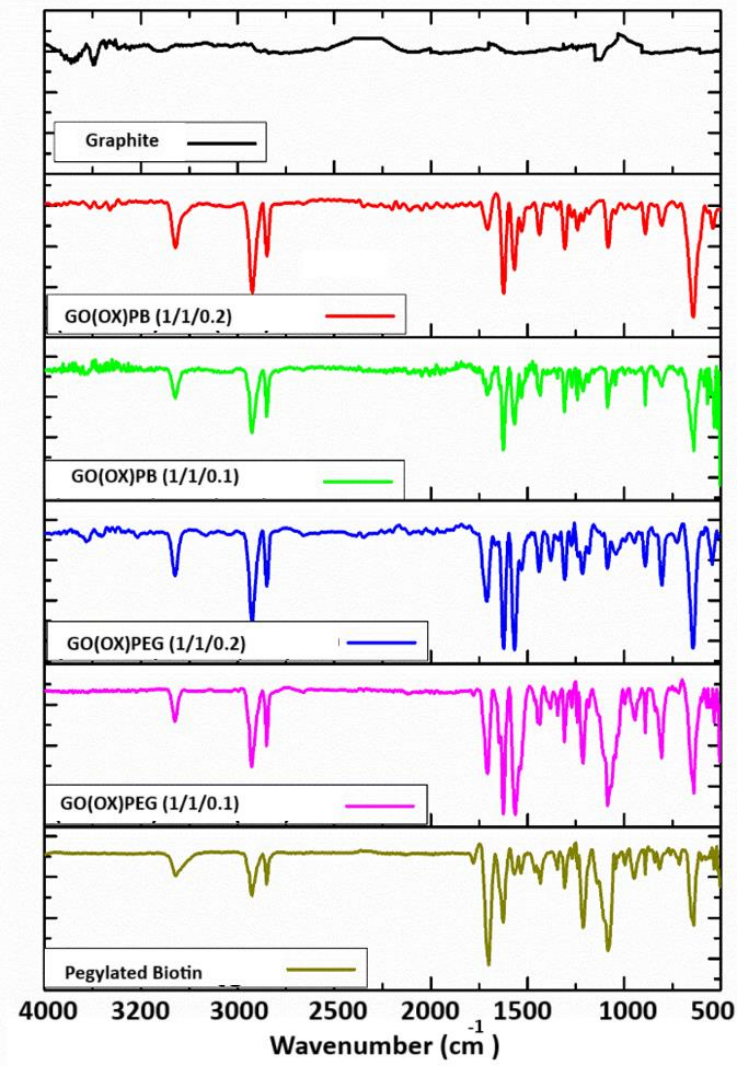

Figure 4.7 FTIR analysis of graphite, GO, and GO conjugates.

The successful conjugation of GO and OX(IV) was further confirmed by the presence of characteristic peaks at 1701 cm^{-1} and 1214 cm^{-1}, which correspond to the ester linkages (O-C=O). In addition, the identification of specific vibration frequencies at 3336 cm^{-1} (-OH stretching), 2923 cm^{-1} (-CH stretching), 1719 cm^{-1} (-C=O), 1619 cm^{-1} (-NH), and 1242 cm^{-1} (-C-O-C) provides supporting evidence for the conjugation of OX(IV) to GO. The FTIR peaks for GO(OX)PEG (1/1/0.2) NPs and GO(OX)PB (1/1/0.2) NPs showed a combination of peaks and characteristics from both GO(OX) and PB indicating the successful conjugation, as depicted in **Fig. 4.9A**. The prominent peak observed at 1600-1700 cm^{-1} signifies the stretching vibrations of the carbonyl group (C=O) within amide bonds, while the peak found at 3300-3500 cm^{-1} corresponds to the stretching vibrations of N-H bonds in amide groups. Additionally, the peak occurring around 1500-1550 cm^{-1} represents a combination of N-H bending and C-N stretching vibrations, further confirming the presence of amide bonds and the success of the conjugation process.

The confirmation of graphite oxidation has also been established by the utilization of Raman spectroscopy. The I_D/I_G ratio is a measure of the level of imperfections on the surface of graphene. The acquisition of in-plane vibrations is attributed to carbon atoms connected through sp^2 hybridization, which are accountable for the G band. Conversely, the development of the D band is attributed to out-of-plane vibrations caused by structural defects seen on the surface of GO. **Fig. 4.12K** displays the Raman spectra of graphite, GO, GO(OX) (1/1), GO(OX)PEG (1/1/0.2) NPs, and GO(OX)PB (1/1/0.2) NPs. The Raman spectra of natural graphite display prominent peaks at 1576.75 cm^{-1} and 2678 cm^{-1}, corresponding to the G band and 2D band, respectively. Conversely, the D band is observed as a very faint peak at 1332.37 cm^{-1} (Chieu et al., 1982; Satti et al., 2010; Tuinstra & Koenig, 1970). The most prominent peaks observed in the Raman spectrum of GO occur at wavenumbers 1583.55 cm^{-1} and 1345.57 cm^{-1}, corresponding to the G and D bands, respectively. As evidenced by the GO spectra, the D

band undergoes a shift toward higher frequency and exhibits increased prominence. The I_D/I_G ratio, which is equal to 0.82, suggests that there has been a decrease in the average size of sp^2 domains because of severe oxidation (Chieu et al., 1982; Stankovich, 2007). The G-band and D-band frequencies of GO(OX) (1/1) exhibited minimal changes in comparison to those of GO, with values of 1591.58 and 1348.66 cm^{-1}, respectively. The I_D/I_G value of GO(OX) (1/1) is 0.83 and indicates that the conjugation of GO with OX(IV) does not lead to the destruction of the aromatic structures of GO, confirming their identical nature. The GO(OX)PEG (1/1/0.2) NPs exhibited a peak at 1590.44 cm^{-1} and 1349.28 cm^{-1}, corresponding to the G and D bands with an I_D/I_G ratio equal to 0.85. On the other hand, GO(OX)PB (1/1/0.2) NPs exhibited a peak at 1596 cm^{-1} and 1355.37 cm^{-1}, corresponding to the G and D band with I_D/I_G ratios of 0.89. GO exhibited a decrease in the D band intensity due to the disruption of sp^2 hybrid bonds on the GO surface. Conversely, the remaining samples displayed an increase in oxygen-containing functional groups following functionalization. The ID/IG ratios were observed to be higher, indicating a greater degree of disorder resulting from the conversion of sp^2 hybridized carbon to sp^3 bonds of alkyl groups on the outer surface of the GO following functionalization.

The X-ray diffraction (XRD) pattern of GO produced using the modified Hummer's method reveals that the (002) reflection of graphite becomes undetectable following the oxidation process. Instead, a distinct diffraction peak at $2\theta = 11.787$ emerges, indicating the presence of the diffraction of the 001-crystal plane (d001 = 7.502 Å). This diffraction pattern is characteristic of GO and signifies successful oxidation of the graphite material. Moreover, it suggests the formation of oxygen-containing groups that are randomly distributed on both the basal plane and edges of the graphene sheets. During X-ray diffraction (XRD) investigation, the compound OX(IV) exhibited distinct peaks at specific 2-theta (°) values, namely 8.51, 15.72, 20.21, 26.23, 32.61, 37.45, and 42.15. The peaks corresponding to OX (IV) and GO were not observed in the lyophilized GO(OX)PEG (1/1/0.2) NPs and GO(OX)PB (1/1/0.2) NPs

(**Fig. 4.9B, 4.8A**) and it was changed to amorphous in nature. The drug carrier system is widely recognized for its amorphous form in drug delivery applications due to its ability to effectively interact with biological systems and facilitate controlled and sustained drug release (Pradeepkumar et al., 2018).

Furthermore, the structure of GO, GO(OX) (1/1), GO(OX)PEG (1/1/0.2) and GO(OX)PB (1/1/0.2) NPs were also verified using X-ray photoelectron spectroscopy (XPS) study. The XPS compositional analysis and fitted parameters of the C 1s, O 1s, and Pt4f spectra of the graphene oxide, GO(OX) (1/1), GO(OX)PEG (1/1/0.2) NPs, and GO(OX)PB (1/1/0.2) are represented in **Table 4.1.** After undergoing deconvolution, it becomes evident, as shown in **Fig. 4.9**, that the C1s spectra of graphite display two separate peaks at energy levels of 284.70 eV and 289.9 eV. The existence of sp^3-hybridized carbon (C–C) is responsible for these peaks, whereas the shake-up satellite peak (π-π^*) can be attributed to them. The GO C1s spectra (**Fig. 4.8B**) displayed a notable degree of oxidation, as shown by the identification of several oxygen groups. More precisely, the peaks seen at 284.65 eV, 286.56 eV, and 288.48 eV were identified as corresponding to carbon atoms in sp^2 carbon (C–C), the epoxide (C-O-C), and the carboxyl functional groups (C=O), respectively. **Fig. 4.8C** presents the core-level spectra of O1s in graphene oxide (GO). When examining oxygenated functional groups, they were observed in the form of C–O, C=O/O-H/C-O-C, with characteristic peaks at 531.48 eV and 532.48 eV, respectively. Following the functionalization of GO with OX(IV), PEG, and PB, the XPS core level spectra exhibited a noticeable shift in the binding energy and a substantial reduction in the intensity of the peaks. In comparison to the C 1s XPS spectrum of GO, the intensity of the C–C peak in the GO(OX) (1/1), GO(OX)PEG (1/1/0.2), and GO(OX)PB (1/1/0.2) NPs increased at 284.65 eV. Conversely, the peaks corresponding to C-O-C and C=O increased at 286.56 eV and 288.48 eV, respectively. These observations suggest that graphene oxide was successfully achieved, followed by successful modification of OX(IV) onto the GO through an

ester reaction, and the conjugation of PEG and PB onto GO(OX) (1/1) through an amide reaction represented in **Fig. 4.9C-N** and **Table 4.1**. Furthermore, the XPS elemental analyses presented in **Table 4.1** provide unambiguous evidence that in addition to C, O, N originating from Biotin, Pt(IV) is also present in the GO(OX)PEG (1/1/0.2) and GO(OX)PB (1/1/0.2) NPs. The Pt4f peaks (Pt(IV) $4f_{7/2}$, Pt(IV) $4f_{5/2,}$ and Pt(IV)) were presented at 72.84 eV, 76.24, and 77.66 for GO(OX) (1/1) conjugate, 72.88, 75.48, and 78.73 for GO(OX)PEG (1/1/0.2) conjugate, and 72.99, 75.88, 78.95 for GO(OX)PB (1/1/0.2) NPs (**Fig. 4.9F, J, and N)**. These findings support the spectroscopic observations, which indicated the formation of the nanoparticles. The XPS analysis results additionally confirm the successful grafting of OX(IV), PEG, and PB onto the graphene oxide (GO) matrix, validating the efficacy of the conjugation process. The presence of these species was in accordance with the findings derived from FTIR and Reman spectra. The thermal analyses, including DTG and TGA, were conducted to assess the thermal properties of newly synthesized GO, free OX, and GO modified with PEG and pegylated biotin nanoparticles. **Fig. 4.10** illustrates TGA curves. The TGA profile of GO revealed an initial thermal degradation below 150 °C, attributed to the evaporation of water within the π–π-stacked layered structure, indicating its thermal instability. Subsequently, a noticeable increase in mass loss occurred in the 160–250 °C range, corresponding to the decomposition of labile oxygen-containing groups. Upon coupling with PEG and PB, the resulting GO(OX)PEG (1/1/0.2) NPs and GO(OX)PB (1/1/0.2) NPs conjugate exhibited an increased thermal stability compared to that of pure GO.

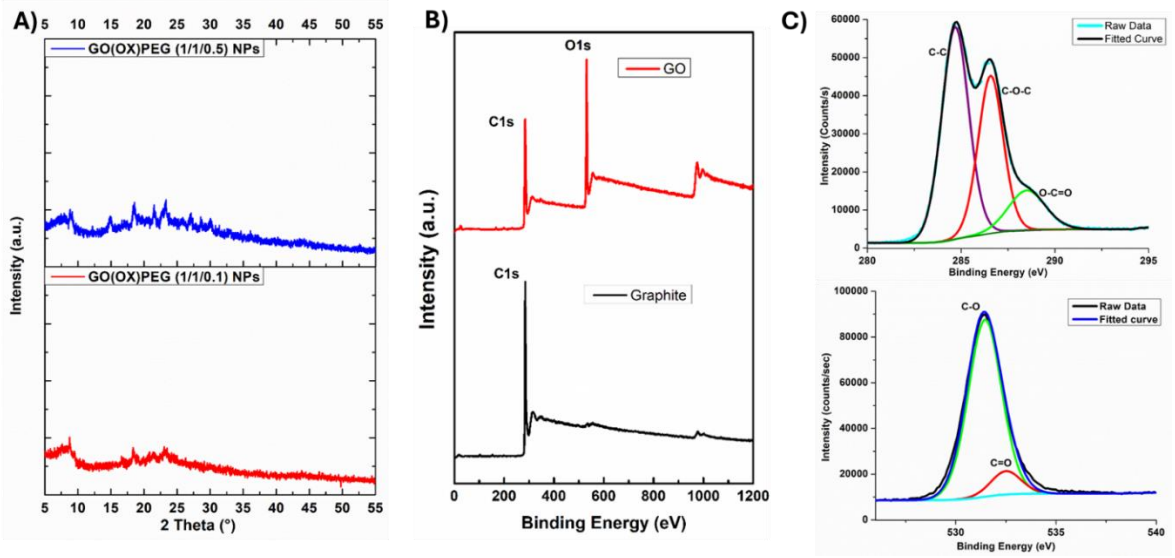

Figure 4.8 XRD analysis of GO(OX)PEG NPs (A); XPS survey spectra of graphite and graphene oxide (B); C1s and O1s spectra of graphene oxide (C).

The utilization of a GO nanocarrier with a high drug loading capacity and selective trapping of drugs has been shown to significantly enhance intracellular activity within cancer cells (Vinothini et al., 2019). The drug loading and entrapment efficiency were evaluated by the AAS spectroscopy method at 266 nm. **Table 4.2** displays the entrapment efficiency (% EE) and drug loading capacity (% DL) of the GO(OX), GO(OX)PEG NPs, and GO(OX)PB NPs copolymer for the chemotherapeutic drug OX. The drug loading capacities varied between 42.96% and 70.6%, whereas the entrapment efficiency ranged from 83.03% to 90.58% across the different ratios of GO(OX), GO(OX)PEG NPs, and GO(OX)PB NPs. The conjugate of GO(OX) with a drug-to-polymer weight ratio of (1/1), GO(OX)PEG (1/1/0.2) NPs, and GO(OX)PB (1/1/0.2) NPs exhibited the lowest particle size, optimum zeta potential and highest

levels of OX encapsulation efficiency and loading, thus warranting further investigation in subsequent studies.

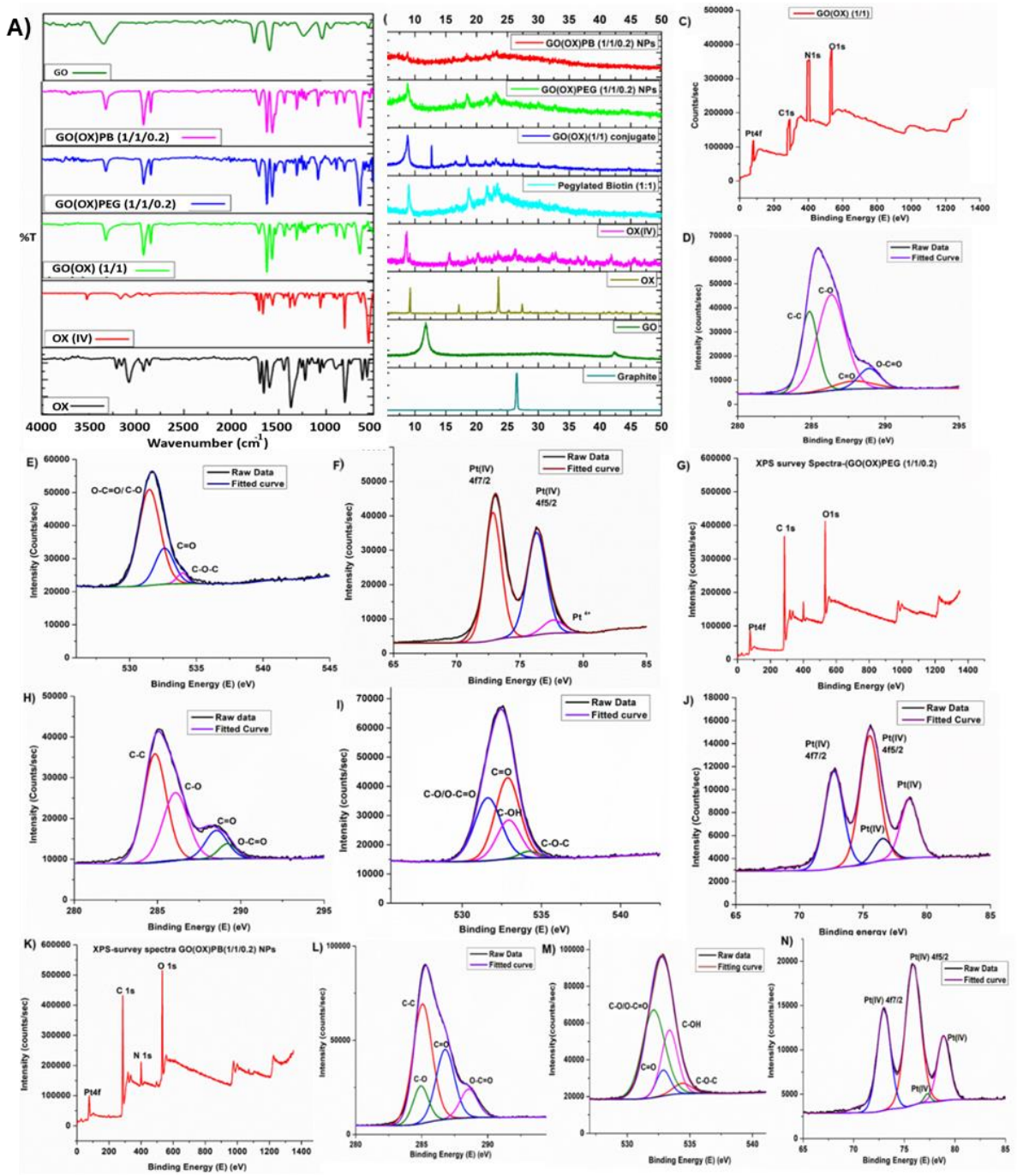

Figure 4.9 Physiochemical characterization of GO(OX) conjugates. FTIR Spectra (A); XRD spectra of graphite, GO, OX, OX(IV), and GO(OX) (1/1) conjugates (B); XPS survey spectra of GO(OX) (1/1) (C); C1s survey spectra of GO(OX) (1/1) (D); O1s survey spectra of GO(OX) (1/1) (E); Pt survey spectra of GO(OX) (1/1) (F); XPS survey spectra of GO(OX)PEG

(1/1/0.2) conjugate (G); C1s survey spectra of XPS survey spectra of GO(OX)PEG (1/1/0.2) conjugate (H); O1s survey spectra of XPS survey spectra of GO(OX)PEG (1/1/0.2) conjugate (I); Pt survey spectra of XPS survey spectra of GO(OX)PEG (1/1/0.2) conjugate (J); XPS survey spectra of GO(OX)PB (1/1/0.2) conjugate (K); C1s survey spectra of XPS survey spectra of GO(OX)PB (1/1/0.2) conjugate (L); O1s survey spectra of XPS survey spectra of GO(OX)PB (1/1/0.2) conjugate (M); Pt survey spectra of XPS survey spectra of GO(OX)PB (1/1/0.2) conjugate (N).

Table 4.1 XPS compositional analysis, and fitted parameters of the C 1s, O 1s, and Pt4f spectra of the graphene oxide, GO(OX) (1/1), GO(OX)PEG (1/1/0.2) NPs, and GO(OX)PB (1/1/0.2) NPs.

Samples	**Peaks**	**Binding energy (eV)**	**FWHM**	**Phase/Groups**
Graphene Oxide	C 1s	284.78	1.85	C-C
	C 1s	286.60	1.26	C-O
	C 1s	288.43	1.36	C=O
	O 1s	531.43	1.76	O-C=O/C-O
	O 1s	532.48	1.53	C=O
	Pt4f	NA	NA	NA
GO(OX) (1/1)	C 1s	284.82	1.23	C-C
	C 1s	286.38	1.29	C-O
	C 1s	288.02	1.68	C=O
	C 1s	288.93	1.59	O-C=O
	O 1s	531.49	1.62	O-C=O/C-O
	O 1s	532.65	1.83	C=O
	O 1s	533.95	1.77	C-O-C
	Pt4f	72.84	1.48	Pt(IV) 4f7/2
	Pt4f	76.24	1.19	Pt(IV) 4f5/2
	Pt4f	77.66	1.89	Pt(IV)
GO(OX)PEG(1/1/0.2) NPs	C 1s	284.80	1.32	C-C
	C 1s	286.68	2.03	C-O
	C 1s	288.53	1.45	C=O
	C 1s	289.31	1.69	O-C=O
	O 1s	531.62	1.80	O-C=O/C-O
	O 1s	532.83	1.68	C=O
	O 1s	533.01	1.55	C-OH
	O 1s	534.19	1.16	C-O-C
	Pt4f	72.88	1.74	Pt(IV) 4f7/2
	Pt4f	75.48	1.63	Pt(IV) 4f5/2

	Pt4f	78.73	2.01	Pt(IV)
	Pt4f	76.58	1.64	Pt(IV)
GO(OX)PB (1/1/0.2) NPs	C 1s	284.80	1.72	C-C
	C 1s	286.68	1.63	C-O
	C 1s	288.53	1.54	C=O
	C 1s	289.31	1.36	O-C=O
	O 1s	531.98	1.79	O-C=O/C-O
	O 1s	532.94	1.27	C=O
	O 1s	533.38	1.53	C-OH
	O 1s	534.46	1.08	C-O-C
	Pt4f	72.99	1.54	Pt(IV) 4f7/2
	Pt4f	75.88	1.44	Pt(IV) 4f5/2
	Pt4f	77.34	2.19	Pt(IV)
	Pt4f	78.95	1.92	Pt(IV)

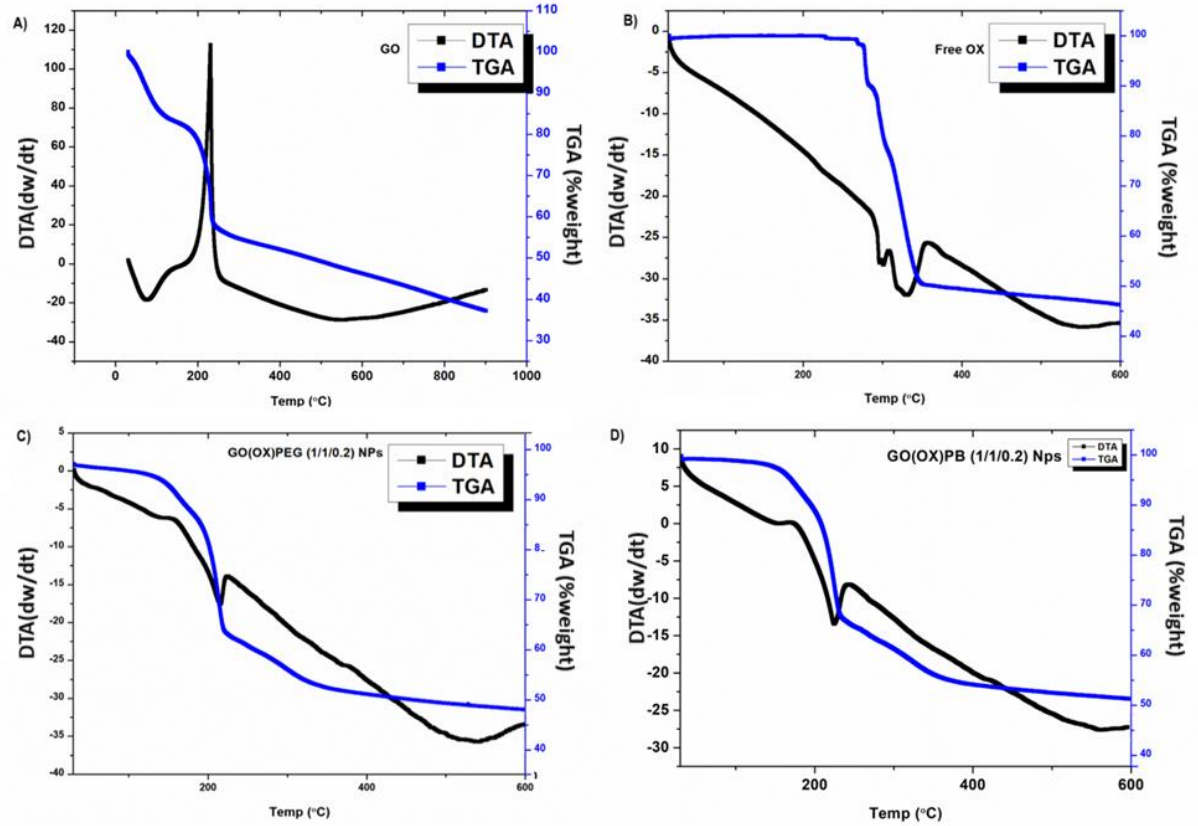

Figure 4.10 DTG and TGA analysis of GO, free OX, GO(OX)PEG (1/1/0.2) NPs, and GO(OX)PB (1/1/0.2) NPs.

The particle sizes of the GO(OX) (1/1), GO(OX)PEG (1/1/0.2) and GO(OX)PB (1/1/0.2) NPs were determined by dynamic light scattering (DLS). The measurements revealed that the particle size of the GO(OX) (1/1) NPs was 150.8 ± 2 nm, GO(OX)PEG (1/1/0.2) measured 158.3 ± 1.6 nm, while the GO(OX)PB (1/1/0.2) NPs had a particle size of 195.7 ± 2.3 nm with

a polydispersity index (PDI) values 0.36, 0.35 and 0.25, respectively (**Fig. 4.12A**). The zeta potential values for GO(OX) (1/1), GO(OX)PEG (1/1/0.2), and GO(OX)PB (1/1/0.2) NPs were determined to be -27.5 ± 0.35, -26.1 ± 1.25, and -23.8 ± 0.75 mV, respectively (**Fig. 4.12B**). These results indicated that the nanocarrier system exhibits favorable colloidal stability, as given in **Table 4.2** and **Fig. 4.12B**. Furthermore, an investigation was conducted to assess the % drug loading, and particle size of GO(OX)PB (1/1/0.2) NPs after a storage period of 21 days at a temperature of 4 ºC. The stability of the GO(OX)PB (1/1/0.2) NPs can be inferred from **Fig. 4.11B**, which demonstrates that their size remained relatively constant at around 195 nm even after being stored at a temperature of 4 ºC. The field emission scanning electron microscopy (FE-SEM) technique was utilized to conduct the morphological evaluation of GO(OX)PEG (1/1/0.2) and GO(OX)PB (1/1/0.2) NPs. The evident characteristic of GO flakes is their layered structure accompanied by a wavy shape. Based on the analysis of **Fig. 4.12E and 4.11A,** it can be shown that the functionalization of graphene oxide (GO) sheets with pegylated Biotin resulted in the modified GO exhibiting a smooth unilamellar morphology with reduced roughness. Notably, the distinctive structure of the native GO flakes was conserved in the modified GO.

Table 4.2 Physiochemical characterization of GO(OX) NPs.

S.No.	Formulation	Particle Size (nm)	PDI	Zeta Potential	(%) Drug loading	(%) Entrapment efficiency
1	**GO(OX) (1/1)**	**150.8 ± 2**	**0.36**	**-27.5 ± 0.35**	**45.29 ± 1.36**	**90.58**
2	GO(OX) (1/2)	153.4 ± 3	0.34	-23.3 ± 0.59	58.23 ± 2.71	87.36
3	GO(OX) (1/5)	161.3 ± 1.8	0.33	-22.1 ± 0.39	69.19 ± 2.11	83.03
4	GO(OX) (1/10)	183.7 ± 3	0.31	-18.3 ± 1.05	70.6 ± 1.49	77.66

5	GO(OX)PEG (1/1/0.1) NPs	154.9 ± 2.8	0.38	-24.9 0.86	±	44.56 ± 1.36	89.59
6	**GO(OX)PEG (1/1/0.2) NPs**	**158.3 ± 1.6**	**0.35**	**-26.1 1.25**	**±**	**44.39 ± 1.53**	**89.06**
7	GO(OX)PEG (1/1/0.5) NPs	179.9±3.3	0.42	-24.2 0.37	±	44.65 ± 1.07	90.26
8	GO(OX)PB(1/1/0.1) NPs	183.7 ± 4	0.31	-24.6 1.16	±	42.96 ± 0.85	88.63
9	**GO(OX)PB(1/1/0.2) NPs**	**195.7 ± 2.3**	**0.25**	**-23.8 0.75**	**±**	**43.56 ± 2.37**	**89.48**
10	GO(OX)PB(1/1/0.5) NPs	199.5 ± 2.5	0.28	-22.2 0.68	±	43.19 ± 1.45	88.39

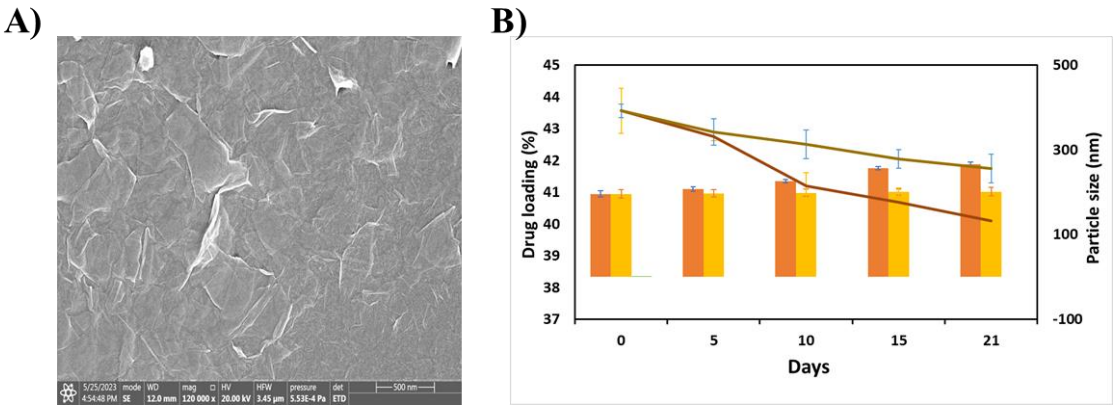

Figure 4.11 SEM analysis of GO(OX)PEG (1/1/0.2) NPs (A); Stability analysis of GO(OX)PB (1/1/0.2) NPs at room temperature and 4 ºC (B).

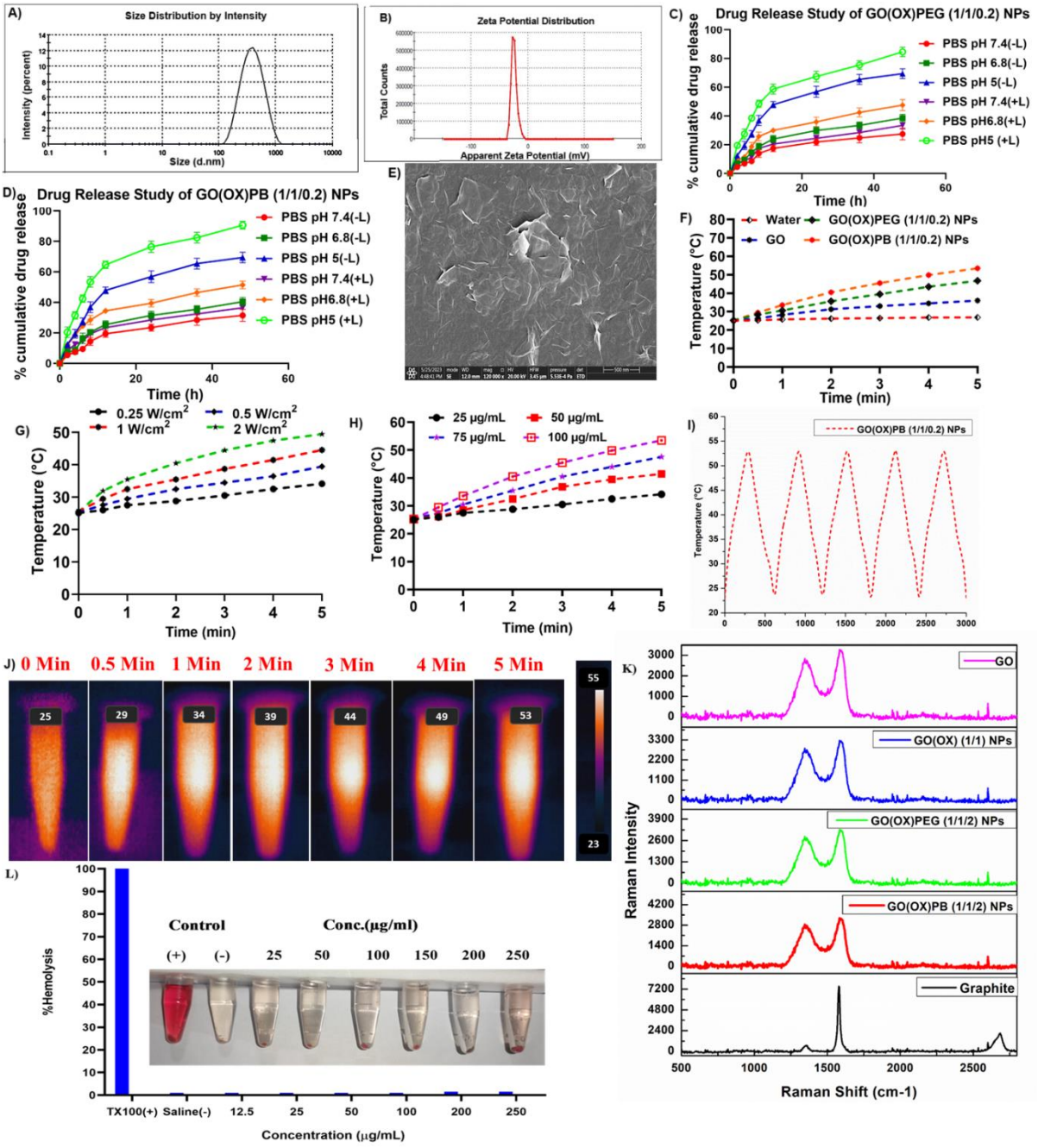

Figure 4.12 Physiochemical characterizations of GO(OX)PB (1/1/0.2) NPs. Particle size (A); Zeta Potential (B); Drug release study of GO(OX)PEG (1/1/0.2) NPs, and GO(OX)PB (1/1/0.2) NPs at various PHs (C, D); SEM morphology (E); Temperature variation curves of pure water, GO, GO(OX)PEG (1/1/0.2) NPs, and GO(OX)PB (1/1/0.2) NPs exposed to 808 nm Laser (0.5 W/cm^2) for 5 min (F); Temperature variation curves of various concentrations of GO(OX)PB (1/1/0.2) NPs exposed to 808 nm Laser (0.5 W/cm^2) for 5 min (G); Temperature variation curves of GO(OX)PB (1/1/0.2) NPs (25 μg/mL) exposed to various power intensities for 5 min

(H); Thermal images of GO(OX)PB (1/1/0.2) NPs exposed to 808 nm Laser (0.5 W/cm^2) for 5 min (J); Thermal Stability study (I); *In vitro* hemolysis study of GO(OX) (1/1) conjugate (K); FTIR spectra of rhodamine B and GO(OX)PB (1/1/0.2)-RhB NPs (L); UV analysis of GO, RhB and GO(OX)PB (1/1/0.2)-RhB NPs (M); and Fluorescence spectra of RhB and GO(OX)PB (1/1/0.2)-RhB NPs (N).

Subsequently, we conducted measurements to assess the release of OX from GO(OX)PEG (1/1/0.2) and GO(OX)PB (1/1/0.2) NPs under pH conditions 5, 6.8, and 7.4, both in the presence and absence of NIR laser radiations (±L). The GO(OX)PEG (1/1/0.2) and GO(OX)PB (1/1/0.2) NPs exhibited sustained *in vitro* OX release over an extended period. The release behavior of OX from the formulations was observed to be dependent on both laser irradiation and pH, as depicted in **Fig. 4.12C, D**. The potential photothermal effect of GO(OX)PEG (1/1/0.2) and GO(OX)PB (1/1/0.2) NPs, which might potentially disrupt the interactions between OX and GO, may indicate an elevated release of OX when exposed to NIR laser irradiation. The study demonstrated that the combination of chemotherapy and photothermal treatment can result in a significant enhancement of chemotherapy efficacy.

Furthermore, the application of mathematical modeling was employed to investigate the release kinetics of GO(OX)PEG (1/1/0.2) and GO(OX)PB (1/1/0.2) NPs, in conjunction with the analysis of release patterns (**Table 4.3, 4.4 and Fig. 4.13**). This study employed various mathematical models, namely the zero order, first order, Higuchi, Korsmeyer-Peppas model, Hixson Crowell model, and the Weibull model, which are widely utilized for the mathematical representation of drug release from NPs. The release exponent (n) is employed to describe the release mechanism, with n = 0.43 denoting a Fickian diffusion and 0.43 < n < 0.85 indicating a non-Fickian transport for NP systems. The release of the drug from GO(OX)PEG (1/1/0.2) NPs at different pH levels exhibited best-fitting R^2 values of 0.966 (pH 7.4 -L), 0.973 (pH 7.4, +L), 0.9756 (pH 6.8, -L, 0.9667 (pH 6.8, +L) followed Higuchi model. While at pH 5 it has

followed the Weibull model with R^2 values of 0.9713 (-L) and 0.9808 (+L). For OX release from GO(OX)PB (1/1/0.2) NPs at pH 7.4 (-L), 6.8, and 5 (±L), it followed the Weibull kinetic model. Meanwhile, at pH 7.4 and 6.8 (-L), it adhered to the Higuchi model. This suggests that the release behavior is affected by the environmental conditions, and the choice of model can be tailored to suit specific pH requirements.

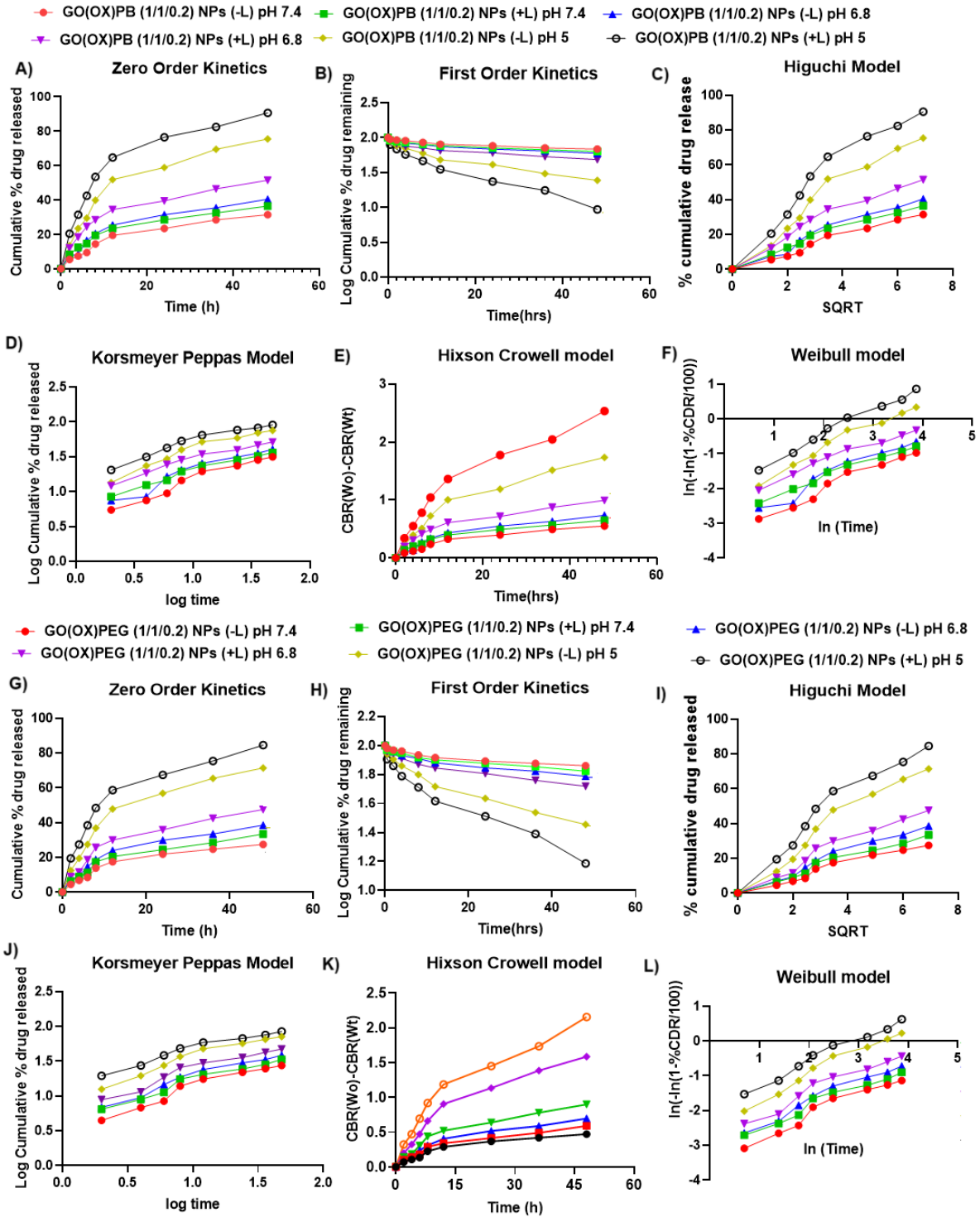

Figure 4.13 Release kinetics of GO(OX)PEG (1/1/0.2) NPs and GO(OX)PB (1/1/0.2) NPs in various pHs.

Table 4.3 Release kinetics of GO(OX)PEG (1/1/0.2) NPs in various pHs.

S.No.	pH	Zero order	First order	Higuchi model	Korsmeyer Peppas model	Hixson Crowel model	Weibull model	Best-Fit model
1	pH 7.4 (-L)	y = 0.5275x + 5.6911 R^2 = 0.8523	y = -0.0027x + 1.975 R^2 = 0.8793	y = 4.2179x - 0.1545 R^2 = 0.966	y = 0.5837x + 0.5164 R^2 = 0.9506	y = 0.0092x + 0.0891 R^2 =0.8704	y = 0.6282x - 3.4365 R^2 = 0.9561	**Higuchi Model**
2	pH 7.4 (+L)	y = 0.6066x + 7.3435 R^2 = 0.8585	y = -0.0033x + 1.9677 R^2 = 0.8946	y = 4.85x + 0.6219 R^2 = 0.973	y = 0.5183x + 0.6802 R^2 = 0.9575	y = 0.0108x + 0.115 R^2 = 0.8829	y = 0.5698x - 3.0565 R^2 = 0.9631	**Higuchi Model**
3	pH 6.8 (-L)	y = 0.7154x + 8.3677 R^2 = 0.8576	y = -0.004x + 1.9633 R^2 = 0.8999	y = 5.7306x + 0.4053 R^2 = 0.9756	y = 0.546x + 0.7116 R^2 = 0.9593	y = 0.0131x + 0.131 R^2 = 0.8863	y = 0.6098x - 2.9937 R^2 = 0.9679	**Higuchi Model**
4	pH 6.8 (+L)	y = 0.8763x + 10.865 R^2 = 0.8419	y = -0.0053x + 1.9521 R^2 = 0.9006	y = 7.0529x + 0.9998 R^2 = 0.967	y = 0.5347x + 0.8244 R^2 = 0.9412	y = 0.017x + 0.1709 R^2 = 0.8822	y = 0.6181x - 2.7423 R^2 = 0.9541	**Higuchi Model**
5	pH 5 (-L)	y = 1.3118x + 16.927 R^2 = 0.8203	y = -0.0104x + 1.9266 R^2 = 0.9195	y = 10.658x + 1.8276 R^2 = 0.96	y = 0.5408x + 1.0007 R^2 = 0.9465	y = 0.03x + 0.2664 R^2 = 0.8899	y = 0.6972x - 2.3901 R^2 = 0.9713	**Weibull model**
6	pH 5 (+L)	y = 1.4742x + 23.764 R^2 = 0.7921	y = -0.0153x + 1.9011 R^2 = 0.9478	y = 12.146x + 6.2318 R^2 = 0.9533	y = 0.4525x + 1.207 R^2 = 0.948	y = 0.0398x + 0.3741 R^2 = 0.9072	y = 0.6627x - 1.9339 R^2 = 0.9808	**Weibull model**

Table 4.4 Release kinetics of GO(OX)PB (1/1/0.2) NPs in various pHs.

S.No.	pH	Zero order	First order	Higuchi model	Korsmeyer Peppas model	Hixson Crowel model	Weibull model	Best-Fit model
1	pH 7.4 (-L)	y = 0.6065x + 6.1083 R^2 = 0.8798	y = -0.0032x + 1.9736 R^2 = 0.9094	y = 4.7996x - 0.4475 R^2 = 0.977	y = 0.5741x + 0.5763 R^2 = 0.9642	y = 0.0107x + 0.0948 R^2 = 0.8998	y = 0.6257x - 3.3042 R^2 = 0.9688	**Higuchi model**
2	pH 7.4 (+L)	y = 0.645x + 9.5157 R^2 = 0.8338	y = -0.0036x + 1.9573 R^2 = 0.8795	y = 5.239x + 2.0962 R^2 = 0.9753	y = 0.4528x + 0.8284 R^2 = 0.9751	y = 0.0118x + 0.1511 R^2 = 0.8648	y = 0.5084x - 2.7057 R^2 = 0.981	**Weibull model**
3	pH 6.8 (-L)	y = 0.7521x + 8.9498 R^2 = 0.8431	y = -0.0043x + 1.9605 R^2 = 0.89	y = 6.0436x + 0.5143 R^2 = 0.9653	y = 0.5522x + 0.7275 R^2 = 0.9269	y = 0.014x + 0.1407 R^2 = 0.875	y = 0.6205x - 2.9592 R^2 = 0.9387	**Higuchi model**
4	pH 6.8 (+L)	y = 0.8859x + 14.6 R^2 = 0.8054	y = -0.0057x + 1.9331 R^2 = 0.8826	y = 7.2767x + 4.1392 R^2 = 0.9634	y = 0.4323x + 1.0157 R^2 = 0.9607	y = 0.0177x + 0.2354 R^2 = 0.8585	y = 0.5178x - 2.2771 R^2 = 0.9746	**Weibull model**
5	pH 5 (-L)	y = 1.3903x + 18.595 R^2 = 0.8233	y = -0.012x + 1.9222 R^2 = 0.9386	y = 11.291x + 2.6065 R^2 = 0.9627	y = 0.5231x + 1.0554 R^2 = 0.9457	y = 0.0336x + 0.2888 R^2 = 0.9058	y = 0.6982x - 2.2764 R^2 = 0.9816	**Weibull model**
6	pH 5 (+L)	y = 1.5877x + 26.665	y = -0.0197x + 1.8946	y = 13.19x + 7.4203	y = 0.4535x + 1.2473 R^2 = 0.9399	y = 0.0477x + 0.4181	y = 0.7148x - 1.8883	**Weibull model**

R^2	=	R^2	=	R^2	=	R^2	=	R^2	=
0.7715		0.9591		0.9441		0.912		0.9847	

The hemolytic assay is a crucial examination conducted on materials that have direct exposure to blood. Based on the ISO standard (document 10 993-5 1992), substances with a hemolysis index below 5% are deemed to be within the realm of safety (Ganjali et al., 2022). **Fig. 4.12L** displays the histogram representing the distribution of hemolysis percentages for nanocarrier (GO(OX) (1/1)), positive control (Triton X-100), and negative control (PBS) following a 2-h incubation period with RBCs. The findings indicated that no statistically significant difference was observed in the hemolytic activity between GO(OX) (1/1) and the negative control ($P > 0.05$). The respective values for hemolytic activity were 3.98 % and 1.08 %. In contrast, the inclusion of Triton X-100 as a positive control resulted in the lysis of nearly all red blood cells.

4.3.2 Photothermal effect of GO(OX)PB (1/1/0.2) NPs

To evaluate the photothermal response of graphene oxide and its derivatives, we simultaneously observed changes in temperature at intervals of 30 sec while exposing them to an 808 nm laser (0.5 W/cm^2). As illustrated in **Fig. 4.12F, J**, the temperatures of GO, GO(OX)PEG (1/1/0.2), and GO(OX)PB (1/1/0.2) NPs solutions exhibited a swift elevation to 39.3, 48.79, and 53.5 °C, respectively, upon exposure to 808 nm laser irradiation (0.5 W/cm^2) for 5 min. This observation suggests that GO(OX)PEG (1/1/0.2) and GO(OX)PB (1/1/0.2) NPs possess remarkable photothermal capabilities. Simultaneously, it was noted that the temperature exhibited dependence on both concentration and laser power intensity (**Fig. 4.12G, H**). Specifically, the temperature of the GO(OX)PB (1/1/0.2) NPs (25 μg/mL) experienced a rapid rise in response to an escalation in power intensity from 0.25 W/cm^2 to 2 W/cm^2 or increase in nanocomposite concentration from 25 μg/mL to 100 μg/mL. Furthermore, the photothermal conversion efficiency of GO(OX)PEG and (1/1/0.2) NPs GO(OX)PB (1/1/0.2)

NPs was determined to be 46.12 % and 50.95 % (**Table 4.5, Fig. 4.14**). This finding prompts us to conduct a more in-depth assessment of the photothermal impact of GO(OX)PB (1/1/0.2) NPs on cellular models. Prior investigations into the photothermal conversion of graphene have demonstrated that optimal near-infrared (NIR) absorption relies on reduced sizes and appropriate surface chemistry (K. Yang et al., 2012). In this context, the photothermal efficiency of GO experienced a substantial enhancement, presumably attributable to the nanoscale structure and the restored sp^2 carbon domains within the skeleton (Sherlock et al., 2011). These domains can serve as conduits for electron transfer, as evidenced by the Raman spectra depicted in **Fig. 4.12K**. Significantly, as illustrated in **Fig. 4.12I**, the temperature of the GO(OX)PB (1/1/0.2) NPs consistently attained levels comparable to those observed in the initial irradiation step across all five on/off laser cycles. This observation suggests that the GO(OX)PB (1/1/0.2) NPs exhibited outstanding photostability, rendering them dependable for practical applications.

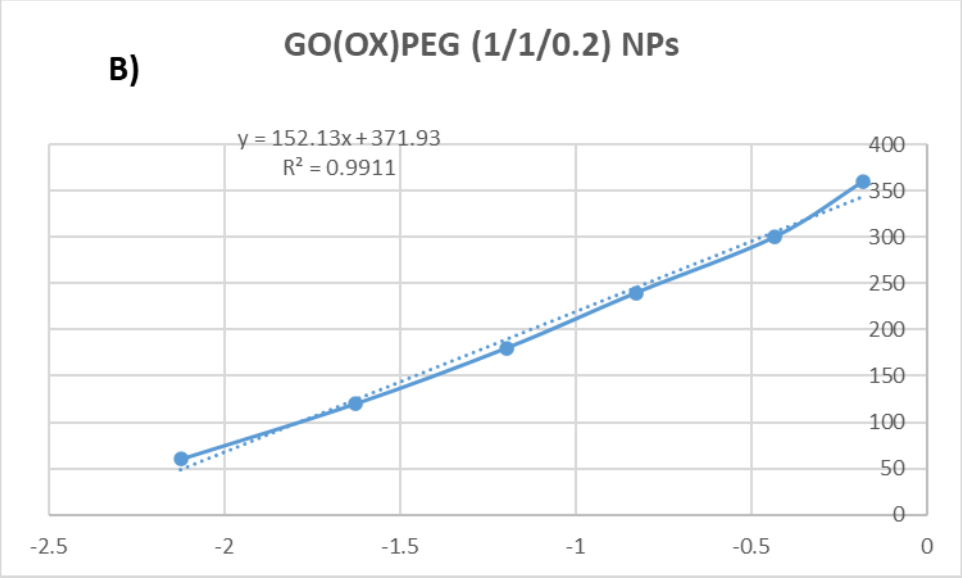

Figure 4.14 The graph of negative ln θ vs. time to calculate the slope to determine the photothermal conversion efficiency.

Table 4.5 Photothermal conversion efficiency parameters

Parameters	**GO(OX)PB (1/1/0.2) NPs**	**GO(OX)PEG (1/1/0.2) NPs**
T max	53.475	46.75
T_{amb} in °C	25	27.5
I in W (laser power)	0.5	0.5
Q_0 in W (heat dissipated from the light absorbed by the solvent)	0.0312	0.0339
A λ(at 808 nm) (Absorbance)	0.345	0.373
m (Mass of Pure Water) in gram	0.5	0.5
Cp (Specific Heat Capacity Of water) in J/g °C	4.2	4.2
τ_s in second	192.7	152.13
hs = $mDC_D/\ \tau_s$	0.0109	0.0139
$\eta = \frac{hA(T_{max}-T_{amb})-Q_0}{I(1-10^{-A_\lambda})}$	50.95 %	46.12 %

4.3.3 *In vitro* assays

4.3.3.1 Cellular internalization studies

The uptake of therapeutic agents into the cytoplasm and nucleus is critical for cancer therapies to be successful. The confocal fluorescence imaging and flow cytometry were used to investigate the specific targeting and cellular uptake capacity of GO(OX)PEG(1/1/0.2) NPs and GO(OX)PB (1/1/0.2) RhB loaded NPs, both qualitatively and quantitatively in MCF-7 cells. The successful loading of RhB on NPs was confirmed by FTIR, UV spectroscopy, and fluorescence spectra analysis, which are represented in **Fig. 4.15**. In the MCF-7 cell line, distinct and intense red fluorescence was detected in both the cytoplasm and nuclei of cells targeted with GO(OX)PB(1/1/0.2) NPs, indicating rapid internalization of GO(OX)PB(1/1/0.2) NPs. From 1 to 4 h, the red fluorescence intensity of GO(OX)PEG(1/1/0.2) NPs and GO(OX)PB(1/1/0.2) NPs was increased, demonstrating time-dependent cellular uptake for

MCF-7 cells. Furthermore, the GO(OX)PB(1/1/0.2) NPs combined with Laser (+L) exhibited significantly greater red fluorescence intensity compared to both GO(OX)PEG(1/1/0.2) NPs (±L) and GO(OX)PB(1/1/0.2) (-L), indicating that the cellular uptake in the MCF-7 cell line was dependent on the presence of laser. In addition, Flow cytometry investigations were conducted to confirm the enhanced uptake and release of the substance inside the cells, as shown in **Fig. 4.16A**. The average fluorescence intensity values for GO(OX)PEG(1/1/0.2) NPs and GO(OX)PB (1/1/0.2) NPs were observed to rise from 1 to 4 h in the histogram of the flow cytometer, which was presented as a bar graph (**Fig. 4.16B, D**). For MCF-7 cells, the geometric mean fluorescence of GO(OX)PEG(1/1/0.2) NPs and GO(OX)PB (1/1/0.2) NPs treated cells without laser rose from 1875.33±49.65 to 3152.43±67 (-L), and 2285.76±87.35 to 3978.48±73.34 (-L) from 1 to 4 h **(Fig. 4.16C)**, whereas the geometric mean fluorescence of GO(OX)PEG(1/1/0.2) NPs and GO(OX)PB (1/1/0.2) NPs treated cells with laser rose from 2014.54±72.65 to 3608.48±83.27 (+L), and 2547.78±67.34 to 4375.29±92.44 (+L) from 1 to 4 h shown a rise in the intensity of fluorescence in the examined cell line that was dependent on both time and laser **(Fig. 4.16E)**. The results regarding the release of the drug intracellularly and the absorption of the drug by cells showed that the exposure to near-infrared (NIR) light caused an increase in temperature that improved the permeability of the cell membrane. This led to an effective intracellular administration of OX for photothermal anticancer therapy.

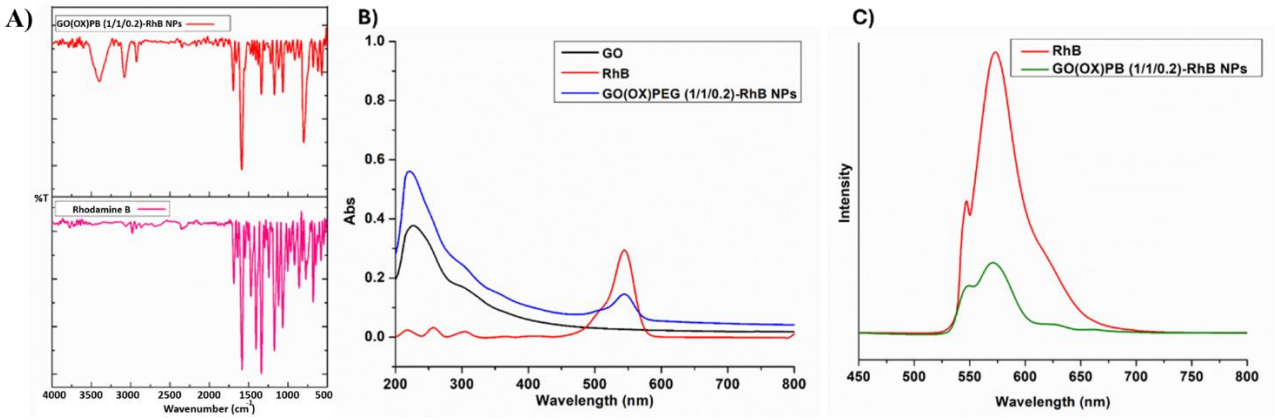

Figure 4.15 FTIR analysis of Rhodamine B and RhB loaded GO(OX)PB (1/1/0.2) NPS (A);

UV analysis of GO, RhB and RhB loaded GO(OX)PEG (1/1/0.2) NPS (B); Fluorescence spectra analysis of Rhodamine B and RhB loaded GO(OX)PB (1/1/0.2) NPs (C).

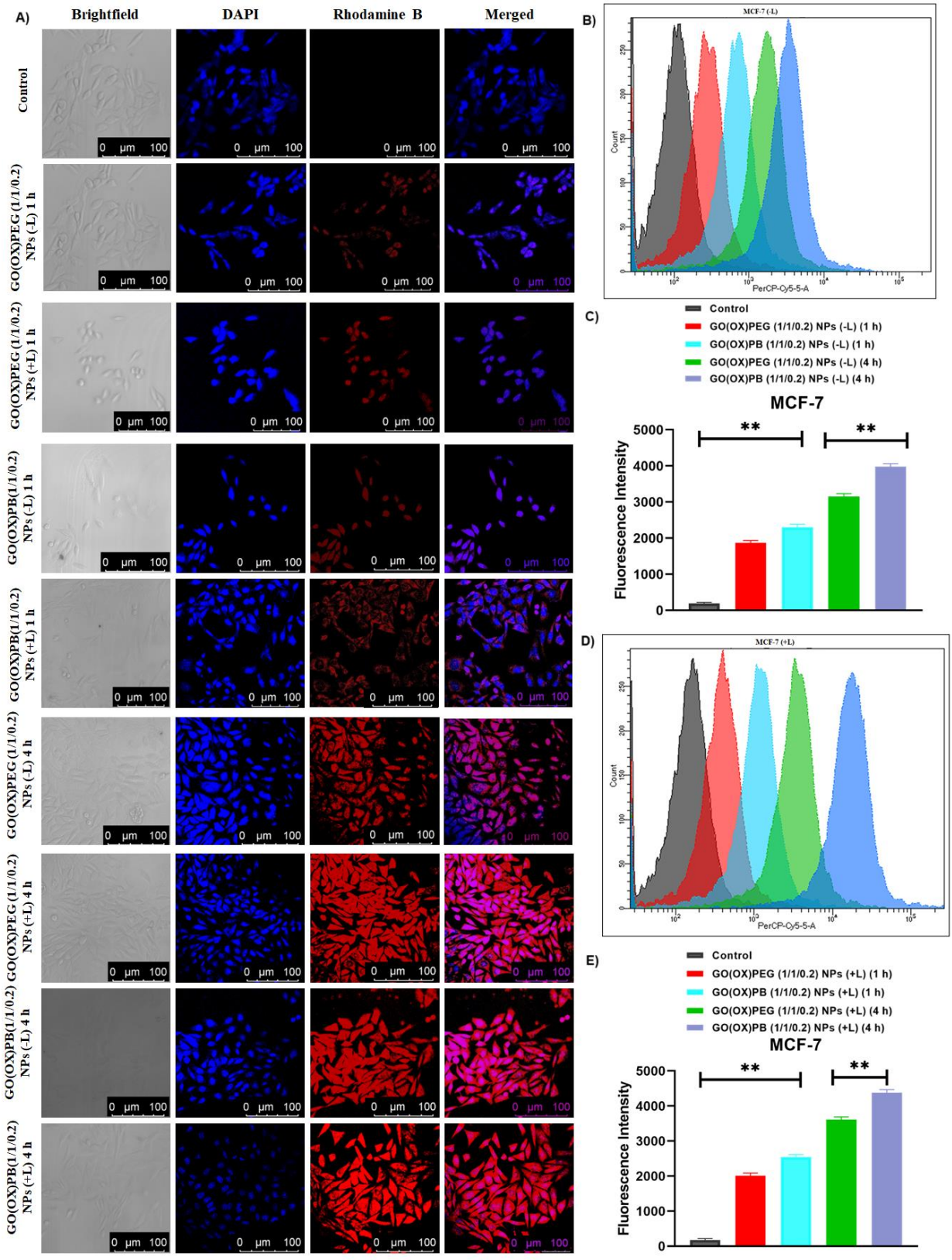

Figure 4.16 *In vitro* photothermal effect on cellular uptake through a cellular internalization study of GO(OX)PEG (1/1/0.2) NPs and GO(OX)PB (1/1/0.2) NPs (±L) at 0.5 W/cm2 in MCF-7 cells.

In vitro photothermal effect on cellular uptake through a cellular internalization study of GO(OX)PEG (1/1/0.2) NPs and GO(OX)PB (1/1/0.2) NPs (±L) at 0.5 W/cm2 in MCF-7 cells (A). The observations were made at 1 and 4 h post-incubation using a confocal microscope. Utilizing flow cytometry, Figures (B, C) illustrate the amount of NPs taken up by MCF-7 cells (-L), while Figures (D, E) represent the uptake in the presence of laser irradiation (+L). The statistical analysis reveals a significant difference with a p-value less than 0.01.

To examine the cellular internalization dynamics of GO(OX)PB (1/1/0.2) NPs, we also assessed the Raman spectra of GO(OX)PB (1/1/0.2) NPs following incubation with MCF-7 cells for durations of 2, 4, 6, and 8 h. As depicted in **Fig. 4.18B**, a low-intensity Raman signal was detected after 2 h of incubation, indicating that the time frame of 2 h was insufficient for a substantial quantity of GO(OX)PB (1/1/0.2) NPs to enter the cells significantly. Robust Raman signals from GO were observed upon incubation of GO(OX)PB (1/1/0.2) NPs with MCF-7 cells for 4 h, with the signal intensity peaking at 8 h of incubation. Based on the spectral data, it is demonstrated that the uptake of GO(OX)PB (1/1/0.2) NPs by MCF-7 cells substantially increased at 4 h of incubation, reaching its zenith at 8 h. Moreover, AAS was employed for the evaluation of platinum (Pt) content in the cell lysis solutions of MCF-7 cells. Cellular Pt levels were quantified and expressed as nanograms of Pt per 10^6 cells, as illustrated in **Fig. 4.18E**. The results reveal a markedly increased Pt absorption by the GO(OX)PB (1/1/0.2) NPs (+L) within the cellular environment compared to free OX, GO(OX)PB(1/1/0.2) NPs (-L), and GO(OX)PEG(1/1/0.2) NPs (±L). Additionally, the GO(OX)PB (1/1/0.2) NPs (+L) exhibit proficiency in delivering and releasing OX.

The investigation of internalization involved the acquisition of *Z*-stacked microscopic images. Confocal laser scanning micrographs depicting cells treated with GO(OX)PEG(1/1/0.2)-RhB NPs and GO(OX)PB (1/1/0.2)-RhB NPs are presented in **Fig. 4.17** at a consistent X–Y plane with a variable *Z*-axis. The GO(OX)PB-RhB (1/1/0.2) NPs exhibited an enhanced RhB fluorescence in the central stack or stacks located farther from the surface. The micrographs of central slices (Z4-Z8) revealed a greater cellular internalization of RhB in GO(OX)PB (1/1/0.2) NPs (+L) compared to GO(OX)PB (1/1/0.2) NPs (-L) and GO(OX)PEG (1/1/0.2) NPs (±L) in MCF-7 cells. Consequently, a decline in fluorescence intensity was observed beyond 8 to 10 μm from the central slices. Various inhibitors were employed to comprehend the internalization mechanism of the GO(OX)PB (1/1/0.2) NPs. As depicted in **Fig. 4.18A**, it was observed that treatment with any of the inhibitors resulted in a reduction in fluorescence intensity compared to control cells without inhibitor treatment. Among the inhibitors, chlorpromazine treatment exhibited a remarkable decrease in fluorescence intensity, whereas nystatin and amiloride treatment demonstrated the highest fluorescence for MCF-7 cells. Collectively, the inhibitor experiment implies that the intracellular internalization of GO(OX)PB (1/1/0.2) NPs primarily occurs via a clathrin-mediated mechanism, with caveolae or actin endocytosis playing a comparatively minor or negligible role. The data was in accordance with the previously documented findings (J. Huang et al., 2012).

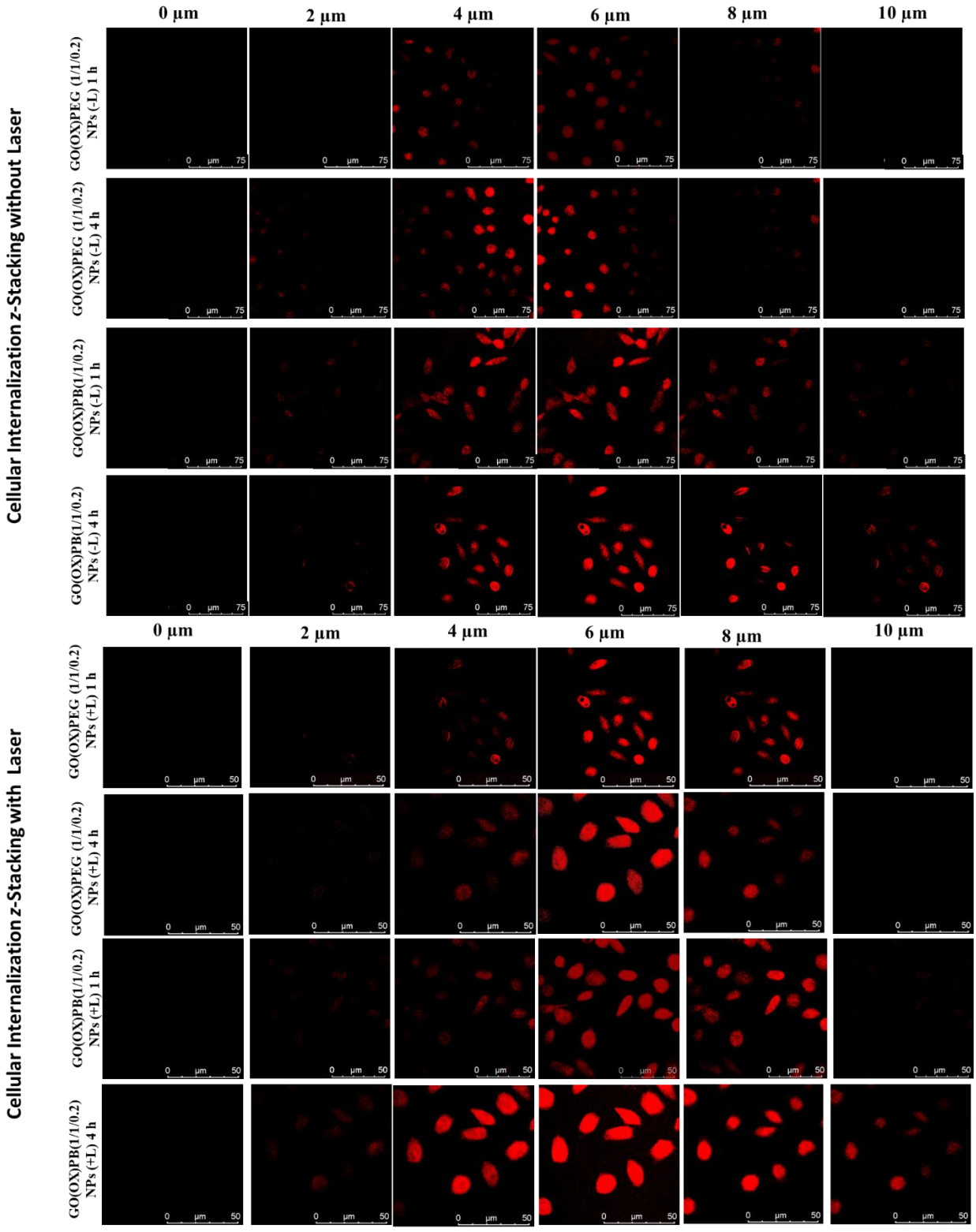

Figure 4.17 Confocal microscopy imaging depicting the z-stack analysis of cellular internalization in MCF-7 cells.

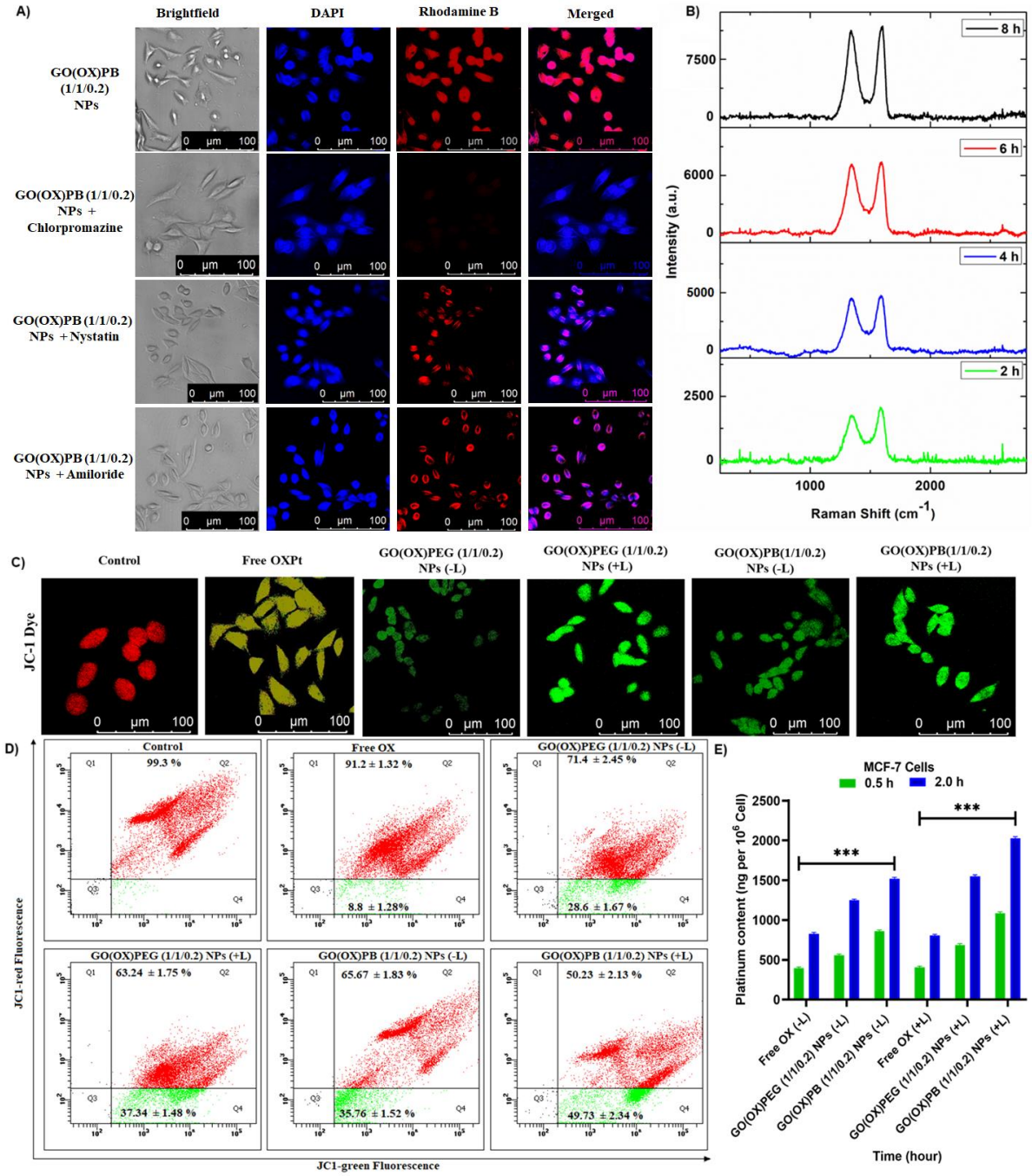

Figure 4.18 Cellular Internalization mechanism of GO(OX)PB (1/1/0.2) NPs (A); Time course entry of GO(OX)PB(1/1/0.2) NPs by Raman Spectroscopy for 8 h (B); Qualitative and quantitative analysis of Mitochondrial membrane depolarization in MCF-7 treated cells by confocal microscopy (C), and flow cytometry (D); and evaluation of Pt content in cells by AAS (E). The significance of the difference was assessed by ANOVA, $^{**}P < 0.01$, $^{*}P < 0.05$.

4.3.3.2 Cytotoxicity study and live/dead cell assay

Additionally, the *in vitro* assessment of the cytotoxic impact on MCF-7 cells was conducted for free OX, GO(OX)PEG(1/1/0.2) NPs, and GO(OX)PB (1/1/0.2) NPs, both with and without laser exposure (±L) at 0.5 W/cm^2, using the MTT test over 24 and 48 h. The results depicted in **Fig. 4.20** indicate that the cell survival rates of the positive control group (+L alone) were comparable to those of the negative control group (PBS, -L). This suggests that laser irradiation alone did not exert any harmful effects. Overall, the laser-irradiated cells (+L) showed cell death greater than the laser-non-irradiated (-L) cells in both the time points (24 and 48 h). In MCF-7 cells, after a 24-h incubation period with GO(OX)PB (1/1/0.2) NPs, the percentages of viable cells were 9.70% (+L) and 14.54% (-L). This viability further decreased to 3.65% (+L) and 5.85% (-L) after 48 h, at the highest equivalent OX concentration of 100 µg/mL. Meanwhile, GO(OX)PEG (1/1/0.2) NPs exhibited cell viability of 19.34% (-L) and 15.86% (+L) after 24 h, and 12.46% (-L) and 8.12% (+L) after 48 h, respectively. In parallel, free OX (100 µg/mL) displayed cell viability of 22.73% (-L) after 24 h and 15.65% (-L) after 48 h in MCF-7 cells. Similarly, in 4T1 cells, after a 24-h incubation period with GO(OX)PB (1/1/0.2) NPs, the percentages of viable cells were 16.45% (+L) and 12.74 % (-L). This viability further decreased to 10.37% (-L) and 8.29% (+L) after 48 h, at the highest equivalent OX concentration of 100 µg/mL. Meanwhile, GO(OX)PEG (1/1/0.2) NPs exhibited cell viability of 26.50% (-L) and 21.45% (+L) after 24 h, and 15.13% (-L) and 13.76% (+L) after 48 h, respectively. In parallel, free OX (100 µg/mL) displayed cell viability of 33.56% (-L) after 24 h and 19.73% (-L) after 48 h in MCF-7 cells. With an increase in both the dose, laser intensity, and duration of GO(OX)PB (1/1/0.2) NPs, a decline in the number of surviving cells was observed, highlighting a dosage, laser, and time-dependent relationship (**Fig. 4.19E, F, G and H**). The potent inhibitory effect of GO(OX)PB (1/1/0.2) NPs in the absence of laser irradiation may be attributed to the release of OX. Furthermore, the inhibitory efficacy of GO(OX)PB (1/1/0.2) NPs was augmented upon laser irradiation, suggesting that the combination of PTT with

chemotherapy could enhance therapeutic effectiveness. Cell viability studies revealed that GO(OX)PB (1/1/0.2) NPs (+L) induced greater cellular absorption, resulting in reduced cell viability compared to free OX. The cytotoxic impact of free OX, graphene oxide-based nanocomposites (GO(OX)PEG(1/1/0.2) NPs) and GO(OX)PB (1/1/0.2) NPs, with or without laser irradiation (±L) at 0.5 W/cm^2, was assessed on MCF-7 and 4T1 cells by comparing IC-50 values, as illustrated in **Fig. 4.19A, B, C, D** and **Table 4.6**. Cells subjected to a 24-h treatment displayed a higher IC-50 value compared to those continuously incubated for 48 h. In the tested cell lines, GO(OX)PB (1/1/0.2) NPs (+L) exhibited the most potent anti-proliferative activity relative to free OX, GO(OX)PEG(1/1/0.2) NPs (±L), and GO(OX)PB (1/1/0.2) NPs (-L), suggesting that the combination of photothermal and chemotherapy enhances treatment efficacy. The decrease in IC50 values from 24 to 48 h indicates a time-dependent cytotoxicity.

Moreover, a live/dead cell assay was conducted to visualize the anticancer efficacy, as illustrated in **Fig. 4.21A**. It is evident that nearly all cells in the control group exhibited vitality, as indicated by the green fluorescence from calcein AM staining. As anticipated, the application of 808 nm NIR laser irradiation (0.5 W/cm^2) to GO(OX)PB (1/1/0.2) NPs for 5 min resulted in a greater extent of cancer cell death and a noticeable increase in red fluorescence (indicative of dead cells) was observed in comparison to cells treated with free OX, GO(OX)PEG(1/1/0.2) NPs (±L), and GO(OX)PB (1/1/0.2) NPs (-L). These findings signify the optimal synergistic therapeutic impact of GO(OX)PB (1/1/0.2) NPs under 808 nm NIR irradiation (0.5 W/cm^2), aligning with the outcomes observed in the MTT assay. Overall, the prepared multifunctional nanoplatform demonstrates efficient utility in the context of chemo-photothermal synergistic therapy for tumors.

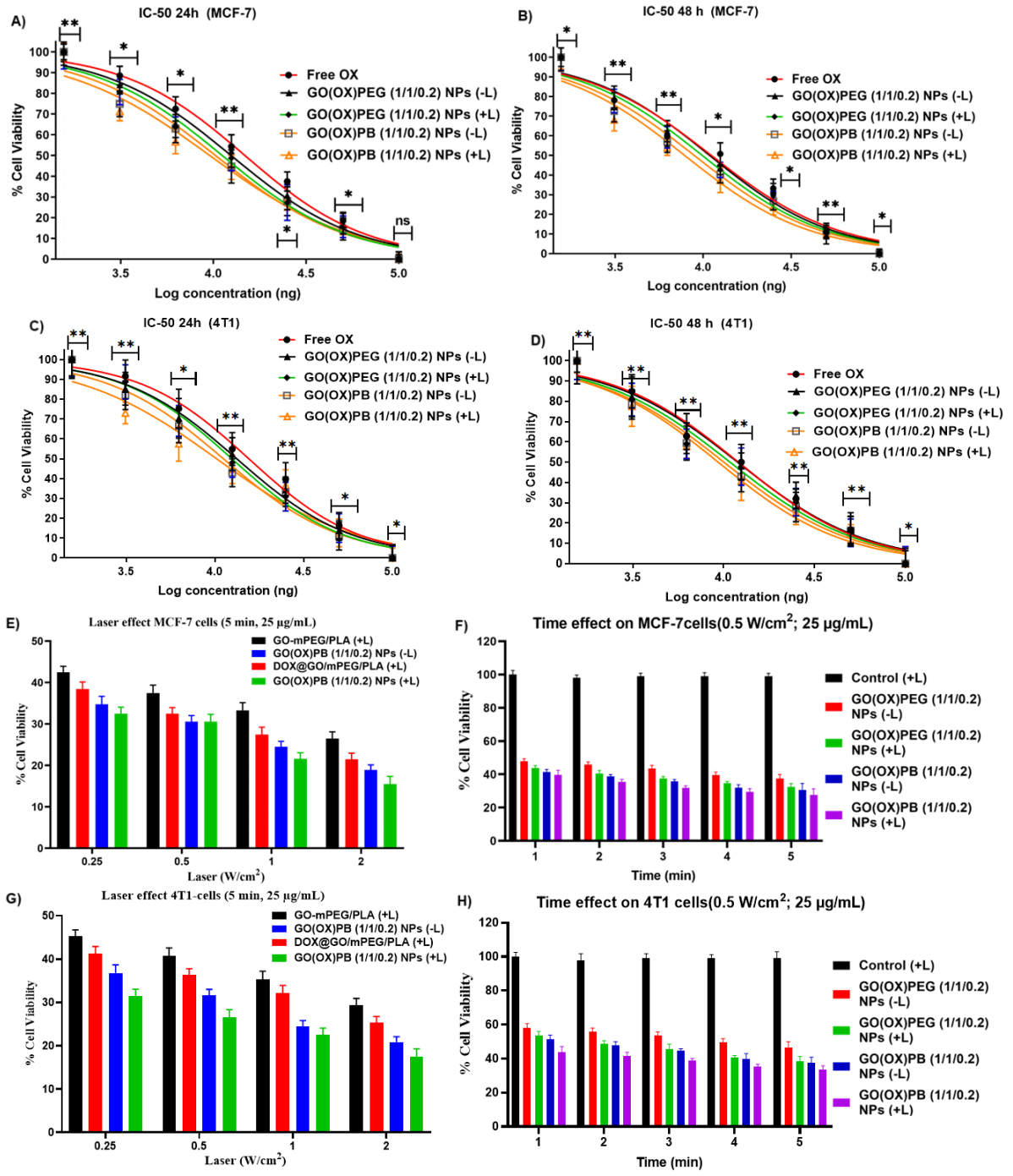

Figure 4.19 *In vitro* cytotoxicity activity of free OX, GO(OX)PEG (1/1/0.2) NPs, and GO(OX)PB (1/1/0.2) NPs (± L) (0.5 W/cm2) by MTT assay. MCF-7 and 4T1 cells were treated with OX at a concentration range of 1.56-100 µg/mL (n=3). The IC50 value of free OX, GO(OX)PEG (1/1/0.2) NPs, and GO(OX)PB (1/1/0.2) NPs (± L) for cultured MCF-7 and 4T1 cells (A, B, C, D) cells at 24 h and 48 h; Effect of laser (E, G) and laser (F, H) on the cytotoxicity

of MCF-7 and 4T1 cells. The significance of the difference was assessed by ANOVA, **P < 0.01, *P < 0.05.

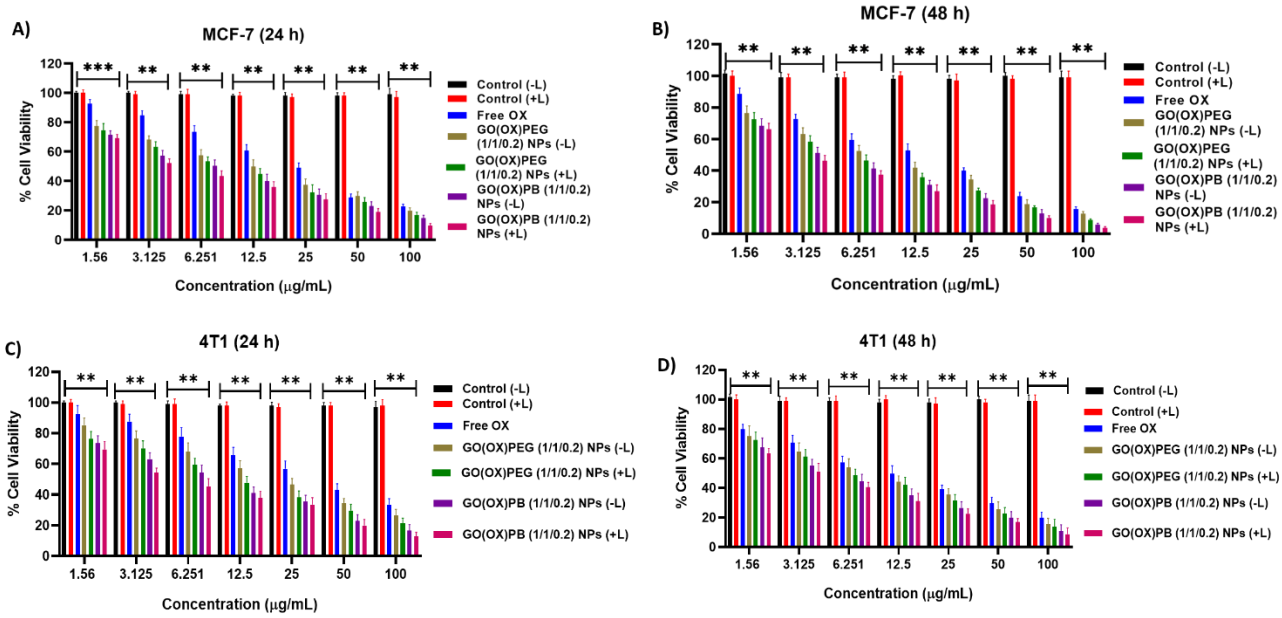

Figure 4.20 *In vitro* cytotoxicity activity of free OX, GO(OX)PEG (1/1/0.2) NPs, and GO(OX)PB (1/1/0.2) NPs (± L) (0.5 W/cm^2) by MTT assay. MCF-7 cells and 4T1 cells were treated with OX at a concentration range of 1.56 to 100 μg/mL (n = 3). The significance of the difference was assessed by ANOVA, **P < 0.01, *P < 0.05.

Table 4.6 IC-50 value of Free OX, GO(OX)PEG (1/1/0.2) NPs (-L), GO(OX)PB (1/1/0.2) NPs (-L), GO(OX)PEG (1/1/0.2) NPs (+L), and GO(OX)PB (1/1/0.2) NPs (+L) in MCF-7 and 4T1 cells.

Compound	**MCF-7**		**4T1**	
	IC-50 (24 h) (μM)	**IC-50 (48h) (μM)**	**IC-50 (24 h) (μM)**	**IC-50 (48h) (μM)**
Free OX	14.051	11.129	15.532	12.077
GO(OX)PEG (1/1/0.2) NPs (-L)	12.469	10.889	13.278	11.960
GO(OX)PEG (1/1/0.2) NPs (+L))	11.167	9.884	12.464	10.872
GO(OX)PB(1/1/0.2) NPs (-L)	10.273	9.004	11.169	10.051

GO(OX)PB (1/1/0.2) NPs (+L)	9.561	7.852	10.224	9.354

4.3.3.3 Intracellular ROS generation assay, Mitochondria Membrane Potential (MMP) study, and Annexin V assay

The DCFH-DA dye, serving as an intracellular sensor, was employed to monitor the reactive oxygen species (ROS) formation in MCF-7 cells induced by free oxaliplatin (OX), graphene oxide-based nanocomposites (GO(OX)PEG(1/1/0.2) NPs ±L), and GO(OX)PB (1/1/0.2) NPs (±L). As depicted in **Fig. 4.21B**, MCF-7 cells treated with GO(OX)PB (1/1/0.2) NPs and subjected to 880 nm laser irradiation (0.5 W/cm^2, 5 min) exhibited significant green fluorescence compared to other groups, whereas less fluorescence was observed in the absence of laser irradiation. Subsequently, **Fig. 4.21C and D illustrate** quantitative fluorescence analysis by flow cytometry, aligning with the fluorescence imaging results. The DCF fluorescence intensity in MCF-7 cells treated with GO(OX)PB (1/1/0.2) NPs (+L) showed higher fluorescence intensity compared to GO(OX)PB (1/1/0.2) NPs (-L), GO(OX)PEG (1/1/0.2) NPs (±L), and free OX. These findings suggest that MCF-7 cells treated with NPs generate elevated intracellular ROS levels upon exposure to laser radiation. Consequently, this phenomenon indicates that GO(OX)PB (1/1/0.2) NPs may offer advantages in enhancing the outcomes of combined chemo photothermal treatment, leading to effective cancer cell eradication. Furthermore, elevated amounts of reactive oxygen species (ROS) can lead to harm to mitochondria by interfering with the mitochondrial permeability transition pore. This disruption causes the rapid dissipation of the mitochondrial transmembrane potential and the swelling of the mitochondrial matrix (S. Jiang et al., 2017; W.-B. Liu et al., 2010). Therefore, the detection of intracellular reactive oxygen species (ROS) is a crucial method for assessing the therapeutic capabilities of GO(OX)PB (1/1/0.2) NP.

As commonly recognized, mitochondria constitute the principal origin of intracellular ROS. Excessive ROS production has the potential to induce mitochondrial membrane dysfunction and dissipate the MMP, culminating in cellular apoptosis (Itoo et al., 2023). In this investigation, JC-1 was employed to monitor alterations in the MMP. In normative cells exhibiting high MMP, JC-1 assumes J-aggregates with red fluorescence, while diminished MMP leads to an increase in green fluorescence (J-monomers). As illustrated in **Fig. 4.18C and D,** the control groups displayed robust red fluorescence and minimal green fluorescence, indicative of high MMP. Conversely, the free OX (red-green merged), GO(OX)PEG (1/1/0.2) NPs, and GO(OX)PB (1/1/0.2) NPs (±L) groups exhibited a notable elevation in green fluorescence signals concomitant with a reduction in red fluorescence, signifying MMP reduction in these groups. Notably, the GO(OX)PB(1/1/0.2) NPs (+L) group demonstrated the most pronounced MMP decrease.

To further elucidate the patterns of cell death, we conducted an annexin V apoptosis assay to quantify the proportions of cells undergoing early-stage and late-stage apoptosis. The cells fed with free OX and GOO(OX)PB(1/1/0.2) NPs (+L) group exhibited 18.34 ± 1.38 and 68.76 ± 1.9% early-stage and late-stage apoptotic cells (**Fig. 4.22A**). In comparison, the GO(OX)PB(1/1/0.2) NPs (-L) exhibited 58.45 ± 2.34% early-stage and late-stage apoptotic cells, while the GO(OX)PEG (1/1/0.2) NPs with or without displayed 45.59 ± 1.57% and 39.34 ± 2.13% total apoptotic cells. The enhanced apoptosis observed with laser-triggered GO(OX)PB(1/1/0.2) NPs compared to free OX and GO(OX)PEG (1/1/0.2) NPs (±L) can be ascribed to the increased cellular uptake facilitated by the nanocarrier system. These findings suggest that GO(OX)PB(1/1/0.2) NPs with laser effectively trigger apoptosis in cancer cells.

4.3.3.4 Cell cycle analysis

The administration of free OX, GO(OX)PEG (1/1/0.2) NPs (±L), and GO(OX)PB (1/1/0.2) NPs (±L) at a dose of 10 μg/mL resulted in the cell population of MCF-7 lines being arrested

in the G2/M phase. The incidence of arrest was significantly greater in cells treated with GO(OX)PB (1/1/0.2) NPs (+L) compared to cells treated with free OX, GO(OX)PB (1/1/0.2) NPs (-L), and GO(OX)PEG (1/1/0.2) NPs (±L) in MCF-7 cell line. **Fig. 4.22C** illustrates the quantity of cell populations in various phases after the therapy. The MCF-7 cancer cells that were halted in the G2 cell division cycle showed a 4.50-fold increase with laser in GO(OX)PB (1/1/0.2) NPs (±L) compared to the cells treated with Free OX. The GO(OX)PB (1/1/0.2) NPs treatment led to a decrease in the number of cells in the G1 population, manifesting significant cell cycle arrest at the G2/M phase.

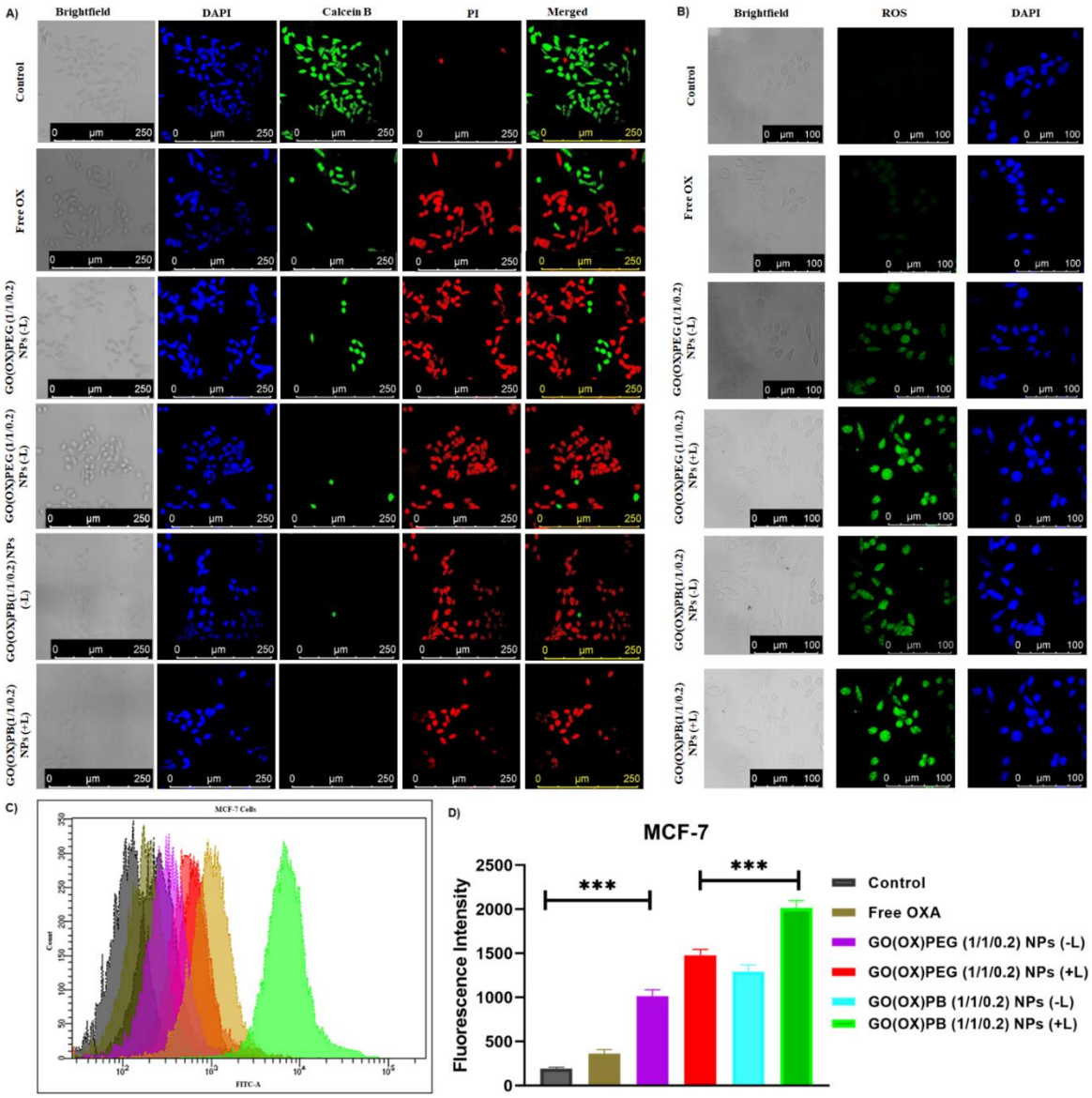

Figure 4.21 *In vitro* photothermal effect on live/dead cell assay and intracellular ROS generation. Live/dead cell study of Free OX, GO(OX)PEG (1/1/0.2) NPs and GO(OX)PB (1/1/0.2) NPs (± L) (0.5 W/cm^2) in MCF-7 cells using calcein B and PI (A); Intracellular ROS generation in MCF-7 cells treated with Free OX, GO(OX)PEG (1/1/0.2) NPs and GO(OX)PB (1/1/0.2) NPs (± L) (0.5 W/cm^2) observed by confocal microscopy (B). The histogram and a bar graph were used to demonstrate the amount of ROS generated by NPs with or without laser using flow cytometry (C, D), with a statistical significance of $p < 0.05$.

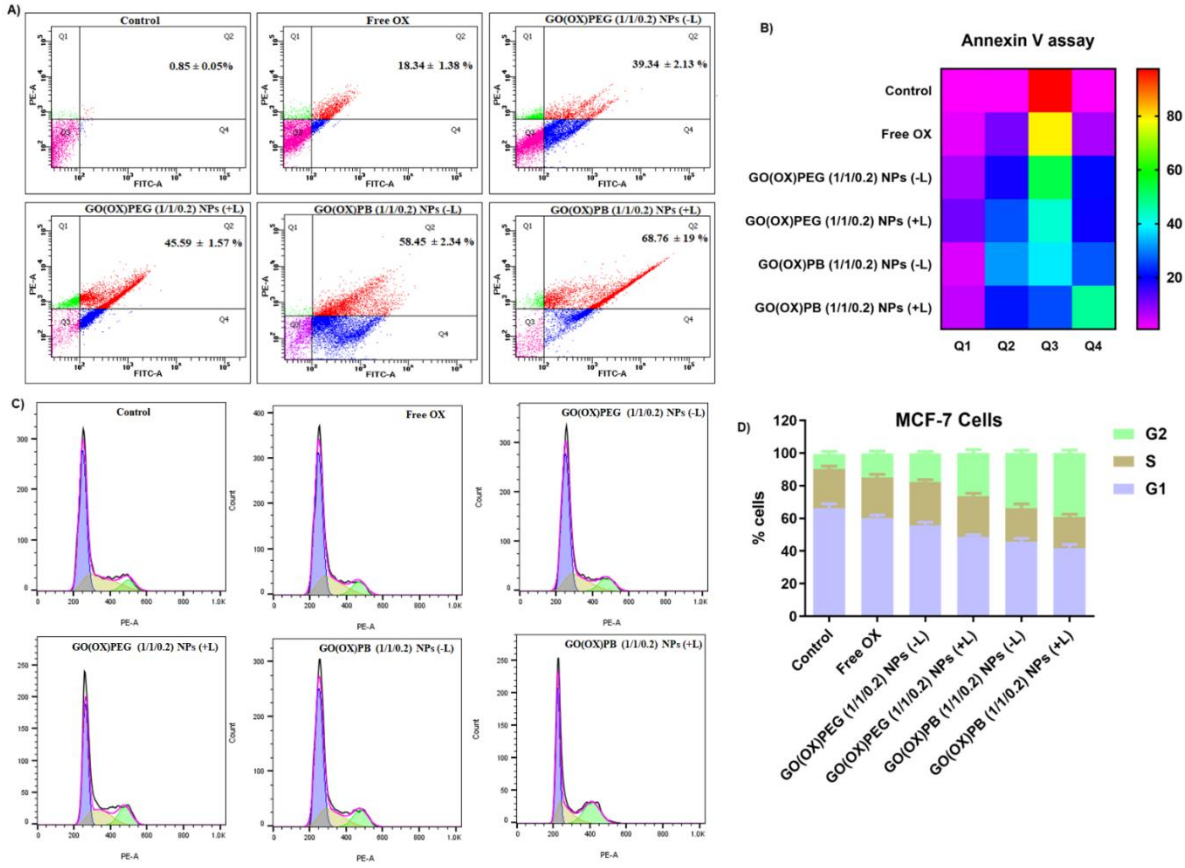

Figure 4.22 Annexin V Assay (A) and cell cycle analysis (C). The assessment involved the examination of apoptosis in MCF-7 cells following exposure to free OX, GO(OX)PEG (1/1/0.2) NPs and GO(OX)PB (1/1/0.2) NPs (± L) (0.5 W/cm^2) after 24 h of incubation. Flow cytometry was employed for data collection, with the Q3 and Q4 quadrants indicating early and late apoptosis stages (A, B). Additionally, the effect of free OX, GO(OX)PEG (1/1/0.2) NPs, and GO(OX)PB (1/1/0.2) NPs (± L) (0.5 W/cm^2) on cell cycle progression was analyzed using histogram plots (C). A representative bar graph illustrates the distribution of cells in various cell cycle stages for MCF-7 cells (D).

4.3.4 Pharmacokinetic (pK) and Nephrotoxicity Study

The pharmacokinetic (pK) characteristics of Free OX, GO(OX)PEG (1/1/0.2) NPs, and GO(OX)PB (1/1/0.2) NPs were assessed by measuring drug concentrations at specific time intervals after intravenous administration into the tail veins of female Wistar rats. **Table 4.7**

and **Fig. 4.24** depict the pharmacokinetic (pK) parameters and plasma concentration-time profiles of OX. The results indicate a swift elimination of free OX from the bloodstream, characterized by a blood retention half-life of 1.15 h. Contrastingly, the blood retention half-life of GO(OX)PEG (1/1/0.2) NPs and GO(OX)PB (1/1/0.2) NPs was determined to be 23.89 and 25.95 h, surpassing that of free OX by a factor of 20.77 and 22.56. Consequently, the area under the curve (AUC) values for GO(OX)PEG (1/1/0.2) NPs and GO(OX)PB (1/1/0.2) NPs escalated approximately 48.77 and 63.41 times higher than those observed for free OX. The pharmacokinetic data demonstrated that both GO(OX)PEG (1/1/0.2) NPs and GO(OX)PB (1/1/0.2) NPs exhibited superior values for $t_{1/2}$, AUC, mean residence time (MRT), and diminished clearance in comparison to free OX. Free OX undergoes rapid clearance from systemic circulation. In contrast, OX loaded onto GO(OX)PB (1/1/0.2) NPs exhibits delayed accessibility to the systemic environment, leading to reduced drug clearance and, consequently, an extended plasma residence time for NPs carrying OX (Ito et al., 2012; W. Zhang et al., 2008). Additionally, the incorporation of PEG into the nanoparticle system contributes to the prolonged circulation of OX. PEGylation serves to diminish interactions with opsonin proteins in the systemic circulation, resulting in unopsonized NPs that evade the immune system, thereby displaying an extended half-life and residence time in the blood (Mohamed et al., 2019). The primary constraint associated with the utilization of oxaliplatin pertains predominantly to nephrotoxicity. To assess the toxicity of nanoparticles, various serum biochemical markers, including blood urea nitrogen (BUN) and creatinine, were examined, as depicted in **Fig. 4.27E, F**. Our findings indicate that the serum biochemical parameters measured after treatments were within the normal ranges, providing evidence that IV formulations do not have a harmful effect on the kidney. At the same dosage, it was shown that GO(OX)PEG (1/1/0.2) NPs and GO(OX)PB (1/1/0.2) NPs have considerably reduced

nephrotoxicity compared to free OXA. The hematological parameters were assessed, revealing no toxicity in any of the groups except for free OX (**Fig. 4.27G, H, I, and J)**.

Table 4.7 The pharmacokinetic (pK) parameters of free OX, GO(OX)PEG (1/1/0.2) NPs, and GO(OX)PB (1/1/0.2) NPs in female Wistar rats.

Parameters	**Unit**	**Free OX**	**GO(OX)PEG (1/1/0.2) NPs**	**GO(OX)PB (1/1/0.2) NPs**
Lambda_z	1/h	0.601092153	0.05707768	0.05035224
$t_{1/2}$	h	1.153146281	12.1439272	13.7659659
C0	µg/ml	65.55541425	23.8978208	25.9582755
Clast_obs/Cmax		0.048229125	0.0540241	0.07550228
AUC 0-t	µg/ml*h	103.3226071	382.95641	430.650638
AUC 0-inf_obs	µg/ml*h	105.9178831	403.454791	465.802998
AUC 0-t/0-inf_obs		0.975497283	0.94919287	0.92453385
AUMC 0-inf_obs	µg/ml*h^2	141.5071564	6877.23606	8941.20887
MRT 0-inf_obs	h	1.336008163	17.0458654	19.1952583
Vz_obs	(mg/kg)/(µg/ml)	0.07853435	0.21712449	0.21318122
Cl_obs	(mg/kg)/(µg/ml)/h	0.047206382	0.01239296	0.01073415

4.3.5 *In vivo* Distribution

The intravenous administration of GO(OX)PEG-RhB (1/1/0.2) NPs and GO(OX)PB-RhB (1/1/0.2) NPs was performed in mice bearing 4T1 tumors to investigate the *in vivo* biodistribution of the nanocomposites. The fluorescence imaging of Rhodamine B (RhB) was carried out within mice at distinct intervals, specifically at 1, 3, 6, 12, 24, and 36 h. **Fig. 4.23A and 4.23B** depict that one hour after injection, both the groups treated with GO(OX)PEG-RhB (1/1/0.2) NPs and GO(OX)PB-RhB (1/1/0.2) NPs showed a significant fluorescence signal originating from the liver. This observation may be attributed to increased uptake by

macrophages in the liver. Subsequently, the fluorescence intensity at the tumor site in the group treated with GO(OX)PB-RhB (1/1/0.2) NPs consistently rose, reaching its peak at 12 h post-injection. In contrast, the GO(OX)PEG-RhB (1/1/0.2) NPs treated group displayed a substantially lower signal compared to GO(OX)PB-RhB (1/1/0.2) NPs, suggesting a gradual accumulation of GO(OX)PB-RhB (1/1/0.2) NPs at the tumor site. Notably, even at 36 h post-injection, the tumor in the GO(OX)PB-RhB (1/1/0.2) NPs treated group exhibited a robust fluorescence signal, underscoring the high targeting and retention capacity of GO(OX)PEG-RhB (1/1/0.2) NPs. **Fig. 4.23C, D** presents *ex vivo* fluorescence images of dissected tissues obtained 36 h after injection. The tumor fluorescence observed in the GO(OX)PB-RhB (1/1/0.2) NPs treated group significantly surpasses that in the GO(OX)PEG-RhB (1/1/0.2) NPs group, indicating efficient nanoparticle accumulation at the tumor site (**Fig. 4.23E**). Furthermore, there were no noticeable fluorescence signals identified in the spleen, heart, and lungs in either group. However, mild fluorescence signals were observed in the liver and kidney organs in both groups, likely due to efficient renal clearance (**Fig. 4.23F**). The nanoparticles were specifically targeted and accumulated in the tumor due to the overexpressed biotin receptors and improved permeability and retention effect, which is the clear rationale for this phenomenon (Itoo, Paul, Ghosh, et al., 2022).

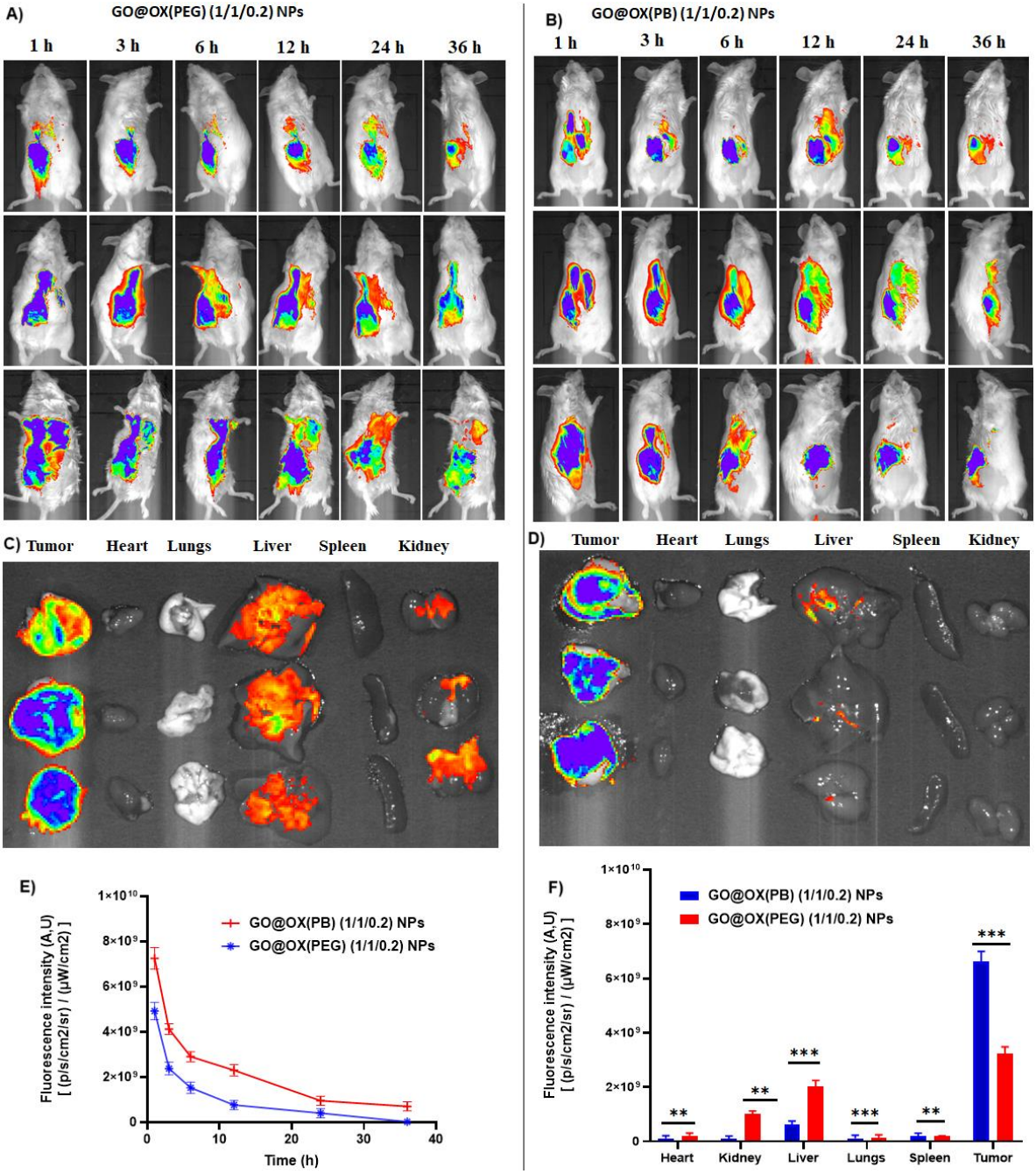

Figure 4.23 *In vivo* biodistribution analysis of GO(OX)PEG (1/1/0.2)-RhB NPs and GO(OX)PB (1/1/0.2)-RhB NPs in 4T1 tumor-bearing mice utilizing IVIS imaging. Representative images captured at specified time points post-injection (A, B); Quantification of RhB levels in vital organs 24 h after injection (C, D); Graph depicting the relationship between fluorescence intensity and time (E); and Bar graph illustrating fluorescence intensity of RhB signals in various organs (F). Data are presented as the average value ± SD.

4.3.6 *In vivo* antitumor activity

We explored the *in vivo* anti-cancer efficacy of GO(OX)PEG (1/1/0.2) NPs and GO(OX)PB (1/1/0.2) NPs, drawing inspiration from the notable *in vitro* combined chemo-photothermal therapeutic capabilities of these nanoparticles. The intravenous administration of PBS, free OX, GO(OX)PEG (1/1/0.2) NPs, and GO(OX)PB (1/1/0.2) NPs was carried out in 4T1-Luc tumor-bearing mice (70 mm^3). The tumor regions of mice in the GO(OX)PEG (1/1/0.2) NPs and GO(OX)PB (1/1/0.2) NPs groups were subjected to 808 nm NIR laser irradiation (1 W/cm^2) for a duration of 5 min. In **Fig. 4.24E, G**, thermal images illustrate the tumor site temperatures in mice treated with GO(OX)PEG (1/1/0.2) NPs and GO(OX)PB (1/1/0.2) NPs under 808 nm laser irradiation. Upon exposure to the 808 nm laser at 1 W/cm^2, the average temperature at the tumor site rapidly elevated to 53.5 ℃ and 57.8 ℃ for GO(OX)PEG (1/1/0.2) NPs and GO(OX)PB (1/1/0.2) NPs, respectively. This temperature surge is deemed adequate for photothermal therapy (PTT) and for inducing the release of OX. Conversely, the tumor area in PBS-treated mice experienced a modest increase of 2-3 ℃ post-laser irradiation, and no temperature alteration was observed in the surrounding tissue in the absence of NIR laser exposure. According to reports, when the temperature exceeds 43 ℃ in photothermal therapy, researchers have observed the breakdown of cell membranes, denaturation of proteins, and the destruction of tumors (Issels, 2008; M. Zheng et al., 2013). The advancement of tumors in the GO(OX)PB (1/1/0.2) NPs group was entirely suppressed by the laser at 1 W/cm^2, owing to the notable targeted synergistic photothermal and chemotherapy characteristics of GO(OX)PB (1/1/0.2) NPs (**Fig. 4.24D**). Moreover, the group treated solely with chemotherapy using GO(OX)PB (1/1/0.2) NPs (-L) also demonstrated suppression of tumor growth, albeit not as efficiently as the combination therapy group. The photothermal heating process likely aids in drug release from GO(OX)PB (1/1/0.2) NPs, enhancing the chemotherapeutic effect and thus

contributing to the outstanding combined therapeutic outcome. Conversely, it is noteworthy that photothermal heating, as demonstrated in numerous prior studies, has the capacity to significantly enhance the internalization of nanomaterials by increasing cell membrane permeability (L. Feng, Yang, et al., 2013; Tian et al., 2011).

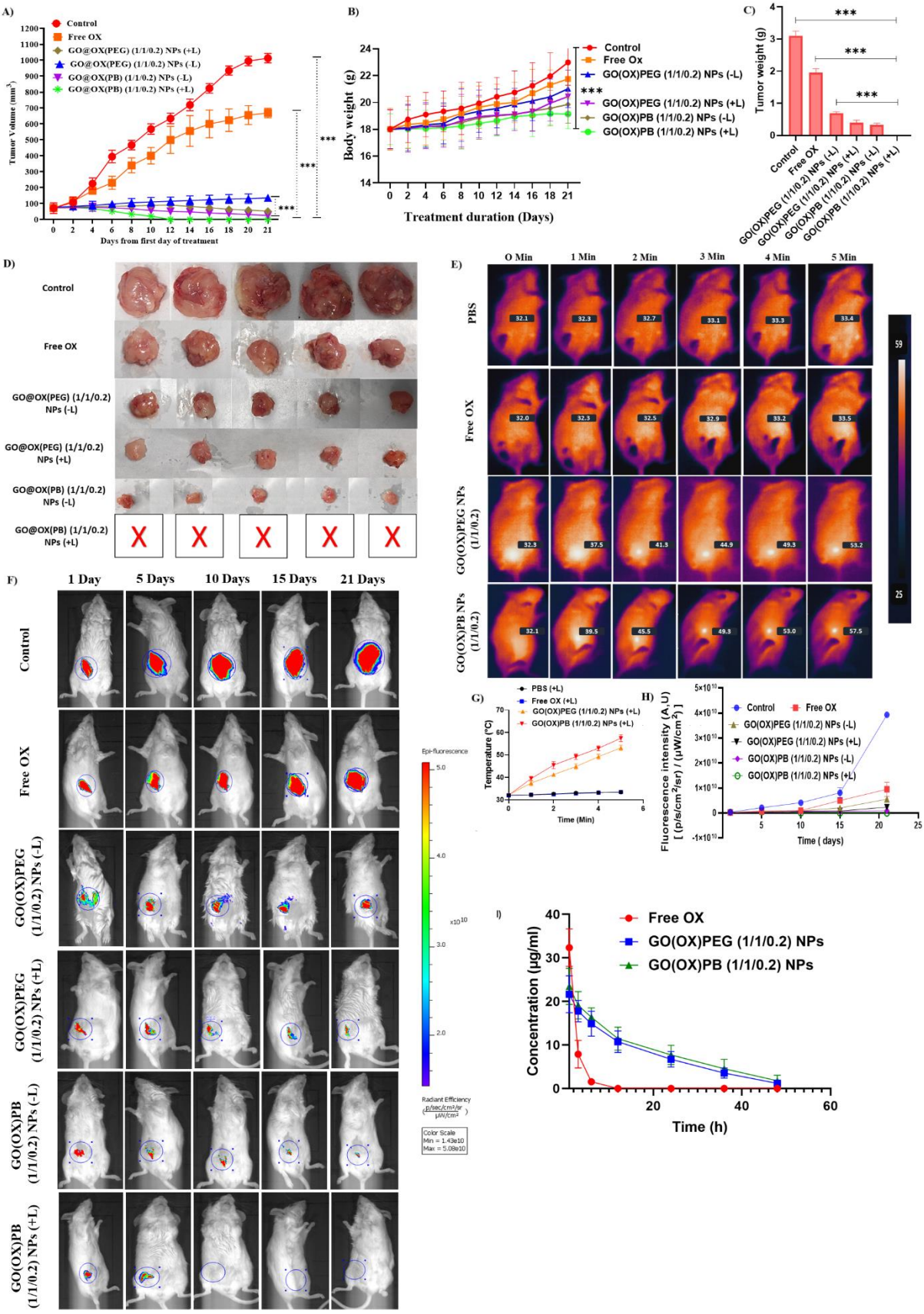

Figure 4.24 Evaluation of the *in vivo* anti-tumoral effect of free OX, GO(OX)PEG (1/1/0.2) NPs and GO(OX)PB (1/1/0.2) NPs (±L) (1 W/cm2) in 4T1-Luc tumor-bearing mice. Graph

depicts the change in tumor volume over the course of treatment (A); assessment of body weight during the treatment period (B); average weight of tumors from different treatment groups (C); representative images of tumors isolated from mice post-treatment (D); infrared thermal images (E) depict the responses of 4T1-Luc tumors injected with PBS, free OX, GO(OX)PEG (1/1/0.2) NPs and GO(OX)PB (1/1/0.2) NPs following laser illumination at 1 W/cm^2; graph (G) depicts the relationship between temperature and time; *in vivo* images of 4T1-LUC tumor-bearing mice following intravenous injection of free OX, GO(OX)PEG (1/1/0.2) NPs and GO(OX)PB (1/1/0.2) NP formulation at an OX dosage of 5 mg/kg employing IVIS imaging System. The images were acquired at predefined post-injection time intervals (F). Additionally, the graph (H) illustrates the correlation between fluorescence intensity and time. Average plasma concentration-time profiles of free OX following intravenous delivery of a single 5 mg/kg dose as well as with the formulations GO(OX)PEG (1/1/0.2) NPs and GO(OX)PB (1/1/0.2) NPs in rats (I). *, **, and *** indicate significance levels of $p < 0.05$, $p < 0.01$, and $p < 0.001$, respectively. Data are presented as mean ± standard deviation, with $n = 5$.

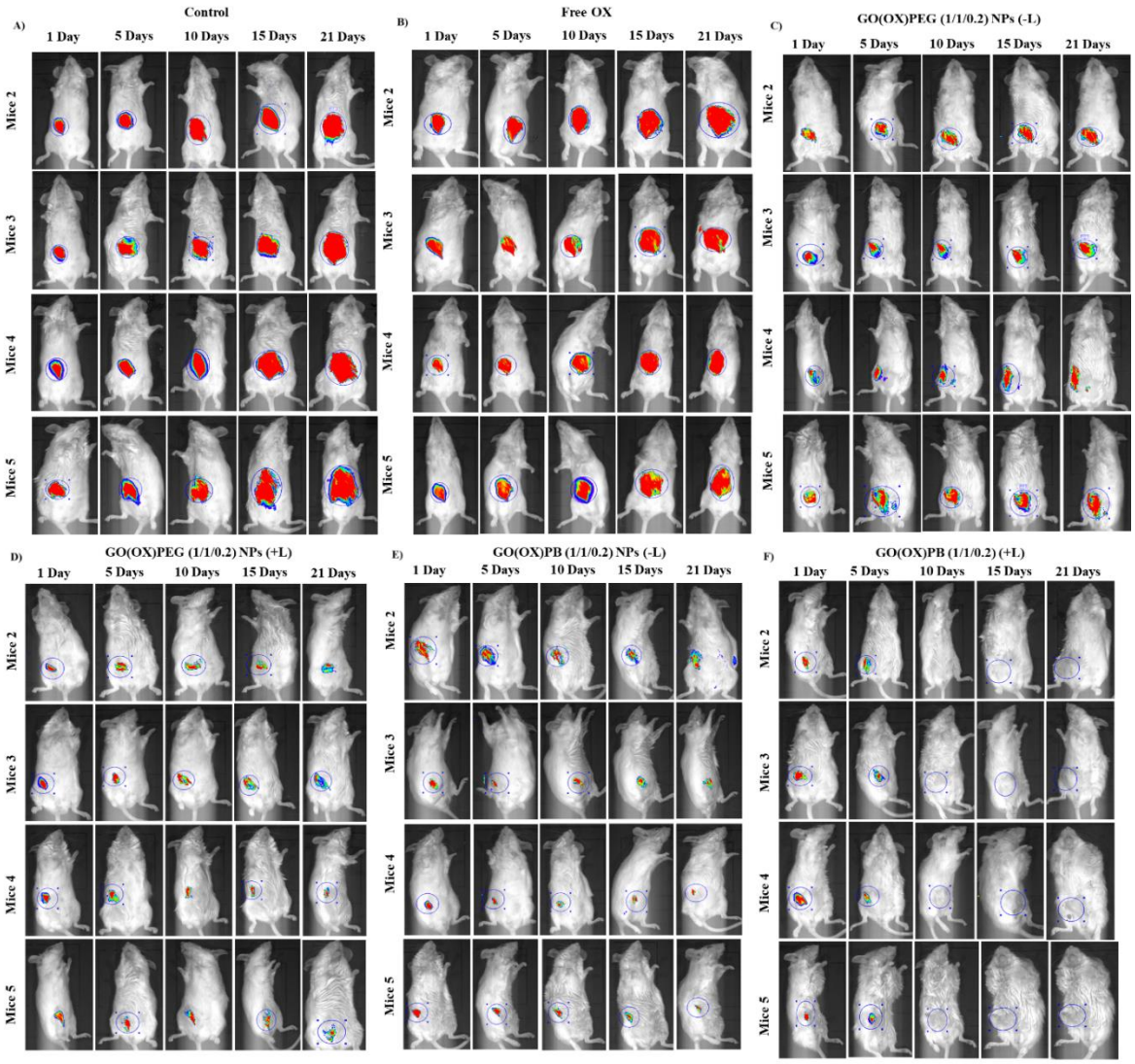

Figure 4.25 *in vivo* images of 4T1-LUC tumor-bearing mice following intravenous injection of free OX, GO(OX)PEG (1/1/0.2) NPs and GO(OX)PB (1/1/0.2) NP formulation at an OX dosage of 5 mg/kg employing IVIS imaging System.

These findings indicate that the integration of GO(OX)PB (1/1/0.2) NPs with NIR laser irradiation can produce a potent combined chemo-photothermal treatment effect for anticancer therapy. In **Fig 4.24A**, the tumor progression over a 21-day period is illustrated for various treatment groups. The tumor volume growth rate was notably swifter in the PBS-treated control animals compared to other treated groups, with GO(OX)PB (1/1/0.2) NPs (+L) demonstrating the slowest increase in tumor volume. The average tumor volumes after 21 days were 1013±29 mm^3 (control), 668±35 mm^3 (Free OX), 135±20 mm^3 (GO(OX)PEG (1/1/0.2) NPs (-L)),

53±12 mm^3 (GO(OX)PEG (1/1/0.2) NPs (+L, 1 W/cm^2), 35±5 mm^3 (GO(OX)PB (1/1/0.2) NPs (-L)), 0 mm^3 for GO(OX)PB (1/1/0.2) NPs (+L, 1W/cm^2), respectively. Furthermore, the body weights of the mice were observed (**Fig. 4.24B**). The data showed that there were no appreciable variations in the body weights of any experimental groups, confirming the good biocompatibility and biosafety of GO(OX)PB (1/1/0.2) NPs (+L, 1 W/cm^2) in *in vivo* applications.

Furthermore, when compared to the other treatment groups, the tumors in the control group showed the greatest BLI intensity, according to bioluminescence imaging (BLI). In **Fig. 4.24H**, the BLI intensities in the region of interest are presented. The GO(OX)PB (1/1/0.2) NPs (+L, 1W/cm^2) group displayed the lowest BLI intensity, followed by the GO(OX)PEG (1/1/0.2) NPs (+L, 1W/cm^2), GO(OX)PB (1/1/0.2) NPs (-L), GO(OX)PEG (1/1/0.2) NPs (-L, 1W/cm^2), and free OX (**Fig. 4.24, 4.25**). The results indicate that tumor volume increased over time in all groups, with the control group exhibiting a significantly higher growth rate compared to the treatment groups, aligning with the tumor volume inhibition study. Upon reaching a tumor volume of approximately 1100 mm^3 in the PBS-injected mice, every mouse was given anaesthesia, and the tumors were excised. In comparison to the other groups, the GO(OX)PB (1/1/0.2) NPs (+L, 1W/cm^2) treated group had a considerably lower tumor weight (**Fig. 4.24C**).

The therapeutic efficacy of the treatment groups was also assessed by staining the tumor tissues with TUNEL, Ki67, and DCFDA dye. These markers enable the immunohistochemical detection of apoptosis, proliferation, and reactive oxygen species (ROS) formation inside the tumor tissue (**Fig. 4.26**). When tumor samples were treated with GO(OX)PB (1/1/0.2) NPs (+L, 1 W/cm^2) in comparison to other groups receiving treatment, a more pronounced bright green fluorescence showed up in the TUNEL and ROS assays (**Fig. 4.26A, B**), validating a higher number of apoptotic structures and significant generation of ROS (Pelicano et al., 2004).

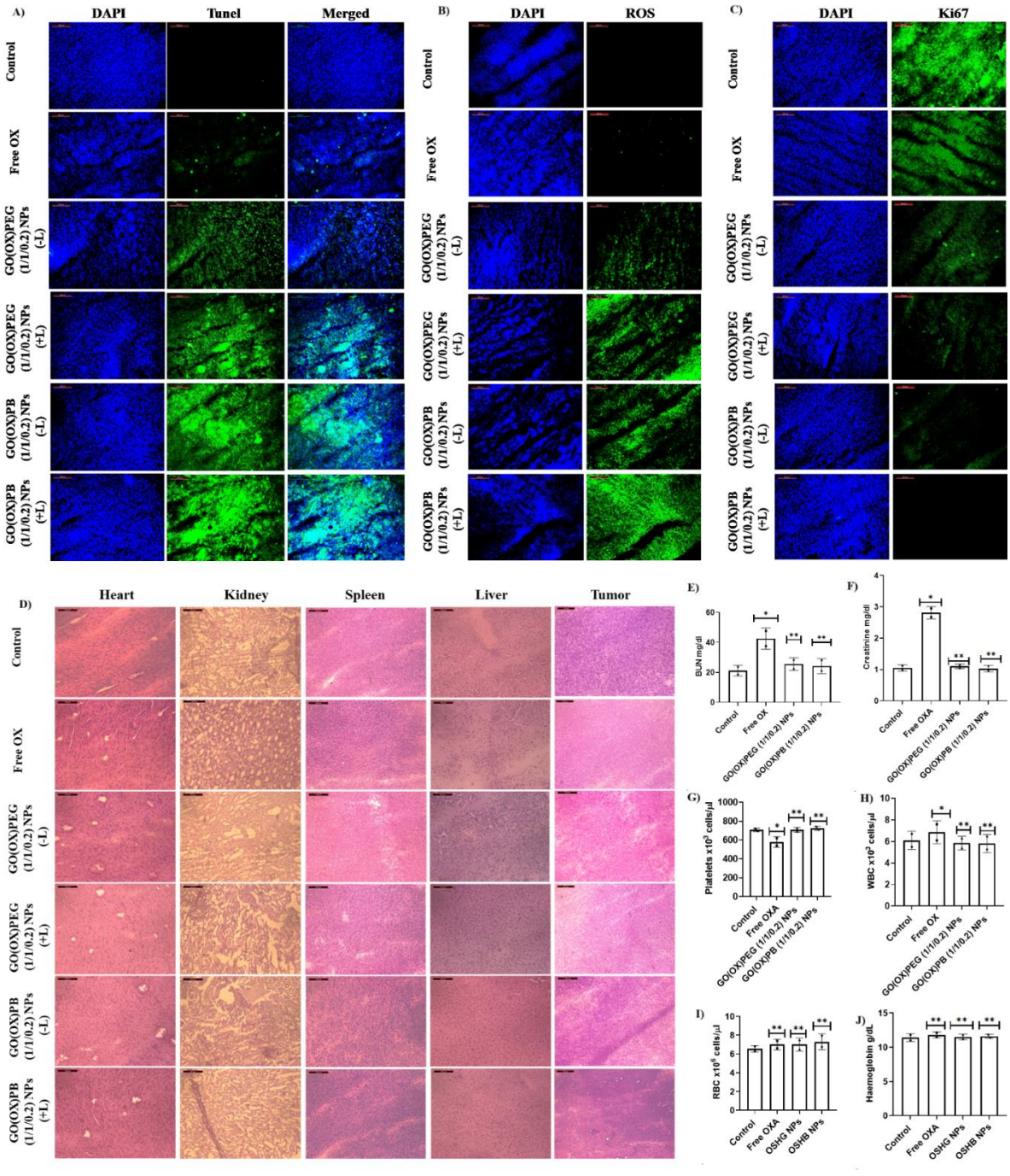

Figure 4.26 Immunohistochemistry *in vivo*. Immunohistochemical staining of tumor tissue for the assessment of TUNEL, Ki67, and ROS observed under fluorescence microscope. Nanoparticle biocompatibility assessment test through preclinical hematological and serum blood analysis. No significant changes in specific markers for kidney were observed in the results, represented as mean ± SD with n = 5.

In the Ki-67 assay (**Fig. 4.26C**), heightened cell proliferation was evident in the control group (with the most intense green fluorescence), while the GO(OX)PB (1/1/0.2) NPs (+L, 1 W/cm^2) treatment group exhibited the least proliferation, indicating a near absence of Ki-67 positive tumor cells and confirming minimal tumor growth.

Hematoxylin and eosin (H&E) staining was used in further assessments to evaluate organ damage in the therapy groups, as shown in **Fig. 4.26D**. Notably, one of the prominent adverse effects linked to Oxaliplatin (OX)-mediated chemotherapy is nephrotoxicity (Itoo, Paul, Ghosh, et al., 2022). Hence, H&E staining was utilized to scrutinize the kidney tissues of mice groups that were administered free OX or various formulations. Significant neutrophil accumulation was noted in the kidney portion of the OX-treated mice group in comparison to the PBS group, suggesting significant nephrotoxicity linked to free OX. Surprisingly, when administered with GO(OX)PB (1/1/0.2) NPs (+L, 1 W/cm²), the nephrotoxicity of OX was significantly reduced, potentially attributed to localized OX release and reduced OX diffusion from the primary tumor to the kidney. No histological damage was observed in other organs, including the liver, lungs, spleen, and heart, confirming the formulation's low toxicity.

The advanced stages of cancer progression are characterized by the occurrence of spontaneous metastasis. Following the completion of the anticancer study, lung organs were harvested and subjected to bioluminescence (BLI) measurements post-luciferin treatment to elucidate the efficacy of GO(OX)PB (1/1/0.2) NPs (+L) animals in suppressing lung metastasis of 4T1 breast tumors. Photographic images revealed the highest BLI signals in the lungs of the PBS and Free OX treated groups, showcasing notable metastasis of 4T1 cancer cells from the primary tumor to the lungs (**Fig. 4.27A, C, E**). The GO(OX)PB (1/1/0.2) NPs (-L) treated group showed partial inhibition of lung metastasis, likely associated with the reduced tumor development induced by OX. Importantly, the lung metastatic lesions shown a significant decrease in the GO(OX)PB (1/1/0.2) NPs (+L, 1 W/cm²) treated group. The quantification of lung metastasis

in mice involved counting the nodules associated with lung metastasis. **Fig. 4.27B and F** depict a remarkable scarcity of metastatic nodules in the mice group treated with GO(OX)PB (1/1/0.2) NPs (+L, 1 W/cm²), in contrast to the lung tissues of the PBS, free OX, and GO(OX)PB (1/1/0.2) NPs (-L) group. This observation suggests that the GO(OX)PB (1/1/0.2) NPs +L-treated group demonstrated the most robust antimetastatic effectiveness, a finding further supported by the hematoxylin and eosin (H&E) staining of the lung tissue (**Fig. 4.27G**). The presence of metastatic nodules led to an observed increase in lung weight in both the control and free OX group (**Fig. 4.27D**). The metastatic lung tissue in the control and free OX group exhibited abnormal cellular features such as enlarged nuclei, irregular nuclear shapes, and increased nuclear-to-cytoplasmic ratios. The lung histology of untreated mice with tumors showed a high concentration of tissue, suggesting the presence of metastatic sites, as observed through histological examination. On the other hand, the lung tissue structure of the GO(OX)PB (1/1/0.2) NPs laser-treated group closely mirrored that of animals without tumors. These data confirm that GO(OX)PB (1/1/0.2) NPs, when used with 808 nm NIR laser irradiation, effectively inhibit tumor spreading.

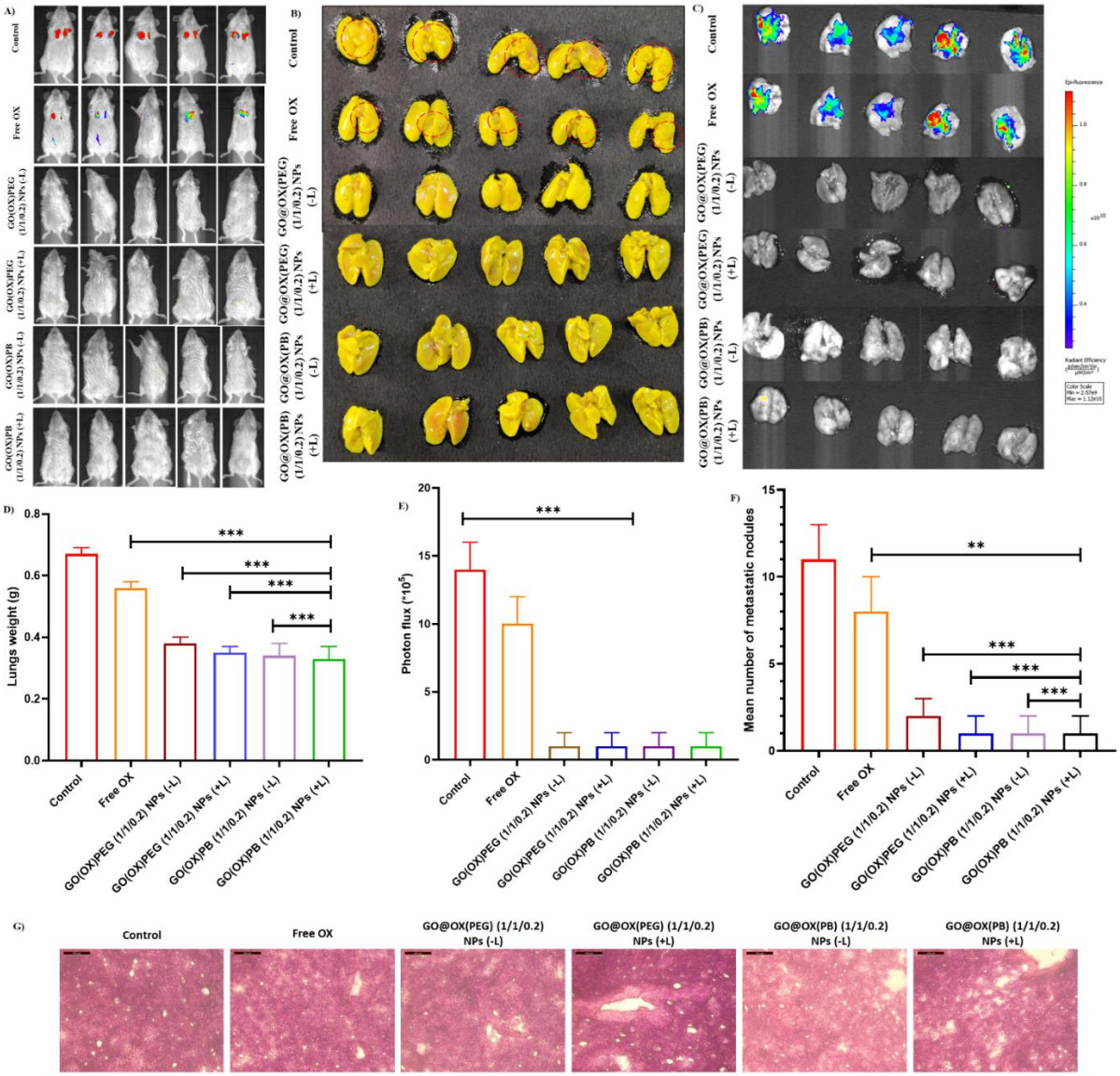

Figure 4.27 Suppression of lung metastasis. The efficacy of GO(OX)PEG (1/1/0.2) NPs and GO(OX)PB (1/1/0.2) NPs (±L) (1 W/cm2) treatment in reducing metastasis of 4T1-Luc cells in the lungs, assessed through live mouse imaging on day 7 post-surgery (n=5) and represented in a bioluminescence bar graph. visual representations of lungs in free OX, GO(OX)PEG (1/1/0.2) NPs and GO(OX)PB (1/1/0.2) NPs (±L)groups illustrate the growth of metastatic nodules of 4T1 cells. Bar graph (F) provides a quantitative comparison of lungs/nodules in the free OX and nanoparticle formulations (±L) treatment groups. Ex-vivo bioluminescence intensities in lung tissues (C, E), along with a bar graph representation of lung weight (D).

Tumor metastasis in lung sections was visualized through hematoxylin and eosin staining, with a scale bar of 100 μm (G).

4.4 Conclusion

In summary, we demonstrated the successful preparation of a multifunctional nanocomposite based on graphene oxide, Pt(IV), PEGylated GO sheets, and pegylated biotin in a single platform for metastatic breast cancer which shows potential for targeted drug delivery and combined photothermal-chemotherapy under near-infrared laser irradiation (NIR-808 nm). The therapeutic effectiveness was assessed both *in vitro* and *in vivo* conditions employing MCF-7 cells, 4T1 cells, and 4T1-Luc tumor-bearing mouse models. The findings demonstrated that GO(OX)PB (1/1/0.2) NPs (+L) were highly effective in causing significant cytotoxicity, ROS generation, mitochondrial membrane depolarization, apoptosis, cell cycle arrest (G2/M) phase, and photothermal effect leading to a higher proportion of cell death than free OX, GO(OX)PEG (1/1/0.2) NPs (±L) and GO(OX)PB (1/1/0.2) NPs (−L). Moreover, the pK data demonstrated that both GO(OX)PEG (1/1/0.2) NPs and GO(OX)PB (1/1/0.2) NPs exhibited superior values for $t_{1/2}$, AUC, mean residence time (MRT), and diminished clearance in comparison to free OX. The *in vivo* photothermal therapy (PTT) experiment validated that the temperature within the tumor site reached 57 °C within a 5-minute timeframe upon IV injection of GO(OX)PB (1/1/0.2) NPs, coupled with laser application. The *in vivo* therapeutic studies on 4T1-Luc tumor-bearing mice revealed that a combination of GO(OX)PB (1/1/0.2) NPs (+L) caused complete destruction of the tumor, no tumor recurrence, prolonged survival, reduced lung metastasis, and mitigated nephrotoxicity. The examination of serum and blood components demonstrated minimal systemic toxicity of GO(OX)PB (1/1/0.2) NPs. The developed nanoplatform may serve as a potential nanomedicine to address conventional nephrotoxicity in breast cancer and prevent metastasis by combining chemo-photothermal therapy.

4.5 Acknowledgements

Prof. Swati Biswas acknowledges the support from the Indian Council of Medical Research, India (Grant no. 2021-8945/F1). The authors also sincerely acknowledge using the *in vivo* imaging facility supported by the DST-FIST research grant [SR/LS-II/2018/210]. The Central Analytical Laboratory, Birla Institute of Technology and Science (BITS), Pilani, Hyderabad Campus, India, is thoroughly gratified by the authors for providing the instrumentation facilities like Confocal microscope, UV, and Fluorescence spectrophotometer, XPS, XRD, DSC, FACS, and SEM instrument for different characterizations. Mr. Asif Mohd Itoo thanks Lady Tata Memorial Trust, India, for the junior research fellowship.

Chapter 5

Comparison of micelles/polymeric graphene oxide nanoparticles

5.1 Introduction

Breast cancer remains a significant global health concern, necessitating the exploration of innovative therapeutic strategies to enhance treatment efficacy and minimize side effects. Nanomedicine represents an innovative and promising approach in the field of cancer therapy, aiming to overcome the limitations associated with conventional treatments and enhance the therapeutic efficacy while minimizing side effects. In the context of breast cancer, three distinct nanomedicine strategies have been explored, each employing unique nanocarriers and treatment modalities. The objective first focused on the development of a chitosan/vitamin E conjugate micellar system for the delivery of oxaliplatin (OXPt) in breast cancer treatment. The study explored the physicochemical characteristics of the micelles and evaluated their therapeutic efficacy both *in vitro* and *in vivo*. The micelles exhibit improved anticancer effects, decreased IC50, and reduced nephrotoxicity compared to free OXPt. The study suggested that this nanomedicine could potentially overcome conventional OXPt-mediated drug resistance and nephrotoxicity in breast cancer. In the second objective, polymeric graphene oxide nanoparticles loaded with doxorubicin for combined photothermal and chemotherapy in triple-negative breast cancer (TNBC) were introduced. The study highlighted the development of a 3D colloidal spherical structure using graphene oxide and an amphiphilic polymer, aiming to achieve efficient drug loading, stability, and therapeutic efficacy. The combination of doxorubicin-loaded nanoparticles with laser treatment showed promising results in inducing apoptosis, cell cycle arrest, and photothermal effects in both *in vitro* and *in vivo* experiments, suggested that this nanoplatform could serve as a potential combination therapy for TNBC. The third objective described a nanocomposite involving biotinylated graphene oxide, a platinum(IV) prodrug, and PEGylated biotin for targeted chemo-photothermal combination therapy in breast cancer. The study explored the physicochemical properties of the nanocomposite and evaluated its therapeutic efficacy *in vitro* and *in vivo*. The nanocomposite demonstrated excellent drug load capacity, photothermal conversion efficiency, and targeted

drug delivery. *In vivo* experiments showed the complete disappearance of tumors with reduced systemic toxicity. The study suggested that this nanoplatform could be a potential nanomedicine for breast cancer treatment, addressing conventional nephrotoxicity and preventing metastasis through combination chemo-photothermal therapy.

In summary, all three objectives focused on the development of nanomedicines for breast cancer treatment, utilizing different nanocarriers and therapeutic modalities. The objective 1 used chitosan/vitamin E conjugate micelles for OXPt delivery, objective 2 employed polymeric graphene oxide nanoparticles for combined photothermal and chemotherapy, and objective 3 utilized biotinylated graphene oxide-conjugated platinum(IV) prodrug nanoparticles for targeted chemo-photothermal combination therapy. Each approach aimed to enhance the therapeutic efficacy of anticancer agents while minimizing side effects.

5.2 Comparison of physicochemical characteristics

The optimized formulations of OXPt@Ch/VES Ms, Dox@GO(mPP) NPs, GO(OX)PEG NPs, and GO(OX)PB NPs were systematically characterized in terms of particle size, zeta potential, encapsulation efficiency (EE%), drug loading (DL%), and release behavior (**Table 5.1**). OXPt@Ch/VES Ms displayed varying particle sizes, with the 15 kDa Chitosan micelle formulation exhibiting sizes ranging from 217 ± 2.3 nm to 282.7 ± 2.5 nm. The 300 kDa nanomicelle formulation exhibited sizes from 251.5 ± 2.3 nm to 292.5 nm. The Chitosan conjugate of 15 kDa with a 1:1 drug-to-polymer weight ratio demonstrated maximum OXPt loading and encapsulation efficiency, presenting a narrow polydispersity index and a positive zeta potential. The spherical morphology of the micelles, as observed through scanning electron micrograph (SEM) analysis, indicated low polydispersity. Additionally, the micelles exhibited pH-dependent drug release, with higher release observed in acidic pH 5.0 compared to alkaline pH 7.4, potentially enhancing efficacy in acidic environments encountered during

endocytosis. The release behavior was analyzed using various mathematical models, with the Weibull model fitting the experimental data well at pH 7.4, pH 6.8, and pH 5.

The particle sizes of the blank (GO) and Dox@GO(mPP) NPs were determined to be 147.2±5 nm and 161.0±4 nm, respectively, with good colloidal stability indicated by zeta potential measurements. Long-term storage at 4 °C demonstrated the stability of Dox@GO(mPP) (1/0.5) NPs, as evidenced by minimal changes in size, fluorescence intensity of Dox, and drug loading after 21 days. The morphological analysis through SEM and AFM revealed the nanosized and spherical nature of Dox@GO(mPP) (1/0.5) NPs, highlighting their potential for intravenous administration and drug delivery to tumor tissues. Furthermore, the study investigated the controlled *in vitro* release of Dox from the NPs under different pH conditions and with or without near-infrared (NIR) laser irradiation. The results indicated a pH-dependent and laser irradiation-dependent release behavior, demonstrating the potential for controlled drug release. Drug release kinetics were modeled, with regression values suggesting that the drug release mechanism followed Fickian diffusion at pH 5 and pH 6.8. Additionally, at pH 7.4, the release followed the Higuchi model.

The dynamic light scattering (DLS) measurements revealed distinct particle sizes for each NP type, with GO(OX) (1/1) NPs at 150.8 ± 2 nm, GO(OX)PEG (1/1/0.2) at 158.3 ± 1.6 nm, and GO(OX)PB (1/1/0.2) at 195.7 ± 2.3 nm. Zeta potential values indicated good colloidal stability for the nanocarrier system. The investigation also included an assessment of GO(OX)PB (1/1/0.2) NP stability after 21 days of storage at 4 ºC, demonstrating consistent particle size around 195 nm, suggesting the maintenance of stability over time. The morphological evaluation through field emission scanning electron microscopy (FE-SEM) revealed the layered structure and wavy shape characteristic of GO flakes. The functionalization with pegylated biotin resulted in a modified GO with a smooth unilamellar morphology and reduced roughness while still preserving the distinctive structure of native GO flakes. Our investigation

into GO(OX)PEG (1/1/0.2) and GO(OX)PB (1/1/0.2) nanoparticles revealed their sustained *in vitro* release of oxaliplatin (OX) under varying pH conditions and with or without NIR laser irradiation. The mathematical modelling elucidated the release kinetics, with the choice of models indicating environmental condition-dependent behaviours. GO(OX)PEG (1/1/0.2) NPs adhered to the Higuchi model at pH 7.4 and 6.8, and the Weibull model at pH 5, while GO(OX)PB (1/1/0.2) NPs followed the Weibull kinetic model under all pH conditions except for pH 7.4 and 6.8 without laser irradiation, where the Higuchi model applied. These findings underscore the potential versatility of these nanocarriers for tailored drug release, offering insights for further advancements in targeted and controlled drug delivery systems.

Table 5.1 Physicochemical characterization of micelles and polymeric NPS

Formulation	Particle Size (nm)	PDI	Zeta potential (mV)	Encapsulation Efficiency (%)	Drug loading (%)
OXPt@Ch/VES Ms	255.5 ± 3	0.31	+31 ± 1	32.67 ± 1.45	16.22 ± 1.12
Dox@GO(mPP) (1/1/0.5) NPs	161.04 ± 4.5	0.32	-28.2 ± 1.5	6.3 ± 0.43	70 ± 2.3
GO(OX)PEG (1/1/0.2) NPs	158.3 ± 1.6	0.35	-26.1 ± 1.25	89.06 ± 1.03	44.39 ± 1.53
GO(OX)PB(1/1/0.2) NPs	195.7 ± 2.3	0.25	-23.8 ± 0.75	89.48 ± 1.23	43.56 ± 2.37

The cytotoxic effect of OXPt@Ch/VES Ms, Dox@GO(mPP) NPs, GO(OX)PEG NPs, and GO(OX)PB NPs with or without laser (±L) on MCF-7, MDA-MB-231 (S, R) and 4T1 cells was compared using IC-50 values, represented in **Table 5.2**. Cells treated for 24 h exhibited a higher IC-50 value than cells incubated continuously for 48 h. When compared to free Dox, free OX, Dox@GO(mPP) (1/0.5) NPs (-L), GO(OX)PEG NPs (-L) and GO(OX)PB NPs (-L) in tested cell lines. The formulation with laser had the strongest anti-proliferative activity, indicating that photothermal combined with chemotherapy has improved treatment efficacy. The fact that the IC-50 values lowered from 24 to 48 h showed that the cytotoxicity was time-dependent.

Table 5.2 *In vitro* cytotoxicity study.

Compound	**MCF-7**		**4T1**		**MDA-MB 231 (S)**		**MDA-MB 231 (R)**	
	IC-50 (24 h) (µM)	**IC-50 (48h) (µM)**	**IC-50 (24 h) (µM)**	**IC-50 (48h) (µM)**	**IC-50 (24 h) (µM)**	**IC-50 (48h) (µM)**	**IC-50 (24 h) (µM)**	**IC-50 (48h) (µM)**
OXPt@Ch/VES Ms	12.485	9.541	-	-	10.06	7.74	13.56	12.74
Dox@GO(mPP) (1/0.5) NPs (-L)	-	-	15.95	14.36	16.41	14.48	-	
Dox@GO(mPP) (1/0.5) NPs (+L)	-	-	14.42	12.83	14.47	12.63	-	
GO(OX)PEG (1/1/0.2) NPs (-L)	12.469	10.889	13.278	11.960	-		-	
GO(OX)PEG (1/1/0.2) NPs (+L)**)**	11.167	9.884	12.464	10.872	-		-	
GO(OX)PB(1/1/0.2) NPs (-L)	10.273	9.004	11.169	10.051	-		-	
GO(OX)PB (1/1/0.2) NPs (+L)	9.561	7.852	10.224	9.354	-		-	

5.3 Conclusion

The above-mentioned physicochemical characteristics of all the polymer-based micelles revealed that micelles and nanoparticles are relatively better in terms of particle size, PDI, drug loading(%), and *in vitro* release, *in vitro* study and *in vivo* study. The resulted NPs have showed better performance compared to conventional formulations of the drug.

Chapter 6

Conclusion

Nanoparticulate drug delivery systems have overcome the drawbacks associated with conventional drug delivery. There are emerging nanotechnology strategies that are being implemented in anti-cancer drug delivery. The non-specificity, adverse effect, and poor physiochemical properties of chemotherapeutic agents can be overcome with nanoparticulate drug delivery. The design of nanocarriers plays a vital role in leading to specific, targeted drug delivery systems. For anti-cancer drug delivery, a wide variety of nanocarriers have been exploited and studied thoroughly to improve the properties and efficacy of drugs.

Chitosan (Ch), a deacetylated form of the naturally occurring polysaccharide chitin, has been an excellent choice for drug delivery or other biomedical. The versatility of Ch as a biomaterial is due to its muco-adhesivity and absorption-enhancing potential through the epithelial layer due to its cationic nature. Many accessible -OH and -NH_2 groups on the surface allow surface modification with hydrophobic groups or other tumor-targeting ligands. Ch NPs were used to load OXPt and investigated their therapeutic efficacy in oral and breast cancer.

Polyethylene glycol (PEG)-polylactide (PLA) is one of the most prominent amphipathic polymers, therefore, it is very suitable for constructing micelles. PLA is a form of biodegradable and biocompatible polyester derived from renewable resources and approved by the Food and Drug Administration (FDA) for clinical use. PEG is the most popular hydrophilic agent due to its various advantages, including linearity, lack of charge, immunogenicity, low polydispersity, and easy activation for conjugation. PEG–PLA micelles have been widely used as drug delivery systems for cancer therapy owing to their excellent physicochemical and biological properties, namely nontoxicity, non-protein adsorption, and weakened uptake by the reticuloendothelial system (RES) after intravenous injection.

Vitamin-based drug targeting is a promising idea since some vitamins, such as riboflavin, vitamin E, biotin, vitamin B12, and folic acid, are selective targeting agents for overexpressed cancer cell receptors. Biotin, also referred to as Vitamin H or B-7, has been scientifically

demonstrated to have a significant impact on the growth and spread of tumors by disrupting essential cellular processes. Moreover, research has demonstrated that cancer cells exhibit a greater abundance of biotin receptors on their cellular membrane compared to normal cells, highlighting the significance of biotin in the development of tumors.

Graphene oxide (GO) is a 2D-carbon atom with hydrophilic groups, including epoxide, carboxyl, and hydroxyl groups, spread across its extensive surface. It can be effortlessly mixed with water and modified using both non-covalent and covalent methods. GO has been thoroughly investigated as a promising photothermal agent for delivering drugs in cancer treatment due to its ability to be taken up by cells, its huge surface area, excellent biocompatibility, and the presence of other functional biomolecules. More significantly, GO is a promising nanoscale substance with the ability to reach elevated temperatures and induce hyperthermia, ultimately leading to the thermal destruction of cancer cells. Non-covalent interactions such as hydrophobic, π-π stacking, and electrostatic interactions are frequently used to modify GO with drug molecules. Additionally, the non-toxicity and excellent biocompatibility of GO make it a promising drug carrier when combined with various polymers, vitamins, and active pharmaceutical ingredients. Utilizing targeting agents like biotin or folic acid to modify graphene oxide (GO) enables the selective targeting of breast cancer cells that have an overexpression of specific receptors. This modification enhances the ability of GO to penetrate tumors, increases its surface potential, and improves its cellular uptake. Consequently, GO becomes suitable for multimodal synergistic therapeutic applications and specific targeted drug delivery while minimizing the heating of healthy cells. GO is a promising material for cancer nanomedicine due to its ability to enhance drug loading and release, as well as its ability to be activated by light for controlled drug release through photothermal processes. Recently, biodegradable polymers such as poly(lactic-co-glycolic) acid (PLGA), poly(lactic acid) (PLA), albumin, chitosan, and gelatin have been utilized to

modify the surface of GO due to their ability to release continuously. Among the stabilizing agents, polyethylene glycol (PEG) is the most widely researched. The functionalization of graphene oxide to polyethylene glycol enhances the stability of the material in aqueous solutions and increases its biocompatibility, making it a suitable candidate for use in drug delivery systems.

Among the highly targeted, selective, and successful anticancer therapies, photothermal therapy (PTT) is another therapeutic modality that uses photothermal conversion agents to convert light energy into heat, resulting in the localized killing of cancer cells. Because of its specificity in both place and time, as well as its synergistic benefits and low invasiveness, this method has attracted attention as an innovative treatment option. PTT has demonstrated reduced harm and fewer adverse impacts on healthy tissues in comparison to chemotherapy due to its safety, non-invasive nature, and enhanced regulation. Moreover, research has shown that PTT is superior to chemotherapy in the treatment of superficial malignancies, including those found in BC. Recently, there has been significant progress in the development of diverse nanomaterials for PTT, exhibiting outstanding capabilities in converting light into heat and delivering effective therapeutic outcomes. Hence, the choice of an optimum photothermal agent is pivotal for the effective management of cancer. Graphene and its derivatives are currently being extensively studied as prospective drug carrier systems for precise and controlled delivery in cancer therapy, leading to a surge in interest.

Doxorubicin and Oxaliplatin are the chemotherapeutic drugs that are now employed most often in clinical applications due to their high antitumor effectiveness against a variety of solid tumors. Dox was, therefore, chosen as the model drug. However, clinical use of Dox has been severely constrained due to the widespread distribution of Dox throughout the body and potential side effects to normal cells, including multidrug resistance, nephrotoxicity, myelosuppression, and dose-dependent cardiotoxicity. Further, the clinical trials on OXPt

reported several side effects such as neuropathy, hematological, nephron, and gastrointestinal tract toxicity. Therefore, it was urgently necessary to build an appropriate drug delivery system for the release of Dox and OXPt.

In the First objective, a novel bioinspired chitosan/vitamin E conjugate (Ch/VES, 1:4) was synthesized, optimized based on chitosan's molecular weight (15, 300 kDa), and was assembled to entrap oxaliplatin (OXPt). ^{1}H NMR, infrared spectroscopy, chromatography, X-ray photoelectron spectroscopy, X-ray diffraction, drug release, hemolysis, and stability studies were performed to characterize OXPt@Ch/VES micelles. The therapeutic efficacy of the micelles was tested *in vitro* in ER+/PR+/HER2− and triple-negative sensitive/resistant breast cancer cells, MCF-7 and MDA-MB-231 via cellular uptake, cytotoxicity, nuclear staining, DNA fragmentation, mitochondrial membrane potential, ROS generation, apoptosis, and cell cycle assays and *in vivo* using 4T1(Luc)-tumor-bearing mice. The OXPt@Ch/VES Ms were stable, biocompatible, and released the loaded drug in a sustained manner. The micelles were taken up by tumor cells in the *in vitro* cell-based studies, demonstrating a better cell-killing impact than the free drug. OXPt@Ch/VES Ms exhibited decreased IC50 towards MCF-7, MDA-MB-231 (sensitive/resistant) than OXPt. OXPt@Ch/VES Ms caused extensive DNA damage, mitochondrial depolarization, apoptosis, and cell-growth arrest (G2/M). OXPt@Ch/VES Ms treatment retarded tumor growth significantly, prolonged survival, and decreased nephrotoxicity than OXPt. The immune histopathological analysis indicated that the OXPt@Ch/VES Ms therapy caused significantly higher apoptosis induction than free OXPt treatment. The OXPt@Ch/VES Ms could serve as a potential nanomedicine to overcome conventional OXPt-mediated drug resistance/nephrotoxicity in breast cancer.

Combining photothermal and chemotherapy is an emerging strategy for tumor irradiation in a minimally invasive manner, utilizing photothermal transduction agents and anticancer drugs. **In the second objective**, we developed a 2D carbon nanomaterial graphene oxide (GO)-based

nanoplatform that converted to 3D colloidal spherical structures upon functionalization with an amphiphilic polymer mPEG-PLA (1: 0.5/1/2) and entrapped doxorubicin (Dox) physically. The Dox@GO(mPP) (1/0.5) NPs displayed the least particle size (161 nm), the highest stability with no aggregation, the highest Dox loading (6.3 %), and encapsulation efficiency (70 %). The therapeutic efficacy was determined *in vitro* and *in vivo* using murine (4T1) human triple-negative breast cancer cells (MDA-MB-231), and 4T1-Luc-tumor-bearing mouse models. The results demonstrated that the Dox@GO(mPP) (1/0.5) NPs treatment with laser (+L) (808 nm) was highly efficient in inducing apoptosis, cell cycle arrest (G2/M) phase, significant cytotoxicity, mitochondrial membrane depolarization, ROS generation, and photothermal effect leading to a higher proportion of cell death than free Dox, and Dox@GO(mPP) (1/0.5) NPs (-L). The anticancer studies in mice harboring the 4T1-Luc tumor showed that a combination of Dox@GO(mPP) (1/0.5) NPs (+L) effectively reduced tumor development and decreased lung metastasis. The developed nanoplatform could be a promising combination chemo-photothermal treatment option for triple-negative breast cancer.

Graphene oxide (GO) and GO-based nanocomposites provide excellent promise in drug delivery and photothermal therapy due to their exceptional near-infrared optical absorption and high specific surface area. **In the third objective**, we have effectively conjugated an oxaliplatin (IV) prodrug, PEGylated graphene oxide, and PEGylated biotin (PB) in a single platform for breast cancer treatment. This platform demonstrates promising prospects for targeted drug delivery and the synergistic application of photothermal chemotherapy when exposed to NIR-laser irradiation. The resulting nanocomposite (GO(OX)PB (1/1/0.2) NPs) displayed an exceptionally large surface area, minimal particle size (195.7 nm), specific targeting capabilities, a high drug load capacity (43.56 %) and entrapment efficiency (89.48 %) and exhibit excellent photothermal conversion efficiency and photostability when exposed to NIR-laser irradiation (808 nm). The therapeutic effectiveness was assessed both *in vitro* and *in vivo*

conditions employing human breast cancer cells (MCF-7), mouse mammary gland adenocarcinoma cells (4T1), and 4T1-Luc tumor-bearing mouse models. The findings demonstrated that GO(OX)PB (1/1/0.2) NPs (+L) were highly effective in causing significant cytotoxicity, G2/M phase cell cycle arrest, ROS generation, mitochondrial membrane depolarization, apoptosis, and photothermal effect. This resulted in a greater percentage of cell death compared to free OX, GO(OX)PEG (1/1/0.2) NPs (±L), and GO(OX)PB (1/1/0.2) NPs (−L). The *in vivo* therapeutic studies on 4T1-Luc tumor-bearing mice revealed that a combination of GO(OX)PB (1/1/0.2) NPs (+L) caused complete destruction of the tumor, no tumor recurrence, reduced lung metastasis, and mitigated nephrotoxicity. The examination of serum and blood components demonstrated minimal systemic toxicity of GO(OX)PB (1/1/0.2) NPs. The developed nanoplatform, in this context, may serve as a potential nanomedicine to address conventional nephrotoxicity in breast cancer and prevent metastasis by combining chemo-photothermal therapy.

Chapter 7

Future scope of work

Polymeric nanocarriers have been the subject of extensive research over the past decade as highly versatile and efficient drug delivery systems in cancer therapy. The design of polymer structures has evolved to achieve increased drug-loading capacity, tumor-specific uptake, and enhanced anticancer effects. Strategies to improve the interaction between drugs and carriers within polymeric nanocarriers have been developed to boost drug-loading capacity. Additionally, the development of biologically active carriers with dual functionality has been explored to further enhance anticancer effects. The incorporation of combination therapeutics involving molecularly targeted biologics and conventional small molecule anti-cancer drugs within these developed nanocarriers holds promise. However, the development of combination therapies poses significant challenges compared to monotherapies, necessitating sophisticated optimization strategies to determine the most effective combination for synergistic effects. These polymeric nanoparticle-based approaches have demonstrated reduced immunogenicity and tumorigenesis, while simultaneously improving drug safety, controlled release, and targeted efficacy. GO has recently been identified as a potential carrier in nanomedicine for drug delivery applications. The surface modification of GO is critical for lowering cytotoxicity, improving solubility in physiological buffers, biocompatibility, and GO stability. Surface-functionalized GO has become a very prominent nanocarrier, especially for cancer treatment and controlled drug delivery systems. GO absorbs radiations in the near-infrared range and used in photothermal therapy. Photothermal therapy (PTT) has gained attention as an emerging treatment strategy due to its spatiotemporal specificity, synergistic effect, and minimum invasiveness. When exposed to an external light stimulus, it causes irreparable destruction. It actively encourages the thermal extirpation of cancer cells locally by converting light energy into heat using photothermal conversion agents.

The future scope of work involves exploring novel therapeutic approaches for combination therapy, representative of emerging trends in cancer treatment. Specifically, simultaneous administration of multiple drugs aims to enhance the targeting of various signaling pathways

involved in tumor growth, leading to a synergistic therapeutic effect. However, these approaches are currently in the early stages of development and face theoretical and technical limitations, along with challenges related to dose-related toxicity and side effects that must be addressed. To advance these innovative strategies, improvements in *in vitro* evaluation systems are crucial for accurately predicting the *in vivo* pharmacokinetics of drugs in humans. Despite the use of small animal models to assess therapeutic effects, they remain imperfect predictors of a drug's effectiveness in humans. Overcoming these challenges and refining *in vitro* evaluation systems will contribute to the development of an even more effective nanocarrier system, advancing the overall landscape of cancer treatment.

In the forthcoming stages of research, the investigation into OXPt@Ch/VES micellar nanoaggregates is poised to shift towards optimization and scale-up for clinical applications. Extensive *in vitro* studies will be undertaken to elucidate cellular uptake mechanisms, while more *in vivo* assessments will be conducted to ascertain safety profiles essential for clinical translation. The mechanistic studies will unravel the molecular underpinnings of enhanced anticancer effects, providing crucial insights that will guide the progression towards preclinical studies and, ultimately, potential clinical trials. Concurrently, research on DOX@GO(mPP) NPs and GO(OX)PB NPs will concentrate on refining formulations to enhance drug delivery and photothermal properties. In-depth mechanistic insights and pharmacokinetic studies will bolster understanding, while advanced *in vivo* studies will explore diverse triple-negative breast cancer (TNBC) models and investigations into biological barriers and targeting strategies will be conducted to enhance specificity. Collaboration with clinical researchers will be pivotal in shaping early-phase clinical trials, ensuring adherence to regulatory guidelines. These concerted efforts aim to advance the development of more effective nanocarrier systems, reshaping the landscape of cancer treatment.

Chapter 8

References

Abu Lila, A. S., Eldin, N. E., Ichihara, M., Ishida, T., & Kiwada, H. (2012). Multiple administration of PEG-coated liposomal oxaliplatin enhances its therapeutic efficacy: A possible mechanism and the potential for clinical application. *International Journal of Pharmaceutics*, *438*(1–2), 176–183. https://doi.org/10.1016/j.ijpharm.2012.08.030

Ahmad, M. Z., Alasiri, A. S., Alasmary, M. Y., Abdullah, M. M., Ahmad, J., Abdel Wahab, B. A., M Alqahtani, S. A., Pathak, K., Mustafa, G., & Khan, M. A. (2022). Emerging advances in nanomedicine for breast cancer immunotherapy: Opportunities and challenges. *Immunotherapy*, *14*(12), 957–983.

Ai, F., Sun, T., Xu, Z., Wang, Z., Kong, W., To, M. W., Wang, F., & Zhu, G. (2016). An upconversion nanoplatform for simultaneous photodynamic therapy and Pt chemotherapy to combat cisplatin resistance. *Dalton Transactions*, *45*(33), 13052–13060.

Akter, Z., Khan, F. Z., & Khan, M. (2023). Gold nanoparticles in triple-negative breast cancer therapeutics. *Current Medicinal Chemistry*, *30*(3), 316–334.

Al-Hajj, M., Wicha, M. S., Benito-Hernandez, A., Morrison, S. J., & Clarke, M. F. (2003). Prospective identification of tumorigenic breast cancer cells. *Proceedings of the National Academy of Sciences*, *100*(7), 3983–3988.

AlFakeeh, A., & Brezden-Masley, C. (2018). Overcoming endocrine resistance in hormone receptor–positive breast cancer. *Current Oncology*, *25*(s1), 18–27.

Aliabadi, M., Yunessnia lehi, A., Shagholani, H., & Gerayeli, A. (2018). Planar polymer-graphene oxide nanohybrid as a 5-fluorouacil carrier in pH-responsive controlled release. *Journal of Drug Delivery Science and Technology*, *43*, 103–106.

https://doi.org/10.1016/j.jddst.2017.09.020

Alkabban, F. M., & Ferguson, T. (2019). *StatPearls*.

Allen, T. M. (2002). Ligand-targeted therapeutics in anticancer therapy. *Nature Reviews Cancer*, *2*(10), 750–763. https://doi.org/10.1038/nrc903

Allen, T. M., & Cullis, P. R. (2004). Drug delivery systems: entering the mainstream. *Science*, *303*(5665), 1818–1822.

Allen, T. M., & Cullis, P. R. (2013). Liposomal drug delivery systems: from concept to clinical applications. *Advanced Drug Delivery Reviews*, *65*(1), 36–48.

Aoki, H., Tottori, T., Sakurai, F., Fuji, K., & Miyajima, K. (1997). Effects of positive charge density on the liposomal surface on disposition kinetics of liposomes in rats. *International Journal of Pharmaceutics*, *156*(2), 163–174. https://doi.org/10.1016/S0378-5173(97)00184-1

Avadi, M. R., Sadeghi, A. M. M., Mohammadpour, N., Abedin, S., Atyabi, F., Dinarvand, R., & Rafiee-Tehrani, M. (2010). Preparation and characterization of insulin nanoparticles using chitosan and Arabic gum with ionic gelation method. *Nanomedicine: Nanotechnology, Biology, and Medicine*, *6*(1), 58–63. https://doi.org/10.1016/j.nano.2009.04.007

Badea, M., Balas, M., Cojocaru, F., Ionita, D., & Dinischiotu, A. (2021). *Nanoconjugates Based on Cisplatin and Single-Walled Carbon Nanotubes for Therapy of Triple Negative Breast Cancer*. 32. https://doi.org/10.3390/iocn2020-07989

Bai, R. G., & Husseini, G. A. (2019). Graphene-based drug delivery systems. In *Biomimetic Nanoengineered Materials for Advanced Drug Delivery*. Elsevier Inc. https://doi.org/10.1016/B978-0-12-814944-7.00011-4

Bao, H., Pan, Y., Ping, Y., Sahoo, N. G., Wu, T., Li, L., Li, J., & Gan, L. H. (2011). Chitosan-functionalized graphene oxide as a nanocarrier for drug and gene delivery. *Small*, *7*(11), 1569–1578. https://doi.org/10.1002/smll.201100191

Bareford, L. M., & Swaan, P. W. (2007). Endocytic mechanisms for targeted drug delivery. *Advanced Drug Delivery Reviews*, *59*(8), 748–758. https://doi.org/10.1016/j.addr.2007.06.008

Barenholz, Y. C. (2012). Doxil®—The first FDA-approved nano-drug: Lessons learned. *Journal of Controlled Release*, *160*(2), 117–134.

Basse, C., & Arock, M. (2015). The increasing roles of epigenetics in breast cancer: Implications for pathogenicity, biomarkers, prevention and treatment. *International Journal of Cancer*, *137*(12), 2785–2794.

Baumann, M., Krause, M., & Hill, R. (2008). Exploring the role of cancer stem cells in radioresistance. *Nature Reviews Cancer*, *8*(7), 545–554.

Bekyarova, E., Itkis, M. E., Ramesh, P., Berger, C., Sprinkle, M., De Heer, W. A., & Haddon, R. C. (2009). Chemical modification of epitaxial graphene: Spontaneous grafting of aryl groups. *Journal of the American Chemical Society*, *131*(4), 1336–1337. https://doi.org/10.1021/ja8057327

Berardi, R., Morgese, F., Onofri, A., Mazzanti, P., Pistelli, M., Ballatore, Z., Savini, A., De Lisa, M., Caramanti, M., & Rinaldi, S. (2013). Role of maspin in cancer. *Clinical and Translational Medicine*, *2*(1), 1–19.

Berrino, F., Bellati, C., Secreto, G., Camerini, E., Pala, V., Panico, S., Allegro, G., & Kaaks, R. (2001). Reducing bioavailable sex hormones through a comprehensive change in diet: the diet and androgens (DIANA) randomized trial. *Cancer Epidemiology Biomarkers &*

Prevention, *10*(1), 25–33.

Bianchini, G., Balko, J. M., Mayer, I. A., Sanders, M. E., & Gianni, L. (2017). HHS Public Access. Triple-Negat. *Breast Cancer Chall. Oppor. Heterog. Dis*, *13*, 674–690.

Biswas, S., Dodwadkar, N. S., Deshpande, P. P., Parab, S., & Torchilin, V. P. (2013). Surface functionalization of doxorubicin-loaded liposomes with octa-arginine for enhanced anticancer activity. *European Journal of Pharmaceutics and Biopharmaceutics*, *84*(3), 517–525. https://doi.org/10.1016/j.ejpb.2012.12.021

Boas, U., & Heegaard, P. M. H. (2004). Dendrimers in drug research. *Chemical Society Reviews*, *33*(1), 43–63.

Boix-Montesinos, P., Soriano-Teruel, P. M., Arminan, A., Orzaez, M., & Vicent, M. J. (2021). The past, present, and future of breast cancer models for nanomedicine development. *Advanced Drug Delivery Reviews*, *173*, 306–330.

Bourlinos, A. B., Gournis, D., Petridis, D., Szabó, T., Szeri, A., & Dékány, I. (2003). Graphite oxide: Chemical reduction to graphite and surface modification with primary aliphatic amines and amino acids. *Langmuir*, *19*(15), 6050–6055. https://doi.org/10.1021/la026525h

Boyages, J. (2017). Radiation therapy and early breast cancer: current controversies. *The Medical Journal of Australia*, *207*(5), 216–222.

Bredin, P., Walshe, J. M., & Denduluri, N. (2020). Systemic therapy for metastatic HER2-positive breast cancer. *Seminars in Oncology*, *47*(5), 259–269.

Brewer, H. R., Jones, M. E., Schoemaker, M. J., Ashworth, A., & Swerdlow, A. J. (2017). Family history and risk of breast cancer: an analysis accounting for family structure. *Breast Cancer Research and Treatment*, *165*, 193–200.

Burguin, A., Diorio, C., & Durocher, F. (2021). Breast cancer treatments: updates and new challenges. *Journal of Personalized Medicine*, *11*(8), 808.

Cao, H., Dan, Z., He, X., Zhang, Z., Yu, H., Yin, Q., & Li, Y. (2016). Liposomes coated with isolated macrophage membrane can target lung metastasis of breast cancer. *ACS Nano*, *10*(8), 7738–7748.

Cao, Z.-T., Chen, Z.-Y., Sun, C.-Y., Li, H.-J., Wang, H.-X., Cheng, Q.-Q., Zuo, Z.-Q., Wang, J.-L., Liu, Y.-Z., & Wang, Y.-C. (2016). Overcoming tumor resistance to cisplatin by cationic lipid-assisted prodrug nanoparticles. *Biomaterials*, *94*, 9–19.

Caruba, T., Cottu, P. H., Madelaine-Chambrin, I., Espié, M., Misset, J. L., & Gross-Goupil, M. (2007). Gemcitabine-oxaliplatin combination in heavily pretreated metastatic breast cancer: A pilot study on 43 patients. *Breast Journal*, *13*(2), 165–171. https://doi.org/10.1111/j.1524-4741.2007.00391.x

Castro Neto, A. H., Guinea, F., Peres, N. M. R., Novoselov, K. S., & Geim, A. K. (2009). The electronic properties of graphene. *Reviews of Modern Physics*, *81*(1), 109–162. https://doi.org/10.1103/RevModPhys.81.109

Catsburg, C., Miller, A. B., & Rohan, T. E. (2015). Active cigarette smoking and risk of breast cancer. *International Journal of Cancer*, *136*(9), 2204–2209.

Cells, C. (2020). *NIR-Triggered Hyperthermal E ff ect of Polythiophene Nanoparticles Synthesized by Surfactant-Free Oxidative Polymerization Method on Colorectal Carcinoma Cells*.

Ch, S., Padaga, S. G., Ghosh, B., Roy, S., & Biswas, S. (2023). Chitosan-poly (lactide-co-glycolide)/poloxamer mixed micelles as a mucoadhesive thermo-responsive moxifloxacin eye drop to improve treatment efficacy in bacterial keratitis. *Carbohydrate*

Polymers, *312*, 120822.

Chabner, B. A., & Roberts Jr, T. G. (2005). Chemotherapy and the war on cancer. *Nature Reviews Cancer*, *5*(1), 65–72.

Chaffer, C. L., & Weinberg, R. A. (2011). A perspective on cancer cell metastasis. *Science*, *331*(6024), 1559–1564.

Chalakur-Ramireddy, N. K. R., & Pakala, S. B. (2018). Combined drug therapeutic strategies for the effective treatment of Triple Negative Breast Cancer. *Bioscience Reports*, *38*(1), 1–14. https://doi.org/10.1042/BSR20171357

Chang, G., Li, S., Huang, F., Zhang, X., Shen, Y., & Xie, A. (2016). Multifunctional Reduced Graphene Oxide Hydrogel as Drug Carrier for Localized and Synergic Photothermal/Photodynamics/Chemo Therapy. *Journal of Materials Science and Technology*, *32*(8), 753–762. https://doi.org/10.1016/j.jmst.2016.06.014

Cheang, T. Y., Lei, Y. Y., Zhang, Z. Q., Zhou, H. Y., Ye, R. Y., Lin, Y., & Wang, S. (2018). Graphene oxide–hydroxyapatite nanocomposites effectively deliver HSV-TK suicide gene to inhibit human breast cancer growth. *Journal of Biomaterials Applications*, *33*(2), 216–226. https://doi.org/10.1177/0885328218788242

Chen, B., Liu, M., Zhang, L., Huang, J., Yao, J., & Zhang, Z. (2011). Polyethylenimine-functionalized graphene oxide as an efficient gene delivery vector. *Journal of Materials Chemistry*, *21*(21), 7736–7741. https://doi.org/10.1039/c1jm10341e

Chen, D., Feng, H., & Li, J. (2012). *Graphene Oxide : Preparation , Functionalization , and Electrochemical Applications*.

Chen, H., Luo, Q., Wang, J., He, H., Luo, W., Zhang, L., Xiao, Q., Chen, T., Xu, X., Niu, W., Ke, Y., & Wang, Y. (2020). Response of pH-Sensitive Doxorubicin Nanoparticles on

Complex Tumor Microenvironments by Tailoring Multiple Physicochemical Properties. *ACS Applied Materials and Interfaces*, *12*(20), 22673–22686. https://doi.org/10.1021/acsami.0c05724

Chen, W., Yi, P., Zhang, Y., Zhang, L., Deng, Z., & Zhang, Z. (2011). Composites of aminodextran-coated Fe3O4 nanoparticles and graphene oxide for cellular magnetic resonance imaging. *ACS Applied Materials and Interfaces*, *3*(10), 4085–4091. https://doi.org/10.1021/am2009647

Cheng, L., Zhou, Z., Flesken-Nikitin, A., Toshkov, I. A., Wang, W., Camps, J., Ried, T., & Nikitin, A. Y. (2010). Rb inactivation accelerates neoplastic growth and substitutes for recurrent amplification of cIAP1, cIAP2 and Yap1 in sporadic mammary carcinoma associated with p53 deficiency. *Oncogene*, *29*(42), 5700–5711.

Chieu, T. C., Dresselhaus, M. S., & Endo, M. (1982). Raman studies of benzene-derived graphite fibers. *Physical Review B*, *26*(10), 5867.

Choi, J. S., & Park, J. S. (2017). Development of docetaxel nanocrystals surface modified with transferrin for tumor targeting. *Drug Design, Development and Therapy*, *11*, 17–26. https://doi.org/10.2147/DDDT.S122984

Choi, M., Kipps, T., & Kurzrock, R. (2016). ATM Mutations in Cancer: Therapeutic ImplicationsATM Mutations in Cancer. *Molecular Cancer Therapeutics*, *15*(8), 1781–1791.

Collaborators, M. W. S. (2003). Breast cancer and hormone-replacement therapy in the Million Women Study. *The Lancet*, *362*(9382), 419–427.

Condorelli, R., & Vaz-Luis, I. (2018). Managing side effects in adjuvant endocrine therapy for breast cancer. *Expert Review of Anticancer Therapy*, *18*(11), 1101–1112.

Crevillen, A. G., Escarpa, A., & García, C. D. (2019). Chapter 1: Carbon-based Nanomaterials in Analytical Chemistry. In *RSC Detection Science* (Vols. 2019-Janua, Issue 12). https://doi.org/10.1039/9781788012751-00001

Dai, Y., Xu, C., Sun, X., & Chen, X. (2017). Nanoparticle design strategies for enhanced anticancer therapy by exploiting the tumour microenvironment. *Chemical Society Reviews*, *46*(12), 3830–3852.

Danhier, F., Feron, O., & Préat, V. (2010). To exploit the tumor microenvironment: Passive and active tumor targeting of nanocarriers for anti-cancer drug delivery. *Journal of Controlled Release*, *148*(2), 135–146. https://doi.org/10.1016/j.jconrel.2010.08.027

Davey, M. G., Lowery, A. J., Miller, N., & Kerin, M. J. (2021). MicroRNA expression profiles and breast cancer chemotherapy. *International Journal of Molecular Sciences*, *22*(19), 10812.

Davis, M. E., Chen, Z., & Shin, D. M. (2008). Nanoparticle therapeutics: An emerging treatment modality for cancer. *Nature Reviews Drug Discovery*, *7*(9), 771–782. https://doi.org/10.1038/nrd2614

de Luna, L. A. V., de Moraes, A. C. M., Consonni, S. R., Pereira, C. D., Cadore, S., Giorgio, S., & Alves, O. L. (2016). Comparative *in vitro* toxicity of a graphene oxide-silver nanocomposite and the pristine counterparts toward macrophages. *Journal of Nanobiotechnology*, *14*(1), 1–17.

Deng, W., Qiu, J., Wang, S., Yuan, Z., Jia, Y., Tan, H., Lu, J., & Zheng, R. (2018). Development of biocompatible and VEGF-targeted paclitaxel nanodrugs on albumin and graphene oxide dual-carrier for photothermal-triggered drug delivery *in vitro* and *in vivo*. *International Journal of Nanomedicine*, *13*, 439–453. https://doi.org/10.2147/IJN.S150977

Deng, X., Liang, H., Yang, W., & Shao, Z. (2020). Polarization and function of tumor-associated macrophages mediate graphene oxide-induced photothermal cancer therapy. *Journal of Photochemistry and Photobiology B: Biology*, *208*, 111913.

Depan, D., Shah, J., & Misra, R. D. K. (2011). Controlled release of drug from folate-decorated and graphene mediated drug delivery system: Synthesis, loading efficiency, and drug release response. *Materials Science and Engineering C*, *31*(7), 1305–1312. https://doi.org/10.1016/j.msec.2011.04.010

Deryugina, E. I., & Quigley, J. P. (2006). Matrix metalloproteinases and tumor metastasis. *Cancer and Metastasis Reviews*, *25*(1), 9–34. https://doi.org/10.1007/s10555-006-7886-9

Desmedt, C., Zoppoli, G., Gundem, G., Pruneri, G., Larsimont, D., Fornili, M., Fumagalli, D., Brown, D., Rothé, F., & Vincent, D. (2016). Genomic characterization of primary invasive lobular breast cancer. *Journal of Clinical Oncology*, *34*(16), 1872–1881.

Detappe, A., Reidy, M., Yu, Y., Mathieu, C., Nguyen, H. V.-T., Coroller, T. P., Lam, F., Jarolim, P., Harvey, P., & Protti, A. (2019). Antibody-targeting of ultra-small nanoparticles enhances imaging sensitivity and enables longitudinal tracking of multiple myeloma. *Nanoscale*, *11*(43), 20485–20496.

Di Santo, R., Digiacomo, L., Palchetti, S., Palmieri, V., Perini, G., Pozzi, D., Papi, M., & Caracciolo, G. (2019). Microfluidic manufacturing of surface-functionalized graphene oxide nanoflakes for gene delivery. *Nanoscale*, *11*(6), 2733–2741. https://doi.org/10.1039/c8nr09245a

Dikin, D. A., Stankovich, S., Zimney, E. J., Piner, R. D., Dommett, G. H. B., Evmenenko, G., Nguyen, S. T., & Ruoff, R. S. (2007). Preparation and characterization of graphene oxide paper. *Nature*, *448*(7152), 457–460. https://doi.org/10.1038/nature06016

Dilruba, S., & Kalayda, G. V. (2016). Platinum-based drugs: past, present and future. *Cancer Chemotherapy and Pharmacology*, *77*, 1103–1124.

Doi, Y., Shimizu, T., Ishima, Y., & Ishida, T. (2019). Long-term storage of PEGylated liposomal oxaliplatin with improved stability and long circulation times *in vivo*. *International Journal of Pharmaceutics*, *564*(February), 237–243. https://doi.org/10.1016/j.ijpharm.2019.04.042

Dong, H., Zhao, Z., Wen, H., Li, Y., Guo, F., Shen, A., Pilger, F., Lin, C., & Shi, D. (2010). Poly(ethylene glycol) conjugated nano-graphene oxide for photodynamic therapy. *Science China Chemistry*, *53*(11), 2265–2271. https://doi.org/10.1007/s11426-010-4114-9

Dong, L., Li, W., Yu, L., Sun, L., Chen, Y., & Hong, G. (2020). Ultrasmall Ag2Te quantum dots with rapid clearance for amplified computed tomography imaging and augmented photonic tumor hyperthermia. *ACS Applied Materials & Interfaces*, *12*(38), 42558–42566.

dos Santos, M. S. C., Gouvêa, A. L., de Moura, L. D., Paterno, L. G., de Souza, P. E. N., Bastos, A. P., Damasceno, E. A. M., Veiga-Souza, F. H., de Azevedo, R. B., & Báo, S. N. (2018). Nanographene oxide-methylene blue as phototherapies platform for breast tumor ablation and metastasis prevention in a syngeneic orthotopic murine model. *Journal of Nanobiotechnology*, *16*(1), 1–17. https://doi.org/10.1186/s12951-018-0333-6

Dreyer, D. R., Park, S., Bielawski, C. W., & Ruoff, R. S. (2010). The chemistry of graphene oxide. *Chemical Society Reviews*, *39*(1), 228–240. https://doi.org/10.1039/b917103g

Dumars, C., Ngyuen, J.-M., Gaultier, A., Lanel, R., Corradini, N., Gouin, F., Heymann, D., & Heymann, M.-F. (2016). Dysregulation of macrophage polarization is associated with the metastatic process in osteosarcoma. *Oncotarget*, *7*(48), 78343.

Duncan, R., & Vicent, M. J. (2010). Do HPMA copolymer conjugates have a future as clinically useful nanomedicines? A critical overview of current status and future opportunities. *Advanced Drug Delivery Reviews*, *62*(2), 272–282.

Elgebaly, H. A., Mosa, N. M., Allach, M., El-Massry, K. F., El-Ghorab, A. H., Al Hroob, A. M., & Mahmoud, A. M. (2018). Olive oil and leaf extract prevent fluoxetine-induced hepatotoxicity by attenuating oxidative stress, inflammation and apoptosis. *Biomedicine & Pharmacotherapy*, *98*, 446–453.

Espinosa, M., Martinez, M., Aguilar, J. L., Mota, A., De La Garza, J. G., Maldonado, V., & Meléndez-Zajgla, J. (2005). Oxaliplatin activity in head and neck cancer cell lines. *Cancer Chemotherapy and Pharmacology*, *55*(3), 301–305. https://doi.org/10.1007/s00280-004-0847-5

Fahlén, M., Fornander, T., Johansson, H., Johansson, U., Rutqvist, L.-E., Wilking, N., & von Schoultz, E. (2013). Hormone replacement therapy after breast cancer: 10 year follow up of the Stockholm randomised trial. *European Journal of Cancer*, *49*(1), 52–59.

Fanelli, S., Zimmermann, A., Totóli, E. G., & Salgado, H. R. N. (2018). FTIR Spectrophotometry as a Green Tool for Quantitative Analysis of Drugs: Practical Application to Amoxicillin. *Journal of Chemistry*, *2018*. https://doi.org/10.1155/2018/3920810

Fang, X., Cao, J., & Shen, A. (2020). Advances in anti-breast cancer drugs and the application of nano-drug delivery systems in breast cancer therapy. *Journal of Drug Delivery Science and Technology*, *57*(February), 101662. https://doi.org/10.1016/j.jddst.2020.101662

Fatima, I., Rahdar, A., Sargazi, S., Barani, M., Hassanisaadi, M., & Thakur, V. K. (2021). Quantum dots: Synthesis, antibody conjugation, and HER2-receptor targeting for breast

cancer therapy. *Journal of Functional Biomaterials*, *12*(4), 75.

Feng, L., & Liu, Z. (2011). *nnm%2E10%2E158.pdf*. *6*, 317–324.

Feng, L., Wu, L., & Qu, X. (2013). New horizons for diagnostics and therapeutic applications of graphene and graphene oxide. *Advanced Materials*, *25*(2), 168–186. https://doi.org/10.1002/adma.201203229

Feng, L., Yang, X., Shi, X., Tan, X., Peng, R., Wang, J., & Liu, Z. (2013). Polyethylene glycol and polyethylenimine dual-functionalized nano-graphene oxide for photothermally enhanced gene delivery. *Small*, *9*(11), 1989–1997. https://doi.org/10.1002/smll.201202538

Feng, L., Zhang, S., & Liu, Z. (2011). Graphene based gene transfection. *Nanoscale*, *3*(3), 1252–1257. https://doi.org/10.1039/c0nr00680g

Feng, R., Zong, Y., Cao, S., & Xu, R. (2019). Current cancer situation in China: good or bad news from the 2018 Global Cancer Statistics? *Cancer Communications*, *39*(1), 1–12.

Feng, T., Tian, H., Xu, C., Lin, L., Xie, Z., Lam, M. H.-W., Liang, H., & Chen, X. (2014). Synergistic co-delivery of doxorubicin and paclitaxel by porous PLGA microspheres for pulmonary inhalation treatment. *European Journal of Pharmaceutics and Biopharmaceutics*, *88*(3), 1086–1093.

Ferrer-Ugalde, A., Sandoval, S., Pulagam, K. R., Muñoz-Juan, A., Laromaine, A., Llop, J., Tobias, G., & Núñez, R. (2021). Radiolabeled Cobaltabis(dicarbollide) Anion-Graphene Oxide Nanocomposites for *in vivo* Bioimaging and Boron Delivery. *ACS Applied Nano Materials*, *4*(2), 1613–1625. https://doi.org/10.1021/acsanm.0c03079

Figueroa, D., Asaduzzaman, M., & Young, F. (2018). Real time monitoring and quantification of reactive oxygen species in breast cancer cell line MCF-7 by 2′,7′–

dichlorofluorescin diacetate (DCFDA) assay. *Journal of Pharmacological and Toxicological Methods*, *94*, 26–33. https://doi.org/10.1016/j.vascn.2018.03.007

Fisher, B., Anderson, S., Bryant, J., Margolese, R. G., Deutsch, M., Fisher, E. R., Jeong, J.-H., & Wolmark, N. (2002). Twenty-year follow-up of a randomized trial comparing total mastectomy, lumpectomy, and lumpectomy plus irradiation for the treatment of invasive breast cancer. *New England Journal of Medicine*, *347*(16), 1233–1241.

Foulkes, W. D., Smith, I. E., & Reis-Filho, J. S. (2010). Triple-negative breast cancer. *New England Journal of Medicine*, *363*(20), 1938–1948.

Fraguas-Sánchez, A. I., Lozza, I., & Torres-Suárez, A. I. (2022). Actively targeted nanomedicines in breast cancer: From pre-clinal investigation to clinic. *Cancers*, *14*(5), 1198.

Fu, M., Tang, W., Liu, J.-J., Gong, X.-Q., Kong, L., Yao, X.-M., Jing, M., Cai, F.-Y., Li, X.-T., & Ju, R.-J. (2020). Combination of targeted daunorubicin liposomes and targeted emodin liposomes for treatment of invasive breast cancer. *Journal of Drug Targeting*, *28*(3), 245–258.

Gan, C. W., & Feng, S. S. (2010). Transferrin-conjugated nanoparticles of Poly(lactide)-d-α-Tocopheryl polyethylene glycol succinate diblock copolymer for targeted drug delivery across the blood-brain barrier. *Biomaterials*, *31*(30), 7748–7757. https://doi.org/10.1016/j.biomaterials.2010.06.053

Ganjali, F., Eivazzadeh-Keihan, R., Aghamirza Moghim Aliabadi, H., Maleki, A., Pouri, S., Ahangari Cohan, R., Hashemi, S. M., & Mahdavi, M. (2022). Biocompatibility and antimicrobial investigation of agar-tannic acid hydrogel reinforced with silk fibroin and zinc manganese oxide magnetic microparticles. *Journal of Inorganic and Organometallic Polymers and Materials*, *32*(10), 4057–4069.

Gao, J., Bao, F., Feng, L., Shen, K., Zhu, Q., Wang, D., Chen, T., Ma, R., & Yan, C. (2011). Functionalized graphene oxide modified polysebacic anhydride as drug carrier for levofloxacin controlled release. *RSC Advances*, *1*(9), 1737–1744. https://doi.org/10.1039/c1ra00029b

Gao, Z., Li, Y., You, C., Sun, K., An, P., Sun, C., Wang, M., Zhu, X., & Sun, B. (2018). Iron oxide nanocarrier-mediated combination therapy of cisplatin and artemisinin for combating drug resistance through highly increased toxic reactive oxygen species generation. *ACS Applied Bio Materials*, *1*(2), 270–280.

García-Aranda, M., & Redondo, M. (2019). Immunotherapy: a challenge of breast cancer treatment. *Cancers*, *11*(12), 1822.

Garutti, M., Pelizzari, G., Bartoletti, M., Malfatti, M. C., Gerratana, L., Tell, G., & Puglisi, F. (2019). Platinum salts in patients with breast cancer: A focus on predictive factors. *International Journal of Molecular Sciences*, *20*(14), 3390.

Gavas, S., Quazi, S., & Karpiński, T. M. (2021). Nanoparticles for cancer therapy: current progress and challenges. *Nanoscale Research Letters*, *16*(1), 173.

Geim, A. K. (2009). Graphene: Status and prospects. *Science*, *324*(5934), 1530–1534. https://doi.org/10.1126/science.1158877

Gelderblom, H., Verweij, J., Nooter, K., & Sparreboom, A. (2001). Cremophor EL: the drawbacks and advantages of vehicle selection for drug formulation. *European Journal of Cancer*, *37*(13), 1590–1598.

Ghamkhari, A., Abbaspour-Ravasjani, S., Talebi, M., Hamishehkar, H., & Hamblin, M. R. (2021). Development of a graphene oxide-poly lactide nanocomposite as a Smart Drug Delivery System. *International Journal of Biological Macromolecules*, *169*, 521–531.

https://doi.org/10.1016/j.ijbiomac.2020.12.084

Giaquinto, A. N., Sung, H., Miller, K. D., Kramer, J. L., Newman, L. A., Minihan, A., Jemal, A., & Siegel, R. L. (2022). Breast cancer statistics, 2022. *CA: A Cancer Journal for Clinicians*, *72*(6), 524–541.

Gibson, G. R., Qian, D., Ku, J. K., & Lai, L. L. (2005). Metaplastic breast cancer: Clinical features and outcomes. *American Surgeon*, *71*(9), 725–730. https://doi.org/10.1177/000313480507100906

Gillies, E. R., & Frechet, J. M. J. (2005). Dendrimers and dendritic polymers in drug delivery. *Drug Discovery Today*, *10*(1), 35–43.

Giuliano, A. E., Connolly, J. L., Edge, S. B., Mittendorf, E. A., Rugo, H. S., Solin, L. J., Weaver, D. L., Winchester, D. J., & Hortobagyi, G. N. (2017). Breast cancer—major changes in the American Joint Committee on Cancer eighth edition cancer staging manual. *CA: A Cancer Journal for Clinicians*, *67*(4), 290–303.

Goenka, S., Sant, V., & Sant, S. (2014). Graphene-based nanomaterials for drug delivery and tissue engineering. *Journal of Controlled Release*, *173*(1), 75–88. https://doi.org/10.1016/j.jconrel.2013.10.017

Gokce, Y., Cengiz, B., Yildiz, N., Calimli, A., & Aktas, Z. (2014). Ultrasonication of chitosan nanoparticle suspension: Influence on particle size. *Colloids and Surfaces A: Physicochemical and Engineering Aspects*, *462*(April), 75–81. https://doi.org/10.1016/j.colsurfa.2014.08.028

Gollavelli, G., & Ling, Y. C. (2012). Multi-functional graphene as an invitro and invivo imaging probe. *Biomaterials*, *33*(8), 2532–2545. https://doi.org/10.1016/j.biomaterials.2011.12.010

Gonçalves, G., Vila, M., Portolés, M. T., Vallet-Regi, M., Gracio, J., & Marques, P. A. A. P. (2013). Nano-graphene oxide: A potential multifunctional platform for cancer therapy. *Advanced Healthcare Materials*, *2*(8), 1072–1090. https://doi.org/10.1002/adhm.201300023

Gong, P., Ji, S., Wang, J., Dai, D., Wang, F., Tian, M., Zhang, L., Guo, F., & Liu, Z. (2018). Fluorescence-switchable ultrasmall fluorinated graphene oxide with high near-infrared absorption for controlled and targeted drug delivery. *Chemical Engineering Journal*, *348*, 438–446. https://doi.org/10.1016/j.cej.2018.04.193

Gong, Z., Chen, M., Ren, Q., Yue, X., & Dai, Z. (2020). Fibronectin-targeted dual-acting micelles for combination therapy of metastatic breast cancer. *Signal Transduction and Targeted Therapy*, *5*(1), 12.

Gote, V., Nookala, A. R., Bolla, P. K., & Pal, D. (2021). Drug resistance in metastatic breast cancer: tumor targeted nanomedicine to the rescue. *International Journal of Molecular Sciences*, *22*(9), 4673.

Greish, K., Mathur, A., Al Zahrani, R., Elkaissi, S., Al Jishi, M., Nazzal, O., Taha, S., Pittalà, V., & Taurin, S. (2018). Synthetic cannabinoids nano-micelles for the management of triple negative breast cancer. *Journal of Controlled Release*, *291*, 184–195. https://doi.org/10.1016/j.jconrel.2018.10.030

Grothey, A. (2005). Clinical management of oxaliplatin-associated neurotoxicity. *Clinical Colorectal Cancer*, *5*(SUPPL. 1), S38–S46. https://doi.org/10.3816/CCC.2005.s.006

Guo, J., Yu, Z., Das, M., & Huang, L. (2020). Nano Codelivery of Oxaliplatin and Folinic Acid Achieves Synergistic Chemo-Immunotherapy with 5-Fluorouracil for Colorectal Cancer and Liver Metastasis. *ACS Nano*, *14*(4), 5075–5089. https://doi.org/10.1021/acsnano.0c01676

Guo, L., Shi, H., Wu, H., Zhang, Y., Wang, X., Wu, D., An, L., & Yang, S. (2016). Prostate cancer targeted multifunctionalized graphene oxide for magnetic resonance imaging and drug delivery. *Carbon*, *107*, 87–99. https://doi.org/10.1016/j.carbon.2016.05.054

Haberman, Y., Karns, R., Dexheimer, P. J., Schirmer, M., Somekh, J., Jurickova, I., Braun, T., Novak, E., Bauman, L., Collins, M. H., Mo, A., Rosen, M. J., Bonkowski, E., Gotman, N., Marquis, A., Nistel, M., Rufo, P. A., Baker, S. S., Sauer, C. G., … Denson, L. A. (2019). Ulcerative colitis mucosal transcriptomes reveal mitochondriopathy and personalized mechanisms underlying disease severity and treatment response. *Nature Communications*, *10*(1). https://doi.org/10.1038/s41467-018-07841-3

Hajdu, I., Bodnár, M., Filipcsei, G., Hartmann, J. F., Daróczi, L., Zrínyi, M., & Borbély, J. (2008). Nanoparticles prepared by self-assembly of Chitosan and poly-γ-glutamic acid. *Colloid and Polymer Science*, *286*(3), 343–350. https://doi.org/10.1007/s00396-007-1785-7

Hamajima, N., Hirose, K., Tajima, K., Rohan, T., Calle, E. E., Heath, C. W., Coates, R. J., Liff, J. M., Talamini, R., & Chantarakul, N. (2002). Alcohol, tobacco and breast cancer--collaborative reanalysis of individual data from 53 epidemiological studies, including 58,515 women with breast cancer and 95,067 women without the disease. *British Journal of Cancer*, *87*(11), 1234–1245.

Hanada, K., Suda, M., Kanai, N., & Ogata, H. (2010). Pharmacokinetics and toxicodynamics of oxaliplatin in rats: Application of a toxicity factor to explain differences in the nephrotoxicity and myelosuppression induced by oxaliplatin and the other platinum antitumor derivatives. *Pharmaceutical Research*, *27*(9), 1893–1899. https://doi.org/10.1007/s11095-010-0189-4

Hao, L., Song, H., Zhan, Z., & Lv, Y. (2020). Multifunctional Reduced Graphene Oxide-

Based Nanoplatform for Synergistic Targeted Chemo-Photothermal Therapy. *ACS Applied Bio Materials*, *3*(8), 5213–5222. https://doi.org/10.1021/acsabm.0c00614

Hasan, M. T., Lee, B. H., Lin, C. W., McDonald-Boyer, A., Gonzalez-Rodriguez, R., Vasireddy, S., Tsedev, U., Coffer, J., Belcher, A. M., & Naumov, A. V. (2021). Near-infrared emitting graphene quantum dots synthesized from reduced graphene oxide for *in vitro*/*in vivo*/ex vivo bioimaging applications. *2D Materials*, *8*(3). https://doi.org/10.1088/2053-1583/abe4e3

He, H., Xiao, H., Kuang, H., Xie, Z., Chen, X., Jing, X., & Huang, Y. (2014). Synthesis of mesoporous silica nanoparticle–oxaliplatin conjugates for improved anticancer drug delivery. *Colloids and Surfaces B: Biointerfaces*, *117*, 75–81.

Hientz, K., Mohr, A., Bhakta-Guha, D., & Efferth, T. (2017). The role of p53 in cancer drug resistance and targeted chemotherapy. *Oncotarget*, *8*(5), 8921.

Holford, J., Raynaud, F., Murrer, B. A., Grimaldi, K., Hartley, J. A., Abrams, M., & Kelland, L. R. (1998). Chemical, biochemical and pharmacological activity of the novel sterically hindered platinum co-ordination complex, cis-[amminedichloro (2-methylpyridine)] platinum (II)(AMD473). *Anti-Cancer Drug Design*, *13*(1), 1–18.

Hormones, E., & Group, B. C. C. (2013). Sex hormones and risk of breast cancer in premenopausal women: a collaborative reanalysis of individual participant data from seven prospective studies. *The Lancet Oncology*, *14*(10), 1009–1019.

Hrkach, J., Von Hoff, D., Ali, M. M., Andrianova, E., Auer, J., Campbell, T., De Witt, D., Figa, M., Figueiredo, M., Horhota, A., Low, S., McDonnell, K., Peeke, E., Retnarajan, B., Sabnis, A., Schnipper, E., Song, J. J., Song, Y. H., Summa, J., … Zale, S. (2012). Preclinical development and clinical translation of a PSMA-targeted docetaxel nanoparticle with a differentiated pharmacological profile. *Science Translational*

Medicine, *4*(128). https://doi.org/10.1126/scitranslmed.3003651

Hu, H., Yu, J., Li, Y., Zhao, J., & Dong, H. (2012). Engineering of a novel pluronic F127/graphene nanohybrid for pH responsive drug delivery. *Journal of Biomedical Materials Research - Part A*, *100 A*(1), 141–148. https://doi.org/10.1002/jbm.a.33252

Hu, Z., Huang, Y., Sun, S., Guan, W., Yao, Y., Tang, P., & Li, C. (2012). Visible light driven photodynamic anticancer activity of graphene oxide/TiO 2 hybrid. *Carbon*, *50*(3), 994–1004. https://doi.org/10.1016/j.carbon.2011.10.002

Huang, C., Hu, X., Hou, Z., Ji, J., Li, Z., & Luan, Y. (2019). Tailored graphene oxide-doxorubicin nanovehicles via near-infrared dye-lactobionic acid conjugates for chemo-photothermal therapy. *Journal of Colloid and Interface Science*, *545*, 172–183. https://doi.org/10.1016/j.jcis.2019.03.019

Huang, C., Wu, J., Jiang, W., Liu, R., Li, Z., & Luan, Y. (2018). Amphiphilic prodrug-decorated graphene oxide as a multi-functional drug delivery system for efficient cancer therapy. *Materials Science and Engineering: C*, *89*, 15–24.

Huang, J., Zong, C., Shen, H., Liu, M., Chen, B., Ren, B., & Zhang, Z. (2012). Mechanism of cellular uptake of graphene oxide studied by surface-enhanced Raman spectroscopy. *Small*, *8*(16), 2577–2584. https://doi.org/10.1002/smll.201102743

Huang, X., Chen, J., Wu, W., Yang, W., Zhong, B., Qing, X., & Shao, Z. (2020). Delivery of MutT homolog 1 inhibitor by functionalized graphene oxide nanoparticles for enhanced chemo-photodynamic therapy triggers cell death in osteosarcoma. *Acta Biomaterialia*, *109*, 229–243. https://doi.org/10.1016/j.actbio.2020.04.009

Huang, X., Qi, X., Boey, F., & Zhang, H. (2012). Graphene-based composites. *Chemical Society Reviews*, *41*(2), 666–686. https://doi.org/10.1039/c1cs15078b

Hussain, Z., Katas, H., Mohd Amin, M. C. I., Kumolosasi, E., Buang, F., & Sahudin, S. (2013). Self-assembled polymeric nanoparticles for percutaneous co-delivery of hydrocortisone/hydroxytyrosol: An ex vivo and *in vivo* study using an NC/Nga mouse model. *International Journal of Pharmaceutics*, *444*(1–2), 109–119. https://doi.org/10.1016/j.ijpharm.2013.01.024

Hussien, N. A., Işıklan, N., & Türk, M. (2018). Aptamer-functionalized magnetic graphene oxide nanocarrier for targeted drug delivery of paclitaxel. *Materials Chemistry and Physics*, *211*, 479–488. https://doi.org/10.1016/j.matchemphys.2018.03.015

Ibarra, J., Encinas, D., Blanco, M., Barbosa, S., Taboada, P., Juárez, J., & Valdez, M. A. (2018). Co-encapsulation of magnetic nanoparticles and cisplatin within biocompatible polymers as multifunctional nanoplatforms: synthesis, characterization, and *in vitro* assays. *Materials Research Express*, *5*(1), 15023.

Imani, R., Mohabatpour, F., & Mostafavi, F. (2018). Graphene-based Nano-Carrier modifications for gene delivery applications. *Carbon*, *140*, 569–591. https://doi.org/10.1016/j.carbon.2018.09.019

Inoue, K., & Fry, E. A. (2015). Aberrant expression of cyclin D1 in cancer. *Signal Transduction Insights*, *4*, STI-S30306.

Issels, R. D. (2008). Hyperthermia adds to chemotherapy. *European Journal of Cancer*, *44*(17), 2546–2554.

Ito, H., Yamaguchi, H., Fujikawa, A., Tanaka, N., Furugen, A., Miyamori, K., Takahashi, N., Ogura, J., Kobayashi, M., Yamada, T., Mano, N., & Iseki, K. (2012). A full validated hydrophilic interaction liquid chromatography-tandem mass spectrometric method for the quantification of oxaliplatin in human plasma ultrafiltrates. *Journal of Pharmaceutical and Biomedical Analysis*, *71*, 99–103.

https://doi.org/10.1016/j.jpba.2012.08.010

Itoo, A. M., Paul, M., Ghosh, B., & Biswas, S. (2022). Oxaliplatin delivery via chitosan/vitamin E conjugate micelles for improved efficacy and MDR-reversal in breast cancer. *Carbohydrate Polymers*, *282*(January), 119108. https://doi.org/10.1016/j.carbpol.2022.119108

Itoo, A. M., Paul, M., Ghosh, B., & Biswas, S. (2023). Polymeric graphene oxide nanoparticles loaded with doxorubicin for combined photothermal and chemotherapy in triple negative breast cancer. *Biomaterials Advances*, *153*(March), 213550. https://doi.org/10.1016/j.bioadv.2023.213550

Itoo, A. M., Paul, M., Padaga, S. G., Ghosh, B., & Biswas, S. (2022). *Nanotherapeutic Intervention in Photodynamic Therapy for Cancer*. https://doi.org/10.1021/acsomega.2c05852

Iyer, A. K., Khaled, G., Fang, J., & Maeda, H. (2006). Exploiting the enhanced permeability and retention effect for tumor targeting. *Drug Discovery Today*, *11*(17–18), 812–818. https://doi.org/10.1016/j.drudis.2006.07.005

Jain, V., Kumar, H., Anod, H. V., Chand, P., Gupta, N. V., Dey, S., & Kesharwani, S. S. (2020a). A review of nanotechnology-based approaches for breast cancer and triple-negative breast cancer. *Journal of Controlled Release*, *326*(April), 628–647. https://doi.org/10.1016/j.jconrel.2020.07.003

Jain, V., Kumar, H., Anod, H. V., Chand, P., Gupta, N. V., Dey, S., & Kesharwani, S. S. (2020b). A review of nanotechnology-based approaches for breast cancer and triple-negative breast cancer. In *Journal of Controlled Release* (Vol. 326). Elsevier B.V. https://doi.org/10.1016/j.jconrel.2020.07.003

Jamil, B., Abbasi, R., Abbasi, S., Imran, M., Khan, S. U., Ihsan, A., Javed, S., & Bokhari, H. (2016). Encapsulation of cardamom essential oil in chitosan nano-composites: In-vitro efficacy on antibiotic-resistant bacterial pathogens and cytotoxicity studies. *Frontiers in Microbiology*, *7*(OCT). https://doi.org/10.3389/fmicb.2016.01580

Jang, Y., Kim, S., Lee, S., Yoon, C. M., Lee, I., & Jang, J. (2017). Graphene oxide wrapped sio2/tio2 hollow nanoparticles loaded with photosensitizer for photothermal and photodynamic combination therapy. *Chemistry - A European Journal*, *23*(15), 3719–3727. https://doi.org/10.1002/chem.201605112

Jasim, D. A., Newman, L., Rodrigues, A. F., Vacchi, I. A., Lucherelli, M. A., Lozano, N., Ménard-Moyon, C., Bianco, A., & Kostarelos, K. (2021). The impact of graphene oxide sheet lateral dimensions on their pharmacokinetic and tissue distribution profiles in mice. *Journal of Controlled Release*, *338*, 330–340.

Jason, C. Y., & Formenti, S. C. (2018). Integration of radiation and immunotherapy in breast cancer-treatment implications. *The Breast*, *38*, 66–74.

Jiang, S., Zhu, R., He, X., Wang, J., Wang, M., Qian, Y., & Wang, S. (2017). Enhanced photocytotoxicity of curcumin delivered by solid lipid nanoparticles. *International Journal of Nanomedicine*, 167–178.

Jiang, W., Mo, F., Lin, Y., Wang, X., Xu, L., & Fu, F. (2018). Tumor targeting dual stimuli responsive controllable release nanoplatform based on DNA-conjugated reduced graphene oxide for chemo-photothermal synergetic cancer therapy. *Journal of Materials Chemistry B*, *6*(26), 4360–4367. https://doi.org/10.1039/c8tb00670a

Jiang, Y., Jiang, Z., Wang, M., & Ma, L. (2022). Current understandings and clinical translation of nanomedicines for breast cancer therapy. *Advanced Drug Delivery Reviews*, *180*, 114034.

Johnson, R., Sabnis, N., McConathy, W. J., & Lacko, A. G. (2013). The potential role of nanotechnology in therapeutic approaches for triple negative breast cancer. *Pharmaceutics*, *5*(2), 353–370.

Johra, F. T., Lee, J. W., & Jung, W. G. (2014). Facile and safe graphene preparation on solution based platform. *Journal of Industrial and Engineering Chemistry*, *20*(5), 2883–2887. https://doi.org/10.1016/j.jiec.2013.11.022

Jung, S., Wang, M., Anderson, K., Baglietto, L., Bergkvist, L., Bernstein, L., van den Brandt, P. A., Brinton, L., Buring, J. E., & Heather Eliassen, A. (2016). Alcohol consumption and breast cancer risk by estrogen receptor status: in a pooled analysis of 20 studies. *International Journal of Epidemiology*, *45*(3), 916–928.

Junnuthula, V., Kolimi, P., Nyavanandi, D., Sampathi, S., Vora, L. K., & Dyawanapelly, S. (2022). Polymeric Micelles for Breast Cancer Therapy: Recent Updates, Clinical Translation and Regulatory Considerations. *Pharmaceutics*, *14*(9), 1860.

Justin, R., Tao, K., Román, S., Chen, D., Xu, Y., Geng, X., Ross, I. M., Grant, R. T., Pearson, A., Zhou, G., MacNeil, S., Sun, K., & Chen, B. (2016). Photoluminescent and superparamagnetic reduced graphene oxide-iron oxide quantum dots for dual-modality imaging, drug delivery and photothermal therapy. *Carbon*, *97*, 54–70. https://doi.org/10.1016/j.carbon.2015.06.070

Kakran, M., G. Sahoo, N., Bao, H., Pan, Y., & Li, L. (2011). Functionalized Graphene Oxide as Nanocarrier for Loading and Delivery of Ellagic Acid. *Current Medicinal Chemistry*, *18*(29), 4503–4512. https://doi.org/10.2174/092986711797287548

Kakran, M., & Li, L. (2012). Carbon nanomaterials for drug delivery. *Key Engineering Materials*, *508*, 76–80. https://doi.org/10.4028/www.scientific.net/KEM.508.76

Kang, D. Il, Kang, H.-K., Gwak, H.-S., Han, H.-K., & Lim, S.-J. (2009). Liposome composition is important for retention of liposomal rhodamine in P-glycoprotein-overexpressing cancer cells. *Drug Delivery*, *16*(5), 261–267.

Kapp, T., Dullin, A., & Gust, R. (2010). Platinum (II)− dendrimer conjugates: synthesis and investigations on cytotoxicity, cellular distribution, platinum release, DNA, and protein binding. *Bioconjugate Chemistry*, *21*(2), 328–337.

Karimi Shervedani, R., Mirhosseini, H., Samiei Foroushani, M., Torabi, M., Rahsepar, F. R., & Norouzi-Barough, L. (2018). Immobilization of methotrexate anticancer drug onto the graphene surface and interaction with calf thymus DNA and 4T1 cancer cells. *Bioelectrochemistry*, *119*, 1–9. https://doi.org/10.1016/j.bioelechem.2017.08.004

Karki, N., Tiwari, H., Tewari, C., Rana, A., Pandey, N., Basak, S., & Sahoo, N. G. (2020). Functionalized graphene oxide as a vehicle for targeted drug delivery and bioimaging applications. *Journal of Materials Chemistry B*, *8*(36), 8116–8148. https://doi.org/10.1039/d0tb01149e

Katiyar, S. S., Muntimadugu, E., Rafeeqi, T. A., Domb, A. J., & Khan, W. (2016). Co-delivery of rapamycin-and piperine-loaded polymeric nanoparticles for breast cancer treatment. *Drug Delivery*, *23*(7), 2608–2616.

Kessel, D. H., Price, M., & Reiners John J, J. (2012). ATG7 deficiency suppresses apoptosis and cell death induced by lysosomal photodamage. *Autophagy*, *8*(9), 1333–1341.

Khan, F. A., & Akhtar, S. (1982). *FMSP-Nanoparticles Induced Cell Death on Human Breast Adenocarcinoma Cell Line (MCF-7 Cells):* https://doi.org/10.3390/biom8020032

Kim, E. S., Lu, C., Khuri, F. R., Tonda, M., Glisson, B. S., Liu, D., Jung, M., Hong, W. K., &

Herbst, R. S. (2001). A phase II study of STEALTH cisplatin (SPI-77) in patients with advanced non-small cell lung cancer. *Lung Cancer*, *34*(3), 427–432.

Kim, H., Namgung, R., Singha, K., Oh, I. K., & Kim, W. J. (2011). Graphene oxide-polyethylenimine nanoconstruct as a gene delivery vector and bioimaging tool. *Bioconjugate Chemistry*, *22*(12), 2558–2567. https://doi.org/10.1021/bc200397j

Kim, J., Pramanick, S., Lee, D., Park, H., & Kim, W. J. (2015). Polymeric biomaterials for the delivery of platinum-based anticancer drugs. *Biomaterials Science*, *3*(7), 1002–1017.

Kispert, S., & McHowat, J. (2017). Recent insights into cigarette smoking as a lifestyle risk factor for breast cancer. *Breast Cancer: Targets and Therapy*, 127–132.

Knight, J. A., Fan, J., Malone, K. E., John, E. M., Lynch, C. F., Langballe, R., Bernstein, L., Shore, R. E., Brooks, J. D., & Reiner, A. S. (2017). Alcohol consumption and cigarette smoking in combination: A predictor of contralateral breast cancer risk in the WECARE study. *International Journal of Cancer*, *141*(5), 916–924.

Kowsalya, E., MosaChristas, K., Jaquline, C. R. I., Balashanmugam, P., & Devasena, T. (2021). Gold nanoparticles induced apoptosis via oxidative stress and mitochondrial dysfunctions in MCF-7 breast cancer cells. *Applied Organometallic Chemistry*, *35*(1), 1–17. https://doi.org/10.1002/aoc.6071

Kumar, M. N. V. R., Muzzarelli, R. A. A., Muzzarelli, C., Sashiwa, H., & Domb, A. J. (2004). Chitosan chemistry and pharmaceutical perspectives. *Chemical Reviews*, *104*(12), 6017–6084. https://doi.org/10.1021/cr030441b

Kumari, P., Muddineti, O. S., Rompicharla, S. V. K., Ghanta, P., Adithya, K. B. B. N., Ghosh, B., & Biswas, S. (2017). Cholesterol-conjugated poly(D, L-lactide)-based micelles as a nanocarrier system for effective delivery of curcumin in cancer therapy.

Drug Delivery, *24*(1), 209–223. https://doi.org/10.1080/10717544.2016.1245365

Kumbham, S., Paul, M., Bhatt, H., Ghosh, B., & Biswas, S. (2020). Oleanolic acid-conjugated poly (D, L-lactide)-based micelles for effective delivery of doxorubicin and combination chemotherapy in oral cancer. *Journal of Molecular Liquids*, *320*, 114389. https://doi.org/10.1016/j.molliq.2020.114389

Kumbham, S., Paul, M., Itoo, A., Ghosh, B., & Biswas, S. (2022). Oleanolic acid-conjugated human serum albumin nanoparticles encapsulating doxorubicin as synergistic combination chemotherapy in oropharyngeal carcinoma and melanoma. *International Journal of Pharmaceutics*, *614*(January), 121479. https://doi.org/10.1016/j.ijpharm.2022.121479

Kwapisz, D. (2021). Pembrolizumab and atezolizumab in triple-negative breast cancer. *Cancer Immunology, Immunotherapy*, *70*(3), 607–617.

Lahmann, P. H., Lissner, L., Gullberg, B., Olsson, H., & Berglund, G. (2003). A prospective study of adiposity and postmenopausal breast cancer risk: the Malmö Diet and Cancer Study. *International Journal of Cancer*, *103*(2), 246–252.

Lambert, J. M., & Chari, R. V. J. (2014). *Ado-trastuzumab Emtansine (T-DM1): an antibody–drug conjugate (ADC) for HER2-positive breast cancer*. ACS Publications.

Lauby-Secretan, B., Scoccianti, C., Loomis, D., Benbrahim-Tallaa, L., Bouvard, V., Bianchini, F., & Straif, K. (2015). International agency for research on cancer handbook working group. *Breast-Cancer Screening—Viewpoint of the IARC Working Group. N Engl J Med*, *372*(24), 2353–2358.

Lee, C. C., MacKay, J. A., Fréchet, J. M. J., & Szoka, F. C. (2005). Designing dendrimers for biological applications. *Nature Biotechnology*, *23*(12), 1517–1526.

Lee, C., Wei, X., Kysar, J. W., & Hone, J. (2008). Measurement of the elastic properties and intrinsic strength of monolayer graphene. *Science*, *321*(5887), 385–388. https://doi.org/10.1126/science.1157996

Lee, J. J., Saiful Yazan, L., & Che Abdullah, C. A. (2017). A review on current nanomaterials and their drug conjugate for targeted breast cancer treatment. *International Journal of Nanomedicine*, 2373–2384.

Lee, K. S., Chung, H. C., Im, S. A., Park, Y. H., Kim, C. S., Kim, S. B., Rha, S. Y., Lee, M. Y., & Ro, J. (2008). Multicenter phase II trial of Genexol-PM, a Cremophor-free, polymeric micelle formulation of paclitaxel, in patients with metastatic breast cancer. *Breast Cancer Research and Treatment*, *108*(2), 241–250. https://doi.org/10.1007/s10549-007-9591-y

Lee, S.-Y., Lee, J.-H., Kim, Y.-H., Mahajan, R. L., & Park, S.-J. (2022). Surface energetics of graphene oxide and reduced graphene oxide determined by inverse gas chromatographic technique at infinite dilution at room temperature. *Journal of Colloid and Interface Science*, *628*, 758–768. https://doi.org/https://doi.org/10.1016/j.jcis.2022.07.183

Lefebvre, C., Bachelot, T., Filleron, T., Pedrero, M., Campone, M., Soria, J.-C., Massard, C., Levy, C., Arnedos, M., & Lacroix-Triki, M. (2016). Mutational profile of metastatic breast cancers: a retrospective analysis. *PLoS Medicine*, *13*(12), e1002201.

Lehmann, B. D., Bauer, J. A., Chen, X., Sanders, M. E., Chakravarthy, A. B., Shyr, Y., & Pietenpol, J. A. (2011). Identification of human triple-negative breast cancer subtypes and preclinical models for selection of targeted therapies. *Journal of Clinical Investigation*, *121*(7), 2750–2767. https://doi.org/10.1172/JCI45014

Lehmann, B. D., & Pietenpol, J. A. (2014). Identification and use of biomarkers in treatment

strategies for triple-negative breast cancer subtypes. *Journal of Pathology*, *232*(2), 142–150. https://doi.org/10.1002/path.4280

Lerebours, F., Cabel, L., & Pierga, J.-Y. (2021). Neoadjuvant endocrine therapy in breast cancer management: state of the art. *Cancers*, *13*(4), 902.

Levêque, D. (2008). Off-label use of anticancer drugs. *The Lancet Oncology*, *9*(11), 1102–1107. https://doi.org/10.1016/S1470-2045(08)70280-8

Li, C. Z., Zhang, P., Li, R. W., Wu, C. T., Zhang, X. P., & Zhu, H. C. (2015). Axillary lymph node dissection versus sentinel lymph node biopsy alone for early breast cancer with sentinel node metastasis: A meta-analysis. *European Journal of Surgical Oncology (EJSO)*, *41*(8), 958–966.

Li, R., Wang, Y., Du, J., Wang, X., Duan, A., & Gao, R. (2021). Graphene oxide loaded with tumor - targeted peptide and anti - cancer drugs for cancer target therapy. *Scientific Reports*, *0123456789*, 1–10. https://doi.org/10.1038/s41598-021-81218-3

Li, T., Wang, B., Wang, Z., Ragaz, J., Zhang, J., Sun, S., Cao, J., Lv, F., Wang, L., Zhang, S., Ni, C., Wu, Z., Xie, J., & Hu, X. (2015). Bevacizumab in combination with modified FOLFOX6 in heavily pretreated patients with HER2/Neu-negative metastatic breast cancer: A phase II clinical trial. *PLoS ONE*, *10*(7), 1–14. https://doi.org/10.1371/journal.pone.0133133

Lian, H., Zhang, T., Sun, J., Liu, X., Ren, G., Kou, L., Zhang, Y., Han, X., Ding, W., Ai, X., Wu, C., Li, L., Wang, Y., Sun, Y., Wang, S., & He, Z. (2013). *Enhanced Oral Delivery of Paclitaxel Using Acetylcysteine Functionalized Chitosan-Vitamin E Succinate Nanomicelles Based on a Mucus Bioadhesion and Penetration Mechanism*. https://doi.org/10.1021/mp400282r

Liang, J., Chen, B., Hu, J., Huang, Q., Zhang, D., Wan, J., Hu, Z., & Wang, B. (2019). PH and Thermal Dual-Responsive Graphene Oxide Nanocomplexes for Targeted Drug Delivery and Photothermal-Chemo/Photodynamic Synergetic Therapy. *ACS Applied Bio Materials*, *2*(12), 5859–5871. https://doi.org/10.1021/acsabm.9b00835

Liao, B., Zhang, Y., Sun, Q., & Jiang, P. (2018). Vorinostat enhances the anticancer effect of oxaliplatin on hepatocellular carcinoma cells. *Cancer Medicine*, *7*(1), 196–207. https://doi.org/10.1002/cam4.1278

Libson, S., & Lippman, M. (2014). A review of clinical aspects of breast cancer. *International Review of Psychiatry*, *26*(1), 4–15. https://doi.org/10.3109/09540261.2013.852971

Lin, G., Mi, P., Chu, C., Zhang, J., & Liu, G. (2016). Inorganic nanocarriers overcoming multidrug resistance for cancer theranostics. *Advanced Science*, *3*(11), 1600134.

Lin, G., Zhu, W., Yang, L., Wu, J., Lin, B., Xu, Y., Cheng, Z., Xia, C., Gong, Q., & Song, B. (2014). Delivery of siRNA by MRI-visible nanovehicles to overcome drug resistance in MCF-7/ADR human breast cancer cells. *Biomaterials*, *35*(35), 9495–9507.

Liu, C. C., Zhao, J. J., Zhang, R., Li, H., Chen, B., Zhang, L. L., & Yang, H. (2017). Multifunctionalization of graphene and graphene oxide for controlled release and targeted delivery of anticancer drugs. *American Journal of Translational Research*, *9*(12), 5197–5219.

Liu, G., Shen, H., Mao, J., Zhang, L., Jiang, Z., Sun, T., Lan, Q., & Zhang, Z. (2013). Transferrin modified graphene oxide for glioma-targeted drug delivery: *in vitro* and *in vivo* evaluations. *ACS Applied Materials & Interfaces*, *5*(15), 6909–6914.

Liu, J.-Y., Chen, T.-J., & Hwang, S.-J. (2016). The risk of breast cancer in women using

menopausal hormone replacement therapy in Taiwan. *International Journal of Environmental Research and Public Health*, *13*(5), 482.

Liu, J., Cui, L., & Losic, D. (2013). Graphene and graphene oxide as new nanocarriers for drug delivery applications. *Acta Biomaterialia*, *9*(12), 9243–9257. https://doi.org/10.1016/j.actbio.2013.08.016

Liu, J., Guo, X., Zhao, Z., Li, B., Qin, J., Peng, Z., He, G., Brett, D. J. L., Wang, R., & Lu, X. (2020). Fe3S4 nanoparticles for arterial inflammation therapy: Integration of magnetic hyperthermia and photothermal treatment. *Applied Materials Today*, *18*, 100457.

Liu, J., Ma, X., Jin, S., Xue, X., Zhang, C., Wei, T., Guo, W., & Liang, X. (2016). *Zinc Oxide Nanoparticles as Adjuvant To Facilitate Doxorubicin Intracellular Accumulation and Visualize pH-Responsive Release for Overcoming Drug Resistance*. https://doi.org/10.1021/acs.molpharmaceut.6b00311

Liu, J., Tao, L., Yang, W., Li, D., Boyer, C., Wuhrer, R., Braet, F., & Davis, T. P. (2010). Synthesis, characterization, and multilayer assembly of pH sensitive graphene-polymer nanocomposites. *Langmuir*, *26*(12), 10068–10075. https://doi.org/10.1021/la1001978

Liu, J., Xiao, Y., Wei, W., Guo, J. X., Liu, Y. C., Huang, X. H., Zhang, R. X., Wu, Y. J., & Zhou, J. (2015). Clinical efficacy of administering oxaliplatin combined with S-1 in the treatment of advanced triple-negative breast cancer. *Experimental and Therapeutic Medicine*, *10*(1), 379–385. https://doi.org/10.3892/etm.2015.2489

Liu, P., Xie, X., Liu, M., Hu, S., Ding, J., & Zhou, W. (2021). A smart MnO2-doped graphene oxide nanosheet for enhanced chemo-photodynamic combinatorial therapy via simultaneous oxygenation and glutathione depletion. *Acta Pharmaceutica Sinica B*, *11*(3), 823–834. https://doi.org/10.1016/j.apsb.2020.07.021

Liu, R., Zhang, H., Zhang, F., Wang, X., Liu, X., & Zhang, Y. (2019). Polydopamine doped reduced graphene oxide/mesoporous silica nanosheets for chemo-photothermal and enhanced photothermal therapy. *Materials Science and Engineering C*, *96*, 138–145. https://doi.org/10.1016/j.msec.2018.10.093

Liu, W.-B., Zhou, J., Qu, Y., Li, X., Lu, C.-T., Xie, K.-L., Sun, X.-L., & Fei, Z. (2010). Neuroprotective effect of osthole on MPP+-induced cytotoxicity in PC12 cells via inhibition of mitochondrial dysfunction and ROS production. *Neurochemistry International*, *57*(3), 206–215.

Liu, W., Chen, B., Zheng, H., Xing, Y., Chen, G., Zhou, P., Qian, L., & Min, Y. (2021). Advances of nanomedicine in radiotherapy. *Pharmaceutics*, *13*(11), 1757.

Liu, W., Zhang, X., Zhou, L., Shang, L., & Su, Z. (2019). Reduced graphene oxide (rGO) hybridized hydrogel as a near-infrared (NIR)/pH dual-responsive platform for combined chemo-photothermal therapy. *Journal of Colloid and Interface Science*, *536*, 160–170. https://doi.org/10.1016/j.jcis.2018.10.050

Liu, Z., Bi, Y., Sun, Y., Hao, F., Lu, J., Meng, Q., Robert, J., Liu, Z., Bi, Y., Sun, Y., Hao, F., Lu, J., & Meng, Q. (2017). *Pharmacokinetics of a liposomal formulation of doxorubicin in rats*. https://doi.org/10.1016/j.jsps.2017.04.019

Liu, Z., Robinson, J. T., Sun, X., & Dai, H. (2008a). Graphene Liu. *Journal of the American Chemical Society*, *130*(33), 10876–10877. http://pubs3.acs.org/acs/journals/doilookup?in_doi=10.1021/ja803688x

Liu, Z., Robinson, J. T., Sun, X., & Dai, H. (2008b). PEGylated nanographene oxide for delivery of water-insoluble cancer drugs. *Journal of the American Chemical Society*, *130*(33), 10876–10877. https://doi.org/10.1021/ja803688x

Loh, K. P., Bao, Q., Ang, P. K., & Yang, J. (2010). The chemistry of graphene. *Journal of Materials Chemistry*, *20*(12), 2277–2289. https://doi.org/10.1039/b920539j

Loibl, S., Darb-Esfahani, S., Huober, J., Klimowicz, A., Furlanetto, J., Lederer, B., Hartmann, A., Eidtmann, H., Pfitzner, B., & Fasching, P. A. (2016). Integrated Analysis of PTEN and p4EBP1 Protein Expression as Predictors for pCR in HER2-Positive Breast CancerPTEN and p4EBP for pCR Prediction. *Clinical Cancer Research*, *22*(11), 2675–2683.

Lovelace, D. L., McDaniel, L. R., & Golden, D. (2019). Long-term effects of breast cancer surgery, treatment, and survivor care. *Journal of Midwifery & Women's Health*, *64*(6), 713–724.

Lu, C. H., Zhu, C. L., Li, J., Liu, J. J., Chen, X., & Yang, H. H. (2010). Using graphene to protect DNA from cleavage during cellular delivery. *Chemical Communications*, *46*(18), 3116–3118. https://doi.org/10.1039/b926893f

Lu, Y.-J., Lin, C.-W., Yang, H.-W., Lin, K.-J., Wey, S.-P., Sun, C.-L., Wei, K.-C., Yen, T.-C., Lin, C.-I., & Ma, C.-C. M. (2014). Biodistribution of PEGylated graphene oxide nanoribbons and their application in cancer chemo-photothermal therapy. *Carbon*, *74*, 83–95.

Łukasiewicz, S., Czeczelewski, M., Forma, A., Baj, J., Sitarz, R., & Stanisławek, A. (2021). Breast cancer—epidemiology, risk factors, classification, prognostic markers, and current treatment strategies—an updated review. *Cancers*, *13*(17), 4287.

Lumachi, F., Luisetto, G., Mm Basso, S., Basso, U., Brunello, A., & Camozzi, V. (2011). Endocrine therapy of breast cancer. *Current Medicinal Chemistry*, *18*(4), 513–522.

Luo, Z., Wang, X., Yang, D., Zhang, S., Zhao, T., Qin, L., & Yu, Z.-Z. (2020). Photothermal

hierarchical carbon nanotube/reduced graphene oxide microspherical aerogels with radially orientated microchannels for efficient cleanup of crude oil spills. *Journal of Colloid and Interface Science*, *570*, 61–71. https://doi.org/https://doi.org/10.1016/j.jcis.2020.02.097

Ma, B., Nishina, Y., & Bianco, A. (2021). A glutathione responsive nanoplatform made of reduced graphene oxide and MnO2 nanoparticles for photothermal and chemodynamic combined therapy. *Carbon*, *178*, 783–791.

Ma, P., Xiao, H., Yu, C., Liu, J., Cheng, Z., Song, H., Zhang, X., Li, C., Wang, J., & Gu, Z. (2017). Enhanced cisplatin chemotherapy by iron oxide nanocarrier-mediated generation of highly toxic reactive oxygen species. *Nano Letters*, *17*(2), 928–937.

Ma, X., Tao, H., Yang, K., Feng, L., Cheng, L., Shi, X., Li, Y., Guo, L., & Liu, Z. (2012). A functionalized graphene oxide-iron oxide nanocomposite for magnetically targeted drug delivery, photothermal therapy, and magnetic resonance imaging. *Nano Research*, *5*(3), 199–212. https://doi.org/10.1007/s12274-012-0200-y

Maffini, M. V, Soto, A. M., Calabro, J. M., Ucci, A. A., & Sonnenschein, C. (2004). The stroma as a crucial target in rat mammary gland carcinogenesis. *Journal of Cell Science*, *117*(8), 1495–1502.

Makarem, N., Chandran, U., Bandera, E. V, & Parekh, N. (2013). Dietary fat in breast cancer survival. *Annual Review of Nutrition*, *33*, 319–348.

Malik, J. A., Ahmed, S., Jan, B., Bender, O., Al Hagbani, T., Alqarni, A., & Anwar, S. (2022). Drugs repurposed: An advanced step towards the treatment of breast cancer and associated challenges. *Biomedicine & Pharmacotherapy*, *145*, 112375.

Mallick, A., Nandi, A., & Basu, S. (2019). Polyethylenimine Coated Graphene Oxide

Nanoparticles for Targeting Mitochondria in Cancer Cells. *ACS Applied Bio Materials*, *2*(1), 14–19. https://doi.org/10.1021/acsabm.8b00519

Mansoori, B., Mohammadi, A., Davudian, S., Shirjang, S., & Baradaran, B. (2017). The different mechanisms of cancer drug resistance: a brief review. *Advanced Pharmaceutical Bulletin*, *7*(3), 339.

Martin, C. R., & Kohli, P. (2003). The emerging field of nanotube biotechnology. *Nature Reviews Drug Discovery*, *2*(1), 29–37. https://doi.org/10.1038/nrd988

Martinez-Balibrea, E., Martínez-Cardus, A., Gines, A., Ruiz De Porras, V., Moutinho, C., Layos, L., Manzano, J. L., Buges, C., Bystrup, S., Esteller, M., & Abad, A. (2015). Tumor-related molecular mechanisms of oxaliplatin resistance. *Molecular Cancer Therapeutics*, *14*(8), 1767–1776. https://doi.org/10.1158/1535-7163.MCT-14-0636

Martínez-Carmona, M., Colilla, M., & Vallet-Regí, M. (2015). Smart mesoporous nanomaterials for antitumor therapy. *Nanomaterials*, *5*(4), 1906–1937. https://doi.org/10.3390/nano5041906

Martínez-García, M., Vargas-Barrón, J., Bañuelos-Téllez, F., González-Pacheco, H., Fresno, C., Hernández-Lemus, E., Martínez-Ríos, M. A., & Vallejo, M. (2018). Public insurance program impact on catastrophic health expenditure on acute myocardial infarction. *Public Health*, *158*, 47–54. https://doi.org/10.1016/j.puhe.2018.01.025

Massagué, J., & Obenauf, A. C. (2016). Metastatic colonization by circulating tumour cells. *Nature*, *529*(7586), 298–306.

Mathew, M. E., Mohan, J. C., Manzoor, K., Nair, S. V., Tamura, H., & Jayakumar, R. (2010). Folate conjugated carboxymethyl chitosan-manganese doped zinc sulphide nanoparticles for targeted drug delivery and imaging of cancer cells. *Carbohydrate Polymers*, *80*(2),

442–448. https://doi.org/10.1016/j.carbpol.2009.11.047

Matsumura, S., Ajima, K., Yudasaka, M., Iijima, S., & Shiba, K. (2007). Dispersion of cisplatin-loaded carbon nanohorns with a conjugate comprised of an artificial peptide aptamer and polyethylene glycol. *Molecular Pharmaceutics*, *4*(5), 723–729. https://doi.org/10.1021/mp070022t

Mauro, N., Scialabba, C., Cavallaro, G., Licciardi, M., & Giammona, G. (2015). Biotin-containing reduced graphene oxide-based nanosystem as a multieffect anticancer agent: Combining hyperthermia with targeted chemotherapy. *Biomacromolecules*, *16*(9), 2766–2775.

Mehnert, W., & Mäder, K. (2012). Solid lipid nanoparticles: production, characterization and applications. *Advanced Drug Delivery Reviews*, *64*, 83–101.

Meiyanto, E., Hermawan, A., Junedi, S., Fitriasari, A., & Susidarti, R. A. (2011). *International Journal of Phytomedicine 3 (2011) 129-137 Nobiletin Increased Cytotoxic Activity Of Doxorubicin On Mcf-7 Cells But Not On T47d Cells*. *January*.

Mendes, R. G., Bachmatiuk, A., Büchner, B., Cuniberti, G., & Rümmeli, M. H. (2013). Carbon nanostructures as multi-functional drug delivery platforms. *Journal of Materials Chemistry B*, *1*(4), 401–428. https://doi.org/10.1039/c2tb00085g

Miao, W., Shim, G., Lee, S., Lee, S., Choe, Y. S., & Oh, Y. K. (2013). Safety and tumor tissue accumulation of pegylated graphene oxide nanosheets for co-delivery of anticancer drug and photosensitizer. *Biomaterials*, *34*(13), 3402–3410. https://doi.org/10.1016/j.biomaterials.2013.01.010

Mills, M. N., Figura, N. B., Arrington, J. A., Yu, H.-H. M., Etame, A. B., Vogelbaum, M. A., Soliman, H., Czerniecki, B. J., Forsyth, P. A., & Han, H. S. (2020). Management of

brain metastases in breast cancer: a review of current practices and emerging treatments. *Breast Cancer Research and Treatment*, *180*, 279–300.

Mohamed, M., Lila, A. S. A., Shimizu, T., Alaaeldin, E., Sarhan, H. A., Szebeni, J., & Ishida, T. (2019). PEGylated liposomes : immunological responses. *Science and Technology of Advanced Materials*, *20*(1), 710–724. https://doi.org/10.1080/14686996.2019.1627174

Mohammadpour, R., Dobrovolskaia, M. A., Cheney, D. L., Greish, K. F., & Ghandehari, H. (2019). Subchronic and chronic toxicity evaluation of inorganic nanoparticles for delivery applications. *Advanced Drug Delivery Reviews*, *144*, 112–132.

Mohammed, F., Ke, W., Mukerabigwi, J. F., Japir, A. A. W. M. M., Ibrahim, A., Wang, Y., Zha, Z., Lu, N., Zhou, M., & Ge, Z. (2019). ROS-Responsive Polymeric Nanocarriers with Photoinduced Exposure of Cell-Penetrating Moieties for Specific Intracellular Drug Delivery [Research-article]. *ACS Applied Materials and Interfaces*, *11*(35), 31681–31692. https://doi.org/10.1021/acsami.9b10950

Mohd, A., Lakshmi, S., Tejasvni, M., & Vilasrao, M. (2022a). Multifunctional graphene oxide nanoparticles for drug delivery in cancer. *Journal of Controlled Release*, *350*(August), 26–59. https://doi.org/10.1016/j.jconrel.2022.08.011

Mohd, A., Lakshmi, S., Tejasvni, M., & Vilasrao, M. (2022b). Multifunctional graphene oxide nanoparticles for drug delivery in cancer. *Journal of Controlled Release*, *350*(May), 26–59. https://doi.org/10.1016/j.jconrel.2022.08.011

Molyneux, G., Geyer, F. C., Magnay, F.-A., McCarthy, A., Kendrick, H., Natrajan, R., MacKay, A., Grigoriadis, A., Tutt, A., & Ashworth, A. (2010). BRCA1 basal-like breast cancers originate from luminal epithelial progenitors and not from basal stem cells. *Cell Stem Cell*, *7*(3), 403–417.

Moreno-Smith, M., Lutgendorf, S. K., & Sood, A. K. (2010). Impact of stress on cancer metastasis. *Future Oncology*, *6*(12), 1863–1881.

Morris, G. J., Naidu, S., Topham, A. K., Guiles, F., Xu, Y., McCue, P., Schwartz, G. F., Park, P. K., Rosenberg, A. L., Brill, K., & Mitchell, E. P. (2007). Differences in breast carcinoma characteristics in newly diagnosed African-American and Caucasian patients: A single-institution compilation compared with the national cancer institute's surveillance, epidemiology, and end results database. *Cancer*, *110*(4), 876–884. https://doi.org/10.1002/cncr.22836

Mu, Y., Wu, G., Su, C., Dong, Y., Zhang, K., Li, J., Sun, X., Li, Y., Chen, X., & Feng, C. (2019). pH-sensitive amphiphilic chitosan-quercetin conjugate for intracellular delivery of doxorubicin enhancement. *Carbohydrate Polymers*, *223*(July), 115072. https://doi.org/10.1016/j.carbpol.2019.115072

Muddineti, O. S. (2017). *Curcumin-loaded chitosan – cholesterol micelles : evaluation in monolayers and 3D cancer spheroid model*.

Muddineti, O. S., Ghosh, B., & Biswas, S. (2017). Current trends in the use of vitamin E-based micellar nanocarriers for anticancer drug delivery. *Expert Opinion on Drug Delivery*, *14*(6), 715–726. https://doi.org/10.1080/17425247.2016.1229300

Muddineti, O. S., Shah, A., Rompicharla, S. V. K., Ghosh, B., & Biswas, S. (2018). Cholesterol-grafted chitosan micelles as a nanocarrier system for drug-siRNA co-delivery to the lung cancer cells. *International Journal of Biological Macromolecules*, *118*, 857–863. https://doi.org/10.1016/j.ijbiomac.2018.06.114

Nallamuthu, I., Devi, A., & Khanum, F. (2015). Chlorogenic acid loaded chitosan nanoparticles with sustained release property, retained antioxidant activity and enhanced bioavailability. *Asian Journal of Pharmaceutical Sciences*, *10*(3), 203–211.

https://doi.org/10.1016/j.ajps.2014.09.005

Nam, J., Son, S., Ochyl, L. J., Kuai, R., Schwendeman, A., & Moon, J. J. (2018). Chemo-photothermal therapy combination elicits anti-tumor immunity against advanced metastatic cancer. *Nature Communications*, *9*(1). https://doi.org/10.1038/s41467-018-03473-9

Neri, D., & Bicknell, R. (2005). Tumour vascular targeting. *Nature Reviews Cancer*, *5*(6), 436–446. https://doi.org/10.1038/nrc1627

Nitheesh, Y., Pradhan, R., Hejmady, S., Taliyan, R., Singhvi, G., Alexander, A., Kesharwani, P., & Dubey, S. K. (2021). Surface engineered nanocarriers for the management of breast cancer. *Materials Science and Engineering: C*, *130*, 112441.

Omidi, Y., Mobasher, M., Castejon, A. M., & Mahmoudi, M. (2022). Recent advances in nanoscale targeted therapy of HER2-positive breast cancer. *Journal of Drug Targeting*, *30*(7), 687–708.

Ourique, F., Otsuka, I., Halila, S., Pedrosa, R. C., Cla, M., Lemos-senna, E., & Muniz, E. C. (2015). *Nanoparticles Made From Xyloglucan- Block-Polycaprolactone Copolymers : Nanoparticles Made From Xyloglucan- Block-Polycaprolactone Copolymers : Safety Assessment for Drug Delivery*. *February 2017*. https://doi.org/10.1093/toxsci/kfv114

Pan, Y., Bao, H., Sahoo, N. G., Wu, T., & Li, L. (2011). Water-soluble poly(N-isopropylacrylamide)-graphene sheets synthesized via click chemistry for drug delivery. *Advanced Functional Materials*, *21*(14), 2754–2763. https://doi.org/10.1002/adfm.201100078

Pan, Y., Sahoo, N. G., & Li, L. (2012). The application of graphene oxide in drug delivery. *Expert Opinion on Drug Delivery*, *9*(11), 1365–1376.

https://doi.org/10.1517/17425247.2012.729575

Paraskar, A., Soni, S., & Roy, B. (n.d.). *Rationally designed oxaliplatin- nanoparticle for enhanced antitumor efficacy*. *075103*. https://doi.org/10.1088/0957-4484/23/7/075103

Parmanik, A., Bose, A., Ghosh, B., Paul, M., Itoo, A., & Biswas, S. (2022). Journal of Drug Delivery Science and Technology Development of triphala churna extract mediated iron oxide nanoparticles as novel treatment strategy for triple negative breast cancer. *Journal of Drug Delivery Science and Technology*, *76*(August), 103735. https://doi.org/10.1016/j.jddst.2022.103735

Pasetto, L. M., D'Andrea, M. R., Rossi, E., & Monfardini, S. (2006). Oxaliplatin-related neurotoxicity: How and why? *Critical Reviews in Oncology/Hematology*, *59*(2), 159–168. https://doi.org/10.1016/j.critrevonc.2006.01.001

Patel, T., Itoo, A. M., Paul, M., Kondapaneni, L. P., Ghosh, B., & Biswas, S. (2023). Block HPMA-based pH-sensitive Gemcitabine Pro-drug Nanoaggregate for Cancer Treatment. *European Polymer Journal*, 111843.

Patil, Y., Sadhukha, T., Ma, L., & Panyam, J. (2009). Nanoparticle-mediated simultaneous and targeted delivery of paclitaxel and tariquidar overcomes tumor drug resistance. *Journal of Controlled Release*, *136*(1), 21–29. https://doi.org/10.1016/j.jconrel.2009.01.021

Pattnaik, S., Surendra, Y., Rao, J. V., & Swain, K. (2020). Carbon family nanomaterials for drug delivery applications. In *Nanoengineered Biomaterials for Advanced Drug Delivery*. Elsevier Ltd. https://doi.org/10.1016/b978-0-08-102985-5.00018-8

Paul, M., Itoo, A. M., Ghosh, B., & Biswas, S. (2022a). Expert Opinion on Drug Delivery Current trends in the use of human serum albumin for drug delivery in cancer. *Expert*

Opinion on Drug Delivery, *19*(11), 1449–1470. https://doi.org/10.1080/17425247.2022.2134341

Paul, M., Itoo, A. M., Ghosh, B., & Biswas, S. (2022b). Hypoxia alleviating platinum (IV)/chlorin e6-based combination chemotherapeutic-photodynamic nanomedicine for oropharyngeal carcinoma. *Journal of Photochemistry and Photobiology B: Biology*, 112627.

Paul, M., Itoo, A. M., Ghosh, B., & Biswas, S. (2023). Hypoxia alleviating platinum (IV)/chlorin e6-based combination chemotherapeutic-photodynamic nanomedicine for oropharyngeal carcinoma. *Journal of Photochemistry and Photobiology B: Biology*, *238*, 112627.

Pelicano, H., Carney, D., & Huang, P. (2004). ROS stress in cancer cells and therapeutic implications. *Drug Resistance Updates*, *7*(2), 97–110.

Pelicano, H., Martin, D. S., Xu, R. H., & Huang, P. (2006). Glycolysis inhibition for anticancer treatment. *Oncogene*, *25*(34), 4633–4646. https://doi.org/10.1038/sj.onc.1209597

Penel, N., Adenis, A., & Bocci, G. (2012). Cyclophosphamide-based metronomic chemotherapy: after 10 years of experience, where do we stand and where are we going? *Critical Reviews in Oncology/Hematology*, *82*(1), 40–50.

Peto, R., Davies, C., Godwin, J., Gray, R., Pan, H. C., Clarke, M., Cutter, D., Darby, S., McGale, P., & Taylor, C. (2012). Early Breast Cancer Trialists' Collaborative G. Comparisons between different polychemotherapy regimens for early breast cancer: meta-analyses of long-term outcome among 100,000 women in 123 randomised trials. *Lancet*, *379*(9814), 432–444.

Pirollo, K. F., & Chang, E. H. (2008). Does a targeting ligand influence nanoparticle tumor localization or uptake? *Trends in Biotechnology*, *26*(10), 552–558. https://doi.org/10.1016/j.tibtech.2008.06.007

Polyak, K. (2007). Breast cancer: origins and evolution. *The Journal of Clinical Investigation*, *117*(11), 3155–3163.

Pooresmaeil, M., & Namazi, H. (2018). β-Cyclodextrin grafted magnetic graphene oxide applicable as cancer drug delivery agent: Synthesis and characterization. *Materials Chemistry and Physics*, *218*(March), 62–69. https://doi.org/10.1016/j.matchemphys.2018.07.022

Pourjavadi, A., Tehrani, Z. M., & Moghanaki, A. A. (2016). Folate-Conjugated pH-Responsive Nanocarrier Designed for Active Tumor Targeting and Controlled Release of Gemcitabine. *Pharmaceutical Research*, *33*(2), 417–432. https://doi.org/10.1007/s11095-015-1799-7

Pradeepkumar, P., Elgorban, A. M., Bahkali, A. H., & Rajan, M. (2018). Natural solvent-assisted synthesis of amphiphilic co-polymeric nanomicelles for prolonged release of camptothecin delivery. *New Journal of Chemistry*, *42*(12), 10366–10375.

Pumera, M. (2011). Nanotoxicology: The molecular science point of view. *Chemistry - An Asian Journal*, *6*(2), 340–348. https://doi.org/10.1002/asia.201000398

Qian, B.-Z., & Pollard, J. W. (2010). Macrophage diversity enhances tumor progression and metastasis. *Cell*, *141*(1), 39–51.

Qian, R., Maiti, D., Zhong, J., Xiong, S. S., Zhou, H., Zhu, R., Wan, J., & Yang, K. (2019). T1/T2-weighted magnetic resonance imaging and SPECT imaging guided combined radioisotope therapy and chemotherapy using functionalized reduced graphene oxide-

manganese ferrite nanocomposites. *Carbon*, *149*, 55–62. https://doi.org/10.1016/j.carbon.2019.04.046

Qiu, Z., Hu, J., Li, Z., Yang, X., Hu, J., You, Q., Bai, S., Mao, Y., Hua, D., & Yin, J. (2020). Graphene oxide-based nanocomposite enabled highly efficient targeted synergistic therapy for colorectal cancer. *Colloids and Surfaces A: Physicochemical and Engineering Aspects*, *593*, 124585.

Qu, Y., Sun, F., He, F., Yu, C., Lv, J., Zhang, Q., Liang, D., Yu, C., Wang, J., Zhang, X., Xu, A., & Wu, J. (2019). Glycyrrhetinic acid-modified graphene oxide mediated siRNA delivery for enhanced liver-cancer targeting therapy. *European Journal of Pharmaceutical Sciences*, *139*(July), 105036. https://doi.org/10.1016/j.ejps.2019.105036

Rajani, C., Patel, V., Borisa, P., Karanwad, T., Polaka, S., Kalyane, D., & Tekade, R. K. (2020). Photothermal therapy as emerging combinatorial therapeutic approach. In *The future of pharmaceutical product development and research* (pp. 297–339). Elsevier.

Rana, V. K., Choi, M. C., Kong, J. Y., Kim, G. Y., Kim, M. J., Kim, S. H., Mishra, S., Singh, R. P., & Ha, C. S. (2011). Synthesis and drug-delivery behavior of chitosan-functionalized graphene oxide hybrid nanosheets. *Macromolecular Materials and Engineering*, *296*(2), 131–140. https://doi.org/10.1002/mame.201000307

Ravdin, P. M., Cronin, K. A., Howlader, N., Berg, C. D., Chlebowski, R. T., Feuer, E. J., Edwards, B. K., & Berry, D. A. (2007). The decrease in breast-cancer incidence in 2003 in the United States. *New England Journal of Medicine*, *356*(16), 1670–1674.

Recchia, F., Saggio, G., Amiconi, G., Di Blasio, A., Cesta, A., Candeloro, G., Carta, G., Necozione, S., Mantovani, G., & Rea, S. (2007). A multicenter phase II study of pegylated liposomal doxorubicin and oxaliplatin in recurrent ovarian cancer. *Gynecologic Oncology*, *106*(1), 164–169. https://doi.org/10.1016/j.ygyno.2007.03.015

Reinbolt, R. E., Mangini, N., Hill, J. L., Levine, L. B., Dempsey, J. L., Singaravelu, J., Koehler, K. A., Talley, A., & Lustberg, M. B. (2015). Endocrine therapy in breast cancer: the neoadjuvant, adjuvant, and metastatic approach. *Seminars in Oncology Nursing*, *31*(2), 146–155.

Rim, H. P., Min, K. H., Lee, H. J., Jeong, S. Y., & Lee, S. C. (2011). PH-tunable calcium phosphate covered mesoporous silica nanocontainers for intracellular controlled release of guest drugs. *Angewandte Chemie - International Edition*, *50*(38), 8853–8857. https://doi.org/10.1002/anie.201101536

Rimawi, M. F., Schiff, R., & Osborne, C. K. (2015). Targeting HER2 for the treatment of breast cancer. *Annual Review of Medicine*, *66*, 111–128.

Rizwanullah, M., Ahmad, M. Z., Ghoneim, M. M., Alshehri, S., Imam, S. S., Md, S., Alhakamy, N. A., Jain, K., & Ahmad, J. (2021). Receptor-mediated targeted delivery of surface-modifiednanomedicine in breast cancer: recent update and challenges. *Pharmaceutics*, *13*(12), 2039.

Roberts, M. R., Sucheston-Campbell, L. E., Zirpoli, G. R., Higgins, M., Freudenheim, J. L., Bandera, E. V, Ambrosone, C. B., & Yao, S. (2017). Single nucleotide variants in metastasis-related genes are associated with breast cancer risk, by lymph node involvement and estrogen receptor status, in women with European and African ancestry. *Molecular Carcinogenesis*, *56*(3), 1000–1009.

Robinson, J. T., Tabakman, S. M., Liang, Y., Wang, H., Sanchez Casalongue, H., Vinh, D., & Dai, H. (2011). Ultrasmall reduced graphene oxide with high near-infrared absorbance for photothermal therapy. *Journal of the American Chemical Society*, *133*(17), 6825–6831. https://doi.org/10.1021/ja2010175

Rosato, V., Bosetti, C., Negri, E., Talamini, R., Dal Maso, L., Malvezzi, M., Falcini, F.,

Montella, M., & La Vecchia, C. (2014). Reproductive and hormonal factors, family history, and breast cancer according to the hormonal receptor status. *European Journal of Cancer Prevention*, *23*(5), 412–417.

Sahoo, N. G., Bao, H., Pan, Y., Pal, M., Kakran, M., Cheng, H. K. F., Li, L., & Tan, L. P. (2011). Functionalized carbon nanomaterials as nanocarriers for loading and delivery of a poorly water-soluble anticancer drug: A comparative study. *Chemical Communications*, *47*(18), 5235–5237. https://doi.org/10.1039/c1cc00075f

Saldanha-araújo, F., Gratieri, T., & Gelfuso, G. M. (2019). Chitosan nanoparticles loading oxaliplatin as a mucoadhesive topical treatment of oral tumors: iontophoresis further enhances drug delivery ex vivo. *INTERNATIONAL JOURNAL OF BIOLOGICAL MACROMOLECULES*. https://doi.org/10.1016/j.ijbiomac.2019.11.001

Saleh, Y., Abdelkarim, O., Herzallah, K., & Abela, G. S. (2021). Anthracycline-induced cardiotoxicity: mechanisms of action, incidence, risk factors, prevention, and treatment. *Heart Failure Reviews*, *26*, 1159–1173.

Saloustros, E., Mavroudis, D., & Georgoulias, V. (2008). Paclitaxel and docetaxel in the treatment of breast cancer. *Expert Opinion on Pharmacotherapy*, *9*(15), 2603–2616.

Saraiva, D., Cabral, M. G., Jacinto, A., & Braga, S. (2017). How many diseases is triple negative breast cancer: the protagonism of the immune microenvironment. *Esmo Open*, *2*(4), e000208.

Satti, A., Larpent, P., & Gun'ko, Y. (2010). Improvement of mechanical properties of graphene oxide/poly (allylamine) composites by chemical crosslinking. *Carbon*, *48*(12), 3376–3381.

Sauer, D. C. E. M. J. G. (2017). A Newman LA Jemal A. *Breast Cancer Statistics*.

Scott, R. W. J., Wilson, O. M., & Crooks, R. M. (2005). Synthesis, characterization, and applications of dendrimer-encapsulated nanoparticles. In *The Journal of Physical Chemistry B* (Vol. 109, Issue 2, pp. 692–704). ACS Publications.

Seetharamu, N., Kim, E., Hochster, H., Martin, F., & Muggia, F. (2010). Phase II study of liposomal cisplatin (SPI-77) in platinum-sensitive recurrences of ovarian cancer. *Anticancer Research*, *30*(2), 541–545.

Selim, A., Lila, A., Kiwada, H., & Ishida, T. (2014). *Nanoparticles for Cancer Therapy Selective Delivery of Oxaliplatin to Tumor Tissue by Nanocarrier System Enhances Overall Therapeutic Efficacy of the Encapsulated Oxaliplatin*. *37*(2), 206–211.

Sgroi, D. C. (2010). Preinvasive breast cancer. *Annual Review of Pathology: Mechanisms of Disease*, *5*, 193–221.

Shahlaei, M., Saeidifar, M., & Zamanian, A. (2020). Increasing the effectiveness of oxaliplatin using colloidal immunoglobulin G nanoparticles: Synthesis, cytotoxicity, interaction, and release studies. *Colloids and Surfaces B: Biointerfaces*, *195*(July), 111255. https://doi.org/10.1016/j.colsurfb.2020.111255

Shan, C., Yang, H., Han, D., Zhang, Q., Ivaska, A., & Niu, L. (2009). Water-soluble graphene covalently functionalized by biocompatible poly-L-lysine. *Langmuir*, *25*(20), 12030–12033. https://doi.org/10.1021/la903265p

Shao, L., Zhang, R., Lu, J., Zhao, C., Deng, X., & Wu, Y. (2017). Mesoporous silica coated polydopamine functionalized reduced graphene oxide for synergistic targeted chemo-photothermal therapy. *ACS Applied Materials and Interfaces*, *9*(2), 1226–1236. https://doi.org/10.1021/acsami.6b11209

Sharma, G. N., Dave, R., Sanadya, J., Sharma, P., & Sharma, K. (2010). Various types and

management of breast cancer: an overview. *Journal of Advanced Pharmaceutical Technology & Research*, *1*(2), 109.

Shen, H., Zhang, L., Liu, M., & Zhang, Z. (2012). Biomedical applications of graphene. *Theranostics*, *2*(3), 283–294. https://doi.org/10.7150/thno.3642

Shen, J., Shi, M., Li, N., Yan, B., Ma, H., Hu, Y., & Ye, M. (2010). Facile synthesis and application of Ag-chemically converted graphene nanocomposite. *Nano Research*, *3*(5), 339–349. https://doi.org/10.1007/s12274-010-1037-x

Sherlock, S. P., Tabakman, S. M., Xie, L., & Dai, H. (2011). Photothermally enhanced drug delivery by ultrasmall multifunctional FeCo/graphitic shell nanocrystals. *Acs Nano*, *5*(2), 1505–1512.

Shi, J.-J., Ge, Y.-W., Fan, Z.-H., Li, Y., Jia, W.-T., & Guo, Y.-P. (2022). Graphene oxide-modified layered double hydroxide/chitosan nacre-mimetic scaffolds treat breast cancer metastasis-induced bone defects. *Carbon*, *200*, 63–74.

Shi, J., Kantoff, P. W., Wooster, R., & Farokhzad, O. C. (2017). Cancer nanomedicine: progress, challenges and opportunities. *Nature Reviews Cancer*, *17*(1), 20–37.

Siegel, R. L., Miller, K. D., & Jemal, A. (2018). Cancer statistics, 2018. *CA: A Cancer Journal for Clinicians*, *68*(1), 7–30.

Siegel, R. L., Miller, K. D., Wagle, N. S., & Jemal, A. (2023). Cancer statistics, 2023. *CA: A Cancer Journal for Clinicians*, *73*(1), 17–48.

Singh, S. K., Singh, S., Lillard Jr, J. W., & Singh, R. (2017). Drug delivery approaches for breast cancer. *International Journal of Nanomedicine*, *12*, 6205.

Smith, R. A., Andrews, K. S., Brooks, D., Fedewa, S. A., Manassaram-Baptiste, D., Saslow, D., & Wender, R. C. (2019). Cancer screening in the United States, 2019: A review of

current American Cancer Society guidelines and current issues in cancer screening. *CA: A Cancer Journal for Clinicians*, *69*(3), 184–210.

Sofias, A. M., Dunne, M., Storm, G., & Allen, C. (2017). The battle of "nano" paclitaxel. *Advanced Drug Delivery Reviews*, *122*, 20–30.

Song, Y.-Y., Li, C., Yang, X.-Q., An, J., Cheng, K., Xuan, Y., Shi, X.-M., Gao, M.-J., Song, X.-L., & Zhao, Y.-D. (2018). Graphene oxide coating core–shell silver sulfide@ mesoporous silica for active targeted dual-mode imaging and chemo-photothermal synergistic therapy against tumors. *Journal of Materials Chemistry B*, *6*(29), 4808–4820.

Song, Z., Lin, Y., Zhang, X., Feng, C., Lu, Y., Gao, Y., & Dong, C. (2017). Cyclic RGD peptide-modified liposomal drug delivery system for targeted oral apatinib administration: Enhanced cellular uptake and improved therapeutic effects. *International Journal of Nanomedicine*, *12*, 1941–1958. https://doi.org/10.2147/IJN.S125573

Sonnenschein, C., & Soto, A. M. (2016). Carcinogenesis explained within the context of a theory of organisms. *Progress in Biophysics and Molecular Biology*, *122*(1), 70–76.

Soroush, A., Farshchian, N., Komasi, S., Izadi, N., Amirifard, N., & Shahmohammadi, A. (2016). The role of oral contraceptive pills on increased risk of breast cancer in Iranian populations: a meta-analysis. *Journal of Cancer Prevention*, *21*(4), 294.

SreeHarsha, N., Maheshwari, R., Al-Dhubiab, B. E., Tekade, M., Sharma, M. C., Venugopala, K. N., Tekade, R. K., & Alzahrani, A. M. (2019). Graphene-based hybrid nanoparticle of doxorubicin. *International Journal of Nanomedicine*, *14*, 7419–7429. https://doi.org/10.2147/IJN.S211224

Stankovich, S. (2007). Dikin DA Piner RD Kohlhaas KA Kleinhammes A. *Jia Y. Wu Y. Nguyen ST Ruoff RS Carbon*, *45*(7), 1558–1565.

Stankovich, S., Piner, R. D., Chen, X., Wu, N., Nguyen, S. T., & Ruoff, R. S. (2006). Stable aqueous dispersions of graphitic nanoplatelets via the reduction of exfoliated graphite oxide in the presence of poly(sodium 4-styrenesulfonate). *Journal of Materials Chemistry*, *16*(2), 155–158. https://doi.org/10.1039/b512799h

Stankovich, S., Piner, R. D., Nguyen, S. B. T., & Ruoff, R. S. (2006). Synthesis and exfoliation of isocyanate-treated graphene oxide nanoplatelets. *Carbon*, *44*(15), 3342–3347. https://doi.org/10.1016/j.carbon.2006.06.004

Su, Y., Wang, X., Li, J., Xu, J., & Xu, L. (2015). The clinicopathological significance and drug target potential of FHIT in breast cancer, a meta-analysis and literature review. *Drug Design, Development and Therapy*, *9*, 5439.

Sudimack, J., & Lee, R. J. (2000). Targeted drug delivery via the folate receptor. *Advanced Drug Delivery Reviews*, *41*(2), 147–162. https://doi.org/10.1016/S0169-409X(99)00062-9

Sun, X., Liu, K., Lu, S., He, W., & Du, Z. (2022). Targeted therapy and immunotherapy for heterogeneous breast cancer. *Cancers*, *14*(21), 5456.

Sun, X., Liu, Z., Welsher, K., Robinson, J. T., Goodwin, A., Zaric, S., & Dai, H. (2008). Nano-graphene oxide for cellular imaging and drug delivery. *Nano Research*, *1*(3), 203–212. https://doi.org/10.1007/s12274-008-8021-8

Sun, Y. S., Zhao, Z., Yang, Z. N., Xu, F., Lu, H. J., Zhu, Z. Y., Shi, W., Jiang, J., Yao, P. P., & Zhu, H. P. (2017). Risk factors and preventions of breast cancer. *International Journal of Biological Sciences*, *13*(11), 1387–1397. https://doi.org/10.7150/ijbs.21635

Sung, H., Ferlay, J., Siegel, R. L., Laversanne, M., Soerjomataram, I., Jemal, A., & Bray, F. (2021). Global cancer statistics 2020: GLOBOCAN estimates of incidence and mortality

worldwide for 36 cancers in 185 countries. *CA: A Cancer Journal for Clinicians*, *71*(3), 209–249.

Tashiro, A., Tatsumi, S., Takeda, R., Naka, A., Matsuoka, H., Hashimoto, Y., Hatta, K., Maeda, K., & Kamoshida, S. (2014). High expression of organic anion transporter 2 and organic cation transporter 2 is an independent predictor of good outcomes in patients with metastatic colorectal cancer treated with FOLFOX-based chemotherapy. *American Journal of Cancer Research*, *4*(5), 528–536. http://www.ncbi.nlm.nih.gov/pubmed/25232494%0Ahttp://www.pubmedcentral.nih.gov/articlerender.fcgi?artid=PMC4163617

Taymaz-Nikerel, H., Karabekmez, M. E., Eraslan, S., & Kırdar, B. (2018). Doxorubicin induces an extensive transcriptional and metabolic rewiring in yeast cells. *Scientific Reports*, *8*(1), 1–14.

Teodorescu, F., Oz, Y., Queniat, G., Abderrahmani, A., Foulon, C., Lecoeur, M., Sanyal, R., Sanyal, A., Boukherroub, R., & Szunerits, S. (2017). Photothermally triggered on-demand insulin release from reduced graphene oxide modified hydrogels. *Journal of Controlled Release*, *246*, 164–173.

Thakur, K. K., Bordoloi, D., & Kunnumakkara, A. B. (2018). Alarming burden of triple-negative breast cancer in India. *Clinical Breast Cancer*, *18*(3), e393–e399.

Thakur, V., & Kutty, R. V. (2019). Recent advances in nanotheranostics for triple negative breast cancer treatment. *Journal of Experimental & Clinical Cancer Research*, *38*(1), 1–22.

Thangam, R., Gunasekaran, P., Kaveri, K., Sridevi, G., Sundarraj, S., Paulpandi, M., & Kannan, S. (2012). A novel disintegrin protein from Naja naja venom induces cytotoxicity and apoptosis in human cancer cell lines *in vitro*. *Process Biochemistry*,

47(8), 1243–1249. https://doi.org/10.1016/j.procbio.2012.04.020

Tharkar, P., Madani, A. U., Lasham, A., Shelling, A. N., & Al-Kassas, R. (2015). Nanoparticulate carriers: An emerging tool for breast cancer therapy. *Journal of Drug Targeting*, *23*(2), 97–108.

Thorn, C. F., Oshiro, C., Marsh, S., Hernandez-Boussard, T., McLeod, H., Klein, T. E., & Altman, R. B. (2011). Doxorubicin pathways: pharmacodynamics and adverse effects. *Pharmacogenetics and Genomics*, *21*(7), 440.

Tian, B., Wang, C., Zhang, S., Feng, L., & Liu, Z. (2011). Photothermally enhanced photodynamic therapy delivered by nano-graphene oxide. *ACS Nano*, *5*(9), 7000–7009. https://doi.org/10.1021/nn201560b

Torchilin, V. (2011). Tumor delivery of macromolecular drugs based on the EPR effect. *Advanced Drug Delivery Reviews*, *63*(3), 131–135. https://doi.org/10.1016/j.addr.2010.03.011

Torchilin, V. P. (2007). Targeted Pharmaceutical Nanocarriers. *The AAPS Journal*, *9*(2), 128–147.

Tran, P., Lee, S. E., Kim, D. H., Pyo, Y. C., & Park, J. S. (2020). Recent advances of nanotechnology for the delivery of anticancer drugs for breast cancer treatment. *Journal of Pharmaceutical Investigation*, *50*(3), 261–270. https://doi.org/10.1007/s40005-019-00459-7

Tuinstra, F., & Koenig, J. L. (1970). Raman spectrum of graphite. *The Journal of Chemical Physics*, *53*(3), 1126–1130.

Tummala, S., Gowthamarajan, K., & Satish Kumar, M. N. (2017). Oxaliplatin immunohybrid nanoparticles *in vitro* synergistic suppression evaluation in treatment of colorectal

cancer. *Artificial Cells, Nanomedicine and Biotechnology*, *45*(2), 261–269. https://doi.org/10.3109/21691401.2016.1146730

van Maaren, M. C., de Munck, L., Strobbe, L. J. A., Sonke, G. S., Westenend, P. J., Smidt, M. L., Poortmans, P. M. P., & Siesling, S. (2019). Ten-year recurrence rates for breast cancer subtypes in the Netherlands: a large population-based study. *International Journal of Cancer*, *144*(2), 263–272.

Vinothini, K., Rajendran, N. K., Munusamy, M. A., Alarfaj, A. A., & Rajan, M. (2019). Development of biotin molecule targeted cancer cell drug delivery of doxorubicin loaded κ-carrageenan grafted graphene oxide nanocarrier. *Materials Science and Engineering: C*, *100*, 676–687.

Vivek, R., Thangam, R., Muthuchelian, K., Gunasekaran, P., Kaveri, K., & Kannan, S. (2012). Green biosynthesis of silver nanoparticles from Annona squamosa leaf extract and its *in vitro* cytotoxic effect on MCF-7 cells. *Process Biochemistry*, *47*(12), 2405–2410. https://doi.org/10.1016/j.procbio.2012.09.025

Vivek, R., Thangam, R., & Nipunbabu, V. (2014). International Journal of Biological Macromolecules Oxaliplatin-chitosan nanoparticles induced intrinsic apoptotic signaling pathway : A " smart " drug delivery system to breast cancer cell therapy. *International Journal of Biological Macromolecules*, *65*, 289–297. https://doi.org/10.1016/j.ijbiomac.2014.01.054

Vogel, V. G. (2008). Epidemiology, genetics, and risk evaluation of postmenopausal women at risk of breast cancer. *Menopause*, *15*(4), 782–789.

Wahby, S., Fashoyin-Aje, L., Osgood, C. L., Cheng, J., Fiero, M. H., Zhang, L., Tang, S., Hamed, S. S., Song, P., & Charlab, R. (2021). FDA approval summary: accelerated approval of sacituzumab govitecan-hziy for third-line treatment of metastatic triple-

negative breast cancer. *Clinical Cancer Research*, *27*(7), 1850–1854.

Waks, A. G., & Winer, E. P. (2019). Breast cancer treatment: a review. *Jama*, *321*(3), 288–300.

Wang, B., Su, X., Liang, J., Yang, L., Hu, Q., Shan, X., Wan, J., & Hu, Z. (2018). Synthesis of polymer-functionalized nanoscale graphene oxide with different surface charge and its cellular uptake, biosafety and immune responses in Raw264.7 macrophages. *Materials Science and Engineering C*, *90*(March), 514–522. https://doi.org/10.1016/j.msec.2018.04.096

Wang, C., Zhang, C., Li, Z., Yin, S., Wang, Q., Guo, F., Zhang, Y., Yu, R., Liu, Y., & Su, Z. (2018). *Extending Half Life of H - Ferritin Nanoparticle by Fusing Albumin Binding Domain for Doxorubicin Encapsulation*. https://doi.org/10.1021/acs.biomac.7b01545

Wang, F., Ogasawara, M. A., & Huang, P. (2010). Small mitochondria-targeting molecules as anti-cancer agents. *Molecular Aspects of Medicine*, *31*(1), 75–92.

Wang, F., Sun, Q., Feng, B., Xu, Z., Zhang, J., Xu, J., & Lu, L. (2016). *Polydopamine-Functionalized Graphene Oxide Loaded with Gold Nanostars and Doxorubicin for Combined Photothermal and Chemotherapy of Metastatic Breast Cancer*. https://doi.org/10.1002/adhm.201600283

Wang, G., Li, R., Parseh, B., & Du, G. (2021). Prospects and challenges of anticancer agents' delivery via chitosan-based drug carriers to combat breast cancer: a review. *Carbohydrate Polymers*, *268*(May), 118192. https://doi.org/10.1016/j.carbpol.2021.118192

Wang, G., Wang, B., Park, J., Yang, J., Shen, X., & Yao, J. (2009). Synthesis of enhanced hydrophilic and hydrophobic graphene oxide nanosheets by a solvothermal method.

Carbon, *47*(1), 68–72. https://doi.org/10.1016/j.carbon.2008.09.002

Wang, H., & Mao, X. (2020). Evaluation of the efficacy of neoadjuvant chemotherapy for breast cancer. *Drug Design, Development and Therapy*, 2423–2433.

Wang, H., Zhou, J., Fu, Y., Zheng, Y., Shen, W., Zhou, J., & Yin, T. (2021). Deeply Infiltrating iRGD-Graphene Oxide for the Intensive Treatment of Metastatic Tumors through PTT-Mediated Chemosensitization and Strengthened Integrin Targeting-Based Antimigration. *Advanced Healthcare Materials*, *10*(16), 2100536.

Wang, X., Zhang, H., & Chen, X. (2019). Drug resistance and combating drug resistance in cancer. *Cancer Drug Resistance*, *2*(2), 141.

Wang, Y., Chen, J. T., & Yan, X. P. (2013). Fabrication of transferrin functionalized gold nanoclusters/graphene oxide nanocomposite for turn-on near-infrared fluorescent bioimaging of cancer cells and small animals. *Analytical Chemistry*, *85*(4), 2529–2535. https://doi.org/10.1021/ac303747t

Wang, Y., Li, Z., Wang, J., Li, J., & Lin, Y. (2011). Graphene and graphene oxide: Biofunctionalization and applications in biotechnology. *Trends in Biotechnology*, *29*(5), 205–212. https://doi.org/10.1016/j.tibtech.2011.01.008

Watkins, E. J. (2019). Overview of breast cancer. *Journal of the American Academy of PAs*, *32*(10), 13–17.

Wei, B., He, M., Cai, X., Hou, X., Wang, Y., Chen, J., Chen, Y., & Lou, K. (2019). *Vitamin E succinate-grafted-chitosan / chitosan oligosaccharide mixed micelles loaded with C-DMSA for Hg 2 + detection and detoxi fi cation in rat liver*.

Wei, G., Yan, M., Dong, R., Wang, D., Zhou, X., Chen, J., & Hao, J. (2012). Covalent modification of reduced graphene oxide by means of diazonium chemistry and use as a

drug-delivery system. *Chemistry - A European Journal*, *18*(46), 14708–14716. https://doi.org/10.1002/chem.201200843

Wein, L., & Loi, S. (2017). Mechanisms of resistance of chemotherapy in early-stage triple negative breast cancer (TNBC). *Breast*, *34*, S27–S30. https://doi.org/10.1016/j.breast.2017.06.023

Wexselblatt, E., & Gibson, D. (2012). What do we know about the reduction of Pt(IV) pro-drugs? *Journal of Inorganic Biochemistry*, *117*, 220–229. https://doi.org/10.1016/j.jinorgbio.2012.06.013

Wheate, N. J., Walker, S., Craig, G. E., & Oun, R. (2010). The status of platinum anticancer drugs in the clinic and in clinical trials. *Dalton Transactions*, *39*(35), 8113–8127.

Wong, B. S., Yoong, S. L., Jagusiak, A., Panczyk, T., Ho, H. K., Ang, W. H., & Pastorin, G. (2013). Carbon nanotubes for delivery of small molecule drugs. *Advanced Drug Delivery Reviews*, *65*(15), 1964–2015.

Wu, Q., Chu, M., Shao, Y., Wo, F., & Shi, D. (2016). Reduced graphene oxide conjugated with CuInS2/ZnS nanocrystals with low toxicity for enhanced photothermal and photodynamic cancer therapies. *Carbon*, *108*, 21–37.

Wu, W., Zheng, Y., Wang, R., Huang, W., Liu, L., Hu, X., Liu, S., Yue, J., Tong, T., & Jing, X. (2012). Antitumor activity of folate-targeted, paclitaxel-loaded polymeric micelles on a human esophageal EC9706 cancer cell line. *International Journal of Nanomedicine*, *7*, 3487–3502. https://doi.org/10.2147/IJN.S32620

Xiao, H., Song, H., Yang, Q., Cai, H., Qi, R., Yan, L., Liu, S., Zheng, Y., Huang, Y., & Liu, T. (2012). A prodrug strategy to deliver cisplatin (IV) and paclitaxel in nanomicelles to improve efficacy and tolerance. *Biomaterials*, *33*(27), 6507–6519.

Xing, H., Tang, L., Yang, X., Hwang, K., Wang, W., Yin, Q., Wong, N. Y., Dobrucki, L. W., Yasui, N., & Katzenellenbogen, J. A. (2013). Selective delivery of an anticancer drug with aptamer-functionalized liposomes to breast cancer cells *in vitro* and *in vivo*. *Journal of Materials Chemistry B*, *1*(39), 5288–5297.

Xiong, G., Stewart, R. L., Chen, J., Gao, T., Scott, T. L., Samayoa, L. M., O'Connor, K., Lane, A. N., & Xu, R. (2018). Collagen prolyl 4-hydroxylase 1 is essential for HIF-1α stabilization and TNBC chemoresistance. *Nature Communications*, *9*(1), 4456.

Xiong, K., Zhang, Y., Wen, Q., Luo, J., Lu, Y., Wu, Z., Wang, B., Chen, Y., Zhao, L., & Fu, S. (2020). Co-delivery of paclitaxel and curcumin by biodegradable polymeric nanoparticles for breast cancer chemotherapy. *International Journal of Pharmaceutics*, *589*, 119875.

Xu, X., Lü, S., Gao, C., Feng, C., Wu, C., Bai, X., Gao, N., Wang, Z., & Liu, M. (2016). Self-fluorescent and stimuli-responsive mesoporous silica nanoparticles using a double-role curcumin gatekeeper for drug delivery. *Chemical Engineering Journal*, *300*, 185–192. https://doi.org/10.1016/j.cej.2016.04.087

Xu, Y., Du, Y., Yuan, H., Liu, L., Niu, Y., & Hu, F. (2011). *Improved cytotoxicity and multidrug resistance reversal of chitosan based polymeric micelles encapsulating oxaliplatin*. *19*(May 2010), 344–353. https://doi.org/10.3109/1061186X.2010.499465

Xu, Z., Wang, S., Li, Y., Wang, M., Shi, P., & Huang, X. (2014). Covalent functionalization of graphene oxide with biocompatible poly(ethylene glycol) for delivery of paclitaxel. *ACS Applied Materials and Interfaces*, *6*(19), 17268–17276. https://doi.org/10.1021/am505308f

Yaghobi Joybari, A., Sarbaz, S., Azadeh, P., Mirafsharieh, S. A., Rahbari, A., Farasatinasab, M., & Mokhtari, M. (2014). Oxaliplatin-Induced Renal Tubular Vacuolization. *Annals*

of Pharmacotherapy, *48*(6), 796–800. https://doi.org/10.1177/1060028014526160

Yamaguchi, N., Fujii, T., Aoi, S., Kozuch, P. S., Hortobagyi, G. N., & Blum, R. H. (2015). Comparison of cardiac events associated with liposomal doxorubicin, epirubicin and doxorubicin in breast cancer: a Bayesian network meta-analysis. *European Journal of Cancer*, *51*(16), 2314–2320.

Yamamoto, Y., Nagasaki, Y., Kato, Y., Sugiyama, Y., & Kataoka, K. (2001). Long-circulating poly(ethylene glycol)-poly(D,L-lactide) block copolymer micelles with modulated surface charge. *Journal of Controlled Release*, *77*(1–2), 27–38. https://doi.org/10.1016/S0168-3659(01)00451-5

Yan, M., Liu, Y., Zhu, X., Wang, X., Liu, L., Sun, H., Wang, C., Kong, D., & Ma, G. (2019). Nanoscale Reduced Graphene Oxide-Mediated Photothermal Therapy Together with IDO Inhibition and PD-L1 Blockade Synergistically Promote Antitumor Immunity. *ACS Applied Materials and Interfaces*, *11*(2), 1876–1885. https://doi.org/10.1021/acsami.8b18751

Yang, C., Liu, H. Z., Fu, Z. X., & Lu, W. D. (2011). Oxaliplatin long-circulating liposomes improved therapeutic index of colorectal carcinoma. *BMC Biotechnology*, *11*. https://doi.org/10.1186/1472-6750-11-21

Yang, K., Feng, L., & Liu, Z. (2016). Stimuli responsive drug delivery systems based on nano-graphene for cancer therapy. *Advanced Drug Delivery Reviews*, *105*, 228–241. https://doi.org/10.1016/j.addr.2016.05.015

Yang, K., Feng, L., Shi, X., & Liu, Z. (2013). Nano-graphene in biomedicine: Theranostic applications. *Chemical Society Reviews*, *42*(2), 530–547. https://doi.org/10.1039/c2cs35342c

Yang, K., Wan, J., Zhang, S., Tian, B., Zhang, Y., & Liu, Z. (2012). The influence of surface chemistry and size of nanoscale graphene oxide on photothermal therapy of cancer using ultra-low laser power. *Biomaterials*, *33*(7), 2206–2214. https://doi.org/10.1016/j.biomaterials.2011.11.064

Yang, K., Wan, J., Zhang, S., Zhang, Y., Lee, S.-T., & Liu, Z. (2011). *In vivo* pharmacokinetics, long-term biodistribution, and toxicology of PEGylated graphene in mice. *ACS Nano*, *5*(1), 516–522.

Yang, K., Zhang, S., Zhang, G., Sun, X., Lee, S. T., & Liu, Z. (2010). Graphene in mice: Ultrahigh *in vivo* tumor uptake and efficient photothermal therapy. *Nano Letters*, *10*(9), 3318–3323. https://doi.org/10.1021/nl100996u

Yang, S. T., Wang, X., Jia, G., Gu, Y., Wang, T., Nie, H., Ge, C., Wang, H., & Liu, Y. (2008). Long-term accumulation and low toxicity of single-walled carbon nanotubes in intravenously exposed mice. *Toxicology Letters*, *181*(3), 182–189. https://doi.org/10.1016/j.toxlet.2008.07.020

Yang, X., Niu, G., Cao, X., Wen, Y., Xiang, R., Duan, H., & Chen, Y. (2012). The preparation of functionalized graphene oxide for targeted intracellular delivery of siRNA. *Journal of Materials Chemistry*, *22*(14), 6649–6654.

Yang, X., Wang, Y., Huang, X., Ma, Y., Huang, Y., Yang, R., Duan, H., & Chen, Y. (2011). Multi-functionalized graphene oxide based anticancer drug-carrier with dual-targeting function and pH-sensitivity. *Journal of Materials Chemistry*, *21*(10), 3448–3454. https://doi.org/10.1039/c0jm02494e

Yang, X., Zhang, X., Liu, Z., Ma, Y., Huang, Y., & Chen, Y. (2008). High-efficiency loading and controlled release of doxorubicin hydrochloride on graphene oxide. *Journal of Physical Chemistry C*, *112*(45), 17554–17558. https://doi.org/10.1021/jp806751k

Yang, X., Zhang, X., Ma, Y., Huang, Y., Wang, Y., & Chen, Y. (2009). Superparamagnetic graphene oxide-Fe3O4 nanoparticles hybrid for controlled targeted drug carriers. *Journal of Materials Chemistry*, *19*(18), 2710–2714. https://doi.org/10.1039/b821416f

Yang, Y., Zhang, Y. M., Chen, Y., Zhao, D., Chen, J. T., & Liu, Y. (2012). Construction of a graphene oxide based noncovalent multiple nanosupramolecular assembly as a scaffold for drug delivery. *Chemistry - A European Journal*, *18*(14), 4208–4215. https://doi.org/10.1002/chem.201103445

Yin, J., Lang, T., Cun, D., Zheng, Z., Huang, Y., Yin, Q., & Yu, H. (2017). *T h e r a n o s t i c s pH-Sensitive Nano-Complexes Overcome Drug Resistance and Inhibit Metastasis of Breast Cancer by Silencing Akt Expression*. *7*(17). https://doi.org/10.7150/thno.21516

Yin, L., Duan, J., Bian, X., & Yu, S. (2020). *Triple-negative breast cancer molecular subtyping and treatment progress*. 1–13.

Yogesh, G. K., Shuaib, E. P., Roopmani, P., Gumpu, M. B., Krishnan, U. M., & Sastikumar, D. (2020). Synthesis, characterization and bioimaging application of laser-ablated graphene-oxide nanoparticles (nGOs). *Diamond and Related Materials*, *104*(January), 107733. https://doi.org/10.1016/j.diamond.2020.107733

Yuan, Z., Yuan, Y., Huang, X., & Gao, F. (2018). *Bufalin-loaded vitamin E succinate-grafted- chitosan oligosaccharide / RGD conjugated TPGS mixed micelles demonstrated improved antitumor activity against drug-resistant colon cancer*. 7533–7548.

Zaaba, N. I., Foo, K. L., Hashim, U., Tan, S. J., Liu, W.-W., & Voon, C. H. (2017). Synthesis of graphene oxide using modified hummers method: solvent influence. *Procedia Engineering*, *184*, 469–477.

Zagouri, F., Sergentanis, T. N., Bartsch, R., Berghoff, A. S., Chrysikos, D., de Azambuja, E.,

Dimopoulos, M.-A., & Preusser, M. (2013). Intrathecal administration of trastuzumab for the treatment of meningeal carcinomatosis in HER2-positive metastatic breast cancer: a systematic review and pooled analysis. *Breast Cancer Research and Treatment*, *139*, 13–22.

Zalba, S., & Garrido, M. J. (2013). Liposomes, a promising strategy for clinical application of platinum derivatives. *Expert Opinion on Drug Delivery*, *10*(6), 829–844.

Zelek, L., Cottu, P., Tubiana-Hulin, M., Vannetzel, J. M., Chollet, P., Misset, J. L., Chouaki, N., Marty, M., Gamelin, E., Culine, S., Dieras, V., Mackenzie, S., & Spielmann, M. (2002). Phase II study of oxaliplatin and fluorouracil in taxane- and anthracycline-pretreated breast cancer patients. *Journal of Clinical Oncology*, *20*(10), 2551–2558. https://doi.org/10.1200/JCO.2002.06.164

Zelnak, A. B., & O'Regan, R. M. (2015). Optimizing endocrine therapy for breast cancer. *Journal of the National Comprehensive Cancer Network*, *13*(8), e56–e64.

Zeng, Y., Yang, Z., Luo, S., Li, H., Liu, C., Hao, Y., Liu, J., Wang, W., & Li, R. (2015). Fast and facile preparation of PEGylated graphene from graphene oxide by lysosome targeting delivery of photosensitizer to efficiently enhance photodynamic therapy. *RSC Advances*, *5*(71), 57725–57734.

Zhang, C., Liu, Z., Zheng, Y., Geng, Y., Han, C., Shi, Y., Sun, H., Zhang, C., Chen, Y., & Zhang, L. (2018). Glycyrrhetinic acid functionalized graphene oxide for mitochondria targeting and cancer treatment *in vivo*. *Small*, *14*(4), 1703306.

Zhang, D. D., Zu, S. Z., & Han, B. H. (2009). Inorganic-organic hybrid porous materials based on graphite oxide sheets. *Carbon*, *47*(13), 2993–3000. https://doi.org/10.1016/j.carbon.2009.06.052

Zhang, H., Li, Y., Pan, Z., Chen, Y., Fan, Z., Tian, H., Zhou, S., Zhang, Y., Shang, J., Jiang, B., Wang, F., Luo, F., & Hou, Z. (2019). Multifunctional Nanosystem Based on Graphene Oxide for Synergistic Multistage Tumor-Targeting and Combined Chemo-Photothermal Therapy. *Molecular Pharmaceutics*, *16*(5), 1982–1998. https://doi.org/10.1021/acs.molpharmaceut.8b01335

Zhang, L., Lu, Z., Zhao, Q., Huang, J., Shen, H., & Zhang, Z. (2011). Enhanced chemotherapy efficacy by sequential delivery of siRNA and anticancer drugs using PEI-grafted graphene oxide. *Small*, *7*(4), 460–464. https://doi.org/10.1002/smll.201001522

Zhang, L., Xia, J., Zhao, Q., Liu, L., & Zhang, Z. (2010). Functional graphene oxide as a nanocarrier for controlled loading and targeted delivery of mixed anticancer drugs. *Small*, *6*(4), 537–544. https://doi.org/10.1002/smll.200901680

Zhang, M., Lee, A. V, & Rosen, J. M. (2017). The cellular origin and evolution of breast cancer. *Cold Spring Harbor Perspectives in Medicine*, *7*(3), a027128.

Zhang, S., Lovejoy, K. S., Shima, J. E., Lagpacan, L. L., Shu, Y., Lapuk, A., Chen, Y., Komori, T., Gray, J. W., Chen, X., Lippard, S. J., & Giacomini, K. M. (2006). Organic cation transporters are determinants of oxaliplatin cytotoxicity. *Cancer Research*, *66*(17), 8847–8857. https://doi.org/10.1158/0008-5472.CAN-06-0769

Zhang, W., Guo, Z., Huang, D., Liu, Z., Guo, X., & Zhong, H. (2011). Synergistic effect of chemo-photothermal therapy using PEGylated graphene oxide. *Biomaterials*, *32*(33), 8555–8561. https://doi.org/10.1016/j.biomaterials.2011.07.071

Zhang, W., Seymour, L., & Chen, E. X. (2008). Determination of intact oxaliplatin in human plasma using high performance liquid chromatography-tandem mass spectrometry. *Journal of Chromatography B: Analytical Technologies in the Biomedical and Life Sciences*, *876*(2), 277–282. https://doi.org/10.1016/j.jchromb.2008.10.055

Zhang, W., Shen, J., Su, H., Mu, G., Sun, J. H., Tan, C. P., Liang, X. J., Ji, L. N., & Mao, Z. W. (2016). Co-Delivery of Cisplatin Prodrug and Chlorin e6 by Mesoporous Silica Nanoparticles for Chemo-Photodynamic Combination Therapy to Combat Drug Resistance. *ACS Applied Materials and Interfaces*, *8*(21), 13332–13340. https://doi.org/10.1021/acsami.6b03881

Zhang, Y., Ali, S. F., Dervishi, E., Xu, Y., Li, Z., Casciano, D., & Biris, A. S. (2010). Cytotoxicity effects of graphene and single-wall carbon nanotubes in neural phaeochromocytoma-derived pc12 cells. *ACS Nano*, *4*(6), 3181–3186. https://doi.org/10.1021/nn1007176

Zhang, Z., Schniepp, H. C., & Adamson, D. H. (2019). Characterization of graphene oxide: Variations in reported approaches. *Carbon*, *154*, 510–521. https://doi.org/10.1016/j.carbon.2019.07.103

Zhao, S., Xu, M., Cao, C., Yu, Q., Zhou, Y., & Liu, J. (2017). A redox-responsive strategy using mesoporous silica nanoparticles for co-delivery of siRNA and doxorubicin. *Journal of Materials Chemistry B*, *5*(33), 6908–6919.

Zhen, S. J., Wang, T. T., Liu, Y. X., Wu, Z. L., Zou, H. Y., & Huang, C. Z. (2018). Reduced graphene oxide coated Cu2−xSe nanoparticles for targeted chemo-photothermal therapy. *Journal of Photochemistry and Photobiology B: Biology*, *180*(February), 9–16. https://doi.org/10.1016/j.jphotobiol.2018.01.020

Zheng, M., Liu, S., Li, J., Qu, D., Zhao, H., Guan, X., Hu, X., Xie, Z., Jing, X., & Sun, Z. (2014). Integrating oxaliplatin with highly luminescent carbon dots: an unprecedented theranostic agent for personalized medicine. *Advanced Materials*, *26*(21), 3554–3560.

Zheng, M., Yue, C., Ma, Y., Gong, P., Zhao, P., Zheng, C., Sheng, Z., Zhang, P., Wang, Z., & Cai, L. (2013). Single-step assembly of DOX/ICG loaded lipid–polymer nanoparticles for highly effective chemo-photothermal combination therapy. *ACS Nano*, *7*(3), 2056–2067.

Zheng, X. T., & Li, C. M. (2012). Restoring basal planes of graphene oxides for highly efficient loading and delivery of β-lapachone. *Molecular Pharmaceutics*, *9*(3), 615–621. https://doi.org/10.1021/mp2005356

Zhong, Y., Meng, F., Deng, C., & Zhong, Z. (2014). Ligand-directed active tumor-targeting polymeric nanoparticles for cancer chemotherapy. *Biomacromolecules*, *15*(6), 1955–1969.

Zhou, Y., Li, J., Lu, F., Deng, J., Zhang, J., Fang, P., Peng, X., & Zhou, S. F. (2015). Astudy on the hemocompatibility of dendronized chitosan derivatives in red blood cells. *Drug Design, Development and Therapy*, *9*, 2635–2645. https://doi.org/10.2147/DDDT.S77105

Zhou, Y., Quan, G., Wu, Q., Zhang, X., Niu, B., Wu, B., Huang, Y., Pan, X., & Wu, C. (2018). Mesoporous silica nanoparticles for drug and gene delivery. *Acta Pharmaceutica Sinica B*, *8*(2), 165–177.

Zhou, Z., Huang, D., Bao, J., Chen, Q., Liu, G., Chen, Z., Chen, X., & Gao, J. (2012). A synergistically enhanced T1–T2 dual-modal contrast agent. *Advanced Materials*, *24*(46), 6223–6228.

Zhu, B., Wu, H., Tu, S., Li, S., Liu, J., Wei, J., Ding, J., & Zhuang, X. (2017). Graphene oxide-reinforced thermo-sensitive hydrogel consistently release alendronate for enhanced cranial defect repair. *Journal of Controlled Release*, *259*, e12–e13.

Zhu, H., Zhang, B., Zhu, N., Li, M., & Yu, Q. (2021). Mitochondrion targeting peptide-modified magnetic graphene oxide delivering mitoxantrone for impairment of tumor mitochondrial functions. *Chinese Chemical Letters*, *32*(3), 1220–1223. https://doi.org/10.1016/j.cclet.2020.09.003

Zhu, Q., Sun, F., Li, T., Zhou, M., Ye, J., Ji, A., Wang, H., Ding, C., Chen, H., Xu, Z., & Yu, H. (2021). Engineering Oxaliplatin Prodrug Nanoparticles for Second Near-Infrared Fluorescence Imaging-Guided Immunotherapy of Colorectal Cancer. *Small*, *17*(13), 1–11. https://doi.org/10.1002/smll.202007882

Zhu, X., Feng, W., Chang, J., Tan, Y.-W., Li, J., Chen, M., Sun, Y., & Li, F. (2016). Temperature-feedback upconversion nanocomposite for accurate photothermal therapy at facile temperature. *Nature Communications*, *7*(1), 10437.

Zhu, X., Huang, C., Li, N., Ma, X., Li, Z., & Fan, J. (2023). Distinct roles of graphene and graphene oxide nanosheets in regulating phospholipid flip-flop. *Journal of Colloid and Interface Science*, *637*, 112–122. https://doi.org/https://doi.org/10.1016/j.jcis.2023.01.080

Zhu, X., Yu, Z., Feng, L., Deng, L., Fang, Z., Liu, Z., Li, Y., Wu, X., Qin, L., Guo, R., & Zheng, Y. (2021). Chitosan-based nanoparticle co-delivery of docetaxel and curcumin ameliorates anti-tumor chemoimmunotherapy in lung cancer. *Carbohydrate Polymers*, *268*(November 2020), 118237. https://doi.org/10.1016/j.carbpol.2021.118237

Zou, L., Wang, H., He, B., Zeng, L., Tan, T., Cao, H., He, X., Zhang, Z., Guo, S., & Li, Y. (2016). Current approaches of photothermal therapy in treating cancer metastasis with nanotherapeutics. *Theranostics*, *6*(6), 762.

Zu, S. Z., & Han, B. H. (2009). Aqueous dispersion of graphene sheets stabilized by pluronic copolymers:Formation of supramolecular hydrogel. *Journal of Physical Chemistry C*, *113*(31), 13651–13657. https://doi.org/10.1021/jp9035887

Appendix

List of Publications/Patent/Conferences

Publications

[1] **Itoo, Asif Mohd**, Balaram Ghosh, and Swati Biswas. "Recent advancements in Nanotechnology-Mediated Platinum-Based cancer therapy." ***Coordination Chemistry Reviews*** 508 (2024): 215796. https://doi.org/10.1016/j.ccr.2024.215796

[2] Padaga, Sri Ganga, Himanshu Bhatt, Sanjay Ch, Milan Paul, **Asif Mohd Itoo**, Balaram Ghosh, Sanhita Roy, and Swati Biswas. "Glycol Chitosan-Poly (lactic acid) Conjugate Nanoparticles Encapsulating Ciprofloxacin: A Mucoadhesive, Antiquorum-Sensing, and Biofilm-Disrupting Treatment Modality for Bacterial Keratitis. ***ACS Applied Materials and Interfaces***. https://doi.org/10.1021/acsami.3c18061

[3] **Itoo, Asif Mohd**, Milan Paul, Balaram Ghosh, and Swati Biswas. "Polymeric graphene oxide nanoparticles loaded with doxorubicin for combined photothermal and chemotherapy in triple-negative breast cancer." ***Biomaterials Advances*** 153 (2023): 213550. https://doi.org/10.1016/j.bioadv.2023.213550.

[4] Patel, Tarun, **Asif Mohd Itoo**, Milan Paul, Likhitha Purna Kondapaneni, Balaram Ghosh, and Swati Biswas. "Block HPMA-based pH-sensitive gemcitabine pro-drug nanoaggregates for cancer treatment." ***European Polymer Journal*** 186 (2023): 111843. https://doi.org/10.1016/j.eurpolymj.2023.111843.

[5] **Asif, Itoo Mohd,** Paul Milan, Ganga Sri Padaga, and Biswas Swati. "Combination Nanotherapy: Stronger Weapon to win Cancer Battle. ***CRS Newsletter*** 14, 36-42.

[6] Paul, Milan, **Asif Mohd Itoo**, Balaram Ghosh, and Swati Biswas. "Hypoxia alleviating platinum (IV)/chlorin e6-based combination chemotherapeutic-photodynamic nanomedicine for oropharyngeal carcinoma." ***Journal of Photochemistry and Photobiology B: Biology*** 238 (2023): 112627. https://doi.org/10.1016/j.jphotobiol.2022.112627.

[7] **Itoo, Asif Mohd**, Milan Paul, Sri Ganga Padaga, Balaram Ghosh, and Swati Biswas. "Nanotherapeutic intervention in photodynamic therapy for cancer." ***ACS omega*** 7, no. 50 (2022): 45882-45909. https://doi.org/10.1021/acsomega.2c05852.

[8] Paul, Milan, **Asif Mohd Itoo**, Balaram Ghosh, and Swati Biswas. "Current trends in the use of human serum albumin for drug delivery in cancer." ***Expert Opinion on Drug Delivery*** 19, no. 11 (2022): 1449-1470. https://doi.org/10.1080/17425247.2022.2134341.

[9] Parmanik, Ankita, Anindya Bose, Bhavna Ghosh, Milan Paul, **Asif Itoo**, Swati Biswas, and Manoranjan Arakha. "Development of triphala churna extract mediated iron oxide

nanoparticles as novel treatment strategy for triple negative breast cancer." ***Journal of Drug Delivery Science and Technology*** 76 (2022): 103735. https://doi.org/10.1016/j.jddst.2022.103735.

[10] **Itoo, Asif Mohd**, Sree Lakshmi Vemula, Mahima Tejasvni Gupta, Mahesh Vilasrao Giram, Sangishetty Akhil Kumar, Balaram Ghosh, and Swati Biswas. "Multifunctional graphene oxide nanoparticles for drug delivery in cancer." ***Journal of Controlled Release*** 350 (2022): 26-59. https://doi.org/10.1016/j.jconrel.2022.08.011.

[11] **Itoo, Asif Mohd**, Milan Paul, Balaram Ghosh, and Swati Biswas. "Oxaliplatin delivery via chitosan/vitamin E conjugate micelles for improved efficacy and MDR-reversal in breast cancer." Carbohydrate Polymers 282 (2022): 119108. https://doi.org/10.1016/j.carbpol.2022.119108.

[12] Kumbham, Soniya, Milan Paul, **Asif Itoo**, Balaram Ghosh, and Swati Biswas. "Oleanolic acid-conjugated human serum albumin nanoparticles encapsulating doxorubicin as synergistic combination chemotherapy in oropharyngeal carcinoma and melanoma." ***International journal of pharmaceutics*** 614 (2022): 121479. https://doi.org/10.1016/j.ijpharm.2022.121479.

Manuscripts under communication

[1] Biotinylated graphene oxide-conjugated platinum(IV) prodrug nanoparticles for targeted and chemo-photothermal combination therapy in breast Cancer, **First Author,** Under Review (Biomaterials Advances).

Patent

[1] Photothermal chemotherapeutic composition comprising polyethylene glycol (PEG) coated graphene-oxide conjugated to Pt (IV) anticancer prodrug: Swati Biswas, Balaram Ghosh, **Asif Mohd Itoo**, Milan Paul: Patent Authority BITS-Pilani: Indian Patent Application Number: 202311082369, Dec 4, 2023.

Conference Presentations/Proceedings

[1] Polymeric Graphene Oxide Nanoparticles Loaded with Doxorubicin for Combined Photothermal and Chemotherapy in Triple Negative Breast Cancer: **Asif Mohd Itoo**, Milan Paul, Balaram Ghosh, Swati Biswas: ***CRS-IC, 21st International Symposium on Advances in Technology and Business Potential of New Drug Delivery Systems*** at

Mukesh Patel Auditorium, NMIMS Campus, Mumbai-400047, India. Feb 24 - 25, 2023.

[2] Polymeric Graphene Oxide Nanoparticles Loaded with Doxorubicin for Combined Photothermal and Chemotherapy in Triple Negative Breast Cancer: **Asif Mohd Itoo**, Milan Paul, Balaram Ghosh, Swati Biswas, ***National Symposium on Convergence of Chemistry & Materials (CCM-2023)*** at Birla Institute of Technology and Science-Pilani Hyderabad Campus, Telangana, India 500078 on 6-7 January 2023.

[3] Multifunctional graphene oxide Nanomedicine for breast cancer therapy. **Asif Mohd Itoo**, Milan Paul, Balaram Ghosh, Swati Biswas. ***20th International e- symposium On Advances in technology and business potential of new drug delivery systems***; Date: 24th-26th February 2021.

[4] Harnessing Chitosan Vitamin E Succinate Conjugated Supramolecular Micellar Nanoaggregate for Effective Loading of Oxaliplatin as Breast Cancer Therapy: **Asif Mohd Itoo**, Milan Paul, Balaram Ghosh, Swati Biswas***: CRS-IC, 19th International e- symposium On Advances in technology and business potential of new drug delivery systems***; Date: 25th-27th February 2021.

Biography

Biography of Asif Mohd Itoo

Mr. Asif Mohd Itoo completed his Bachelor of Pharmacy from the University of Kashmir, Hazratbal, Srinagar, Jammu and Kashmir, India, in 2017. Subsequently, he pursued his Master of Pharmacy in Pharmaceutics from the same university, completing it in 2019. During his master's program, he worked as a research intern in R&D at Sun Pharma Industries Ltd, Gurgaon, India. Mr. Asif Mohd Itoo joined the Nanomedicine Research Laboratory under Prof. Swati Biswas in the Department of Pharmacy at BITS Pilani Hyderabad Campus to pursue his doctoral research. He worked on "Polymeric Micelles and Multifunctional Graphene Oxide Nanomedicine for Breast Cancer Therapy." Moreover, Asif Mohd Itoo has received a junior and senior research fellowship from the Lady Tata Memorial Trust-India (LTMT) to carry out his Ph.D. research work. Furthermore, he was awarded the first prize for the poster presentation at the 21st International Symposium on Advances in Technology and Business Potential of New Drug Delivery Systems, organized by the Controlled Release Society India chapter (CRS-IC), held in Mumbai, India, on February 24-25, 2023. Recognized with this prestigious award, he has been sponsored by CRS-IC to attend the CRS 2023 Annual Meeting and Expo on Advanced Delivery Science in Las Vegas, Nevada, USA, from July 24th to 28th, 2023. His scholarly contributions include five peer-reviewed scientific publications as the first author and seven as a co-author in reputed international journals. Additionally, he has filed one Indian Patent application and presented papers at various international conferences.

Biography of Prof. Swati Biswas

Prof. Swati Biswas currently serves as a professor in the Department of Pharmacy at Birla Institute of Technology and Science, Pilani, Hyderabad Campus. She obtained her B. Pharm degree in 1998 and M. Pharm in 2000 from Jadavpur University, India. In 2008, she earned her Ph.D. in Pharmaceutical Sciences from Wayne State University, USA. Following the completion of her doctoral studies, she joined as a Postdoctoral Research Associate (March 2009-June 2013) at the Center for Pharmaceutical Biotechnology and Nanomedicine, Department of Pharmaceutical Sciences at Northeastern University, USA (2013). In 2013, she joined BITS-Pilani Hyderabad campus as an Assistant Professor (June 2013-June 2018), later progressing to Associate Professor (June 2018-June 2022), and currently holding the position of Professor (since June 2022). Her research interests encompass drug delivery and targeting, nanomedicine, multifunctional and stimuli-sensitive pharmaceutical nanocarriers, biomedical polymers, and experimental ocular infections and cancer therapy. Prof. Biswas has an impressive academic record with over 120 research publications, two US patents, and seven Indian Patents granted and published, along with 19 patents filed. Google Scholar reflects more than 7,000 citations of her papers, with an H-index of 39. Prof. Biswas is an editorial advisory board member for ACS Publications' Molecular Pharmaceutics for the tenure 2021-2023 and serves as an associate editor for the journal Frontiers in Biomaterials Sciences in the specialty section of delivery systems and controlled release since 2021. Recognized as one of the world's top 2% scientists in the years 2019, 2021, and 2022 in the fields of pharmacology, pharmacy, nanoscience & nanotechnology, and clinical medicine, she continues to contribute significantly to her field. Having successfully completed numerous sponsored projects, Prof. Biswas is currently managing projects sponsored by DST, DBT, and ICMR. She has supervised eight Ph.D. students and is currently guiding nine students in their Ph.D. work.